BULETINUL INSTITUTULUI POLITEHNIC DIN IASI

Publicat de
UNIVERSITATEA TEHNICĂ "GH. ASACHI", IAŞI

Tomul LIII (LVII)

Fasc. 1

Secția
ŞTIINȚA ŞI INGINERIA MATERIALELOR

2007

BULETINUL INSTITUTULUI POLITEHNIC DIN IAŞI
BULLETIN OF THE POLYTECHNIC INSTITUTE OF IAŞI
Tomul LIII (LVII) 2007

MATERIALS SCIENCE AND ENGINEERING

CONTENTS

BULETINUL INSTITUTULUI POLITEHNIC DIN IAŞI
BULLETIN OF THE POLYTECHNIC INSTITUTE OF IAŞI
Tomul LIII (LVII) 2007

STIINTA SI INGINERIA MATERIALELOR

CUPRINS

BULETINUL INSTITUTULUI POLITEHNIC DIN IAŞI
Tomul LIII (LVII), Fasc. 1, 2007
Secția
ŞTIINȚA ŞI INGINERIA MATERIALELOR

EFFECT OF MECHANICAL ALLOYED TERNARY Ni-Fe-W ADDITION ON THE MICROSTRUCTURAL EVOLUTION OF LIQUID PHASE SINTERED TUNGSTEN HEAVY ALLOYS

BY

BURAK ÖZKAL[(1)], MERT CANARAN[(2)] and M. LUTFI ÖVECOGLU[(1)]

Abstract: The comparative high temperature sintering behaviors of W-Ni-Fe heavy alloy systems prepared with addition of the mechanical alloyed ternary Ni-Fe-W fraction were investigated. In order to achieve this, preblended powder mixtures constituting the composition of 56Ni-24Fe-20W were mechanically alloyed in an attritor mill up to 50 hours and the mechanical alloyed composition was added to initial W powder to obtain heavy alloys mixtures ranging 75 to 95 W (balance 7/3 Ni:Fe). After compaction and liquid phase sintering at high temperatures, samples were characterized by analytical microscopy techniques. Microstructural homogenization and fineness were obtained with the increasing mechanical alloying time and these features led to early densification in comparison with no mechanical alloyed counterparts. Although selection of higher sintering temperatures normalized the positive effects of the mechanical alloyed additions, by selection of lower sintering temperatures, it is possible to produce tungsten heavy alloys having relatively smaller grain sizes.

Keywords: tungsten heavy alloys, mechanical alloying and liquid phase sintering

1. Introduction

Tungsten heavy alloys (WHAs) are a category of tungsten-based materials that typically contain more than 80 wt% W along with the alloying elements of transition metals like Ni, Fe and Co. WHAs have two phase typical microstructure consist of the principal phase being nearly pure tungsten in association with a binder phase also called as matrix containing the transition metals and dissolved tungsten in it and liquid phase sintering (LPS) is the usual applied practice to reach full densities for WHAs [1].

Therefore a typical liquid phase sintered W-Ni-Fe heavy alloy microstructure is consisted from two contiguous phases; spherical W grains in the Ni-Fe-W matrix. Solubility of tungsten in the matrix phase is the major driving force for the rapid densification via solution-precipitation process during liquid phase sintering. Although mass transfer through liquid phase leads to densification, microstructural coarsening which degrades mechanical properties occurs inevitably during same process. Also in most cases heating rate to liquid phase sintering temperature is not so slow therefore tungsten diffusion to matrix can not reach to the thermodynamically possible levels prior to liquid formation.

For a multi-ingredient liquid forming system like Ni and Fe in W-Ni-Fe heavy alloy system, first melting realizes around the Ni rich and Fe rich regions and compositional homogenization within the matrix phase can not be accomplished during early densification stage unless pre-alloyed powders are not used as starting

material. Therefore by mechanical alloying of WHA elemental powders [2] or by mechanical alloying of a powder mixture near to matrix phase composition [3], the diffusion distances can be reduced.

The mechanical distribution of W phase, in the Ni and Fe rich regions prior to liquid formation was the motivation behind this study. In our early works [4, 5], mechanical alloying of same system was only discussed for solid state sintering stage. In this work more detailed discussion were done after focusing on a broader composition range of heavy alloys and investigating kinetics of sintering.

2. Experimental procedure

Elemental Ni, Fe powders which were produced by atomization were screened using 38 μm sieve and the finer fraction mixed together with the W powders having the average particle size of 6 μm to constitute 56Ni-24Fe-20W alloy composition. Preblended powder mixture of 56Ni-24Fe-20W was mechanically alloyed for 10, 20, 30, 40, 50 hours. Mechanically alloying performed in ethyl alcohol using attritor (Union Process 01-HD). For the experiments WC balls (D = 6.25 mm) were selected as milling media and ball to powder weight ratio (BPR) was maintained as 5:1 and 500 rpm attritor shaft speed were selected. Attrition was performed up to 50 hours and every 10 hours samples were withdrawn from the system and adjustment were done to keep the upper mentioned parameters constant.

In first set, in order to see the effect of mechanical alloying time, the mechanically alloyed powders were mixed with suitable amount of initial W powder to obtain the powder mixtures having exactly 90W7Ni3Fe heavy alloy composition. A second experimental set was also prepared by using only 50 hours mechanically alloyed powder mixture to obtain the target compositions of 75W-80W-85W-90W-95W-(7/3 Ni:Fe) heavy alloys. Resultant powder mixtures were compacted into cylindrical shapes under 150 MPa and liquid phase sintered at 1460^{o}C and 1500^{o}C under a protective atmosphere.

In the experimental studies; scanning electron microscopy (SEM) observations of mechanical alloyed powders were carried out to observe degree of homogeneity after mechanical alloying. Dilatometric studies were performed to observe online sintering behavior of compacts. Characterization of after sintering samples were performed by density measurements according to Archimedes Principles and optical microscopy observations were realized from the polished sample surfaces and hardness values were also measured in order to characterize the processing effects.

3. Experimental Results and Discussion

Compaction Behaviour of Prepared Powders

As it can be followed from Table.1 by the increase of mechanical alloying time a decreasing trend was obtained for the green density values for the compacts after pressing at 150 MPa. This behavior is related with degree of deformation were attained during mechanical alloying of 56Ni-24Fe-20W powders. It is expected behavior for ductile Ni and Fe powders to reach higher surface area and finer particle size

characteristics by means of effective deformation during mechanical alloying. It is clear that packaging characteristics of initial powders were negatively affected after mechanical alloying; the compact prepared directly from initial powders has approximately 5 % less porosity compared to 50 hours mechanical alloyed counterpart (Table 1).

Both Secondary electron image (SEI) and backscattered electron image (BEI) mode SEM micrographs of the fracture surfaces of after 150 MPa compaction of 90W7Ni3Fe heavy alloy powders (prepared from 50 h MA`ed 56Ni24Fe20W powders) were given in Figure 1 for different magnifications. Ni and Fe rich dark regions can easily be followed from BEI images in compare to tungsten rich white areas. However it should be noted that darker Ni and Fe rich regions have also 20 % W in it. Although increasing mechanical alloying time negatively affected the compactability of the powders, after overall investigation of fracture surfaces of compacted specimens it is concluded that better microstructural homogenization and fineness were obtained with the increasing mechanical alloying time.

Table 1. Green densities of the compacts pressed after 150 MPa for the 90W7Ni3Fe composition.

Attrition Time (hours)	**Compacted Density (g/cm^3)**	**Theoretical Density (g/cm^3)**	**% Theoretical Density**
0	9,29	17,15	54,19
10	9,23	17,15	53,84
20	8,42	17,15	49,12
30	8,30	17,15	48,44
40	8,41	17,15	49,08
50	8,49	17,15	49,50

Sintering Behaviour of Prepared Compacts

Samples having 90W7Ni3Fe alloy composition (constant composition different mechanical alloying times) and samples having 75W-80W-85W-90W-95W-(7/3 Ni:Fe) compositions (prepared from 50hs mechanical alloyed powders) were sintered in a horizontal tube furnace at 1500^{o}C for 1 hr under flow of H_2 gas. After sintering density measurements of sintered compacts were performed according to Archimedes principles and results are given in Table.2. As it can be easily followed from the table, almost all samples showed high sintered densities near to their theoretical density values. For the 90W7Ni3Fe composition, increased homogeneity with increasing mechanical alloying time had a positive effect for the densification.

Since the green densities of the compacts were initially different (see Table.1), densification parameter (DP) may give better comparison about the effect of mechanical alloying. The calculated DP value for sintered sample of 10 hrs mechanical alloyed powder was 0.87 where as 1.0 was found for 50 hrs mechanical alloyed powder which proves the positive effect of mechanical alloying on densification. Microstructures of 90W7Ni3Fe heavy alloys as a function of mechanical alloying time are given Figure 2.

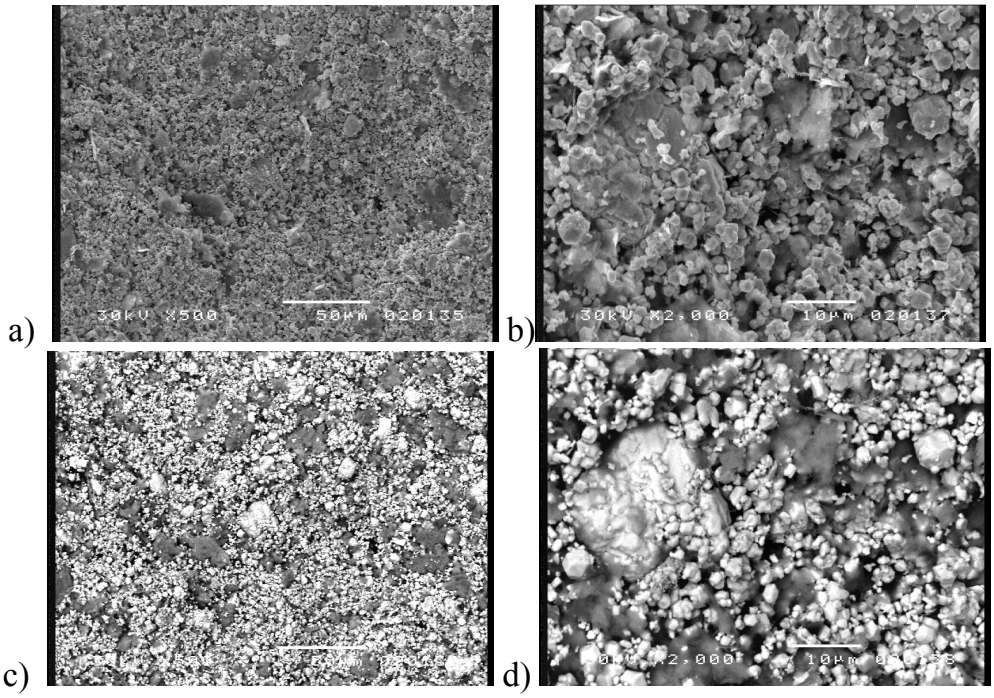

Fig.1 SEM micrographs of the fracture surfaces of after 150 MPa compacted 90W7Ni3Fe alloy prepared from 50 h MA`ed 56Ni24Fe20W powders (a and b SEI, c and d BEI images of same area).

Table.2 After sintering densities of the samples for the two experimental sets.

	Tungsten wt.% content	**Theoretical Density**	**Sintered Density**	**% Theoretical Density**
Prepared from 50 hrs Mechanical Alloyed Powders	75%	14,69	14,52	98,87
	80%	15,43	15,51	100
	85%	16,24	16,27	100
	90%	17,15	17,50	100
	95%	18,16	17,58	96,81
90W7Ni3Fe Composition	**Mechanical Alloying Time (hr)**	**Theoretical Density**	**Sintered Density**	**% Theoretical Density**
	10	17,15	16,16	94,24
	20	17,15	16,70	97,37
	30	17,15	17,07	99,57
	40	17,15	16,72	97,50
	50	17,15	17,50	100

Relatively at high sintering temperature like 1500^{o}C, all compositions were normalized and showed nearly similar microstructural features. However microstructure of heavy alloys having different tungsten contents showed different tungsten contiguity levels; this behavior can be seen in Figure 3, it is clear that with

the increasing W content connectivity of W grains in the microstructure increased. Also higher hardness values obtained with the increasing W content. However no specific trend was observed as a function of mechanical alloying time after hardness measurements for the samples sintered at 1500^{o}C; all samples showed similar hardness values between 310-334 HV proving the normalization behavior discussed above.

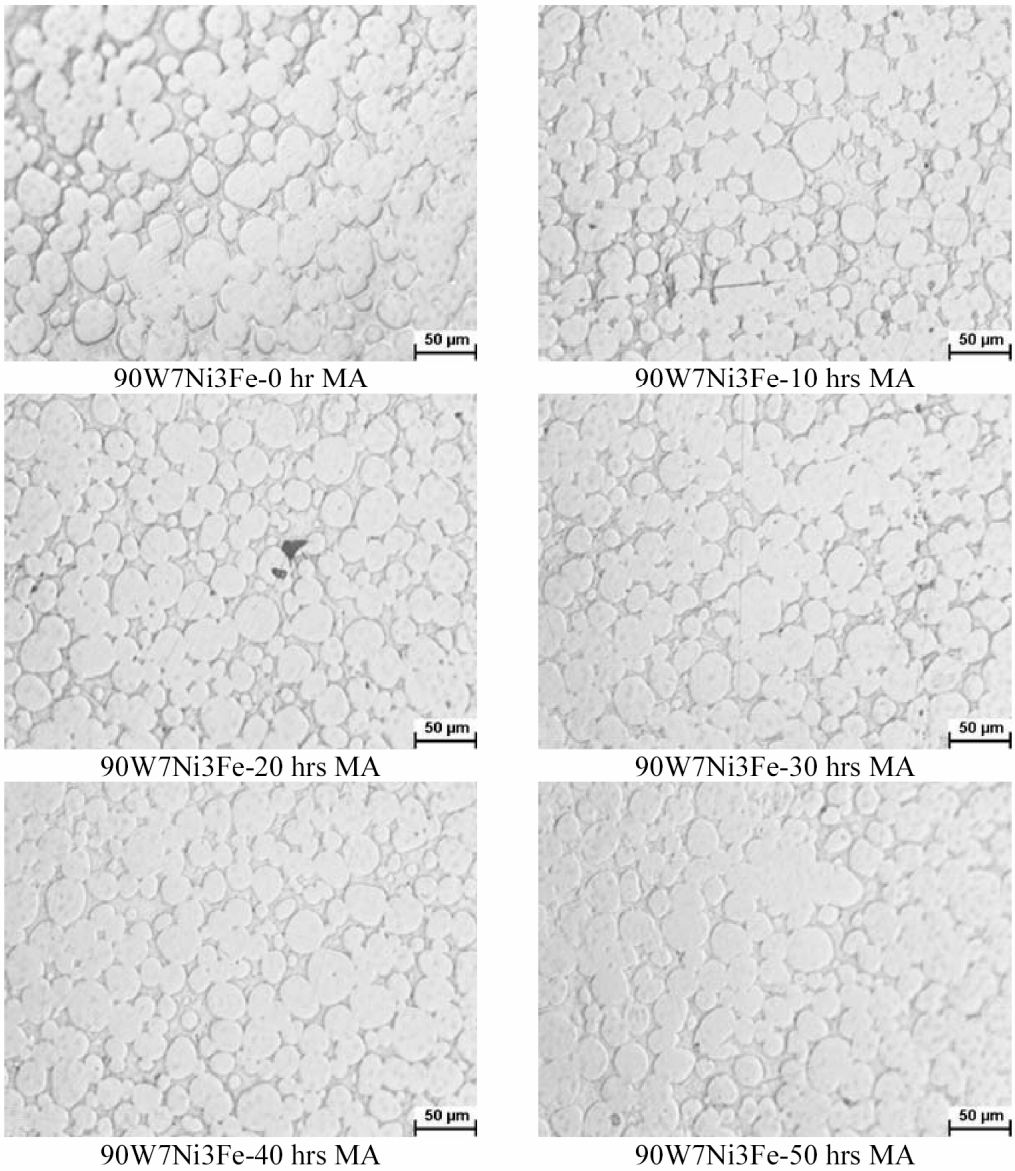

Fig.2 Microstructure of 90W7Ni3Fe Heavy alloys as a function of mechanical alloying time.

Therefore after careful investigations conducted with dilatometer, time dependent sintering experiments at 1460^{o}C for the duration of 1min. to 1 hour sintering time were realized. Also in order to reduce diffusion supported mass transport prior to liquid phase formation, a special sintering method were applied [6] at 1460^{o}C and kinetic sintering experiment realized at this temperature for duration of 1 min., 10 min., 30 min. and 60 min.

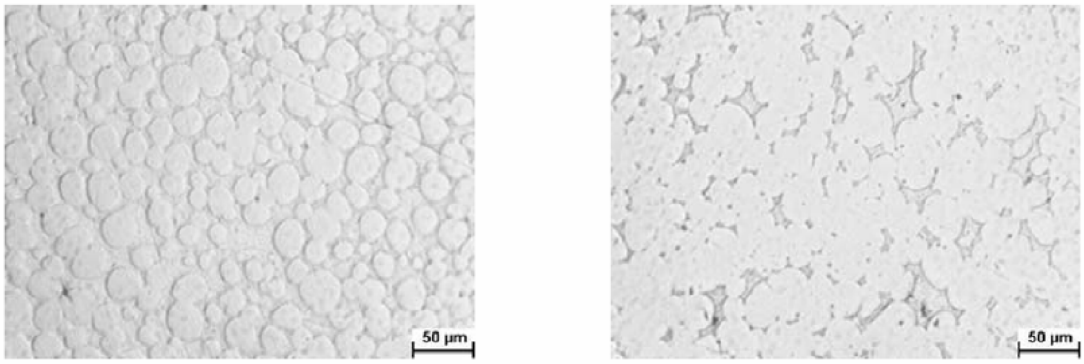

75W(7/3 Ni /Fe)- 50 hrs MA 95W(7/3 Ni /Fe)- 50 hrs MA

Fig.3 Microstructure of Heavy alloys 75W and 95W (7/3 Ni /Fe) prepared from 50 hrs mechanical alloyed powders.

The experiment was showed clear microstructural differences and it is believed that this is a good sign for the lower temperature sintering production of tungsten heavy alloys with smaller tungsten grain sizes and better mechanical properties.
In Figure 4, microstructures of the samples sintered 1460^{o}C were given and from these figures it is very obvious that there are no characteristic heavy alloy structure were obtain up to 1 hour sintering for initial powders, whereas increasing mechanical alloying of binder phase led to characteristic heavy alloy microstructure even after 1 minute sintering at 1460^{o}C. Shape and size of the liquid pockets also gives information on the densification of the system. Indeed, with increasing mechanical alloying time size of the liquid pockets were decreased and homogeneously distributed within the microstructure.

Also one of the major problems during liquid phase sintering is void formation in the center of the liquid pockets during capillary spreading to neighborhoods. Such voids are proportional to initial powder size (for this study Ni and Fe size, liquid forming constituents) and sometimes such voids can not be eliminated further sintering. This kind of void formation is also known as “swelling behavior” in literature and usually be seen in the systems where solid phase solubility is limited in the forming liquid. As it can be seen from Figure.4, these kinds of voids did not appear in the mechanical alloyed samples. With the increasing sintering time again all mechanical alloyed structures normalized and showed approximately same W average grain size except no mechanical alloyed system.

4.CONCLUSIONS

For the 90W7Ni3Fe heavy alloy system almost all samples showed full densification after sintering at 1500^{o}C and this behavior was independent from mechanical alloying time. However densification parameter (DP) values proved the positive effect of mechanical alloying on densification. Microstructural evaluation of the sintered samples showed that selection of relatively high sintering temperature like 1500^{o}C, normalizes initial processing effects created during mechanical alloying. In

this case all sintered samples have similar characteristic heavy alloy structure leading rounded W spheres in the Ni-Fe-W matrix phase. However, after investigating microstructure of the samples sintered at 1460 ^{o}C, it was concluded that mechanical alloying has a positive effect on microstructural development.

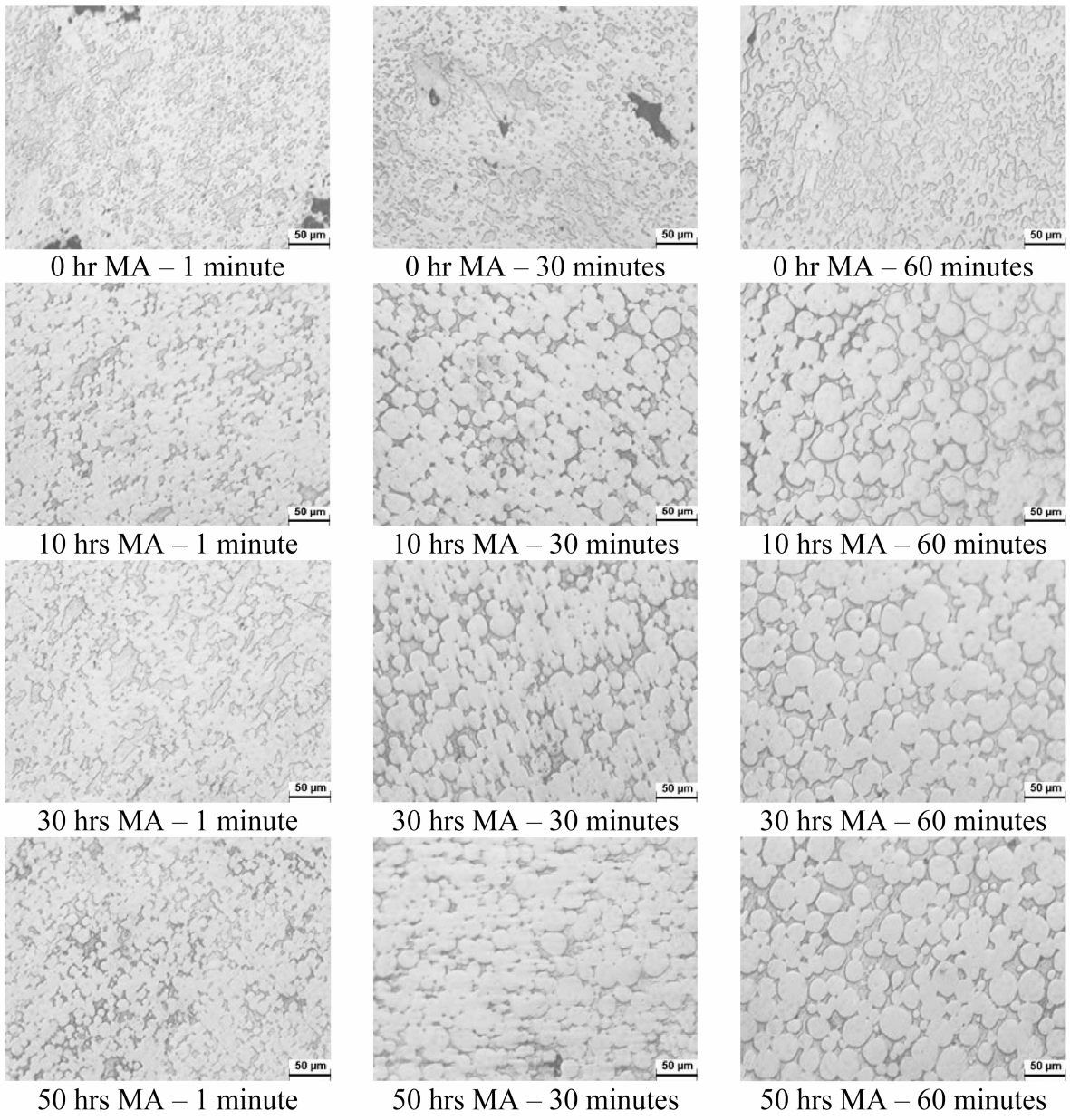

Fig.4 Microstructure of 90W7Ni3Fe Heavy alloys having different levels of mechanical alloying sintered at 1460^{o}C as a function of time.

The characteristic heavy alloy microstructures were observed during microstructural investigations of all mechanical alloyed 90W7Ni3Fe heavy alloy samples after sintering at 1460^{o}C. However, compacts prepared directly from initial powder mixtures (no mechanical alloyed) did not show such microstructural evolution. Investigation of the fracture surfaces of the unsintered compacts proved that microstructural refinement and homogeneity level were increased by mechanical

alloying time. Since the initial Ni and Fe powders selected for the study was coarser than W powders, intense deformation and refinement of ductile Ni and Fe phase were observed. W powders and its fragments were dispersed in this ductile matrix. Such a structure is compositionally more homogeneous in compare to initial powder mixture and degree of attained homogeneity level were increased by mechanical alloying time by approaching to alloy composition of 56Ni24Fe20W in microscale. Observed faster rearrangement densification during early liquid phase sintering was conducted with decreasing diffusion distances prior to liquid formation.

Received March 28, 2007

(1) Istanbul Technical University, Metallurgical and Materials Engineering Department PML LAB. 34469 Maslak – Istanbul, Turkey
(2) Bantboru San. Tic. A.S. No:36 34857 Maltepe-Istanbul, Turkey

REFERENCES

1. ASM Metals Handbook Vol.7 1998 p.914.
2. M.L Övecoglu., B Özkal. ve C Suryanarayana. "A Comparison of Sintering Characteristics of Ball-milled and Attrition-milled W-Ni-Fe Heavy Alloy" *J..Mater. Res.*, 11, 1673-1682 ,1996.
3.C.G. Mukira and T. H. Courtney The structure and properties of Mechanical Alloyed and Consolidated Ni-W(Fe) Alloys, P 2 C *Tungsten Refract Metals*, 157-167, 1995.
4. B. Özkal , ve M.L.Övecoglu " Mechanical Milling Studies in the Ni-Fe-W System and their Solid State Sintering Behaviors", *9th International Metallurgy and Materials Congress*, Proceedings Book Vol 1, p 487-492, Istanbul, Turkey, June 1997.
5. B. Özkal , ve M.L.Övecoglu " " Mechanical Milling Studies in the Ni-Fe-W System and their Sintering Behaviors in Heavy Alloys,Vol:1, p.287-292, *PM98 World Congress*, Granada, Spain, October 1998.
6.M. Canaran`, *M. S. Dissertation* , Istanbul Technical University, 2002

EFECTUL ADIȚIEI TERNARE DE Ni-Fe-W ALIAT MECANIC ASUPRA EVOLUȚIEI MICROSTRUCTURALE A ALIAJELOR GRELE DE TUNGSTEN SINTERIZATE ÎN FAZĂ LICHIDĂ

Rezumat: Au fost studiate comportamentele comparative, în timpul sinterizării la temperaturi înalte a sistemelor de aliaje grele W-Ni-Fe preparate cu adiții ternare de Ni-Fe-W aliate mechanic. Pentru a realiza aceasta, pulberile preamestecate, cu compoziția de 56Ni-24Fe-20W, au fost aliate mechanic într-o moară atritor, pe durate de până la 50 de ore iar compoziția aliată mechanic a fost adăugată pulberii inițiale de W, pentru a obține amestecuri de aliaje grele între 75 şi 95 W (raport 7/3 Ni:Fe). După compactare şi sinterizare în fază lichidă la temperature înalte, probele au fost caracterizate prin tehnici de microscopie analitică. Omogenizarea şi finisarea microstructurală au fost obținute odată cu creşterea duratei de aliere mecanică iar aceste caracteristici au dus la o densificare timpurie în comparație cu contrapiesele care nu au fost aliate mechanic. Deşi alegerea unor temperature mai înalte de sinterizare a normalizat efectele positive ale adițiilor aliate mechanic, este posibil ca, prin selectarea unor temperature mai scăzute de sinterizare să se produce aliaje grele de tungsten cu granulații relative mici.

BULETINUL INSTITUTULUI POLITEHNIC DIN IAŞI
Tomul LIII (LVII), Fasc. 1, 2007
Secția
ŞTIINȚA ŞI INGINERIA MATERIALELOR

Ni-Ti BASED FUNCTIONAL BIO-COMPOSITE DESIGNED FOR MEDICAL DEVICES

BY

GABRIEL BATIN[(1)], CĂTĂLIN POPA[(1)], VIOREL CÂNDEA[(1)], DAN MÂNDRU[(2)], IOAN VIDA-SIMITI[(1)]

Abstract: The shape memory effect showed by Nitinol can be used to produce artificial muscles. These are made of composites with bio-polymers that act as matrices for the active shape memory alloys reinforcements. The authors proposed a new set of materials with the same properties as those used now, but with lower costs.

Keywords: biomaterials, artificial muscles, polymer matrix composites, Nitinol, shape memory alloys

1. Introduction

Ni-Ti shape memory alloys are used in many applications such as dentures, orthodontic arch wires, guide wires, needles, heart valves, stents, minimally invasive surgery and so on.

These applications are using Ni-Ti's alloys thermomechanical properties: superelasticity and shape memory effect.

Artificial muscles have a complex character, as the actuator elements made of shape memory alloys are in close contact with the other elements of the devices and / or with the organism systems.

The ability of artificial muscles to produce mechanical movement is in direct relation to the constructive geometry. Thus, typical constructions are made of composites with bio-polymers that act as matrices for the active shape memory alloys reinforcements.

Direct exposure of the alloys to the body fluids may result in adverse reactions. The corrosion resistance of metal alloys is based on a passivation phenomenon [1], which arises as a result of the metal oxide layer that forms on the surface of the metal. The surface of NiTi consists mainly of stable titanium oxides (TiO_2) and lower amounts of nickel oxides (NiO and Ni_2O_3) and metallic Ni, while nickel-titanium constitutes the inner layer [2, 3, 4].

Accidental or functional disruption of the oxide layer may determine adverse reactions, ranging from low intensity to metallosis. During the recovery to the trained shape, process that takes place in direct contact with the body fluids (blood, lymph, interstitial liquid), corrosion products may be formed (Ti or Ni ions, as well as complexes) and cause adverse reactions. The most dangerous reactions are provoked by nickel which is known for its toxicity and possible carcinogenicity [5]. To avoid the

direct contact between shape memory alloy fibres and tissue, the nitinol fibres are coated with a thin layer of polymer.

2. Materials and methods

Several types of composites were manufactured, using Ni – Ti wires as reinforcing elements. The wires have 315 and 700 μm in diameter. The most commercial Ni-Ti shape memory alloys (Nitinol) have concentrations close to equiatomic. This corresponds to a peak in the variation of properties (mechanical, electrical, etc.) for the solid solution.

Matrices were of epoxy resin or silicon rubber. Epoxy resin was produced by Policolor S.A. Bucureşti.

Several composite constructions were manufactured. Among them: single layers for planar muscles, stretching springs, compression springs.

The samples were analysed in terms of the mechanical capability when exerting the shape memory effect (SME). Heating in order to obtain the shape memory effect was performed electrically, using a D.C. current generator. Temperature was measured continuously by a thermo-couple.

3. Experimental results and discussion

3.1. Single layer lamella usable for planar muscles

Fig. 1. Single layer lamella; epoxy matrix, Ni-Ti thin wire

Samples are made of epoxy – Nitinol wire composite (Figure 1). The wire (315 μm diameter) is continuous, arranged parallel to the longitudinal axis of the device on most of its length. A better adhesion between wire and matrix was achieved by a preliminary coating of the reinforcement with araldit (epoxy glue). The optimal concentration of the glue was determined experimentally. The upper limitation of thickness comes from two reasons:

- a high concentration of the resin, that leads to a high thickness, results in a non-uniform layer, with external gas bubbles;
- the strains in the coated wire may produce surface cracks.

The Nitinol wire was placed in a plane that is displaced with 0.5 mm from the median plane of the lamella. Thus, when heating the wire, SME produces bending of the single layer.

During cooling, the recovery force is exerted by the epoxy matrix in the region under the median plane, where there is no reinforcement.

The lamella was blocked at one end, while the other was free to move and loaded with increasing weights. The sample was plugged and the value of the electric current was measured continuously. The best motion was obtained for 400 mA acting current. Experimental measurements have shown that this device can develop forces of maximum 157 N with a displacement of 15 mm, as shown in Figure 2. The value of the force was determined for weights that recover the shape to the initial planar one. Then, a higher temperature determines the lifting of the weight; subsequently, the applied force is increased until the sample is totally unbent. The experiment went on up to the moment when further heating couldn't produce additional force. For a long functioning life time, the displacement is most important. For high bending angles, sliding between matrix and wire may occur, leading to a malfunctioning of the device.

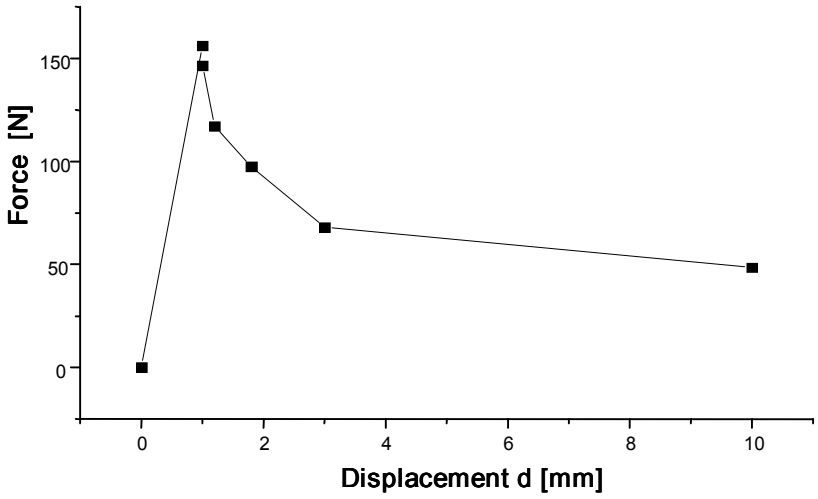

Fig. 2. Displacement vs. recovery force for single layer lamella

This type of composite is utilizable for exoprostheses of the upper limbs. The multi – layer construction, bringing together several single layers with different orientations of the Nitinol wire would be preferable.

3.2. Stretching actuator usable for the osteo – muscular cantilevers

The sample is made of a Nitinol stretching composed spring, engulfed in a silicon rubber matrix. Reinforcement is made of three 315 μm parallel wires that were interlaced. The transus temperature was 0 °C .

Manufacturing of the interlaced spring was made by rolling on a steel shaft. The Nitinol wire was rolled keeping a constant tension. After obtaining the final shape, the stretching tension in the triple wire was maintained. Subsequently, a heat treatment was performed, in order to train the spring to the obtained shape. Heat treatment was performed at 600°C and cooling was in air. Multiple heating were performed up to 600°C, followed by cooling to room temperature. Heat treatment was performed in four stages:

- heating to the regime temperature;

- dwelling for 30 minutes;
- air cooling to the room temperature.

After completion of the heat treatment, the spring was transferred on a PTFE shaft, pre-tensioned and completely engulfed in silicon rubber. The pretension was necessary considering the use of the device for actuator in the osteo-muscular cantilevers.

Mechanical testing was performed with the sample positioned on a vertical PTFE shaft. A guided plate was positioned on top of the device. Increasing mass value weights were placed on the plate, applying a compressive force to the spring. Subsequently, the sample was gradually heated. A displacement of 0,8 mm was obtained for 58 °C, applying a force of 11968,2 N; for a temperature of 80 °C, a 1 mm displacement of the same weight could be achieved.

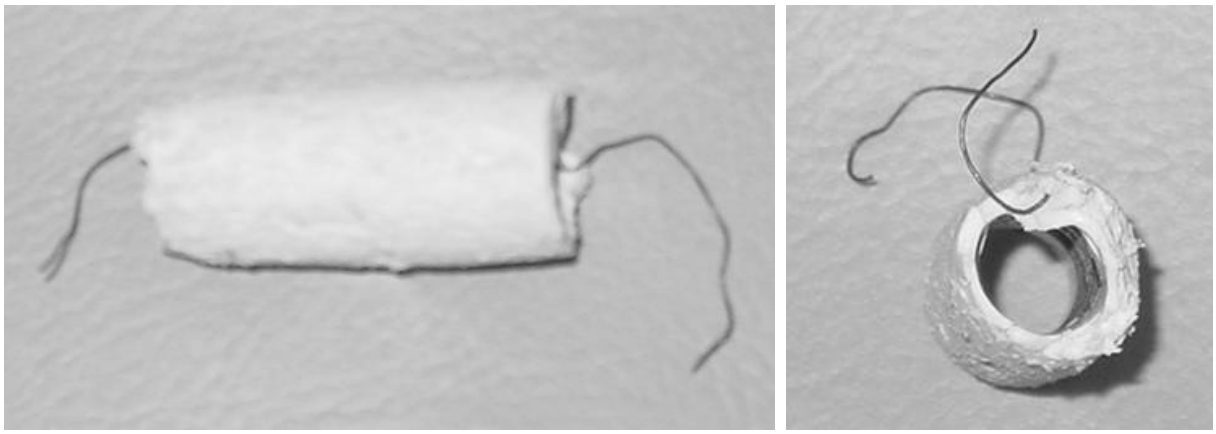

(a) (b)

Fig. 3. Stretching composite actuator: a) side view, b) top view

The structure of the reinforcing spring was studied before and after the heat treatment. Under the transus temperature, the structure is entirely martensitic, displaying a marked orientation due to the rolling manufacturing of the half-product. Above the transition temperature, the austenite is still oriented, with small grains.

3.3. Compression actuator that simulates the action of long muscles

The sample is formed by a compression spring made of 750 μm diameter Nitinol wire. The top end of the spring was attached to a tie-rod, while the bottom one supported a plate where weights were positioned in succession. The sample was tested both in the martensite and in the austenite state. For testing the mechanical capability of the spring in an austenitic state, heat was applied permanently, even when the increasing force produced strain. The maximum displacement of a capable force was of 15 mm / 1274 N (Figure 4.a.). This is very suitable for muscular actuators of upper limbs.

The mechanical capability of the actuator in a martensitic state was determined starting at the room temperature. After stretching under a G force at the ambient temperature, the sample was heated to recover the initial shape, than cooled and loaded more. The capable displacement / force was 20 mm / 882 N (Figure 4.b.).

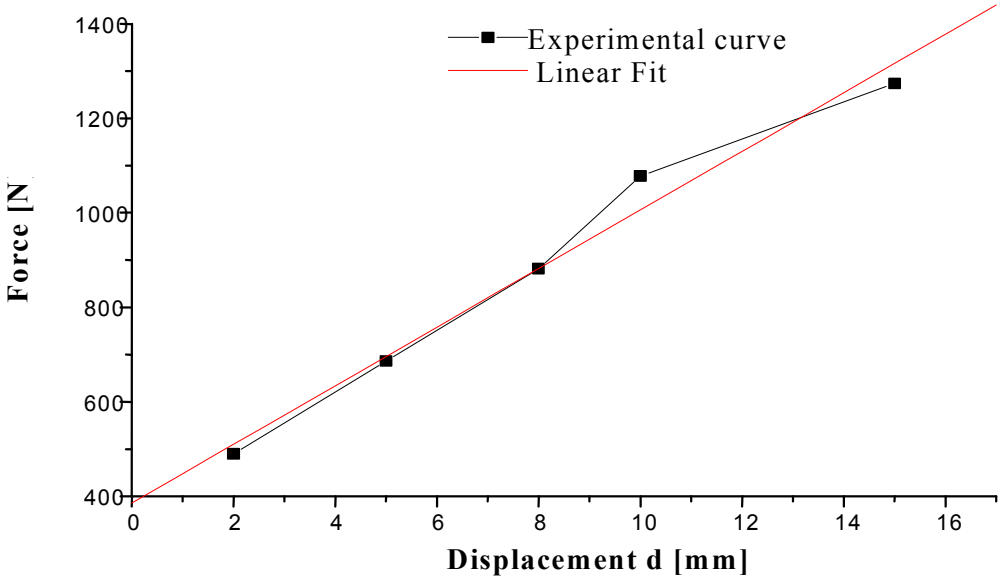

(a)

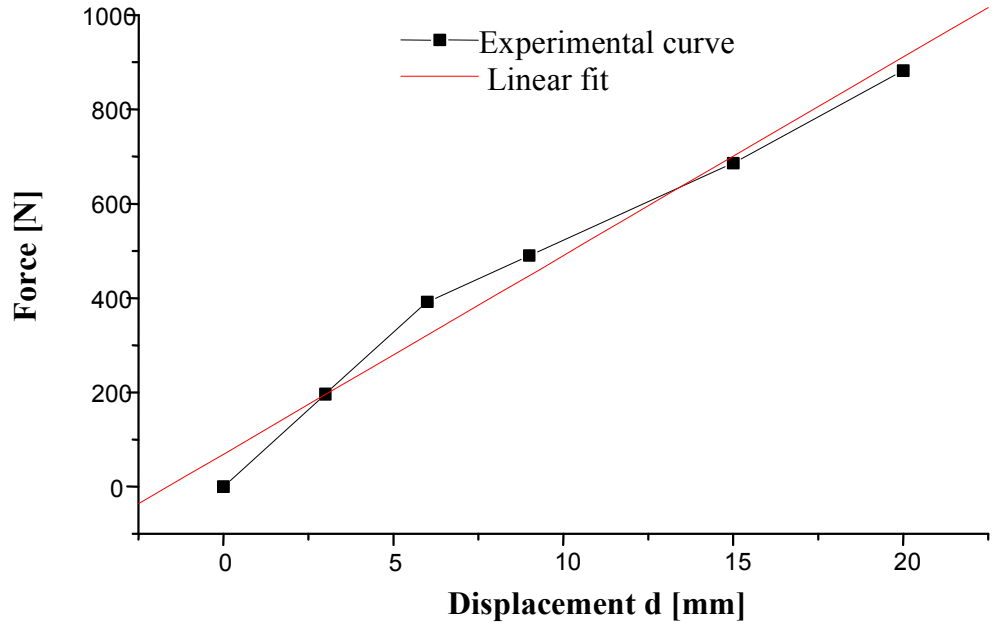

(b)

Fig. 4. a) Straining force vs. recovery displacement, austenitic state; b) Straining force vs. recovery displacement, martensitic state

4. Conclusions

Several constructive variants of Nitinol reinforced polymers shape memory composites were produced, targeting actuating applications in endo / exoprostheses.

In order to achieve a strongly bonded wire – matrix interface, a prior coating with epoxy glue is recommended.

The heating time for the Nitinol wire has to be as short as possible, not to induce a significant increase in the matrix temperature. This could lead to a decrease in the

matrix stiffness, so to an altering of the mechanical behaviour, mainly during the recovery stage.

The stretching composite spring comprising three parallel 350 μm diameter Nitinol wires and a silicon rubber matrix is able to develop, during the recovery stage, very high forces compared to its size.

The compression shape memory spring shows linear force / displacement characteristic both in the martensitic and austenitic state. The elastic constant (F/d) is of 1.47 times higher in the austenitic state compared to the martensitic one.

Received April1 12, 2007

(1) Faculty of Materials Science and Technology, Technical University of Cluj-Napoca, 400641, Cluj-Napoca, Romania
(2) Faculty of Mechanics, Technical University of Cluj-Napoca, 400641 Cluj-Napoca, Romania

REFERENCES

1. Kruger J., Fundamental aspects of the corrosion of metallic implants. In: Rubin LR (ed) Biomaterials in reconstructive surgery. Mosby, St Luis, 145-157, 1983.
2. Endo K., Sachdeva R., Araki Y & Ohno H , Effects of titanium nitride coatings on surface and corrosion characteristics of Ni-Ti alloy. Dent Mater J 13: 228-239, 1994.
3. Shabalovskaya S.A., Surface, corrosion and biocompatibility aspects of Nitinol as an implant material. Biomed Mater Eng 12: 69-109, 2002.
4. Kujala S., Biocompatibility and biomechanical aspects of nitinol shape memorymetal implants, Acta Univ. Oul. D 748, 88p., 2003.
5. Oller A.R., Respiratory carcinogenicity assessment of soluble nickel compounds. Environ Health Perspect 110 Suppl 5: 841-844, 2002.

BIO-COMPOZITE FUNCȚIONALE PE BAZĂ DE NI-TI DESTINATE APLICAȚIILOR MEDICALE

Rezumat: Datorită efectului de memorie a formei, nitinolul poate fi utilizat pentru obținerea de mușchi artificiali. Mușchii artificiali sunt construcții tipice din compozit biopolimer - aliaj cu memoria formei. Autorii propun un set nou de material cu aceleaşi proprietăți ca şi a celor utilizate în prezent, dar cu un preț de cost mai redus.

BULETINUL INSTITUTULUI POLITEHNIC DIN IAŞI
Tomul LIII (LVII), Fasc. 1, 2007
Secția
ŞTIINȚA ŞI INGINERIA MATERIALELOR

MICROALLOYED STEEL LONG PRODUCTS, WITH HIGH STRENGTH AND TOUGHNESS FOR AUTOMOTIVE INDUSTRY

BY

MIRCEA BRĂILOIU and VASILE MIRON

Abstract: Researches refers to bars manufacturing from steels with 0.1-0.5% C, 0.5-1.9% Mn, microalloyed with Nb, V, rare earth elements, i.e. These steels could replace the 1% Cr, 0.3% Mo and 1.5% Ni alloyed steels for automotive parts manufacturing: block, connecting rod, crankshaft, axles, assembling parts, auxiliary rod, flanges, couplings. This new technology refers to manufacturing of bars from microalloyed steel; steel forging is performed under controlled condition (e.g. at 950^0C) cooling with air, or with air forced or with water and have the advantage to eliminate normalizing, quenching and tempering treatments. Other advantages of this new technology refers to the environmental risk - pollution diminution (by removing of heat treatments it is decreased the CO_2 emission) and also to economic advantages - low costs microalloyed steel due to the replacement of Cr, Ni, Mo contents (approx. total content of 2.8%) with a microalloying elements content 0.4% V, Nb ,rare earth elements and to the diminution of energy costs as a result of heat treatments removing. Classic technology consists of manufacturing of Ø20 - Ø90 mm bars from 1% Cr,0.3% Mo and 1.5% Ni alloyed steel; by forging at about 1000^0C there are obtained bars, and after that they are normalized (900^0C/air), quenched (850^0C/oil) and tempered (550^0C - 600^0C) with a subsequent difficult machining due to parts dimensional changes as result of heat treatments. In this paper it is shown the experimental results for a 50 kg heat micro-alloyed grade steel.

Keywords: micro-alloyed steel, bars, high resistance

1. Introduction

The present research contributes to develop the field "New products - bars from microalloyed steels" currently researched at European level. The researches have proposed the solving important problems, of high complexity for the given thematic area "Microalloyed steels" i.e. the setting of optimum chemical composition in order to achieve the required mechanical characteristics. Since nowadays, in Romania, there were not realized long products from microalloyed steels for forgings for automotive industry.

The research work has a character at the interface of the scientific and technical knowledge, being studied the mechanisms by which micro-alloying with Nb, V and rare earth elements influence the microstructure and the material characteristics; it will be used electronic microscopy and X-ray diffraction analysis.

This research comprise the following:

- Establishment of the charge formula for steelmaking induction furnace (50 kg weight) in order to achieve the optimum chemical composition of new products;
- Establishment of the production operating parameters; optimization of the sulfur and phosphorus elimination parameters; decrease of the gas content (oxygen, nitrogen, hydrogen) in order to achieve the imposed quality;

- Setting of the parameters for hot plastic deformation;
- Relationships setting: technological parameters – steel quality; optimum chemical composition – mechanical characteristics; plastic deformation degree – mechanical characteristics; nonmetallic inclusions content – toughness; residual elements content – steel macroscopic segregation level.

2. Experimental results

The charge from the micro-alloyed grade steel (50 kg weight) has been elaborated in an electric induction furnace; it was cast an ingot which had forging in Ø20 – Ø90 mm bars with followed by air cooling.

The results obtained are presented below.

2.1 Chemical composition

The chemical liquid composition from the experimental heat is given in Table 2.1

Table 2.1 – The chemical composition of liquid steel

%C	%Mn	%Si	%Al	%S	%P	%Nb	%V	%Ce	%La	N ppm	O ppm
0.43	1.38	0.36	0.024	0.010	0.013	0.030	0.05	0.04	0.02	61	41

In Table 2.1 it is observed a advantageous chemical composition (low sulphur content and nitrogen and oxygen moderately contents) in order to achieve a low nonmetallic inclusions, to obtain a high toughness of the steel.

2.2 Non-metallic inclusions content

In Table 2.2 it is presented the results concerning the purity of steel determined through optic microscopy from the polished specimen steel. It is noticed the high purity of the steel; the individual inclusion points is max. 1.5 for A type, thin series (S), max. 1.0 for B type, thin series (S), max. 0.5 for D type, thin series (S) and max. 0.5 for D type, thick series (G). According to the control specimen by ASTM E 45 – D method, if individually punctuation from the non-metallic inclusions small series is under 2 value and from coarse series is under 1.5 value the steel is considered of a high purity. This low values for the non-metallic inclusions level concur to increase the plasticity and tenacity mechanical characteristics.

Tab. 2.2 – Maximum points for the inclusion type (sulphides, oxides, silicates, nitrides)

Microscopic field	**Inclusion type (A,B,C,D) series S – thin series G - thick**							
	A		**B**		**C**		**D**	
	S	**G**	**S**	**G**	**S**	**G**	**S**	**G**
1	1,5	-	1,0	-	-	-	0,5	-
2	0,5	-	0,5	-	0,5	-	0,5	-
3	1,0	-	0,5	-	0,5	-	-	0,5

2.3 The metallographic analysis

The austenite grains has been pointed out on polished specimen steel, picric etching and optic microscopy exanimate. Through the picric etching relieved austenite grains. This specimen has a fine granulation (6-7 size) according as it is shown in Fig. 2.1.

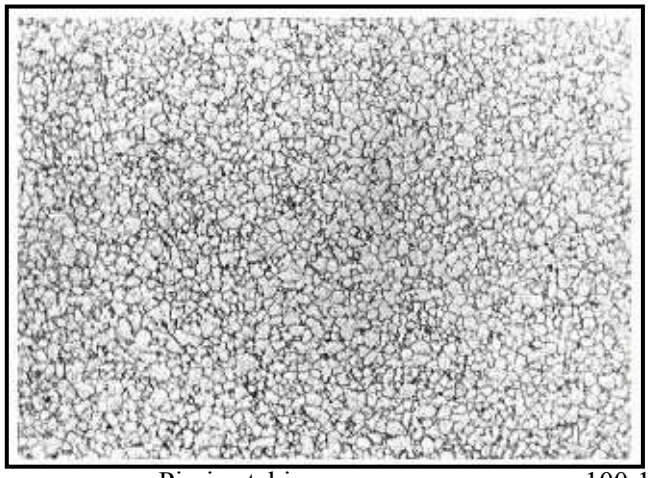

Picric etching 100:1

Fig. 2.1 Microstructural aspect: austenite ex - grains at end forging temperature (850^0)

Real steel granulation is with a ferrite - pearlite microstructure as a result of air-cooled after hammering (the ingot has been hot forged after heating hour-long at 1150^0C, after which end temperature hammering for the bars has been 850^0C). Real granulation is fine (8 size).

2.4 Electronic microscope and X – ray diffraction analyses

AlN, VC, NbC, VN and NbN have importance in the grain refining of steel. In Fig. 2.2 it is shown the microstructure of this particles in the micro-alloyed steel C-Mn-V-Nb-Al at X 26000 size (electronic microscope analyses).

X: 26000 (electronic microscopice)

Fig. 2.2 The particles form (nitrides, carbides and carbide-nitrides) in the micro-alloyed steel C-Mn-Nb-V-Al

For the particles evidence it was analysed a specimen of steel through X-ray (with DRON 3 difractometer) and it was established the interplanar distance d [Å]; with the ASTM sheets for the crystalline particles it was established crystalline phases from the Tab. 2.3. We see in the table 2.3 that the experimental steel heat contains particles (AlN, VC, VN, NbC, NbN) which is finishing the austenite and ferrite - pearlite grains. The values of interplanar distance for VC and VN, on the one hand, and NbN and NbC, on the other hand, are very close, which means that few particles had formed carbide-nitrures of V and Nb.

Table 2.3 – Particles nature in the micro-alloyed steel C-Mn-Nb-V-Al

Phase	d (Å)	(hkl)	θ	2 θ
AlN	1,3	(112)	15	30
AlN	2,3	(101)	8,5	17
AlN	2,6	(200)	7,5	15
VC	1,4	(220)	14	28
VC	2,4	(111)	8,5	17
VN	1,2	(311)	16	32
NbC	1,3	(311)	15	30
NbC	2,5	(111)	8	16
NbN	1,6	(220)	13	26

θ – the diffraction angle (degrees)

2.5 The mechanical properties

From the experimental bars were prepared traction and resilience specimens; it is remembered that the bars cooling after forging was made in air. In Tab. 2.4 it showed the experimental established mechanical results: tensile strength R_m, yield strength $R_{p0,2}$, elongation A_5 and impact value KV on Charpy V specimen.

Table 2.4 – The mechanical properties

R_m (N/mm^2)	$R_{po,2}$ (N/mm^2)	A_5 (%)	KV (0^0C) (J)	KV (-30^0C) (J)	Remarks
842	752	26	88	60	Bars diameter 90 mm.
866	774	22	79	49	Bars diameter 20 mm.

The steel has a tensile strength R_m of the 800 N/mm^2 class, and high low-temperature toughness KV (-30^0C) at the same time. Ferrite – pearlite steel has a high yield ratio (yield strength/tensile strength) of 0.89 value.

3. Conclusions

A 50 kg charge was steel smelted in an induction furnace, in order to realise the necessary experimental researches; the steel was micro-alloyed with Al, Nb, V, Ce and

La. The austenite and ferrite-pearlite grains of the bars forged in the temperature interval 1150 - 850^{0}C (the bars diameter of 20 - 90 mm., air cooled after forging) was fine because the micro-alloyed elements. The steel purity was high, due to steel making process and the micro-alloying with Ce and La. The microstructure was evidenced through the electronic microscope and with X-ray diffraction; it was established that the particles which blocked up the grain rise at the heating for forging and which dressed the structure at solid recristalization (in the time of the cooling of bars in air after hot plastic deformation) was AlN, VC, VN, NbC, NbN and carbide-nitrides.

The mechanical properties are as same as an alloy steel (with Cr, Ni, Mo) quenched and high tempered. The advantage of this technology is that the micro-alloyed steel may be used in the stamping of automotive parts without heat treatments as normalisation, quenching and tempering. Other advantages of this new technology refers to the environmental risk - pollution diminution (by removing of heat treatments it is decreased the CO_2 emission) and also to economic advantages - low costs micro-alloyed steel due to the replacement of Cr, Ni, Mo elements (approx. total content of 2.8%) with a micro-alloying elements content 0.4% V, Nb, rare earth elements and to the diminution of energy costs as a result of heat treatments removing.

Received April 18, 2007 *Metallurgical Research Institute ICEM S.A., Bucharest*

REFERENCES

1. Yashiro Koyasu, Hiroshi Shinozaki, Nobuyuki Ishii, Nabukazu Suzuki, Akira Sakaguchi – **HSLA Steel Bar for Hot Forging without Subsequent Quenching and Tempering**, Nippon Steel Technical Report no. 30/1986
2. Yashiro Koyasu, Tatsuro Ochi, Hiromasa Takada, Husao Ishikawa, Hideo Kanisawa, Masato Yanase, Kenichiro Naito – **Development of Special Steel Bars and Wire Rods for High-Strength Automobile Parts**, Nippon Steel Technical Report no. 53/1992
3. Yashiro Koyasu, Toshihiko Takahashi, Nobuyuki Ishii, Hiromasa Takada, Hidetoshi Takeda – **High Strength and Toughness Microalloyed, Forging Steels for Fabrication of Automobile Underbody Parts without Subsequent Heat Treatment**, Nippon Steel Technical Report no. 47/1990

PRODUSE LUNGI DIN OŢELURI MICROALIATE CU REZISTENŢĂ ŞI TENACITATE RIDICATĂ PENTRU INDUSTRIA DE AUTOVEHICULE

Rezumat: Cercetările se referă la fabricaţia barelor din oţeluri cu 0,1-0,5% C, 0,5-1,9% Mn, microaliate cu Nb, V, lantanide, etc. Aceste oţeluri pot înlocui oţelurile aliate cu 1% Cr, 1,5% Ni şi 0,3% Mo în fabricaţia pieselor pentru autovehicule: butuc, bielă, arbore cotit, axe, organe de asamblare, bieletă, flanşe, cuplaje. Noua tehnologie se refera la realizarea barelor din oţel microaliat; matriţarea pieselor se realizează în regim controlat (de ex. la temperatura de 950^{0}C) cu răcire în aer, sau aer ventilat, sau apă cu avantajul eliminării tratamentelor termice de normalizare, călire şi revenire. Alte avantaje ale acestui procedeu sunt cele de mediu - reducerea noxelor prin evitarea tratamentelor termice (eliminarea emisiei de CO) şi cele economice – reducerea preţului de cost al piesei matriţate prin înlocuirea elementelor Cr, Ni, Mo (total 2,8%) cu 0,4 % elemente de microaliere V, Nb, pământuri rare şi reducerea energiei integrate în produs, ca urmare a eliminării tratamentelor termice. Tehnologia clasică, utilizată la fabricaţia produselor lungi destinate forjării (matriţării) pieselor pentru autovehicule, prevede realizarea de bare cu diametrul Ø20 – Ø90 mm din oţel aliat; piesele se obţin prin matriţare la temperatura de cca. 1000^{0}C, după care acestea sunt tratate prin normalizare (900^{0}C/aer) şi în continuare călire (850^{0}C/ulei) şi revenire (550^{0}C - 600^{0}C). Prelucrarea acestora prin aşchiere este dificilă ca urmare a modificărilor dimensionale a pieselor tratate termic. In această lucrare sunt prezentate rezultatele experimentale obţinute pentru o şarjă cu masa de 50 kg realizată dintr-o marcă de oţel microaliat.

BULETINUL INSTITUTULUI POLITEHNIC DIN IAŞI
Tomul LIII (LVII), Fasc. 1, 2007
Secția
ŞTIINȚA ŞI INGINERIA MATERIALELOR

MICROSTRUCTURAL CHANGES OCCURRING DURING THE CONVENTIONAL PROCESSING OF Fe-Mn BASED SHAPE MEMORY ALLOYS

BY

LEANDRU-GHEORGHE BUJOREANU[(1)], SERGIU STANCIU[(1)] and VASILE DIA[(2)]

Abstract: The paper reports the experiments performed in order to produce Fe-Mn based shape memory alloys (SMAs). By means of optical microscopy (OM) the microstructural evolution of the processed alloy was monitored during the conventional production flow, comprising casting, homogenization and plastic deformation. This evolution has been accompanied by the increase of the amount of plates of ε martensite, which is responsible for the existence of thermal memory. Finally the occurrence of shape memory effect has been emphasized by free recovery in bending.

Keywords: martensite plates, microstructural evolution, shape memory effect, shape recovery degree

1. Introduction

Among Shape Memory Alloys (SMAs) four have become of commercial use, namely: Ti-Ni, Cu-Zn-Al, Cu-Al-Ni and Fe-Mn-Si [1]. From the point of view of the crystalline structure of the parent phase (austenite) the first three alloys are of the β type (with bcc structure) while the last is of the γ type (with fcc structure) [2].

Fe-Mn-Si SMAs, typically containing 30 wt% Mn and 6 wt. % Si, were developed as SMAs with perfect memory by A. Sato et al. in 1982 [3]. These alloys experience a reversible martensitic transformation γ (fcc)↔ε (hcp) but no shape memory effect (SME) can be revealed unless ε stress induced martensite is formed [4].

The main characteristics of thermal memory of Fe-Mn-Si SMAs are summarized in Fig.1. As noticeable from Fig.1(a), a Shape Memory Effect (SME) characterized by a shape recovery degree of 90 % is obtained in the composition range Fe-(28-34)Mn-(4-6,5)Si [5, 6]. Fig.1(b) shows the variation of yield stress and SME with deformation temperature applied in order to obtain a cold shape characterized by a permanent strain of 1.5 %.. The lower part of this figure shows the decrease of SME from 100 % for the alloy deformed at M_s to bellow 20 % for the alloy deformed at M_d. In this case the magnitude of bending SME was determined with the relationship:

$$SME = (\theta_i - \theta_f)/\theta i \cdot 100 \quad (1)$$

where θ_i is the bending angle, in martensitic state, of the specimen with linear initial hot shape and θ_f is the remanent angle after heating. For perfect recovery, $\theta_f = 0$ and SME = 100. The reported experimental values of SME ranged between 61 to 80 % [7].

Unlike β-phase alloys, the martensitic transformation γ (fcc)↔ε (hcp), from Fe-Mn-Si, SMAs is neither thermoelastic nor ordered [8]. The transformation shear induces low energy stacking faults in austenite that are unable to permanently deform the parent phase.

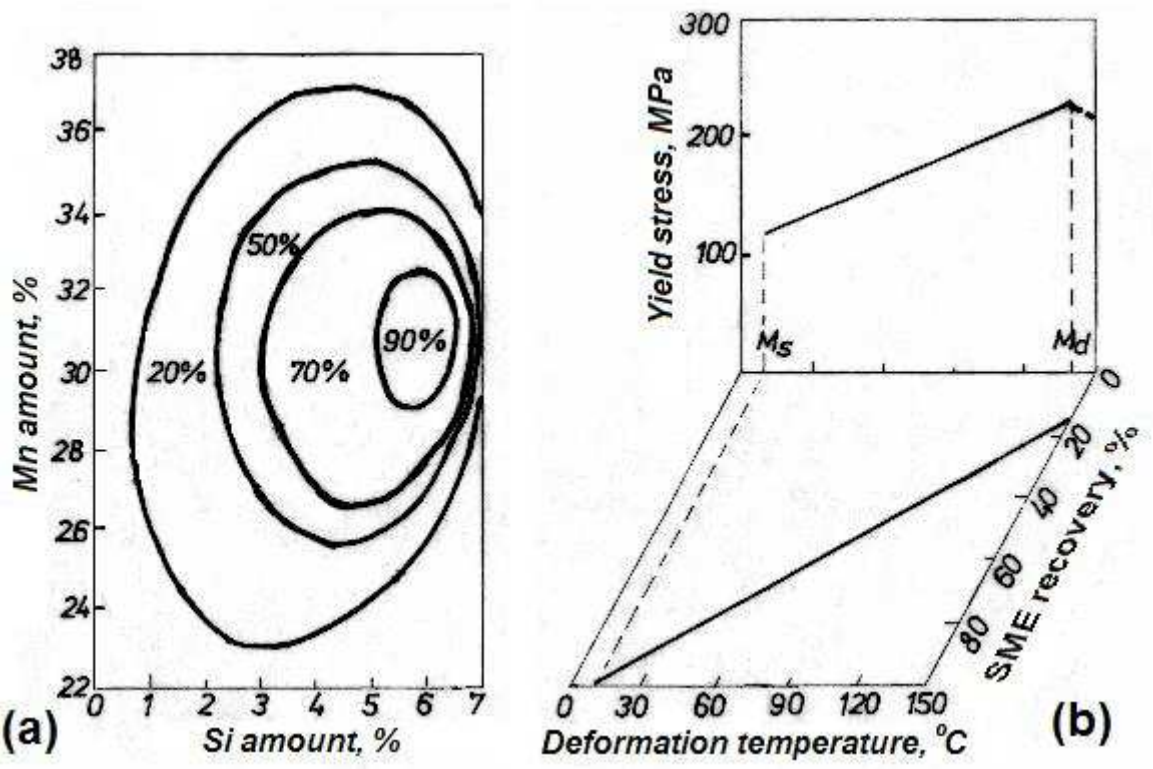

Fig.1. Characteristics of thermal memory at Fe-Mn-Si SMAs: (1) structural diagram for SME values as a function of chemical composition; (b) dependence of bending SME and yield stress on the deformation temperature applied for obtaining the cold shape [5, 6, 7]

Since austenite is elastically deformed during martensitic transformation, martensite reversion is favored during subsequent heating. It has been shown that martensite reversion is also favored by austenite strengthening , the best results being obtained by disperse precipitation of NbC nanoparticles [9].

The present paper aims to report the presence of SME in bending at specimens with chemical compositions different from the well known Fe-30Mn-6Si (wt. %).

2. Experimental procedure

Fe-Mn-Si alloys were produced in a high frequency induction furnace with a 0.2 kg Al_2O_3 crucible and insulated chamber with Ar atmosphere, starting from a Fe-20 wt.% Mn prealloy. After casting, the ingots (6 x 5 x $60 \cdot 10^{-3}$ m) were homogenized (1373K/24·3.6 ksec in Ar/ water) and quenched (1273K/ 1.8 ks/water) then subjected to hot forging (1173-1373 K) and quenching (1273K/ 1.8 ks/water), to the dimensions 3 x 3 x $100 \cdot 10^{-3}$ m. A final hot rolling was applied (1273K) with 15 % thickness reductions per pass, each followed by instant quenching, to thickness of $0.2 \cdot 10^{-3}$ m.

The final chemical composition of rolled specimens, determined by SEM, showed a maximum standard deviation of 0.92, which proves that the specimens were homogeneous.

Optical microscopy observations were performed on specimens etched with 10 % Nital solution.

Free recovery-bending cycles were applied comprising: (i) room temperature (RT) bending, (ii) heating until no shape recovery is observed and (iii) cooling to RT.

3. Experimental results and discussion

The typical structure of the as-cast binary Fe-20 % Mn prealloy is shown in Fig.2.

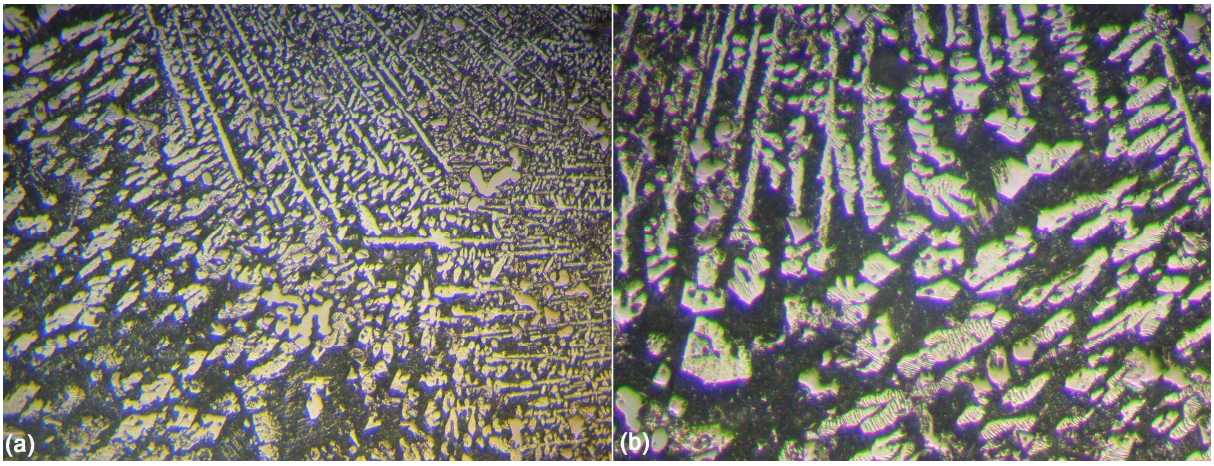

Fig.2 Typical optical micrographs of Fe-20%Mn as-cast prealloy: (a) intersection zone between F_α dendrites with two orientation and individual grains with dendritic aspect, 200x; (b) detail of the intersection zone revealing the transition of F_α from dendritic growth to individual grains; 400x

The structure is typical for casting. The white crystallites are alpha ferrite (F_α) with typical form and color since the alloy is ferromagnetic. As a result of the gamma forming action of Mn the dark background matrix is austenitic.

After the ternary addition of Si, no marked changes were observed in the structure of as-cast specimens. However, after homogenization and quenching, the dendritic structure disappeared and α' or ε martensites were formed depending on the Mn content. These aspects are illustrated in Fig.3, in the case of Fe-20 Mn-6 Si (%) alloy.

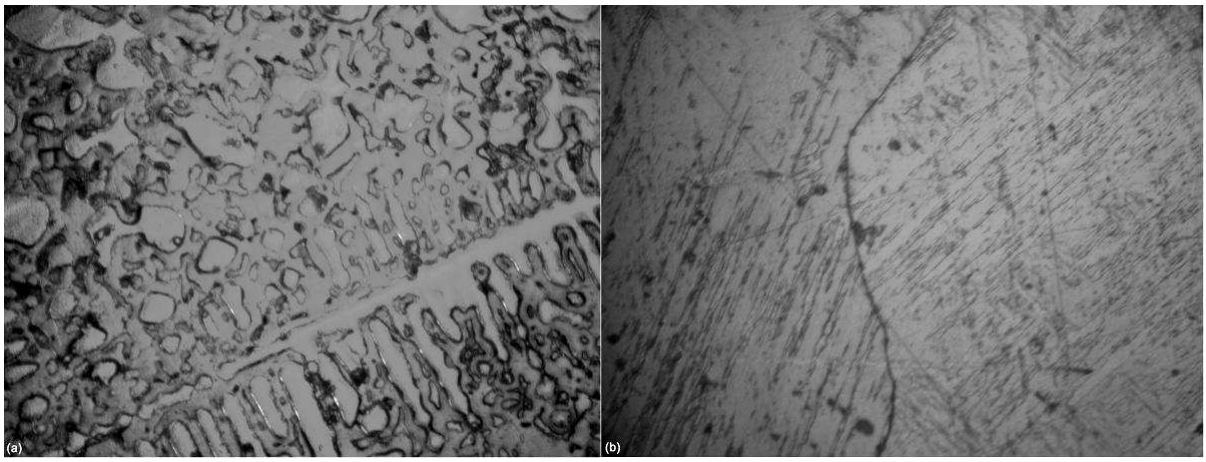

Fig.3 Optical micrographs revealing the effects of homogenization (1273K/12·3.6 ksec/ water) and quenching (1273K/ 1.8 ks/water) on the structure of cast Fe-20Mn-6Si (%) alloy: (a) initial dendritic structure, 200x; (b) formation of α' acicular martensite, after homogenization and quenching, 500x

Fig.3(a) reveals a typical casting structure, with F_α dendrites, the specimen being ferromagnetic. Fig.3(b) shows the boundary between two austenitic grains within which α' acicular ferromagnetic martensite was formed after homogenization and quenching, as an effect of water quenching and of the low value of Mn amount.

With increasing the Mn content, the specimen became paramagnetic and ε martensite became obvious after homogenization, as shown in Fig.4, for a Fe-30Mn-6Si (wt.%) specimen

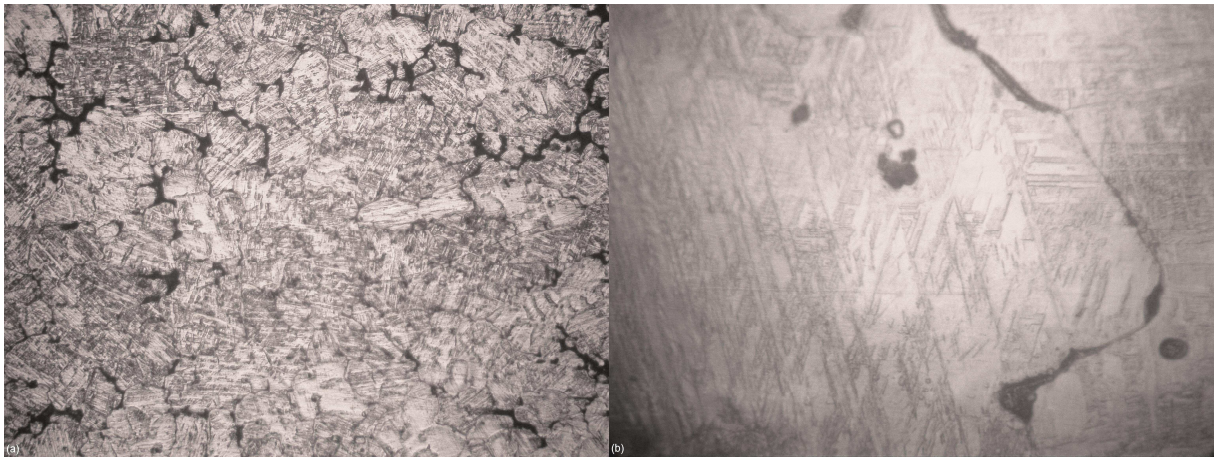

Fig.4 Optical micrographs of homogenized and quenched Fe-30Mn-6Si (wt. %) alloy revealing the formation of ε martensite with typical triangular morphology: (a) general aspect, 100x; (b) detail of ε martensite, 500x

The occurrence of both ε martensite plates is obvious even at low magnification, Fig.4(a). Higher magnifications reveal the typical triangular morphology of ε martensite, Fig.4(b).

Since the alloys with high manganese content proved to be very brittle for further experiments a Fe-23Mn-3 Si (wt. %) alloy was selected. The typical structures after hot forging and water quenching are shown in Fig.5.

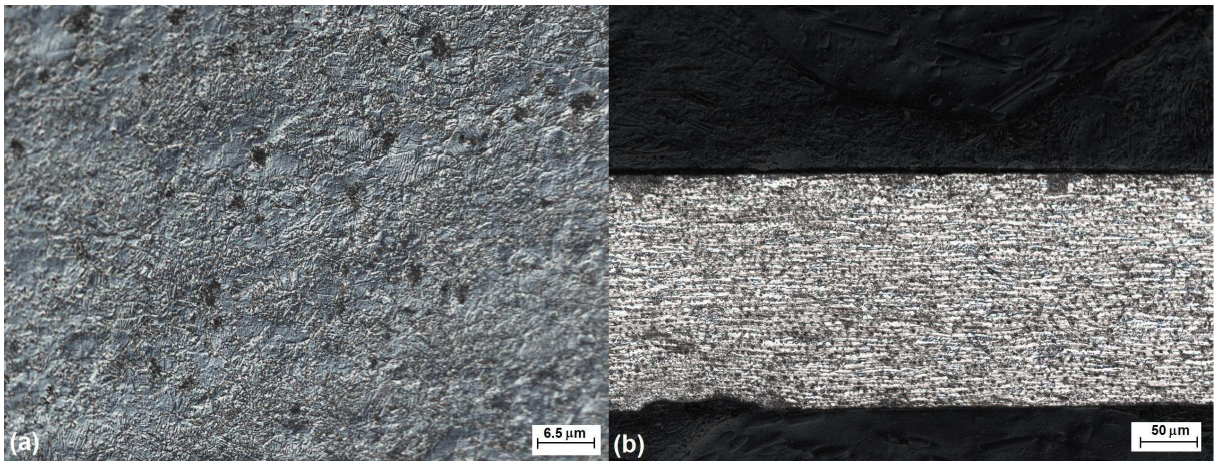

Fig.5 Optical micrographs on the axial surfaces of hot rolled and quenched specimens of Fe-23 Mn-3 Si (wt.%) alloy: (a) cross section on specimen's width; (b) cross section on specimen's thickness

As an effect of hot rolling and quenching ε martensite plates were formed but plastic deformation induced an aspect which is rather different from homogenized specimens, from two points of view: (i) no obvious grain boundaries are noticeable neither on width nor on thickness cross section; (ii) a marked texture is present on thickness cross section, mainly formed by elongated α' plates, since the specimen if ferromagnetic. ε martensite plates are noticeable only on width thickness and are less numerous than in undeformed homogenized and quenched Fe-30Mn-6Si (wt.%).

In order to emphasize the existence of SME, four cycles were applied to Fe-23Mn-3Si lamellar specimens, comprising room temperature (RT) bending – heating – cooling, as illustrated in Fig.6.

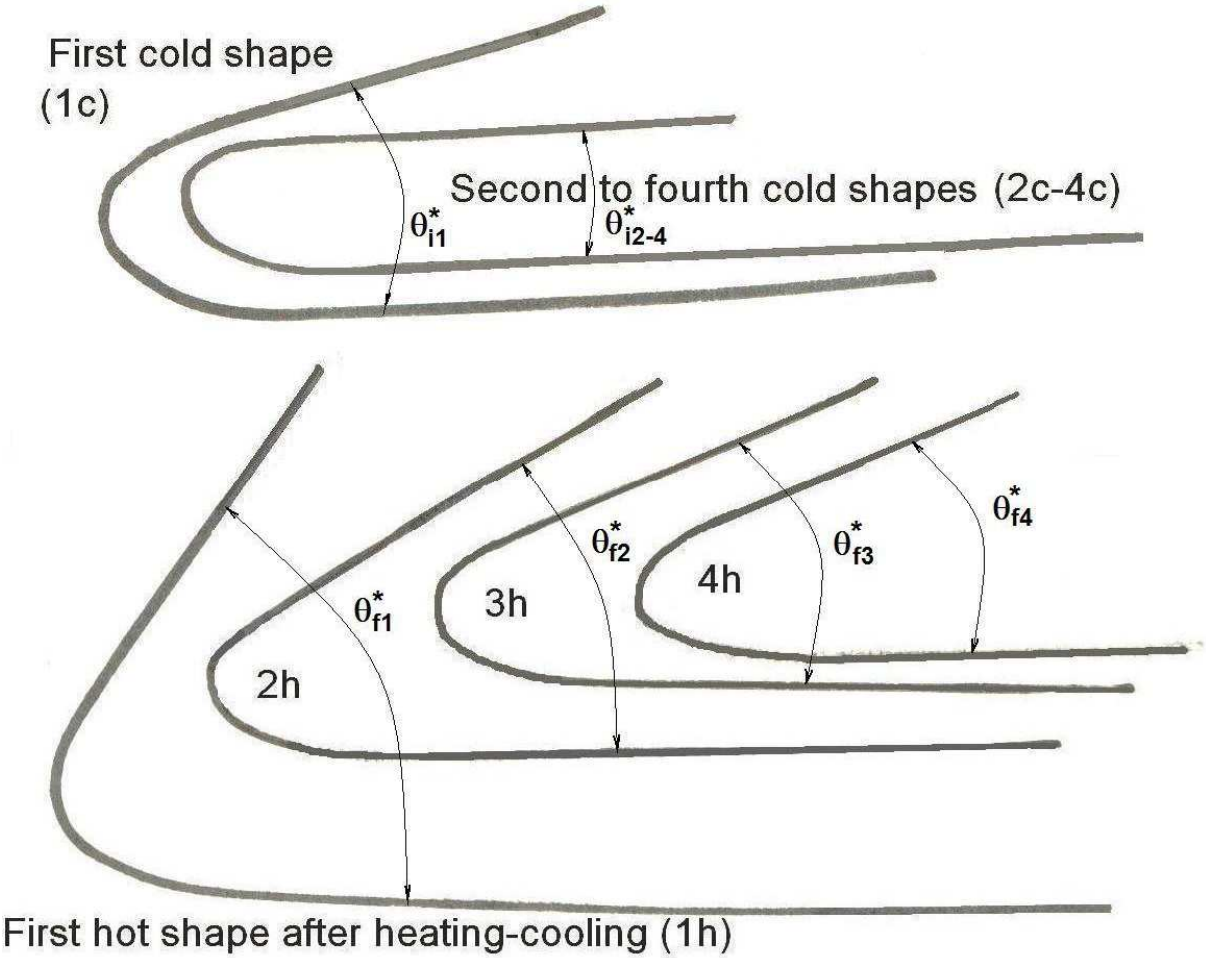

Fig.6 Recordings of the consecutive evolution of Fe-23Mn-3Si (wt./%) specimen contours during four cycles comprising RT bending-heating-cooling. 4 cold shapes (1c – 4c) were obtained by bending with the angles $180-\theta_i^*$ and 4 hot shapes (1h – 4h) were caused by free-recovery SME characterized by the angles $180-\theta_f^*$

The values of the θ_i and θ_f angles, measured as complements of the angles θ_i^* and θ_f^*, from Fig.6, and the resulting SME values, determined according to relationship (1), are listed in Table 1.

Table 1

Parameter	Number of cycle			
	1	2	3	4
θ_i, ^{0}	166	180	180	180
θ_f, ^{0}	123	150	156	158
SME, %	26	17	13	12

The decrease of SME value could be determined by the irreversible deformation of α' martensite. However, the excellent plasticity of the alloy, which accommodates bending angles as high as 180^0 is to be noticed.

4. Conclusions

The formation of ε martensite was observed both in Fe-30Mn-6Si (wt. %) in homogenized and quenched state and in Fe-23Mn-3Si (wt. %) after homogenization, quenching, and hot rolling with instant quenching. It was assumed that the presence of α' stress induced martensite in Fe-23Mn-3Si limited the value of SME in bending to 26 %, value which is however higher then that reported in literature (20 %) for such chemical compositions. During cycling, the irreversible deformation of α' could be the cause of the gradual decrease of the SME value, from 26 to 12 % after 4 cycles.

Acknowledgements

This work was financially supported by the Romanian National University Research Council (grant A CNCSIS 275/2006, 2007).

Prof. L.G.Bujoreanu wishes to bring special thanks to dr. Takahiro Sawaguchi and Mr. Motomochi Koyama, from NIMS Tsukuba, Japan, for kind expertise and fruitful discussions and for technical support in specimen preparation, respectively.

Received April 30, 2007

(1)The "Gh.Asachi" Technical University Iaşi
(2)S.C.MITTAL STEEL Iaşi S.A.

REFERENCES

1. Hornbogen, E. – *Alloys with shape memory-New materials for the technology of the future?,* **Progress in Shape Memory Alloys**, (Eucken, S., editor), DGM Informationsgesellschaft Verlag, Bochum, 1992, **3-22**
2. Bujoreanu, L.G – *Materiale inteligente,* **Editura JUNIMEA**, Iaşi, 2002
3. Sato, A., Soma, K. and Mori, T. – *Hardening due to pre-existing ε-martensite in an Fe-30Mn-1Si alloy single crystal*, **Acta metallurgica**, **30**¸1982, **1901-1907**
4. Pandey, D. and Lele, S. – *On the study of the f.c.c – h.c.p. martensitic transformation using a diffraction approach – I. f.c.c.→h.c.p. transformation*, **Acta metall.**, **34**¸1986, **405-413**
5. Frémond, M. and Miyazaki, S. – **Shape Memory Alloys. CISM Courses and Lectures**, Springer, Wien-New York, 1996
6. Dubois, B. – *Aciers à mémoire de forme. Espoir ou réalité?*, **Traitement thermique, 234**, 1990, **27-34**
7. Sade, M., Halter, K. and Hornbogen, E. – *Transformation behaviour and one-way shape memory effect in Fe-Mn-Si alloys,* **Progr.Shape Mem.All.**, (Eucken, S. ed.), DGM-Informationsgesellschaft Verlag, Bochum, 1992, **191-199**
8. Sato, A., Chishima, E., Yamaji, Y. and Mori, T. – *Orientation and composition dependencies of shape memory effect in Fe-Mn-Si alloys,* **Acta Metall., 32,** 1984, **539-547**
9. Sawaguchi, T., Kikuchi T., Kajiwara, S., *The pseudoelastic behavior of Fe-Mn-Si-based shape memory alloys containing Nb and C*, **Smart Materials and. Structure 14** (2005) **S317**

MODIFICĂRI MICROSTRUCTURALE PRODUSE ÎN TIMPUL PRELUCRĂRII CONVENȚIONALE A ALIAJELOR PE BAZĂ DE Fe-Mn, CU MEMORIA FORMEI

Rezumat: Lucrarea prezintă experimentele effectuate pentru a produce aliaje cu memoria formei (AMF) pe bază de Fe-Mn. Prin intermediul microscopiei optice (MO) a fost urmărită evoluția microstructurală a aliajului prelucrat, în timpul fluxului convențional de producție ce presupune turnare, omogenizare şi deformare plastică. Această evoluție a fost însoțită de creşterea cantității de plăci de martensită ε, care este responsabilă pentru existența memoriei termice. În final a fost evidențiată apariția efectului de memoria formei prin revenire liberă la încovoiere.

BULETINUL INSTITUTULUI POLITEHNIC DIN IAŞI
Tomul LIII (LVII), Fasc. 1, 2007
Secţia
ŞTIINŢA ŞI INGINERIA MATERIALELOR

RESEARCH ON THE PROCESSING OF A Ni-Ti BASE SHAPE MEMORY ALLOY THROUGH POWDER METALLURGY TECHNOLOGY

BY

VIOREL CÂNDEA, SMARANDA LĂPUŞAN, GEORGE ARGHIR, IONUŢ GLIGOR, CODRUŢA PAVEL, CĂLIN PRICĂ

Abstract. The present paper investigates the processing technology of a "smart" Ni-Ti base alloy (50 at.% Ni and 50 at.% Ti), with practical applications in the medical field. In this study, the Ni-Ti alloy was obtained by liquid phase atomization using an inert gas (Argon) as the spraying agent. Chemical composition, morphological and structural analysis of the resulting powder were conducted through optical microscopy, scanning electron microscopy (SEM) and X-ray diffraction analysis.

Keywords: NiTi, atomization, X-ray diffraction.

1. Introduction.

Previous research and studies on certain materials, for use as permanent or provisional medical implants, showed that only certain materials can be tolerated by the human body and can ensure a perfect functionality of the organism in its presence. Important progress in orthopedics, dentistry, neurology and cardiology was made by using materials with special properties (like shape memory, superelastic rubber-like behavior etc.) [1][4]. Among these materials, the Ni-Ti base alloys proved to be the most efficient, due to its excellent mechanical stability, very good corrosion resistance and remarkable biofunctionality and biocompatibility [2][3].

On these grounds, the material presented in this work is the equiatomic Ni-Ti alloy with 55.1 wt% Ni and 44.9 wt% Ti.

2. Experimental, results and discussion.

In order to obtain the Ni-Ti alloy with the specified chemical composition, first three micro-ingots were elaborated through electron-beam vacuum melting, weighing 2200 g, 1800 g, and 1100 g, respectively. The elaboration process consisted in subsequent meltings, as Titanium was progressively added to the composition until it reached the necessary content. The three micro-ingots, with the average chemical composition presented in table 1, were used as raw material for obtaining the Ni-Ti powder. The X-Ray diffraction diagram of the first micro-ingot is presented in figure 1. The powder elaboration process was carried out in a liquid atomization installation where the melting of the micro-ingots was made in an induction melting furnace at 1300°C, with a vacuum pressure of 10^{-2} Torr. Before the vacuuming of the furnace the remaining air was flushed out with Argon gas. The melt was overheated with 100°C before atomization to ensure the optimal fluidity. After 5 Argon gas flushings of the

atomization container, the melt vein was disintegrated by high purity 4,5 Argon gas spraying. A ring-shaped spraying device was used with 12 circular section nozzles. The Argon gas spraying pressure was 20 bar. An increase of the spraying pressure could modify the grain size distribution, but would also lead to an increased quantity of unwanted spherical shaped powder particles.

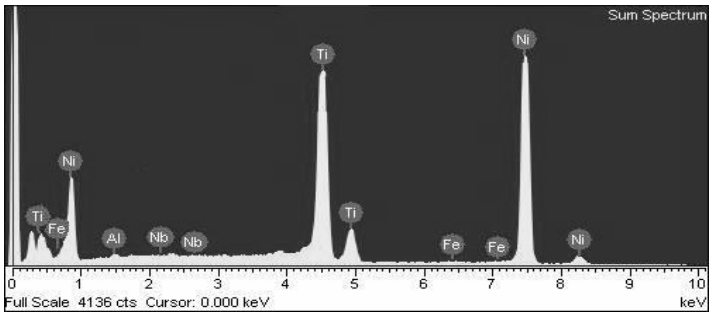

Fig. 1. EDX analysis of micro-ingot no.1(Ni-Ti).

Table 1. Average chemical composition of the Ni-Ti micro-ingots

Chemical composition, wt%				
Ni	Ti	Nb	Fe	Al
54.28	45.26	0.13	0.10	0.23

The obtained Ni-Ti powder was subjected to grain size analysis, microscopy, micro hardness and X-Ray diffraction. Table 2 shows the granulometric distribution of the powder.

Table 2. Granulometric analysis results.

Granulometric fraction, [µm]	< 40	40 – 63	63 – 80	80 – 100	100 – 200	>200
Granulometric fraction share, [%]	7.2	8.3	22.8	24.7	20.5	16.5

The SEM images from figures 2 and 3 show various particle shapes, from spherical to biscuit shape, and particle surface from smooth to rippled. The surface of the spherical shape particles is clearly smooth, sometimes with a dendritic aspect, figure 2, and in the case of irregular shape particles, severily rippled.

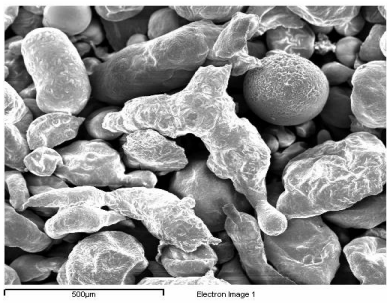

Fig. 2. SEM image of the atomized Ni-Ti powder.

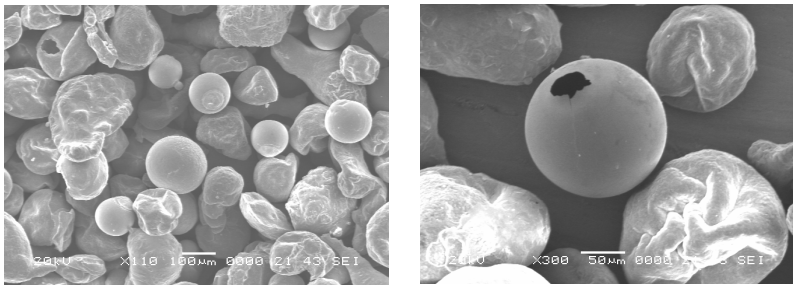

a b

Fig. 3 a, b. SEM images of the atomized Ni-Ti powder: a – spherical particles, b - hollow particles.

A very distinct phenomena is the presence of hollow powder particles. The craters seen on their surface is the result of gas evacuation from the interior of the powder particle, figure 3. This process is probably due to the gas absorption phenomena by some of the powder particles. These gases later explode at the contact with the cold water from the atomization chamber. The fabrication of implants using hollow powder particles would have the advantage of highly reduced specific weights,

much easier to tolerate by the patient, and with much higher osteo-integration possibilities.

The chemical composition of the atomized powder, 53.61 wt% Ni, 43.32 wt% Ti, 0.28 wt% Fe, 0.24 wt% Al, 2.38 wt% O ad 0.17 wt% Mg, was obtained through EDX analysis, figure 4, using a JEOL 560 LV SEM microscope. The Ni and Ti content is close to the stoichiometric composition. The small quantities of Magnesium, Aluminum and Iron probably resulted from the melting furnace lining. The Oxygen is present in a fairly large quantity, of 2.38 wt%, and most probably in the form of titanium oxides.

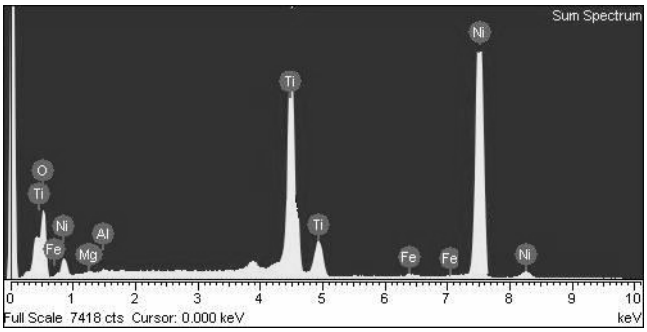

Fig. 4. EDX analysis of the atomized Ni-Ti powder.

Depending on the shape and size of the powder particles, after chemical etching with $1HF + 4HNO_3 + 5H_2O$ solution for 18 to 30 seconds, three types of structures could be distinguished:

a. fine dendritic structure, with a central orientation of the dendrites, figures 5 a, b, and c;

b. cellular aspect structure, with a clearly visible outline, figure 6;

c. mixed structure, where the dendritic formations alternate with cellular formations, figure 7.

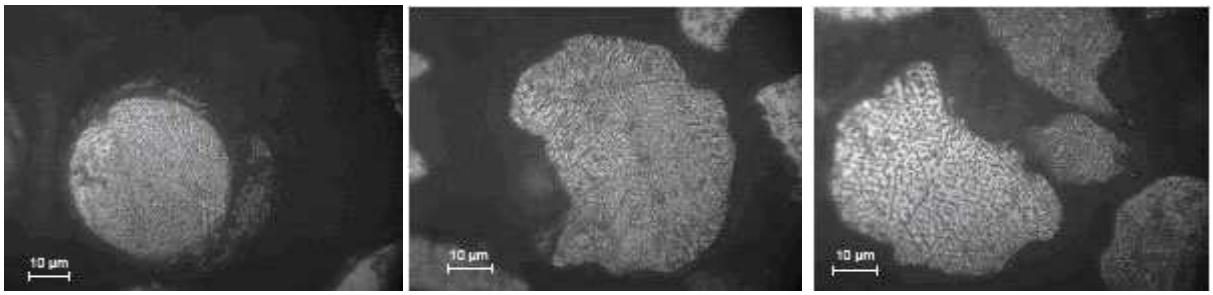

a b c

Fig. 5 a, b, c. Optical micrographs of the atomized Ni-Ti powder. Etched with $1HF+4HNO_3+5H_2O$.

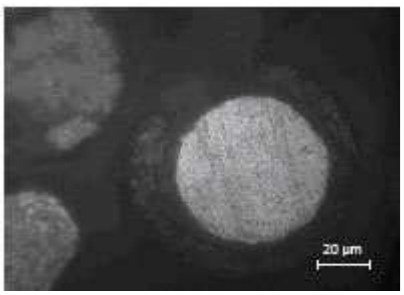

Fig. 6. Ni-Ti powder obtained by inert gas atomization.

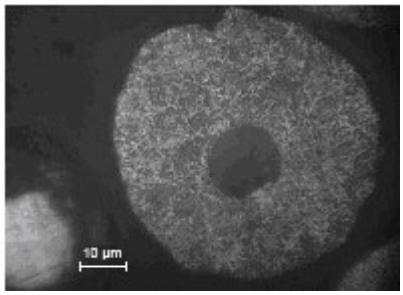

Fig. 7. Ni-Ti powder obtained by inert gas atomization.

Responsible for this difference in structure is supposed to be the different cooling rates of the powder particles caused by the difference in their size. The dendritic structure, corresponding to inhomogeneous phases, is normal for liquid phase processing where the cooling rates have very high values. Theoretically, applying a heat treatment could increase the homogeneity grade, but it is hoped this drawback will resolved after sintering.

For identifying the different possible phases present in the Ni-Ti powder, micro hardness measurements were carried out, using a 20 gf load, and X-Ray diffraction analysis using a DRON 4 equipment.

The average measured micro hardness values are presented in table 3, values that refer to the dendritic and cellular aspect structures.

Table 3. Vickers micro hardness values corresponding to the liquid phase atomized Ni-Ti powder.

Particle aspect	Micro hardness, $HV_{0,02}$	Comments
Dendritic structure	641	Fine dendrites
Dendritic structure	626	Coarse dendrites
Cellular aspect structure	753	Edge of grain
Cellular aspect structure	626	Center of grain

A short analysis of the micro hardness values from table 3 points out close values, whatever the surface aspect. However, in the case of the finer dendritic structure powder particles, and at the edge of the grain in the case of the cellular aspect structure, respectively, the measured micro hardness values were higher.

To find a more precise explanation, X-Ray diffraction analysis was carried out on different granulometric fractions of the Ni-Ti powder. The five XRD diagrams, together with the working parameters used, are presented in figures 8, 9, 10, 11, 12. The result of the XRD diagrams analysis are shown in table 4.

Table 4. XRD diagrams analysis results for the atomized Ni-Ti powder.

Analyzed sample	**Ni [%]**	**Ti [%]**	**Ni_3Ti [%]**	**NiTi [%]**	**$NiTi_2$ [%]**
Ni-Ti powder, -200 …+100 µm	-	-	-	98	2
Ni-Ti powder, -100 … +80 µm	4	2	-	91	3
Ni-Ti powder, -80 … +63 µm	34	6	2	56	2
Ni-Ti powder, -63 … +40 µm	31	15	3	46	5
Whole Ni-Ti powder, -100 µm embedded and grinded	25	4	8	52	11

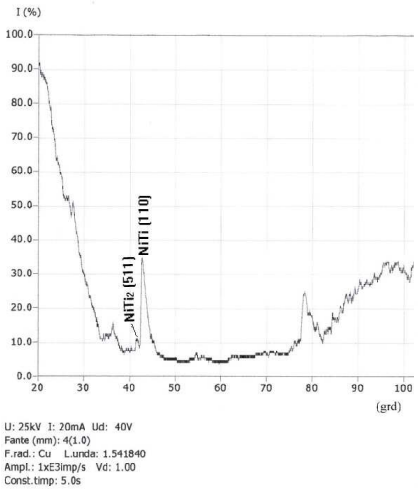

Fig. 8. XRD diagram for the atomized Ni-Ti powder, -200 … +100 μm fraction.

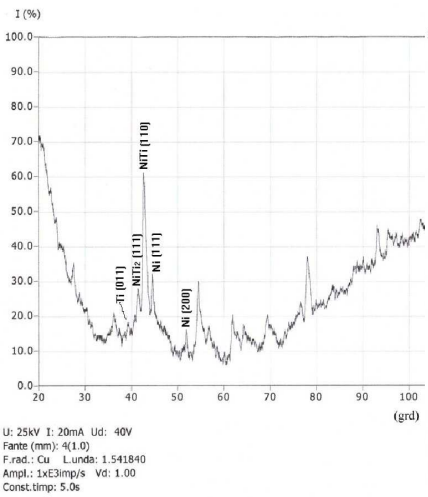

Fig. 9. XRD diagram for the atomized Ni-Ti powder, -100 … +80 μm fraction.

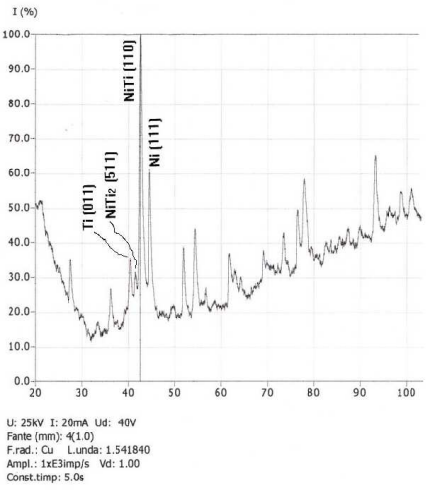

Fig. 10. XRD diagram for the atomized Ni-Ti powder, -80 … +63 μm fraction.

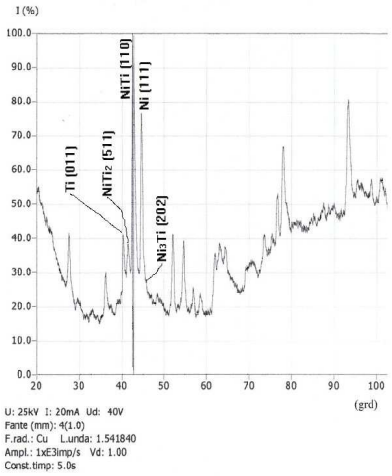

Fig. 11. XRD diagram for the atomized Ni-Ti powder, -63 … +40 μm fraction.

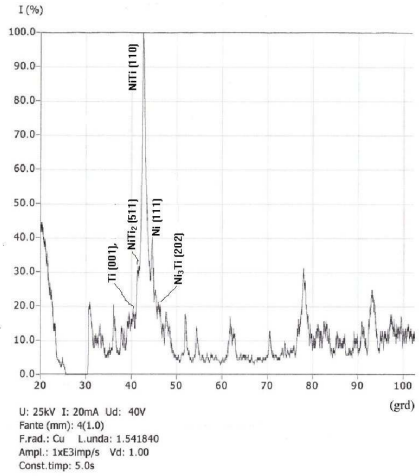

Fig. 12. XRD diagram for the atomized whole Ni-Ti powder, embedded and grinded, -100 μm fraction.

3. Conclusions

The present work established the processing technology of equiatomic Ni-Ti alloy in the form of metallic powder obtained through inert gas atomization.

Based on the chemical and structural analysis, the chemical composition of the processed alloy was in the range of the alloy we intended to obtain, 55.1 wt% Ni and 44.9 wt% Ti.

The studies on the alloy's microstructure, pointed out the presence of a number of phases, as follows:

- solid solution of NiTi intermetallic compound, as a predominant phase, with an essential role in obtaining the special characteristics of the alloy;
- solid solution of Ni_3Ti intermetallic compound;
- solid solution of $NiTi_2$ intermetallic compound;
- pure Nickel (Ni);
- pure Titanium (Ti).

The authors of this work intend to test the so obtained Ni-Ti powder in pressing and sintering operations. The use of a heat treatment will be necessary in order to drop down the Oxygen content, as well as a milling operation to modify the spherical shape of the powder particles, an essential condition to improve the pressability of the powder.

Received April 2, 2007 *Technical University from Cluj-Napoca*

References

1. J.B. Park and R.S. Lakes, **Biomaterials**: An Introduction, Plenum Press, 1992.
2. Hodgson, Darel E., Ming H. Wu, and Robert J. Biermann. **Shape Memory Alloys**. Online. Available SMA INC
3. Krone, L. et. al., The potential of powder metallurgy for the fabrication of biomaterials on the basis of nickel-titanium: A case study with a staple showing shape memory behavior, *Advanced Engineering Materials* 7 (2005), 7, 613 – 619
4. L. Gh. Bujoreanu, **Materiale inteligente**, Editura Junimea, Iaşi 2002

CERCETĂRI PRIVIND ELABORAREA UNUI ALIAJ CU MEMORIA FORMEI, DIN SISTEMUL Ni-Ti, PRIN TEHNOLOGIA METALURGIEI PULBERILOR

Rezumat: Lucrarea de faţă prezintă preocupări ale colectivului în domeniul elaborării unor aliaje „inteligente" din clasa Ni-Ti (50%at.Ni şi 50%at.Ti), destinate domeniului medical. A fost experimentată elaborarea prin pulverizare din fază lichidă cu argon (gaz inert) a aliajul Ni-Ti, determinându-se parametrii tehnologici de elaborare. Pulberea obţinută a fost analizată din punct de vedere morfologic, chimic şi structural, efectuându-se determinări prin microscopie optică, electronică şi difractometrie cu raze X. Au fost identificaţi trei compuşi chimici diferiţi: NiTi, Ni_3Ti şi $NiTi_2$, precizându-se forma, aspectul şi caracteristicile acestora.

BULETINUL INSTITUTULUI POLITEHNIC DIN IAŞI
Tomul LIII (LVII), Fasc. 1, 2007
Secția
ŞTIINȚA ŞI INGINERIA MATERIALELOR

THE POSSIBILITIES TO OBTAIN FINE STRUCTURES IN SINTERED STEELS BY SEVERE PLASTIC DEFORMATION

BY

VIORICA CHERTES, RADU L. ORBAN

Abstract: The paper presents an analysis of the possibilities to improve mechanical properties of structural sintered steels by the bulk severe plastic deformation method. The results, obtained by the method application in the bulk mechanical alloying variant to the sintered carbon steels, proved the possibility of advanced pore elimination, as well as of the microstructure refining even up to the nanometric scale, in tight correlation with the deformation parameters and with the attained deformation degree. Their combined effects resulted in an important improvement of the determined mechanical properties.

Keywords: sintered structural steels, bulk severe plastically deformation

1. Introduction

Severe plastic deformation is a relatively new method applied to metallic materials with the purpose to improve their mechanical properties through the microstructure refining [1]. It has been successfully applied to the wrought steels – the method being under development and industrial implementation [2]. However, only few published papers have been found related to the method extension to the sintered structural steels [3]. Or, their wider application – required by the market owing to the known advantages in their production conferred by powder metallurgy, is still limited even by the possibilities to obtain high mechanical properties – similar with of the wrought steels [4]. The present paper aims to establish the possibilities to extend the method application to the mechanical properties of sintered carbon steels improving.

The approached problem, regarding the application of the bulk severe plastic deformation method to the sintered carbon steels, was to establish a correlation between deformation pressure applied on the sintered performs, microstructure and mechanical properties. It was analyzed the typical microstructure of the steel in the sintered and repressed conditions, an important crushing of the structure through repressing being expected. Consequently the investigations have been firstly focused on the influence of the conditions of severe plastic deformation on the crystal grain dimensions. Then, the density variation as a function of the re-pressing conditions has been investigated. Finally, in this first approach of the problem, the hardness variation as a function of the re-pressing pressure has been determined.

2. Theoretical considerations

Among the known methods of the severe plastic deformation [1], it was selected the bulk mechanical alloying (BMA), applied, with good results, by T.

Aizawa for the solid state synthesis of functional materials [5] because it was considered to be the most suitable for sintered materials. It consists in the multiple pressing in close dies that have the diameter a little greater then that of the sintered compact. So, the produced deformation is a combination of plastic deformation through compressing and shearing, i.e. pressing with transverse deformation. Consequently, the sintered preform must have a transverse section smaller and with a simpler shape then the final part. This deformation mode theoretically ensures, at a great enough deformation degree, the elimination of pores and the obtaining of a compact material, leading to superior properties (Fig. 1).

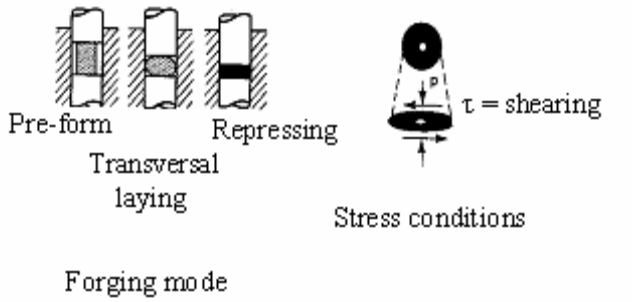

Fig.1 Compaction with the material transversal deformation [6].

The effective deformation degree has to be smaller then the value of the critical one - which corresponds to cracking.

3. Experimental conditions

ASC 100.29 type iron powder has been selected for experiments, as it has a high purity and good compactness, being widely used to the manufacturing of structural sintered parts, commonly in mixture with 0.4÷0.8 wt.% graphite to obtain a sintered carbon steel [4]. In the present investigations a proportion of 0.6 wt. % graphite has been adopted. Also, a proportion of 0.6 wt.% zinc stearate has been added as the compaction lubricant. The powder mixture homogenization has been realized in a TURBULA type blender, for 30 min, at a constant rotation speed of 100 r.p.m. Cylindrical samples of a cross section of 0.5 cm^2 (die diameter 8.2 mm) and 8 mm height were realized from these mixtures by cold axial bi-lateral compaction in rigid dies with compacting pressures of 200, 400, 500, 600, 700 MPa. For each determination 3 samples were realized, in the same conditions.

For the obtained green samples there were determined density, compactness and porosity by the standard methods [7]. The obtained values were used as the base for the determination, in the next step, of the density variation through sintering.

Sintering was performed in a tubular furnace, at 1120 °C for 40 min., using endo-gas as sintering atmosphere (dew point –35 °C). To avoid the steel quenching after sintering, the subsequent cooling was realized with a low cooling rate (~ 30 ^{0}C/min).

For the BMA application after sintering, the obtained samples with the nominal diameter of 8.2 mm (compacting die diameter) were successively re-pressed in dies with a diameter of 11.28 mm and 13 mm respectively, with re-pressing

pressures of 1400, 1600 and 1800 MPa, without a recrystallization annealing between the re-pressing steps.

The final characterization of the re-pressed samples was realized by the density variation as a function of the re-pressing pressure determination, by microstructural analyses and mechanical testing. To establish the effect of the applied BMA on the microstructure refinement, the final crystalline grain size was determined by the Scherre's method [8]. Finally, for the resulted effect on mechanical properties, among the known characteristics of their defining, only hardness was adopted in this first assessment of the topic. It was determined in a cross section, by the standard Rockwell B method.

4. Results and discussions

Figure 2 presents the variation of density of the sintered and re-pressed compacts as a function of the re-pressing pressure.

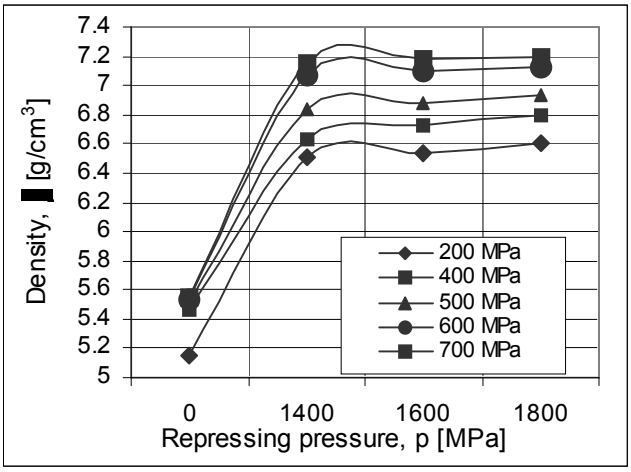

Fig. 2. The density variation of the sintered compacts by re-pressing, for various compacting pressures.

As it can be seen, even at repressing with the lowest adopted pressure (1400 MPa), a significant rising of the density comparing to the sintering density occurs. The value of this rising is influenced also by the compacting pressure used for the powder compaction, the highest final density being obtained for the highest value of the compacting pressure.

As it was expected, the material cold straining, during the repressing, leads to an important microstructure refining. Comparing the microstructures of the repressed compacts in cross sections perpendicular on the repressing direction, with those of the sintered samples analyzed in the same sections (Fig. 3), it can be seen a notable difference in the pores concentration and dimensions, but especially in the shape and dimensions of grains. It can be observed that almost all of the existing pores have been eliminated through BMA, especially by shearing through material radial flow in the die of bigger diameter or by solid state welding.

In an axial cross-section (Fig. 4), it can be clearly seen the preferential deformation along the flow direction under BMA. The pores are almost entirely eliminated - the residual ones heaving very small dimensions, and the crystal grains

have shapes with irregular contours – emphasizing the radial flow, which is a characteristic for the deformation through shearing produced by repressing in a die with a bigger diameter.

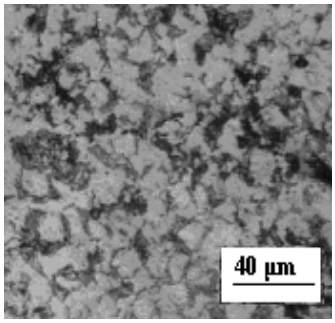

a)

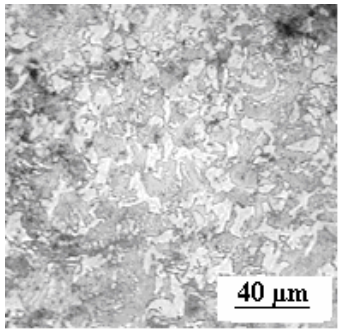

b)

Fig. 3. Typical microstructure of samples in a transversal cross-section: a) without repressing; b) re-pressed at 1600 [MPa].

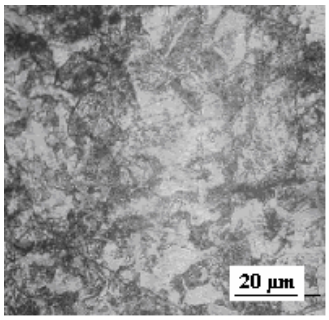

a)

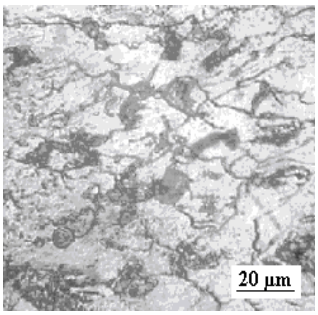

b)

Fig. 4. Typical microstructure of samples in an axial cross-section: a) without repressing; b) re-pressed at 1600 [MPa].

The variation of the crystalline grains dimensions by re-pressing was determined through XRD analysis, by their calculation with the Scherrer's relationship, which considers the variation of the experimentally determined diffraction lines width at their half height, β, [3]:

$$ß = K*\lambda / D*\cos\theta \quad (1)$$

where D is the average dimension of crystallites, θ – Bragg angle and K a constant depending on the crystallites shape, on the Miller indexes, on the diffraction line characteristics and on the defining mode of D. The values of ß were measured on the obtained XRD patterns, while, according to some published recommendations [8], the value K = 1 was adopted.

Figure 5 illustrates the growth of the diffraction line width at their half height - corresponding to the reflections on crystallographic planes (110) and (200) with the increasing of the re-pressing pressure, which indicates the decreasing of the crystal grains dimensions. By calculating the average grain size value for the above mentioned crystallographic planes, a diminishing of the crystalline grains dimensions can be observed, depending on the repressing pressure – as shown in Figure 6.

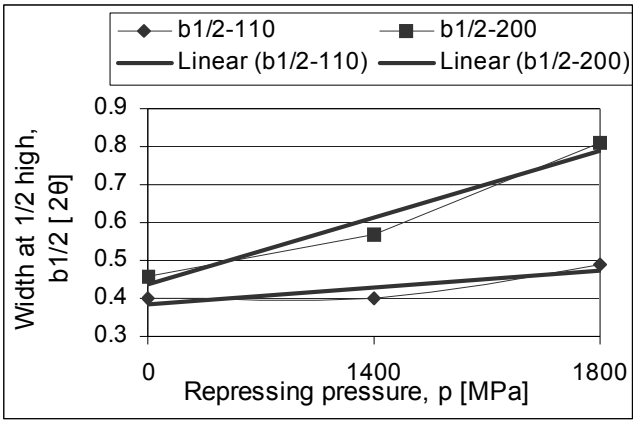

Fig. 5. Variation of the width at 1/2 height of the diffraction lines depending on the repressing pressure

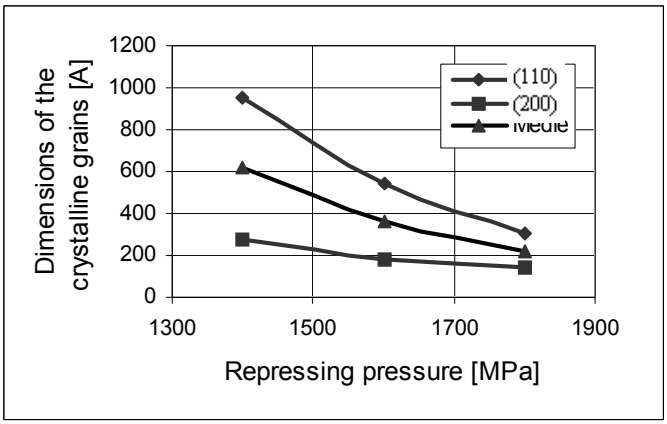

Fig. 6. Variation of the crystal grain dimensions vs. re-pressing pressure.

It is to be remarked that for the maximum re-pressing pressure these values are even in the nanometric domain. So, by BMA applying to the sintered carbon steels under appropriate conditions, even nanocrystalline structures can be obtained.

The resulted denser and finer microstructure, combined with the material cold-hardening during re-pressing, lead, as expected, to a notable increasing in the steel hardness (Fig. 7).

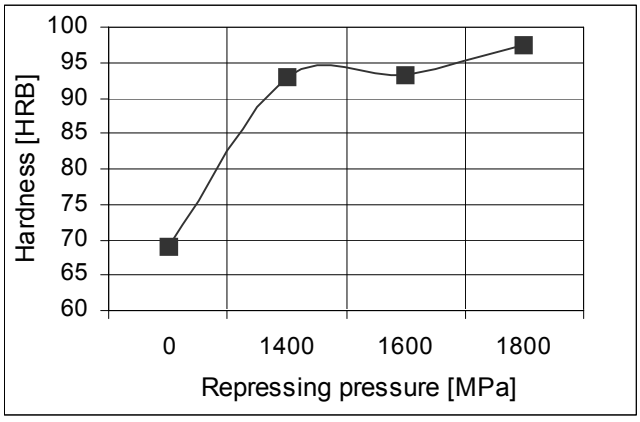

Fig. 7. The hardness variation for the re-pressed compacts vs. re-pressing pressure

Although it was not directly determined, it is expected that the tensile strength of these steels would also increase. However, as it can be seen, the hardness increasing is very abrupt for the first step of re-pressing and becomes shallower for the further

pressure increasing. The explanation is related to the prominent pore elimination in the first step of repressing and to the increase of the grain boundaries volume fraction density as the crystallites size approaches the nanometric scale.

5. Conclusions

The performed researches have demonstrated the possibility to improve the mechanical properties of structural sintered steels by the bulk severe plastic deformation. This is achieved by the combined effects of almost complete elimination of pores, microstructure refining and material cold hardening.

The behavior of the ASC 100.29 sintered steel at severe plastic deformation, obtained on the principle of bulk mechanical alloying, is in a close correlation with the powder compressibility, which determines the achievable deformation degree under acceptable conditions from the technical and economical points of view. The achievable improvement of mechanical properties depends on the attained deformation degree – determined by the applied pressure but also by the powder compressibility. At a deformation degree higher then the critical one, which corresponds to the cold hardening, an advanced structure refining – even to the nanometric domain is obtained, which leads to important improvements of mechanical properties.

Received March 12, 2007 *Technical University of Cluj – Napoca*

REFERENCES

1. Pranghell P. B., J. R. Bowen, **Mechanism of Formation of Sub micron Grain Structure During Sever Deformation**, T. M. S. Document Center, 2004.
2. Han B. Q., Laverne E. J., and Mohamed F. A., **Dislocation structure and deformation in iron processed by equal-channel-angular pressing** (2004). Metallurgical and Materials Transactions A, 35A (4), p. 1343-1350.
3. Kvackaj, T., Zemko, M., Kusculic, T. , et. al., **Nano & Ultra-fine Grained Materials, Severe Plastic Deformation**, Proceedings pf the World Congress of Powder Metallurgy, Busan, Korea, 2006, part 2.
4. X X X, **Höganäs Iron and Steel Powders for Sintered Components**. Höganäs AB Sweden, 1998.
5. Aizawa, T., Zhou C., **Bulk Mechanical Alloying for Solid-State Synthesis of Functional Materials**. Advanced Engineering Materials, Volume 2, Issue 1-2, 2000, p.11-59.
6. Chertes, V., Orban, R. **Analiza factorilor determinanți ai geometriei și dimensiunilor preformelor sinterizate pentru matriță**re, Ştiinţă şi Inginerie, vol. VI, Ed. AGIR, 2004.
7. ASM HANDBOOK, vol. 7, **Powder Metallurgy,** 1993, 897 p.
8. Pop, V., Chicinaş, I., Jumate, N., **Fizica Materialelor**, Presa Universitară Clujeană, Cluj-Napoca, 2001, 355 p.

POSIBILITĂȚI DE OBȚINERE A STRUCTURILOR FINE, ÎN OȚELURILE SINTERIZATE, PRIN DEFORMARE PLASTICĂ SEVERĂ

Rezumat: Lucrarea prezintă o analiză a posibilităților de îmbunătățire a proprietăților mecanice ale oțelurilor structurale sinterizate, prin metoda deformării plastice severe a materialului masiv. Rezultatele obținute prin aplicarea metodei în varianta alierii mecanice masive, la oțelurile carbon sinterizate, au dovedit posibilitatea eliminării avansate a porilor precum şi a fnisării microstructurii, chiar până la scară nanometrică, în strânsă corelație cu parametrii de deformare şi cu gradul de deformare atins. Efectele lor combinate au dus la o importantă îmbunătățire a proprietăților mecanice determinate.

BULETINUL INSTITUTULUI POLITEHNIC DIN IAŞI
Tomul LIII (LVII), Fasc. 1, 2007
Secția
ŞTIINȚA ŞI INGINERIA MATERIALELOR

MAGNETIC STRUCTURE OF $La_{0.54}Ho_{0.11}Sr_{0.35}Mn_{1-x}Co_xO_3$ MANGANITES

BY

MIHAIL-LIVIU CRAUS[1, 2], NICOLETA CORNEI[3], CARMEN MATA[3] and MIHAI LOZOVAN[1]

Abstract: The aim of present paper is to establish a correlation between the structure and microstructure parameters, on a side, and physical properties of $La_{0.54}Ho_{0.11}Sr_{0.35}Mn_{1-y}Co_yO_3$ manganites, on other side. Presintered and sintered manganites were monitored by X-ray analysis to determine begin of solid-state reaction, the phase composition, the parameters of unit cell, the average size of coherent blocks and the microstrains. Mn-O distances, Mn-O-Mn angles, atoms positions in the unit cell were determined. Variation of the average size of the coherent blocks and microstrains with Co concentration were studied. We discussed the dependence between the tolerance factor, the chemical disorder degree and the bandwidth, on a side, and the Curie temperature on other side.

Keywords: manganites, magnetic structure, XRD analysis, microstructure parameters

1. Introduction

The manganites were synthesized about 50 years ago, but the most important properties were discovered in early nineties. The $AMnO_3$ manganites, where A is a rare earth or an earth alkali cation, manifest a strong dependence of resistivity with applied magnetic field and temperature. For more manganites a metallic behaviour was observed at low temperatures. The presence of intrinsic and/or extrinsic magnetoresistance in rare-earth hole-doped manganites justifies the study on related compounds. The substitution of rare-earth cations with an earth alkali cations implies the appearance of Mn^{4+} cations, which are bounded with Mn^{3+} cations by O anions: $Mn^{3+}(t_{2g}^3 e_g^1)$-O^{2-}—$Mn^{4+}(t_{2g}^3 e_g^0)$. The double exchange aligns ferromagnetic the spins of Mn^{3+} and Mn^{4+} cations and allows a metallic behaviour of the manganite below Curie temperature. On other side, the substitution of rare earth with earth alkali cations leads to a modification of the average size of A places and of the Curie temperature. The magnetic and electrical properties of the manganites are explained by Zener double exchange theory [1]. If we substitute a Mn cation with a transition cation, as Co, Fe, Cr, Cu etc takes place a change in the local structure of the manganites. Presence of Co^{3+} and Co^{4+} cations lead to appearance of colossal magnetoresistance (CMR) and to a complex magnetic phase diagrams because Co cations exhibit more than two spin configurations [2, 3, 4]. $La_{1-x}Sr_xMnO_3$ manganites exhibit ferromagnetic (T_C) and metal-insulator (T_{MI}) transitions for $x>0.1$, with $T_C \in (150 \div 350$ K) [5].

2. Experimental procedure

The $La_{0.54}Ho_{0.11}Sr_{0.35}Mn_{1-x}Co_xO_3$ ($x=0.0 \div 0.2$) manganites were synthesized by

means of ceramic technology. Stoichiometric mixtures of La_2O_3, Ho_2O_3, $SrCO_3$, MnO_2 and $Co(NO_3)_2 \cdot 6H_2O$ were milled in an agate mill, pressed and treated at 800ºC for 17 hours in air**.** The presintered samples were grinded again, pressed and finally sintered at 1200 ºC for 10 hours in air. The heating and cooling rates were 200 ºC/hour.

Samples were investigated by X-ray diffraction, by using a diffractometer with Cu anode tube and data acquisition system. XRD data were handled with DICVOL, CellRef and a Rietveld type programs (PowderCell [6], to obtain the phase composition, lattice parameters, atoms position in the unit cell, average size of coherent blocks and the microstrains. (Mn,Co)-O distances and (Mn,Co)-O-(Mn,Co) angles were also determined. Magnetic properties (specific/molar magnetization, Curie temperature) were determined from the variation of magnetization with the temperature, by using a Foner type magnetometer with data acquisition system, between 77 and 600 K. Resistance dependence on the temperature and the magnetic field intensity were obtained by means of four probe method, using a data acquisition system.

3. Experimental results and discussion

The sintered samples contain as major phase a manganite. The structure of the major phase was tested as being a Pnma (space group 62) structure (s. Fig.1 ÷ 3). Some authors indicated for similar compounds ($La_{0.7}Sr_{0.3}Mn_{1-x}Co_xO_3$ ($x \in 0.0 \div 1.0$)), a rhombohedral structure as possible [7]. Recently, Bindu et al have obtained by means of ceramic technology $La_{1-x}Sr_xMnO_3$ manganites with rhombohedral structure for $x \in 0.1 \div 0.4$ and orthorhombic structure for $x \in 0.5 \div 0.9$ [8].

We are trying now other structure variants, but the preliminary results indicate that the volume/formula unit, the distances Mn(Co)-O and the angle of the Mn(Co)-O-Mn(Co) bonds remain practically unchanged.

The lattice parameters associated with Pnma unit cell were determined with CellRef program and refined, together the positions of the cations/anions in the unit cell and the lattice parameters by a Rietveld program (s. Fig.1 ÷ 3 and Tab.1). The $La_{0.54}Ho_{0.11}Sr_{0.35}Mn_{0.9}Co_{0.1}O_3$ manganite synthesized by ceramic technology contains a small amount of foreign phase corresponding (s. Fig.2), while similar samples synthetisezed by sol-gel method are pure.

Table 1 Cations and anions positions in the Pnma (GS 62) unit cell for $La_{0.54}Ho_{0.11}Sr_{0.35}Mn_{0.9}Co_{0.1}O_3$ manganite

Atom	Wykoff position	X	Y	Z	B_{iso}	Occupation
La	4c	0.50575	0.25000	0.49733	0.8000	0.54
Sr	4c	0.50575	0.25000	0.49733	0.8000	0.35
Ho	4c	0.50575	0.25000	0.49733	0.8000	0.11
Mn	4b	0.00000	0.00000	0.50000	0.6936	0.90
Co	4b	0.00000	0.00000	0.50000	0.6936	0.10
O_{ap} *)	4c	0.02562	0.25000	0.62381	0.5784	1.00
O_{eq} **)	8d	0.71978	-0.00988	0.26760	0.8000	2.00

*) O_{ap} – oxygen in apical position;
**) O_{eq} - oxygen in equatorial position.

The unit cell volume have a minimum, while the average size of the coherent blocks and the microstrains have a maximum with the Co concentration in the samples (s.Tab.2).

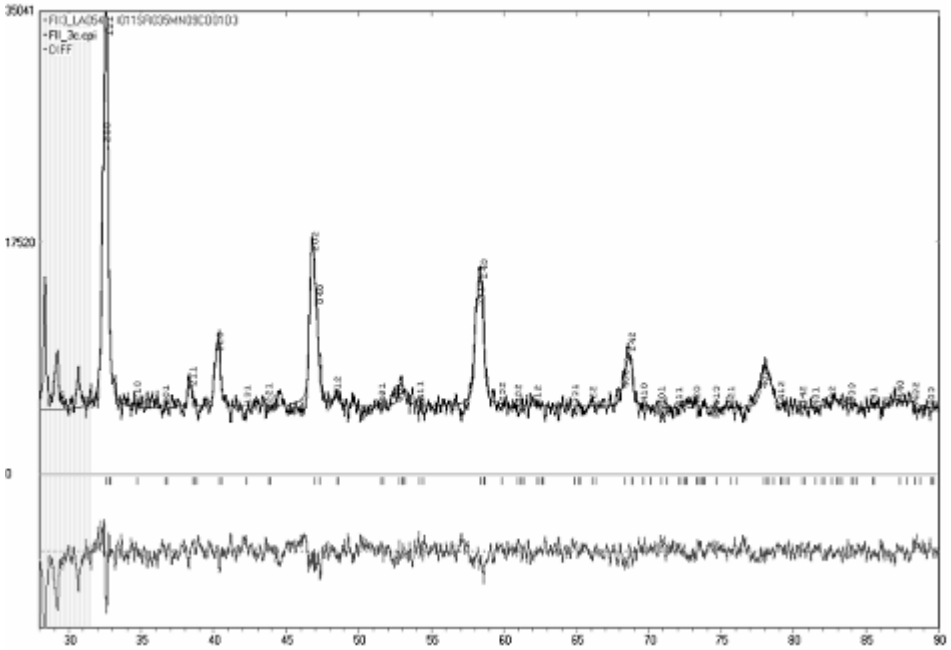

Figure 1 Difractogram of $La_{0.54}Ho_{0.11}Sr_{0.35}Mn_{0.9}Co_{0.1}O_3$ manganite (CuKα) (bottom-diffrence between calculated and observed difractograms)

The Mn-O_{ap} and Mn-O_{eq} distances and the Mn-O_{ap}-Mn bond angle have also maxima, while the Mn-O_{eq}-Mn bond angle increases monotonously, on the Co concentration in the manganites (s.Tab.3). The substitution of Mn^{3+}/Mn^{4+} cations (r_{Mn3+} = 0.785Å (high spin state); r_{Mn4+} = 0.530 Å) with Co^{3+}/Co^{4+} cations (r_{Co3+} = 0.75 Å (high spin state); r_{Co3+} = 0.685 Å (low spin state); r_{Co4+} = 0.67 Å) lead to a complex variation of the unit cell volume, Mn(Co)-O distances and Mn(Co)-O-Mn(Co) bond angles (s. Tab.3), because Co^{3+} can be found in a low state, an intermediate state or high state of spin.

Table 2 Lattice constants (a, b, c), unit cell volume (V), average size of the coherent blocks (D) and microdistortions (**ε**) for $La_{0.54}Ho_{0.11}Sr_{0.35}Mn_{1-x}Co_xO_3$ manganites

x	a (Å)	b (Å)	c (Å)	V (Å^3)	D (Å)	ε
0.00	5.5160	7.7155	5.4627	232.485	329.0	0.001089
0.10*	5.4841	7.6872	5.4502	229.766	365.1	0.001178
0.15	5.4875	7.6925	5.4498	230.050	368.7	0.001206
0.20	5.4974	7.6950	5.4598	231.457	240.9	0.000651

*) large amount of foreign phase

The observed change in the lattice constants are due to the variation of the Co^{3+}, Co^{4+}, Mn^{3+} and Mn^{4+} concentration with the chemical composition of the samples and to a possible appearence of Co cations in a low state of valence.

The unit cell volume has a minimum, while average size of the coherent blocks and the microstrains have a maximum with the Co concentration in the samples (s.Tab.3).

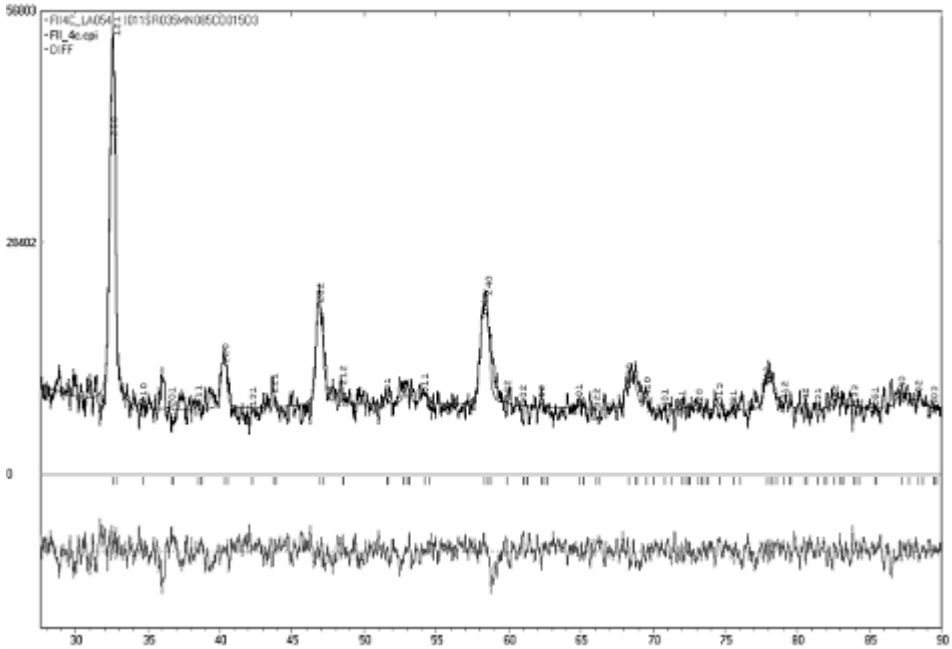

Figure 2 Difractogram of $La_{0.54}Ho_{0.11}Sr_{0.35}Mn_{0.85}Co_{0.15}O_3$ manganite (CuKα) (bottom-diffrence between calculated and observed difractograms)

Table 3 Mn-O_{ap} (d_{MnOap}), Mn-Oeq (d_{MnOeq}) distances and (∠Mn-O_{ap}-Mn) (∠Mn-O_{eq}-Mn) angles at $La_{0.54}Ho_{0.11}Sr_{0.35}Mn_{1-x}Co_xO_3$ manganites

x	d_{MnOap} (Å)	d_{MnOeq} (Å)	∠Mn-O_{ap}-Mn(°)	∠Mn-O_{eq}-Mn(°)
0.00	1.9563	1.9656	160.792	161.552
0.10*)	1.9492	1.9576	160.771	161.547
0.15	1.9582	1.9523	160.803	161.525
0.20	1.9648	1.9576	160.968	161.408

*) large amount of foreign phase

The Mn-O distances present a minimum, while the Mn-O-Mn bonds have a minimum, respectively, a monotonous decrease, on the diferent crystallographic directions, with the increase of Co concentration in the samples

We are investigating the cation distribution on valence and the spin state in $La_{0.54}Ho_{0.11}Sr_{0.35}Mn_{1-x}Co_xO_3$ manganites and the results will be published later.

The variation of the specific magnetization with Co concentration in the samples indicate a decrease of the specific magnetization maximum with the increase of Co concentration in the samples (s.Fig.3 and Tab.4). We supposed that the cation distribution in the samples is given by:

$$\left(La^{3+}_{0.54}Ho^{3+}_{0.11}Sr^{2+}_{0.35}\right)_A\left(Mn^{4+}_{y}Mn^{3+}_{1-x-y}Co^{4+}_{z}Co^{3+}_{x-z}\right)_B O_3 \qquad (1)$$

and calculated the Mn^{4+} and Co^{4+} concentration by using the molar magnetization.

The calculated value of y and z should support the supposition that the Mn and Co cations participate together to the double exchange interaction. Because we have obtained y>1 and z<0, that means that this model is not correct. On other hand, if we suppose that only Mn cations form the magnetic structure, we are obtaining a decrease of the Mn^{4+} concentration with the increase of Co concentration, implicitly a decrease of Mn concentration in the samples (s.Tab.4).

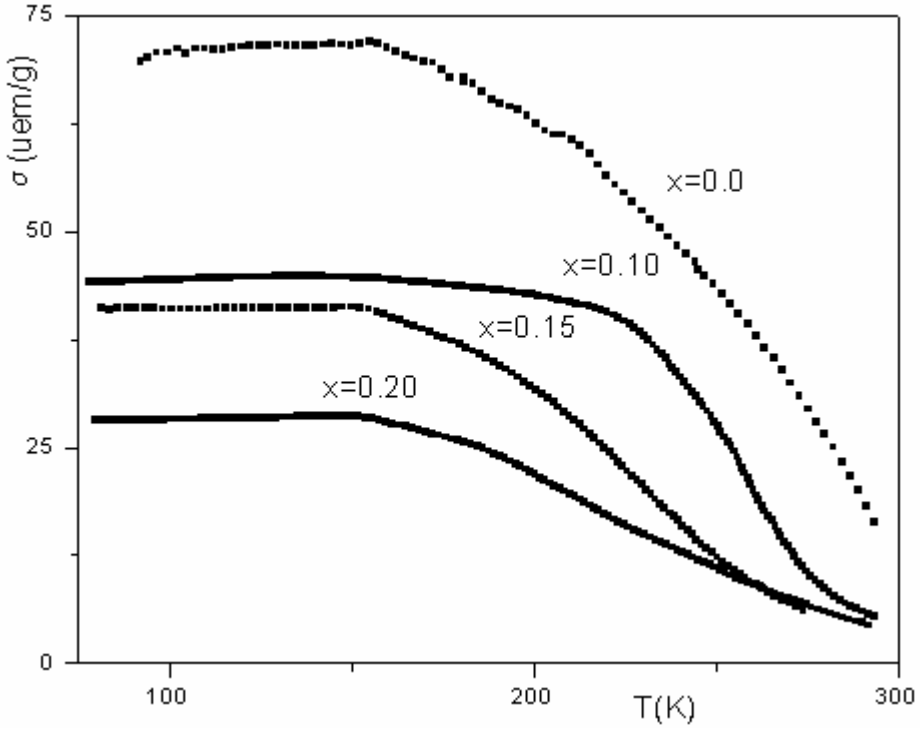

Figure 3 Variation of the specific magnetization with Co concentration (x) in $La_{0.54}Ho_{0.11}Sr_{0.35}Mn_{1-x}Co_xO_3$ manganites

A strong decrease of the Curie temperature takes place with the increase of the Co concentration in the manganites, in agreement with the decrease of the Mn^{3+}-O-Mn^{4+} bonds and with the increase of the absolute value of the band width (s. Tab.4).

Table 4 Magnetic moment per formula unit (p), bandwidth (w), the Curie temperature, (T_C), concentration of Mn^{4+} and the tolerance factor (t) for the $La_{0.54}Ho_{0.11}Sr_{0.35}Mn_{1-x}Co_xO_3$ manganites

x	p(μ_B)	$\lvert w \rvert$	T_C (K)	y	t
0.0	2.747	0.056	>300	0.392	0.957
0.10	1.824	0.059	264	0.260	0.943
0.15	1.683	0.060	231	0.240	0.941
0.20	1.249	0.065	208	0.177	0.934

The band width is given by:

$$w \propto \frac{\cos(\frac{\pi - \angle(Mn-O-Mn)}{2})}{d_{Mn-O}^{3.5}} \qquad (2)$$

The linear dependence betwen the tolerance factor and Curie temperature are in agreement with the well known literature data. A decrease of the double exchange interaction (s. variation of bandwidth in Tab.4) and a corresponding increase of superexchange interaction takes places with the increase of Co concentration in the samples.

4. Conclusions

We have obtained a row of $La_{0.54}Ho_{0.11}Sr_{0.35}Mn_{1-x}Co_xO_3$ manganites with the Curie temperature between 200 K and room temperature. The substitution of Mn with Co lead to a decrease of the Curie temperature and the calculated bandwidth, implicitly to a decrease of double exchange interaction between Mn^{3+} and Mn^{4+} cations. The variation of the molar magnetization and the Curie temperature with Co concentration confirm that the Co cations do not participate to the magnetic structure of the manganite.

Received Mar. 31nd, 2007

(1) National Institute of R & D for Technical Physics Iaşi, Romania
(2) Joint Institute for Nuclear Research, Dubna, Russia
(3) Chemistry Departament, "Al.I.Cuza" University,Iasi, Romania

REFERENCES

1. C.Zener, **Phys. Rev., 81**, 1951, **440**
2. T. P. Dhakal, K. Miyoshi, K. Fujiwara, J. Takeuchi, **J.M.M.M.**, **226-230**, 2001, **824**
3. E. Syskakis, G. Choudalakis and C. Papastaikoudis, J**. Phys.: Condens. Matter, 15,** 2003, **7735**
4. M.F. Tai, F.Y. Lee, J.B. Shi, **J.M.M.M.**, **209,** 2000, **148**
5. T. Suzuki and M. Awano, **J. Am. Ceram. Soc.**, **89,** 2006, **3854**
6. G. Nolze and W.Kraus, PowderCell , J. Appl.Cryst., **29**, 1996, **301**
7. X. J. Fan, J. H. Zhang, X. G. Li, W. B. Wu, J. Y. Wan, T. J. Lee and H.C.Ku, **J. Phys.: Condens. Matter**, **11,** 1999, **3141**
8. R.Bindu, S.K.Pandey, A. Kumar, S.Khalid and A.V.Pimpale, **J. Phys.: Condens. Matter, 17,** 2005, **6393**

STRUCTURA MAGNETICA A MANGANITILOR $La_{0.54}Ho_{0.11}Sr_{0.35}Mn_{1-x}Co_xO_3$

Rezumat: Scopul articolului este de a stabili o corelatie intre parametrii structurii si ai microstructurii, pe de o parte, si proprietatile fizice ale manganitilor $La_{0.54}Ho_{0.11}Sr_{0.35}Mn_{1-y}Co_yO_3$, pe de alta parte. Probele au fost obtinute prin tehnologia ceramica, utilizand oxizi (La_2O_3, Ho_2O_3, MnO_2 and Co_2O_3) si carbonati ($SrCO_3$). Manganitii presinterizati si cei sinterizati au fost monitorizati prin difractie de raze X pentru determinarea inceputului reactiei in faza solida, a compozitiei de faza, a parametrilor celulei elementare, a dimensiunilor medii ale blocurilor de mozaic si a microdistorsiunilor. Au fost determinate distantele Mn-O, unghiurile legaturilor Mn-O-Mn si pozitiile atomilor in celula elementara. A fost studiata dependenta dimensiunilor medii ale blocurilor de mozaic si a microdistorsiunilor in functie de concentratia de Co din proba. Am discutat dependenta intre factorul de toleranta, gradul de dezordine chimica si latimea de band, pe de o parte, si temperature Curie, pe de alta parte.

BULETINUL INSTITUTULUI POLITEHNIC DIN IAŞI
Tomul LIII (LVII), Fasc. 1, 2007
Secția
ŞTIINȚA ŞI INGINERIA MATERIALELOR

CRYSTALLINE AND MAGNETIC CHANGES INDUCED BY THERMAL TREATMENT AT $(Nd_{0.67}In_{0.33})_{1-x}Sr_xMnO_3$ MANGANITES

BY

MIHAIL-LIVIU CRAUS[1, 2], MIHAI LOZOVAN[1] AND NICOLETA CORNEI[3]

Abstract: The aim of present paper is to establish a correlation between the structure and microstructure parameters, on a side, and physical properties of $(Nd_{0.67}In_{0.33})_{1-x}Sr_xMnO_3$ manganites, on other side. Presintered and sintered manganites were monitored by X-ray analysis to determine begin of solid-state reaction, the phase composition, the parameters of unit cell, the average size of coherent blocks and the microstrains. Mn-O distances, Mn-O-Mn angles, atoms positions in the unit cell were determined. We discussed the dependence between the tolerance factor, the chemical disorder degree and the bandwidth, on a side, and the Curie temperature on other side. We consider also the influence of the change of the crystalline structure on the magnetic properties. The appearance at low temperature of the spin-glass behaviour is discussed in function on microstructure parameters.

Keywords: manganites, magnetic structure, XRD analysis, spin-glass behaviour

1. Introduction

The $AMnO_3$ manganites, where A is a rare earth or an earth alkali cation, manifest a strong dependence of resistivity with applied magnetic field and temperature. The substitution of rare-earth cations with an earth alkali cations implies the appearance of Mn^{4+} cations, which are bounded with Mn^{3+} cations by O anions: $Mn^{3+}(t_{2g}^3e_g^1)$-O^{2-} -$Mn^{4+}(t_{2g}^3e_g^0)$. The double exchange aligns ferromagnetic the spins of Mn^{3+} and Mn^{4+} cations and allows a metallic behaviour of the manganite below Curie temperature. The substitution of trivalent rare earth cations with other trivalent cations modifies the chemical disorder degree and the tolerance factor and influences the magnetic and transport properties of the manganites. The substitution of rare earth with earth alkali cations leads to a modification of the average size of A places and of the Curie temperature. The magnetic and electrical properties of the manganites are explained by Zener double exchange theory [1]. Different thermal treatments can lead to a change of the phase composition, a modification of the Mn^{3+}/Mn^{4+} concentration, implicitly to a modification of the structure and microstructure characteristics of manganites. Our aim is to investigate the change induced in the crystalline and magnetic structure of $(Nd_{0.67}In_{0.33})_{1-x}Sr_xMnO_3$ (x=0.2; 0.35; 0.50; 0.67) manganites by thermal treatments and due to substitution of Nd/In cations with Sr cations.

2. Experimental procedure

The $(Nd_{0.67}In_{0.33})_{1-x}Sr_xMnO_3$ (x=0.2; 0.35; 0.50; 0.67) manganites were synthesized by means of standard ceramic technology. Stoichiometric mixtures of

Nd_2O_3, In_2O_3, $SrCO_3$ and MnO_2 were milled in an agate mill, pressed and treated at 900ºC for 10 hours in air**.** The presintered samples were grinded again, pressed and finally sintered at 1200ºC for 5 hours in air, again grinded, pressed and treated 25 hours at 1200 ºC, in air. Samples were investigated by X-ray diffraction, by using a STOE (Guinier type) diffractometer with Cu anode tube and data acquisition system. XRD data were handled with DICVOL, CellRef and a Rietveld type programs (PowderCell [6-2], to obtain the phase composition, lattice parameters, atoms position in the unit cell, average size of coherent blocks and the microstrains. Mn-O distances and Mn-O-Mn bonds angles were also determined. Magnetic properties (specific/molar magnetization, Curie temperature) were obtained from the variation of magnetization with the temperature, by using a Foner type magnetometer with data acquisition system, between 77 and 300 K. The samples were cooled until 77 K without magnetic field, the magnetic measurements being performed in a 1 T magnetic field.

3. Experimental results and discussion

The treated $(Nd_{0.67}In_{0.33})_{1-x}Sr_xMnO_3$ samples contain as major phase a perovskite, with a Pnma (space group 62) structure unit cell (s. Fig.1 ÷ 2) for x=0.2 and 0.35. For higher concentration of Sr, the main phase is characterized by the I4/mcm (GS 140) unit cell. A small amount of In_2O_3 (cubic, Ia3, GS 206) and of pyrolusite was observed. Some manganites can be characterized by a rhombohedral structure [3]. Bindu et al have obtained by means of ceramic technology $La_{1-x}Sr_xMnO_3$ manganites with rhombohedral structure for $x \in 0.1 \div 0.4$ and orthorhombic structure for $\in 0.5 \div 0.9$ [4]. We have tested the possibility that the treated manganites to be formed by a mixture of orthorhombic/rhombohedral/tetragonal phases, but the results a less reliable, as comparing with those obtained by supposing that the sample is formed by one main phase (orthorhombic/tetragonal) and a small amount of impurities.

Table 1 Atomic positions in the Pnma (GS 62) unit cell for $(Nd_{0.67}In_{0.33})_{0.8}Sr_{0.2}MnO_3$ manganites

Atom	Wykoff position	X	Y	Z	B_{iso}
Nd, In, Sr	4c	0.0426	0.2500	0.9946	0.8000
Mn	4b	0.0000	0.0000	0.5000	0.6936
O_{ap} *)	4c	0.4829	0.25000	0.0572	0.5784
O_{eq} **)	8d	0.2819	0.0371	0.7270	0.8000

*) O_{ap} – oxygen in apical position;
**) O_{eq} - oxygen in equatorial position.

Actually, we have found that all supplemental XRD maxima can be attributed to a superstructure like $P2_1/a$. The XRD data are being tested with a Rietveld programme, to obtain an exact answer to this question. A long duration of thermal treatment at high temperature induces a change in the phase composition, as comparing with similar compounds treated a shorter time [5]. We attributed this behaviour to a small change of the chemical composition of the main phase, including the modification of the Mn^{3+}/Mn^{4+} concentrations ratio. A smaller Mn^{3+} concentration means a more symmetrical structure, with the same nominal composition [5].

The lattice parameters associated with Pnma and I4/mcm unit cells were determined with CellRef program and refined, together the positions of the cations/anions in the unit cell and the lattice parameters, by a Rietveld program (s. Fig.1, 2 and Tab.1, 2).

Table 2 Atomic positions in the I4/mcm (GS 140) unit cell for $(Nd_{0.67}In_{0.33})_{0.33}Sr_{0.67}MnO_3$ manganites

Atom	Wykoff position	X	Y	Z	B_{iso}
Nd, In, Sr	4b	0.0000	0.5000	0.2500	0.61
Mn	4c	0.0000	0.0000	0.0000	0.25
O_{ap} *)	4a	0.0000	0.0000	0.2500	1.28
O_{eq} **)	8h	0.7800	0.2800	0.0000	1.01

*) O_{ap} – oxygen in apical position;
**) O_{eq} - oxygen in equatorial position.

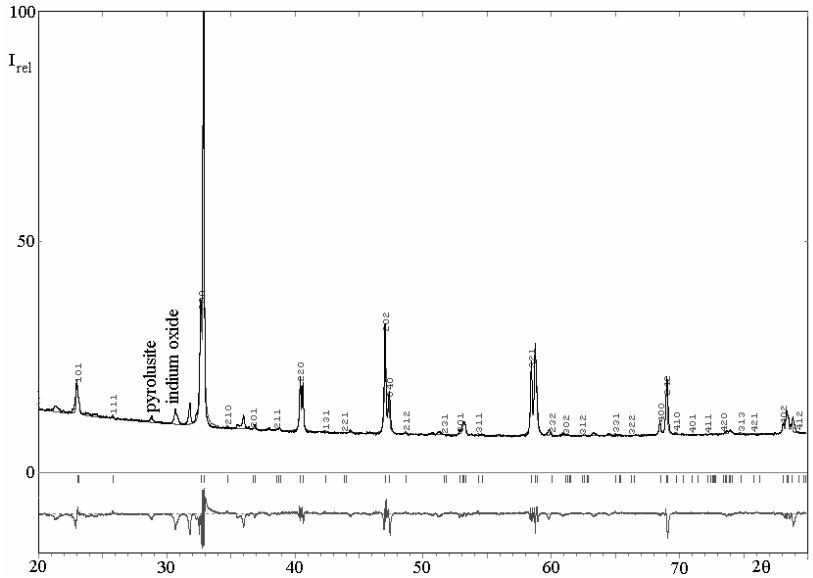

Figure 1 Difractogram of $(Nd_{0.67}In_{0.33})_{1-x}$ Sr_xMnO_3 manganites *(x=0.2).Bottom part represents the difference between the observed and calculated diffractogram.*

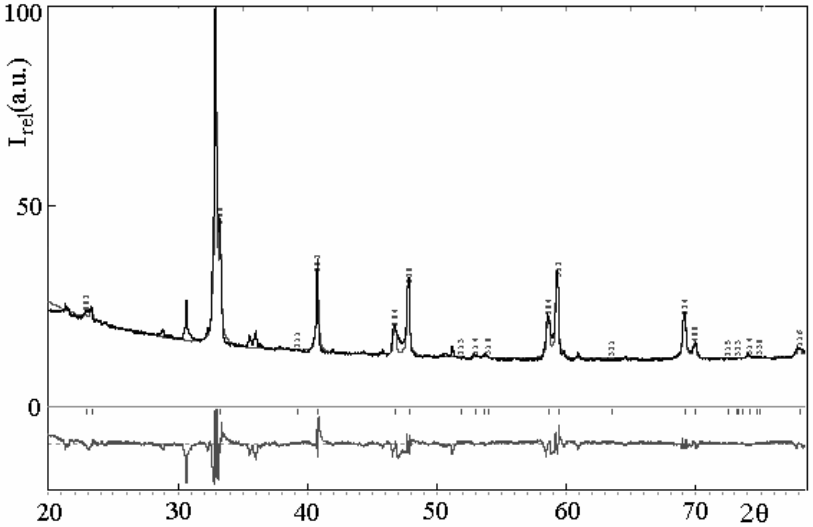

Figure 2 Difractogram of $(Nd_{0.67}In_{0.33})_{1-x}$ Sr_xMnO_3 *manganites (x=0.67).Bottom part represents the difference between the observed and calculated diffractogram.*

The volume corresponding to the formula unit have a maximum with the increase of Sr concentration in the samples (s.Tab.3).

The substitution of Nd^{3+}/In^{3+} cations (r_{Nd3+} = 1.303 Å; r_{In3+} = 1.12 Å) with Sr^{2+} cations (r_{Sr2+} = 1.45 Å) leads to a modification of Mn^{3+}/Mn^{4+} concentration (r_{Mn3+} = 0.785 Å; r_{Mn4+} = 0.67 Å) and to a complex variation of the unit cell volume, Mn-O distances and Mn-O-Mn bond angles (s. Tab.2 and 3).

An important effect of the substitution of A^{3+} cations with Sr^{2+} cations is a decrease of the Mn^{3+} concentration, a cation characterized by Jahn-Teller effect. On the data concerning the Mn-O distances and lattices parammeters, the substitution of rare earth with Sr has a stronger effect as the increase of Mn^{4+} concentration for composition with $x \leq 0.35$, while for compounds with $x > 0.35$ dominate the effect of increase of Mn^{4+} concentration; the apparence of a large amount of Mn^{4+} symmetrical cations leads to the transition from orthorombic to tetragonal structure.

The Mn-O_{ap} and Mn-O_{eq} distances and the Mn-O_{ap}-Mn bond angle have maxima with the increase of Sr concentration (s.Tab.3).

Table 2 Lattice constants (a, b, c), unit cell volume (V), average size of the coherent blocks (D) and microdistortions (**ε**) for $(Nd_{0.67}In_{0.33})_{1-x}$ Sr_xMnO_3 manganites

x	a (Å)	b (Å)	c (Å)	V (Å^3)	D (nm)	ε
0.20	5.4746	7.6710	5.4375	228.351	75.88	0.000194
0.35	5.4615	7.7358	5.4597	230.639	75.32	0.000205
0.50	5.3848	5.3848	7.7708	225.314	49.36	0.000223
0.67	5.3725	5.3725	7.7553	223.847	47.63	0.001137

Table 3 Mn-O_{ap} (d_{MnOap}), Mn-Oeq (d_{MnOeq}) distances and (∠Mn-O_{ap}-Mn) (∠Mn-O_{eq}-Mn) angles for $(Nd_{0.67}In_{0.33})_{1-x}$ Sr_xMnO_3 manganites

x	d_{MnOap} (Å)	d_{MnOeq} (Å)	∠Mn-O_{ap}-Mn(°)	∠Mn-O_{eq}-Mn(°)
0.20	1.9451	1.9614	160.774	159.152
0.35	1.9612	1.9632	160.874	159.051
0.50	1.9427	1.9174	180.000	166.315
0.67	1.9388	1.9131	180.000	166.314

An important change has been observed in the variation of the average size of coherent blocks, with becomes smaller, with the transition to a higher symmetry structure (s.Tab.3).

We supposed that the cation distribution in the samples is given by:

$$\left(Nd^{3+}_{0.67(1-x)}In^{3+}_{0.33(1-x)}Sr^{2+}_{x}\right)_A (Mn^{4+}_{x}Mn^{3+}_{1-x})_B O_3 \quad (1)$$

and calculated the Mn^{4+} concentrations and molar magnetizations. The variation of the specific magnetization with Sr concentration indicates a sudden change of the specific magnetization maximum for $x \geq 0.5$ (s.Fig.3 and Tab.4). If we consider that Nd^{3+} did not participate to the magnetic structure of the samples, we obtained the data corresponding to the third column (Tab.4). The experimental molecular

magnetizations were calculated from the specific magnetization data at 77 K (s. second column, Tab.4). A fair agreement exists between the calculated and experimental data of magnetization for the manganites corresponding to x≤0.35 (s.Fig.3 and Tab.4).

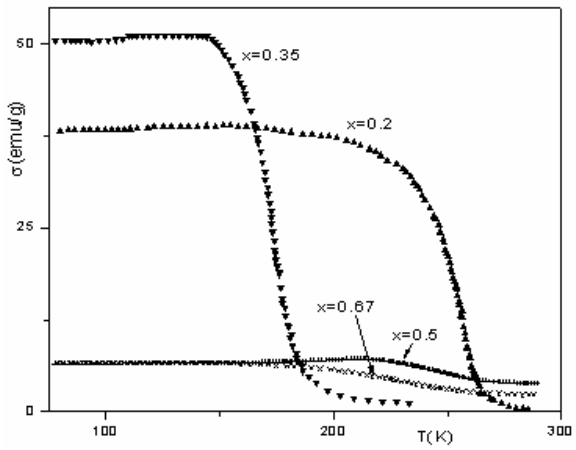

Figure 3 Variation of the specific magnetization with Sr concentration (x) for $(Nd_{0.67}In_{0.33})_{1-x}Sr_xMnO_3$ manganites

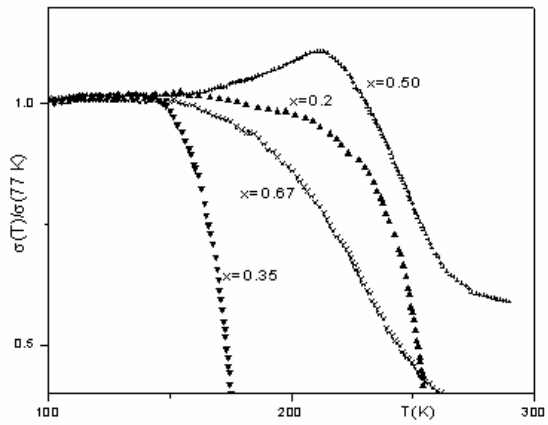

Figure 4 Variation of the normalized magnetization (σ(T)/σ(77K)) with Sr concentration (x) for $(Nd_{0.67}In_{0.33})_{1-x}Sr_xMnO_3$ manganites

The manganites with x>0.35 have small specific magnetizations, as comparing with those calculated (s.Fig.3 and Tab.4). We have associated this change with the transition to a more symmetrical lattice, implicitly an increase of the superexchange interaction as comparing with the double exchange interaction for the samples with x>0.35.

Table 4 Magnetic moment per formula unit (p), bandwidth (w), the Curie temperature, (T_C), concentration of Mn^{4+} (y_{teor}), the observed tolerance factor (t_{obs}), chemical degree disorder (σ^2), average size of coherent blocks (D_m) and microstrains (ε) for $(Nd_{0.67}In_{0.33})_{1-x}Sr_xMnO_3$ manganites

x	$p_{exp,77K}$ (μ_B)	$p_{calc,0K}$ (μ_B)	y_{teor}	t_{obs}	σ^2	$\lvert w \rvert$	T_C (K)	D_m (nm)	ε
0.20	1.55	1.40	0.20	0.915	0.013	0.094	254.6	75.88	0.000194
0.35	1.98	2.45	0.35	0.915	0.015	0.093	173.7	75.32	0.000205
0.50	0.25	3.50	0.50	0.994	0.014	0.100	246.3	49.36	0.000223
0.67	0.24	2.31	0.67	0.994	0.012	0.101	230.6	47.63	0.001137

$$w \propto \frac{\cos\left(\frac{\pi - \angle(Mn-O-Mn)}{2}\right)}{d_{Mn-O}^{3.5}} \qquad (2)$$

The observed tolerance factor (t_{obs}) and the band width ($\lvert w \rvert$) (s.Eq.2) remanin practically unchanged in the limits of the same structure and is associated more with molar magnetizations data as with the Curie temperature (s.Tab.4). On other hand the tolerance factor increases with the increase of the crystalline symmetry, as expected. The increase of the chemical disorder degree (σ^2) with the Sr concentration (x) in the samples can explain the variation of the Curie temperature in the limits of the same

structure. A specific contribution to the decrease of the Curie temperature has also the disorder degree at the crystallite level: a decrease of the average size of crystalline blocks and an increase of the microstrains means an increase of the disorder at the crystallite level and a decrese of the Curie temperature (s.Tab.4). At low temperatures for some samples, specially for those with tetragonal structure, we have observed a spin-glass behavior of the magnetization (s. Fig.4): an increase of the magnetization with the temperature

4. Conclusions

We have obtained a modified row of $(Nd_{0.67}In_{0.33})_{1-x}Sr_xMnO_3$ manganites with the Curie temperature between 170 and 255 K, due to a supplemental thermal treatment. The substitution of Nd/In with Sr leads to a decrease of Mn^{3+} cations concentration, associated with Jahn-Teller effect. The transition from a Pnma (orthorhombic) type structure to an I4/mcm (tetragonal) type structure can be associated with an increase of the Mn^{4+} concentration in the manganites, because Mn^{4+} cation is smaller, as comparing with Mn^{3+} cation. It is possible the appearance of a long range order (a superstructure), characterized by the space group $P2_1/a$. The observed variation of the unit cell volume was explained by the combined effects of the increase of Sr^{2+} and Mn^{4+} concentrations. The change of the crystalline structure determines a modification in the ratio between the superexchange and double exchange interactions and the reduction of the magnetic regions in the tetragonal manganites. The disorder at the crystalline level can induce the appearance of the spin-glass behavior of the manganites at low temperatures.

Received Mar. 31nd, 2007

(1) National Institute of R & D for Technical Physics Iaşi, Romania
(2) Joint Institute for Nuclear Research, Dubna, Russia
(3) Chemistry Departament, "Al.I.Cuza" University,Iasi, Romania

REFERENCES

1. C.Zener, **Phys. Rev., 81**, 1951, **440**
2. G. Nolze and W.Kraus, PowderCell , J. Appl.Cryst., **29**, 1996, **301**
3. X. J. Fan, J. H. Zhang, X. G. Li, W. B. Wu, J. Y. Wan, T. J. Lee and H.C.Ku, **J. Phys.: Condens. Matter**, **11,** 1999, **3141**
4. R.Bindu, S.K.Pandey, A. Kumar, S.Khalid and A.V.Pimpale, **J. Phys.: Condens. Matter, 17,** 2005, **6393**
5. N.Cornei and M.-L.Craus, **J.O.A.M.**, **6**, 2004, **269**

COMPORTARE DE STICLA DE SPIN INDUSA PRIN TRATAMENT TERMIC LA MANGANITII $(Nd_{0.67}In_{0.33})_{1-x}Sr_xMnO_3$

Rezumat: Scopul articolului este de a stabili o corelaţie intre parametrii structurii şi ai microstructurii, pe de o parte, şi proprietăţile fizice ale manganiţilor $(Nd_{0.67}In_{0.33})_{1-x}Sr_xMnO_3$, pe de altă parte. Probele au fost obţinute prin tehnologia ceramică, utilizând oxizi (Nd_2O_3, In_2O_3 si MnO_2) şi carbonaţi ($SrCO_3$). Manganiţii presinterizaţi şi cei sinterizaţi au fost monitorizaţi prin difracţie de raze X pentru determinarea inceputului reacţiei in fază solidă, a compoziţiei de fază, a parametrilor celulei elementare, a dimensiunilor medii ale blocurilor de mozaic şi a microdistorsiunilor. Au fost determinate distanţele Mn-O, unghiurile legăturilor Mn-O-Mn şi poziţiile atomilor in celula elementară. Am discutat dependenţa intre factorul de toleranţă, gradul de dezordine chimică şi lăţimea de bandă, pe de o parte, şi temperatura Curie, pe de altă parte. Este luată in considerare schimbarea structurii cristaline asupra proprietatilor magnetice. Apariţia comportării de spin la temperaturi joase este discutată in funcţie de microstructură.

BULETINUL INSTITUTULUI POLITEHNIC DIN IAŞI
Tomul LIII (LVII), Fasc. 1, 2007
Secția
ŞTIINȚA ŞI INGINERIA MATERIALELOR

STUDY ON THE STRUCTURE AND TRANSITION TEMPERATURES OF $Ni_{50+x}Mn_{25}Ga_{25-x}$ SHAPE MEMORY ALLOYS

BY

VIOREL DOBREA, MIHAIL-LIVIU CRAUS and MIHAI LOZOVAN

Abstract: The results of structure and transition points investigations of Ni-Mn-Ga alloys in polycrystalline state are evidenced by RX diffractometry and electrical measurements. The martensitic and premartensitic temperatures were evidenced by study of electrical resistivity variation versus temperature in range of 240 to 430 K.

Keywords: shape memory alloys, Heusler alloys, NiMnGa, martensitic transition

1. Introduction

The Ni_2MnGa Heusler alloy, which is a ferromagnetic intermetallic compound, undergoing a martensitic transition from cubic $L2_1$ structure to a complex tetragonal structure, has been investigated as a potential smart material and also as a candidate for actuator materials [1-3].

The Ni_2MnGa Heusler compound exists in a wide compositional domain. For the stoechiometric Ni_2MnGa, the alloy was found to be ferromagnetic with a Curie temperature of 376 K. Structural phase transition from the cubic austenite (a= 0.582 nm at T=295 K) to the tetragonal martensite (a=0.592 nm and c=0.557 nm at T = 4.2 K) takes place on cooling below T_M = 202 K. This phase transition is hysteretic, but reversible on heating, showing the shape-memory effect [4].

Work on alloys with nonstoechiometric compositions shows that the Curie temperature and the martensitic transition can be varied with the concentration [3, 5, 6].

The aim of the present work was to prepare polycrystalline samples with a different Ni content (at the expense of Ga) and to study the composition dependence of their structural transitions in order to obtain a Ni-Mn-Ga shape memory-alloy (SMA) with higher structural transition temperature than Ni_2MnGa compound.

2. Experimental procedure

Polycrystalline $Ni_{50+x}Mn_{25}Ga_{25-x}$ alloys were prepared by three times arc-melting into buttons of the high-purity nickel, manganese and gallium under argon atmosphere. The composition of the alloys was characterized by Ni excess x in the range x = 0 - 4. Buttons were then remelted and drop-cast into a copper mold to obtain rods with a diameter of 1 and 5 mm and a length of 40 mm and lamella with 40x5x1 mm dimensions. For homogenization they were annealed at 1073 K for 4 days in a vacuum

quartz ampoule. After homogenization the samples were quenched into ice-water. Although quenching increases the brittleness of the samples it was considered to be important to obtain the highest degree of chemical order. The phase structure of the samples was identified by X-ray diffraction measurements at room temperature using a DRON 2.0 diffractometer with Cu *Kα* radiation. The structural transition (martensitic and premartensitic) temperatures of the alloys were evidenced by study of electrical resistivity variation versus temperature in range of 240 to 430 K.

3. Experimental results and discussion

The X-ray diffraction patterns of the annealed $Ni_{50+x}Mn_{25}Ga_{25-x}$ (x = 2, 4) polycrystalline alloys at room temperature indicate a cubic (austenitic) phase for $Ni_{52}Mn_{25}Ga_{23}$ alloy and a two phase mixture (austenite + martensite) for $Ni_{54}Mn_{25}Ga_{21}$ alloy, as shown in Fig. 1.

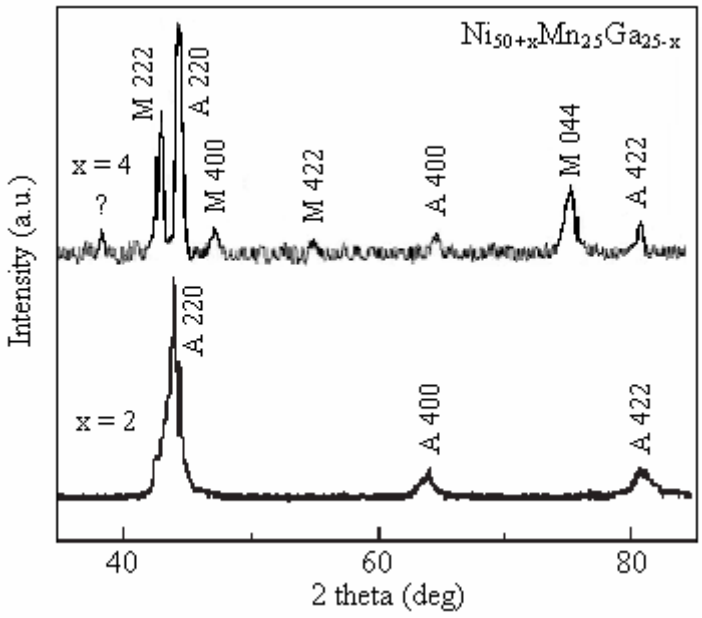

Fig.1 The X-ray diffraction patterns of the $Ni_{50+x}Mn_{25}Ga_{25-x}$ (x = 2, 4) polycrystalline alloys at room temperature after homogenized treatment at 1073 K for 4 days

Presence of two phases in structure of $Ni_{54}Mn_{25}Ga_{21}$ sample indicates that martensitic transition temperature for this alloy is near room temperature, while the existence of a single phase $Ni_{52}Mn_{25}Ga_{23}$ sample shows that structural transition temperature is situated under the room temperature. We observed an unidentified phase (probably a compound of Mn with Ga: Mn_3Ga or similar) in the phase structure of the $Ni_{54}Mn_{25}Ga_{21}$, that is present in very small amount.

In comparison with lattice parameters of stoichiometric $Ni_{50}Mn_{25}Ga_{25}$ Heusler compound, the lattice parameters of these nonstoichiometric compounds at room temperature are presented in Table 1. The tetragonal coefficient of martensite (*c*/*a*) of the $Ni_{54}Mn_{25}Ga_{21}$ alloy has the value of 0.781 and for the $Ni_{50}Mn_{25}Ga_{25}$ stoechiometric compound (at 4.2 K) the value is 0.941. It is possible that this kind of martensitic structure should be different from that of the stoechiometric Ni_2MnGa.

The data presented in Table 1 show that the increase of Ni substitution in the Ga detriment from the alloy leads to an easy decrease of the lattice parameter of austenitic phase.

Table 1 Lattice parameters of $Ni_{50+x}Mn_{25}Ga_{25-x}$ (x = 0, 2, 4) alloys structures at room temperature

Sample	Austenite (cubic)	Martensite (tetragonal)	
	a, nm	a, nm	c, nm
$Ni_{50}Mn_{25}Ga_{25}$ [3]	0.582 (at 295 K)	0.592 (at 4,2 K)	0.557 (at 4,2 K)
$Ni_{52}Mn_{25}Ga_{23}$	0.579	-	-
$Ni_{54}Mn_{25}Ga_{21}$	0.577	0.767	0.599

Direct current resistivity measurements provide a simple and effective tool to detect structural (martensitic and premartensitic) transitions. As shown in Figs. 2 and 3, at martensitic transition temperature (*Tm*) the resistivity exhibits a pronounced jump-like behavior, while at premartensitic transition temperature (*Tp*) only change in the slope takes place.

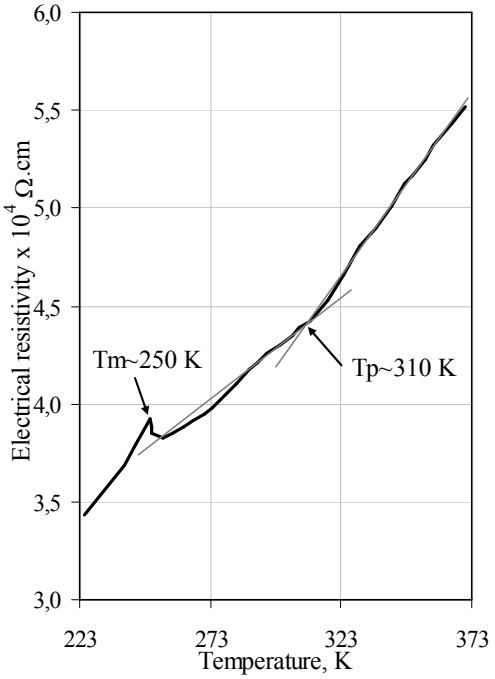

Fig.2 Resistivity as a function of temperature for the $Ni_{52}Mn_{25}Ga_{23}$ sample

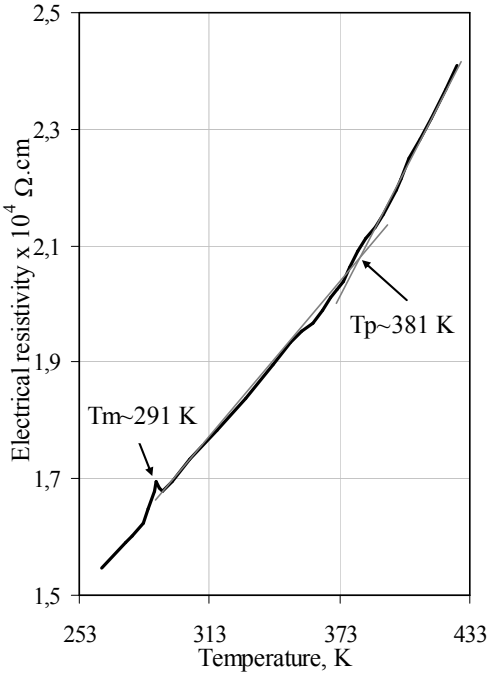

Fig.3 Resistivity as a function of temperature for the $Ni_{54}Mn_{25}Ga_{21}$ sample

Table 2 Structural transition temperatures for $Ni_{50+x}Mn_{25}Ga_{25-x}$ (x =0, 2, 4) alloys

Sample	Structural transition temperature	
	martensitic, Tm, K	premartensitic, Tp, K
$Ni_{50}Mn_{25}Ga_{25}$ [3]	205	245
$Ni_{52}Mn_{25}Ga_{23}$	250	310
$Ni_{54}Mn_{25}Ga_{21}$	291	381

In Table 2, martensitic and premartensitic transition temperatures determined by study of resistivity variation versus temperature are presented. For comparison were

presented structural transition temperatures for $Ni_{50}Mn_{25}Ga_{25}$ stoichiometric alloy obtained by the same method (s. reference [3] in Tab.3).

4. Conclusions

The martensitic transformation temperatures of the $Ni_{50+x}Mn_{25}Ga_{25-x}$ (x = 0, 2, 4) alloys monotonically increase with the increase of Ni substitution for Ga from around 205 K to 291K. In the same time, the premartensitic transition temperature arises from about 245 K to 381 K (Fig. 4).

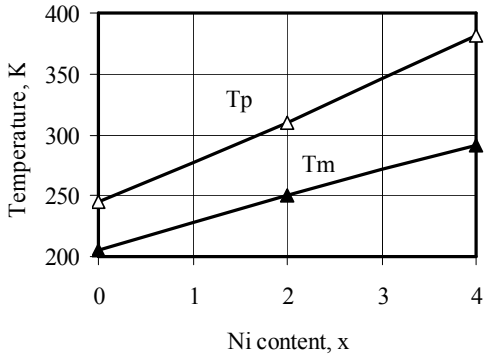

Fig.4. The structural transition temperatures Tm and Tp versus Ni content in $Ni_{50+x}Mn_{25}Ga_{25-x}$ (x = 0, 2, 4) alloys.

These experiments have proved that with increasing Ni content in stoechiometric $Ni_{50}Mn_{25}Ga_{25}$ Heusler compound, the structural transition temperature (*Tm*) increased significantly, and it can increase over the room temperature for higher Ni content. Also, it is interesting to study the evolution of the magnetic properties (magnetization, Curie temperature) versus Ni content for $Ni_{50+x}Mn_{25}Ga_{25-x}$ (x = 2, 4) alloys.

REFERENCES

1. K. Ullakko, J. K. Huang, C. Kantner, R. C. O'Handley, and V. V. Kokorin, **Appl. Phys. Lett. 69**, 1996, **1966**
2. K. Ullakko, J. K. Huang, C. Kantner, R. C. O'Handley, and V. V. Kokorin, **Appl. Phys. Lett**. **69**, 1996, **1966**
3. Huibin Xu, Yunging Ma and Chengbao Jiang, **Appl. Phys. Lett**. **82**, 2003, **3206**
4. Gen Feng, Chengbao Jiang, Ting Liang and Huibin Xu, JMMM **248**, 2002, **312-317**
5. A. N. Vasil'ev, A. D. Bozhko and V. V. Khovailo, **Phys. Rev. B 59**, 1999, **1113**
6. F. Zuo, X. Su, P. Zhang, G. C. Alexandrakis, F. Yang and K. H. Wu, **J. Phys.: Condens. Matter 11**, 1999, **2821-2830**
7. F. Albertini, L. Pareti, A. Paoluzi, L. Morellon, P. A. Algarabel, M. R. Ibarra and L. Righi, **Appl. Phys. Lett. 81**, 2002, **4032**

Received Mar. 31nd , 2007 *National Institute of R & D for Technical Physics Iaşi*

STUDIU PRIVIND STRUCTURA ŞI TEMPERATURILE DE TRANSFORMARE ALE UNOR ALIAJE $Ni_{50+x}Mn_{25}Ga_{25-x}$ CU MEMORIA FORMEI

Rezumat: Sunt prezentate rezultatele obtinute prin difractometrie de raze X şi măsuratori electrice privind structura şi temperaturile de tranziţie pentru aliaje Ni-Mn-Ga. Temperaturile corespunzătoare transformării martensitice şi premartensitice au fost evidenţiate prin măsurători ale rezistivităţii electrice funcţie de temperatură in domeniul 240 to 430 K..

BULETINUL INSTITUTULUI POLITEHNIC DIN IAŞI
Tomul LIII (LVII), Fasc. 1, 2007
Secția
ŞTIINȚA ŞI INGINERIA MATERIALELOR

OPTIMUM ACTIVE CONTROL OF AUTOVIBRATIONS GENERATED BY STICK-SLIP PHENOMENON

BY

BARBU DRAGAN and CEZAR OPRISAN

Abstract: The position accuracy in a high performance motion control system is highly affected by vibrations due to compliance and nonlinear effects such as friction. The modelling and compensation of nonlinear friction are difficult tasks for precise motion control. The control will be even more difficult when other nonlinearities and mechanical compliance exist together with friction. A summary on friction phenomena, modelling and identification is presented. Methods for vibration suppression have also been studied. This paper presents theoretical and experimental results concerning the establishing of an active control strategy of the auto vibrations generated by the stick-slip phenomenon. Experiments show that the proposed controller with friction feed-forward compensation, not only is the positioning error reduced to within the range of the encoder resolution, it is also more robust to model uncertainties.

Key words: active control, nonlinear friction, stick-slip, vibrations.

1. Introduction

The dynamic phenomenon that arise in the kinematics couplings, where there is slip relative speed, are determinate by the interactions between elastic mechanical system and the working process. The actions of the working process son the elastic system are, generally, forces or moments. As result relative displacements of the elastic system components arise that, represent the reaction of the elastic system at the working process and lead to the modification of the functioning parameters.

Schematization of the interdependence between elastic system and friction process leads to the realization of a closed circuit (Fig. 1) that presents the elements of the dynamic system with the following notations: F(t) actions of the external factors that not depend by the system dynamic parameters; F - action of the friction process on the elastic system; y - elastic system reaction; y(t) - variation of the adjustment of the friction regime parameters that produce forced vibrations on the elastic system depending by the friction process.

The base parameter that characterises interaction between elastic system and friction process is the damping coefficient that depends not only elastic system parameters but also by the working process parameters included into the equivalent elastic system. The necessary values of the damping coefficient to study the dynamic behaviour of the mechanical systems must correspond to the system real operating conditions and can not be considered as universal valuable values.

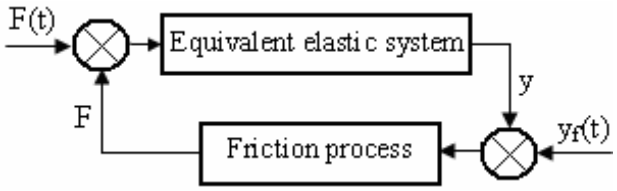

Fig. 1. Schematization of the interdependence between elastic system and friction process

The instability of a dynamic system, where there is an interaction between the elastic system and the friction process behaves as a stick-slip movement of the contact masses. This phenomenon arises at low slip speeds (0.18÷180 mm/min), in dry, mixed or limit friction conditions

Arising of the stick-slip phenomenon is conditioned by the slip movement and auto-vibrations generation.

There are three fundamental strategies to control the auto vibrations generated by the stick-slip phenomenon: passive control, active control and semi-active control.

Usually, the elimination or attenuation of the vibrations is realized by the passive control systems. However, these systems present an important disadvantage: impossibility to modify the damping coefficient that leads to the different behaviour in the case of the external conditions changes.

Active control systems realize a variation of the energy flux of the mechanical structure by a continuously measuring with sensors, the response of the mechanical system and using the actuators to apply external loads to optimize the dynamic behaviour.

Semi-active control systems recently developed make a compromise between the active and passive control systems and realize the vibrations control by the selective dissipation of the energy.

2. Theoretical considerations

Friction effects are often modeled as a combination of coulomb and viscous terms, with an occasional mention of stiction effects. Currently identified friction behavior includes viscous, coulomb, stiction, the Stribeck's effect, pre-sliding displacement, hysteretic or memory based effects, a dependency on normal force, a dependency on rate of an applied external force, a dependency on temperature, a dependency on machine life, a dependency on recent levels of activity and a dependency on the workspace location (fig. 2). The study of the auto-vibration generated by the stick-slip phenomenon can be realised using a dynamic model, one freedom degree, with damping presented in Fig. 3.

If the damping is considered proportional with the speed the movement, equation is given by:

$$m\ddot{x} + c_1(\dot{x} - v) - k(x_o + vt - x) + F - c_2\dot{x} = 0, \quad (1)$$

where: c_1 – damping viscous coefficient of the system; $F - c_2\dot{x}$ - kinematics friction force that has a constant component F and variable component proportional with the movement speed having the damping coefficient c_2.

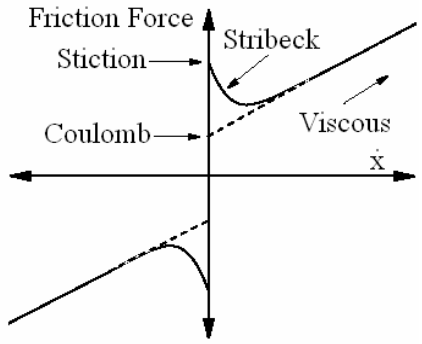

Fig. 2. Friction model effects

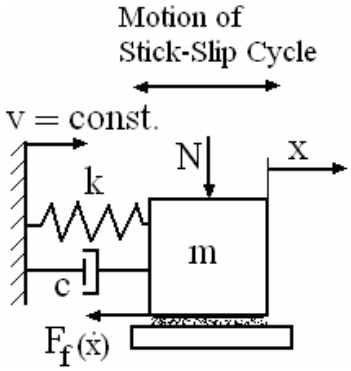

Fig. 3. Spring and damper representation of stick-slip

$$x = \frac{c_1 v}{k} + vt + \frac{\Delta F}{k} + \frac{v}{\omega_o} e^{-\alpha\omega_o t} \cdot \left[(2\alpha - A)\cos\omega_o t - (1 - A\alpha)\sin\omega_o t \right] \quad (2)$$

where: $\alpha = \frac{c_1 - c_2}{2\sqrt{km}}$; $\omega_o = \sqrt{\frac{k}{m}}$; $A = \frac{\Delta F}{v\sqrt{km}}$; $\Delta F = F_o - F$; F_o- static friction force.

The displacement speed of the mass m:

$$\dot{x} = v\left\{ 1 - e^{-\alpha\omega_o t}\left[\cos\omega_o t + (\alpha - A)\sin\omega_o t\right]\right\} \quad (3)$$

The stick-slip movement corresponds, for a given value of the critical damping coefficientα, at a critical value of the non-dimensional parameter A that can be determined by the transcendent function $A_c = f(\alpha)$ resulted from the equation:

$$2\alpha \cdot arctg\frac{A_c}{A_c\alpha - 1} = ln(1 + A_c^2 - 2A_c\alpha) \quad (4)$$

To the critical value A_c - that depends by the friction force characteristic of the kinematics friction couple, stiffness of the acting system and by the reduced mass of the mobile element - corresponds a critical movement of the mass m, that represents the minimum speed of the continuing movement of the mobile element of the kinematics couple and that can be determined by the relation:

$$v_c = \frac{\Delta F}{A_c\sqrt{km}} \quad (5)$$

For $v < v_c$ results a periodical jump movement presented in Fig. 4.

The jump duration can be determined from the equation:

$$\omega \cdot t_2 = \frac{1 + A_c^2 - 2A_c\alpha}{A_c - \alpha - ctg \cdot \omega_o t_1} \quad (6)$$

and the jump value s is:

$$s = \frac{\Delta F}{k}(2 - \pi\alpha) \quad (7)$$

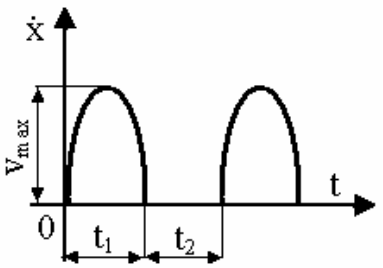

Fig. 4. Periodical jump movement

According to the given value, the movement can be stopped during the mobile element stationation or during jump, and, in the last case results a position maximum error given by:

$$\varepsilon = 2\frac{\Delta F}{k}, \text{ for } \alpha = 0 \tag{8}$$

3. Experimental equipment

To study the posibilities of active control of the auto-vibrations generates by the stick-slip phenomenon a test rig, schematically presented in Fig. 5, was used. A belt transmission transforms the rotational movement of a continuously current motor in a translation movement of the mobile element of mass m, supported by a linear bearing.

The position of the mobile element is measured by a linear displacement transducer with a precision of 5μm, and the slip speed by a piesoelectric accelerometer.

The aquisition and processing of the data, and the implementation of the active system control was realised by an aquisition device National Instruments şi with the LabVIEW programme. Identification of the inertia and friction of the dynamic model of the system was off-line realised, by several experiments.

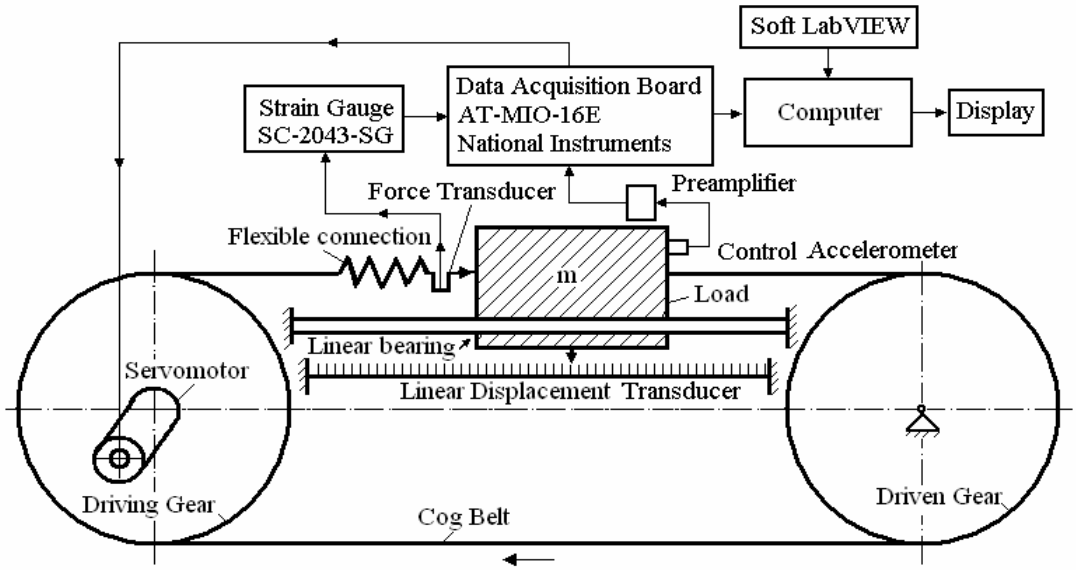

Fig. 5. Schematic of the experimental active control system

4. Active control strategies for auto- vibration suppression

If an accurate nonlinear friction model is available, it is easy to compensate friction by applying a force command equal and opposite to the instantaneous friction force, this can be implemented either by feedforward control [1],[2],[3]. The block diagram of the feedforward control system can be drawn as in Figure 6, from which the sampled error signal can be written as:

$$e(n) = d(n) + g\,u(n) \tag{9}$$

where d(n) is the disturbance, g is the vector of impulse response coefficients of the plant and u(n) is the vector of past values of the input signal to the plant. An angular velocity is used, as the reference signal, for feedforward control. Equation (8) allows a cost function equal to the mean square error signal,

$$J = E[e^2(n)], \tag{10}$$

where E denotes the expectation operator, to be written as a quadratic function of the

coefficients of the control filter.

The friction model parameters are identified by sets of simple experiments.

One difficulty of friction identification is the requirement of measuring acceleration which is needed in order to observe the friction force and take into account inertia effects at the same time.

Unfortunately, acceleration is immeasurable in many practical motion control [4] systems unless additional expensive equipment is used. An alternative is to use the desired acceleration as an estimate of true acceleration, and then the parameters of an inertia and friction model are individually identified through a set of experiments.

.

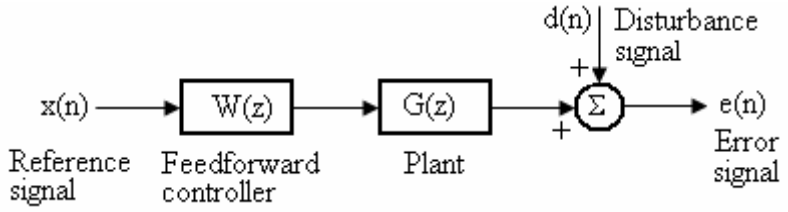

Fig. 6. Block diagram of a single channel feedforward control system

Fig. 7 shows the experimental results of this controller with also friction feed-forward compensation. The results show that the system stability is very sensitive to the change of the friction model parameters.

To reduce the final position error, when linear controllers are used, the nonlinear friction has to be compensated. If an accurate friction model is available, it is easy to compensate friction by applying a force command equal and opposite to the instantaneous friction force. However, since the friction varies with position, it is difficult to guarantee the robustness in terms of both stability and ffected by modeled dynamics and friction. performance by using fixed friction compensation.

Under the assumption of exact modeling and linearity of the physical system, perfect tracking may be obtained by feed-forward compensation.

However, due to the uncompensated nonlinear friction and an imperfect model of the system, the positioning error still can not be reduced to the required level and the robustness of the control is also degraded. Referring to the above results, it is apparent that the nonlinear controllers offer superior performance in both robustness and final positioning accuracy. Especially when uncertainties and nonlinear effects represent differences in parameters among individual machines, it would be beneficial to use the same controller settings for all the machines, i.e., without individual tuning while satisfying the required performance. There is a wide range of friction compensation techniques developed for applications involving high precision tracking or/and position control systems.

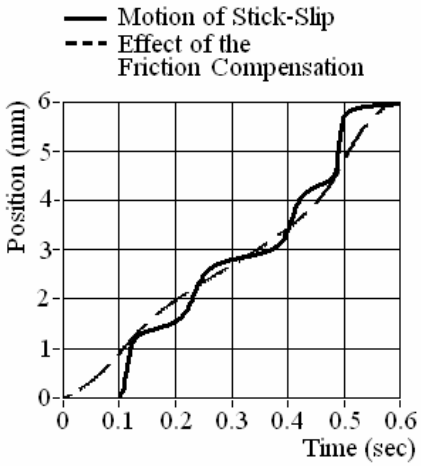

Fig. 7. Performance measures

6. Conclusions

Nonlinearities usually present difficulties for motion controlled systems to achieve high performance control, since the nonlinearities can not be completely compensated by a linear controller. Experiments show that the proposed controller has a strong robustness to the nonlinear friction. Friction compensation is not needed because the nonlinear controller in the position loop compensates the remaining disturbance of the friction.

The successful design of a model based compensation depends heavily on the accuracy of the friction models. Since the nonlinear friction in this complex system is not only time-varying but also position-dependent, to find an accurate friction model is almost impossible.

Received May 24th 2007

Technical University of Iassy
Department of Machine Design and Mechatronic

REFERENCES

1. Yu-Feng, Li, *Nonlinear Motion Control in the Presence of Friction and Mechanical Flexibility,* Licentiate Thesis Mechatronics Lab Department of Machine Design Royal Institute of Technology, Stockholm, 1999.
2. Yu-Feng, Li, *High Precision Motion Control Based on a Discrete-time Sliding Mode,* Doctoral Thesis, Mechatronics Lab, Department of Machine Design, Royal Institute of Technology, Stockholm, 2001
3. You-Feng, Li, Eriksson, B. & Wikander, J., *Sliding mode control of two-mass systems*, Proceedings of IFAC'99, Vol. *C*, Beijing, China, 5-9 July, 1999, 151-156.
4. Vedagarbha, P., Dawson, D., M., Feemster, M., *Tracking Control of Mechanical Systems in the Presence of Nonlinear Dynamic Friction Effects*, IEEE Transactions on Control Systems Technology, Vol.7, No.4, July 1999, 446-456.

CONTROLUL ACTIV OPTIM AL AUTOVIBRATIILOR GENERATE DE FENOMENUL DE STICK-SLIP

Rezumat Apariția fenomenului stick-slip este condiționată de: (1) existența alunecării; (2) generarea autovibrațiilor. În prezent există trei strategii fundamentale pentru controlul autovibrațiilor generate de fenomenul stick-slip: (i) controlul pasiv; (ii) controlul activ; (iii) controlul semi-activ. De obicei, eliminarea sau atenuarea autovibrațiilor se realizează cu ajutorul controlului pasiv, prin utilizarea unor izolatori pentru disiparea energiei. Acest tip de control nu necesită o sursă de energie exterioară şi este robust. Ca dezavantaj se menționează imposibilitatea modificării coeficientului de amortizare, ceea ce conduce la comportări diferite, în cazul schimbării condițiilor exterioare. Sistemele de control activ realizează o variație a fluxului de energie din structura mecanică, prin măsurarea continuă, cu ajutorul senzorilor, a răspunsului sistemului mecanic şi aplicarea unor acțiuni exterioare prin intermediul actuatorilor, pentru a obține o comportare dinamică optimă. În lucrare sunt prezentate rezultatele cercetarilor teoretice si experimentale realizate de autori în scopul stabilirii unei strategii de control activ optim a autovibrațiilor generate de fenomenul stick-slip.

BULETINUL INSTITUTULUI POLITEHNIC DIN IAŞI
Tomul LIII (LVII), Fasc. 1, 2007
Secția
ŞTIINȚA ŞI INGINERIA MATERIALELOR

STUDY REGARDING THE OBTAINING OF METAL MATRIX COMPOSITES REINFORCED WITH CARBON NANOTUBES

BY

LILIANA FODOR and VALER MICLE

Abstract: The paper presents a scientific study of the newest technologies in the world regarding the obtaining of metal matrix composites reinforced with carbon nanotubes. The majority of researchers approached the methodology in order to obtain metal matrix composite with carbon nanotubes through the utilization of the powder metallurgy and through the infiltration of molten metal. The obtained materials show different characteristics, that depend on the process used and of course on the matrix. The study is aimed to present the dates from specialty literature which will be the base of some future experiments in order to obtain metal matrix composites reinforced with carbon nanotubes.

Keywords: carbon, nanotubes, metal, matrix, composites

The scientific investigation and applied research on composite materials can date back to 1940's, and these advanced materials have been introduced gradually in our daily life. Composites are also recognized as high-tech materials, which not only turn up in various sports, such as tennis, golf and sailing, but also constitute an increasing proportion of modern airplane and automobile [1].

The actual period is characterized through a true explosion in the field of fabrication and the usage of composite materials, which lead to a diversification without precedent in history. In present, in developed countries, are made currently composite materials with high specific resistance and rigidity, resistance at high temperatures, wear resistance, thermal-protective properties etc.

1. Principal properties of metal matrix composite materials

Physical properties of metal-matrix composites (MMCs) are improved as a result of the incorporation of reinforcements. As evidenced by the increased demand within the aerospace and commercial industries for materials with mechanical and physical properties superior to those of advanced monolithic alloys, it is becoming increasingly clear that composites will have many actual applications**.** The specific benefits of MMCs include:

- increased strength and stiffness per unit density, which reduce structural weight and increase performance,
- a decrease in the coefficient of thermal expansion (CTE), which reduce thermal strains in structures undergoing thermal cycles,
- increased creep strength, which is necessary for improving operating temperatures and performance of turbine engines,

- other specialized attributes, such as wear resistance and high conductivity [2].

Currently, metal matrix composites are commercially available with a variety of forms. They are used predominately in a wide range of applications, ranging from brake discs in trains to critical rotating parts in helicopters, from thermal substrates for advanced electronic and power modules to spikes for track shoes, and from tool materials to combustion engine components, from structural to electronic applications. In the sector of automotive and ground transportation, metal matrix composites are used for their specific stiffness, high temperature strength and excellent wear properties. In aerospace applications, metal matrix composites satisfy the principal requirements such as low thermal expansion coefficient, low density, high stiffness, and high strength. Indeed, in addition to the concern of absolute weight saving to reduce the launch costs, the primary demand in space technology is often the dimensional stability of the components, which are submitted to the inevitable thermal cycles associated with passing in and out of the Sun's shadow in the absence of convective heat transfer. Examples include beam structures and optical gimbals, which must not deform despite significant temperature fluctuations and gradients typical of space applications [1].

2. Carbon nanotubes

The aim of developing composites is to combine the mechanical properties of the components in order to meet diverse industrial requirements. In numerous fields of applications like aerospace and automobile industry, low density and good mechanical properties such as high damping, high strength and high stiffness are demanded for the materials. The stiffness of a metal matrix composite is strongly dependent on many parameters and factors such as the volumetric fraction of ceramic fibers, the elastic Young's modulus of the fibers and the matrix, and the aspect ratio of the fibers. On the other hand, increasing a mechanical property may cause a decrease in another, for instance, larger volumetric fraction may result in higher Young's modulus but lower damping capacity of the composite. The discovery of carbon nanotubes, with light weight, smaller dimensions and unique mechanical properties could fulfill further goals of higher damping capacity and better mechanical properties, compared to the conventional composites [1].

What stimulates the activity of researchers over nanotubes is the fact that these have more interesting properties. The one-dimensional character of nanotubes and the force of carbon-carbon bond give them excellent mechanical and electrical properties. Young modulus of a multi wall carbon nanotubes was calculated to be until 1.4 bigger than whisker graphite (1 TPa), the measurement being realized with the frequency of thermal vibrations of carbon nanotubes with a transmission electronic microscope, leading to values between 0.4 and 3.7 TPa [3].

A study realized by Wong and co. [4] with the help of an atomic force microscope permitted the measurement of Young modulus of average 1.28MPa, independent of the diameter of the tube.

Although their high stiffness, carbon nanotubes form kink-like ridges that can relax elastically when the stress is released. The direct observation with TEM at high resolution has shown their extraordinary flexibility; the curve seems completely

reversible until a critical angle of 110^o for a tube with a single wall. According to calculations by Jerzy Bernholc and colleagues at North Carolina State University in Raleigh, a nanotube could be elongated by several per cent before it would fracture. Unlike carbon fibers, however, single-wall nanotubes are remarkably flexible. They can be twisted, flattened and bent into small circles or around sharp bends without breaking. Moreover, molecular dynamics simulations by Bernholc and colleagues indicate that in many cases the nanotube should regain its original shape when the stresses distorting it are removed [5].

The last researches of Jianyu Huang from Boston College discovered the super plasticity phenomenon over nanotubes [6]. In theory, single-walled carbon nanotubes have a maximum tensile strain of around 20%. But by stretching the nanotubes at high temperature, researchers at Boston College, Lawrence Livermore National Laboratory and Massachusetts Institute of Technology, all in the US, have extended nanotubes by almost 280%. The researchers made a 24 nm-long single-walled carbon nanotube by breaking down a multiwalled nanotube inside a high-resolution transmission electron microscope. They used a piezo manipulator to stretch the nanotube at a bias of 2.3 V. The nanotube failed when it became 91 nm long, a tensile elongation of 280%. Its diameter at failure was 0.8 nm, 15 times smaller than its initial diameter of 12 nm. The scientists reckon that the temperature inside the nanotube was more than 2000°C during deformation. Another advantage of nanotubes is their comportament to compression. As opposed to carbon fibers, which crack very easy to compression, CNT presents an elastic relaxation when compression force is canceled.

3. Realizing metal matrix composite materials with carbon nanotubes

Regarding metal matrix composites, Kuzumanki and co.[3] have prepared composites with carbon nanotubes in metal matrix by sintering under charge (600^{o}C, in vacuum, 100MPa) and by extrusion (500^{o}C, in vacuum, 1 cm. per min.). It has been used multi walls carbon nanotubes synthesized by electric discharge. It was determined at TEM that the nanotubes have not been deteriorated during the densification of composite material and that the reactivity at the interface nanotube-Al was zero because it wasn't evidenced any aluminum carbide. The composite material Al-carbon nanotube presents a tensile strength compared with the one of pure aluminum, but is not degraded by heating like the pure metal which resistance go down regularly with the growing of the hardness through a thermal treatment.

Xu and co.[7] have studied electric properties of composites Al-carbon nanotubes prepared by sintering at 520^{o}C (25 MPa, 30 min.) of a mixture of the two components. They used multi wall carbon nanotubes obtained by catalytic decomposition. Authors shows that the resistivity grows with the temperatures and that a big leap can be seen at 80 K- tend to a null resistance, which correspond to a transition to a superconductive state.

Researchers from Zhejiang University from China [8] realized aluminum matrix composites reinforced with carbon nanotubes by pressure less infiltration. The pressure less infiltration process employs a spontaneous infiltration of a molten Al alloy containing Mg into a ceramic filler of preform, under a nitrogen atmosphere in a pressure less state and without any aid of vacuum or externally applied pressure .In

this study, pressure less infiltration process employed the spontaneous infiltration of a molten Al alloy into CNTs-Mg-Al performs and CNTs/Al composites were fabricated. Multi-walled carbon nanotubes were prepared by chemical catalytic vapor deposition (CCVD). Al, Mg metal powders with a purity of 99.8%, and an industrial Al-based alloy trademarked as LY12 were used as raw materials. CNTs, Al and Mg powders were mixed with predetermined ratios by ball milling at 300r/min for 7 hours in Ar atmosphere. Those milled powders then were pressed into preforms (diameter 70mm, thickness 15mm) for the following pressure less infiltration. In order to investigate the mechanism of infiltration we have prepared the performs with or without Mg. CNTs/Al composites were then produced by melt infiltrating LY12 Al alloy into above preforms at 800ºC for 5 hours under N2 atmosphere.

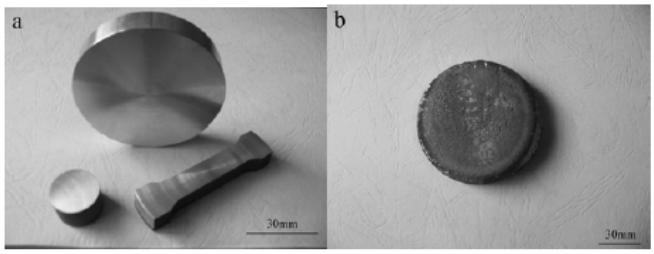

Fig.1 a) The composite containing 10vol% CNTs well infiltrated, b) the composite containing 10vol%CNTs and without Mg,which is not infiltrated at all

It was concluded that the results of pressure less infiltration are strongly related with the existence of Mg and nitrogen. The molten Al alloy had never infiltrated into well-mixed Al-CNTs performs without Mg in the temperature range of 700ºC to 900ºC in nitrogen atmosphere, and never infiltrated in Air atmosphere as well. Fig.1 (a) shows that the composite containing 10vol% CNTs and Mg produced under N_2 atmosphere is well infiltrated. Fig.1 (b) shows the composite containing 10vol%CNTs and without Mg, which is not infiltrated at all. Mg is an active metal that may easily react with nitrogen to form Mg_3N_2 at high temperature. It is suggested that Mg reacted with N_2 during infiltration to form Mg_3N_2, which greatly enhanced the wetting ability between molten Al alloy and powders. Mg initiates the infiltration by reducing the native alumina layer on the surface of Al-alloy therefore bringing about the contact of molten Al-alloy with the preform. The role of Mg during infiltration is to get the residual O_2 in the N_2 by vapor phase reaction and to make the infiltration front free of any passivating oxide layer. The abrupt termination of infiltration has been attributed to the formation of passivating alumina layer at the infiltration front due to the local depletion of Mg. Fracture surface morphology of the composite with 10vol.% CNT is shown in Fig. 2. It can be found that CNTs appear well dispersed and are fully embedded in the Al matrix. The micro hardness of the composites with different volume fractions of CNTs are listed in Table 1. It is evident that the hardness of the composite increases with increasing the volume fraction of CNTs, but then decreases with further increasing the volume fraction.

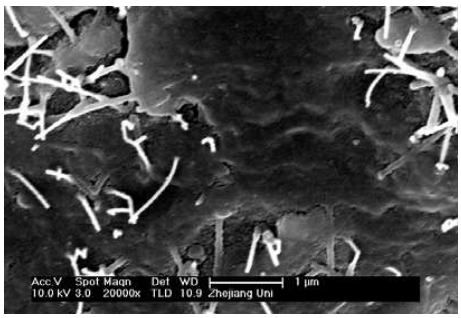

Fig. 2. SEM images of fracture surface of composite with 10 vol.% CNTs

Table 1. Volume fraction of CNTs and microhardness of the composites

Volume fraction of CNTs in composite (%)	0	5	10	15	20
Microhardness of composites (HV)	106.5	117.8	165.9	173.9	169

As shown in Table 1, the hardness of the composite with 15vol.% CNTs is the highest. Researchers from Institute of Metal Research, Chinese Academy of Sciences [9] innovated a technology of fabrication of composites from nano-Al reinforced with single wall carbon nanotubes. Several studies have been made of the mechanical properties of composites in which CNTs were employed as a reinforcing phase, and it was found that their performance was not as good as had been expected.

One reason is that the properties of CNT composites with a purity of 60 vol.% might be reduced by the contaminants they contain, such as graphitic particles and amorphous carbons. As a one-dimensional nanostructured material (nanomaterial), CNTs are different from other traditional reinforcing fibres because of their excellent mechanical properties and much smaller size. Used as the matrix of composites, nano-materials may be more compatible with CNTs than traditional matrices of metal, ceramic and polymer. Single-walled carbon nanotube (SWNT)- reinforced nanocrystalline Al composite (SWNT/nano-Al) was fabricated, and the morphology and mechanical properties of the composite were studied. The nano-Al particles used, were produced by H plasma evaporation method in a chamber with a mixed gas of 60 pct H and 40 pct Ar from commercial aluminum with purity of 99.85%. SWNTs were produced by a semi-continuous hydrogen arc discharge method. With the addition of cocatalysts such as Fe, Ni, Co and a sulfur-containing growth promoter, web-like substances and thin films made up of SWNTs, catalyst particles and amorphous carbon were obtained from multi-walled carbon nanotubes and carbon fibres at a rate of about 2.5 grams per hour in a mixed atmosphere of H and Ar . The raw materials were oxidized in air at about 520 8C for 40 min to eliminate the graphite particles, and the catalyst particles were removed by hydrochloric acid washing. The purity of the purified SWNTs was estimated to be about 90% from the results TEM and SEM observations. Nano-Al particles mixed with 5.0 wt. % SWNTs were soaked in alcohol and stirred ultrasonically for 30 min and then dried. In the obtained mixture, SWNT bundles were dispersed homogeneously in the nano-Al particles. The nano-Al particles, whose size was determined to be about 50 nm in average by X-ray diffraction (XRD) analysis, were almost spherical with a thin outer layer of $Al_2 O_3$. The content of oxygen in the nano-Al particles was 3.1%. The homogeneous dispersion of SWNTs shows that the ultrasonic energy could overcome the Van der Waals force between SWNT bundles and between nano-Al particles. In addition, it is probable that SWNT should be easily dispersed into the nano-Al matrix because of the large grain boundary area in nano-materials. The mixture then was compacted into a disk (d=831.2mm) under 1.50 GPa pressure at room temperature. The disks were then consolidated for 30 min under 1.0 GPa pressure at temperatures ranging from 260 to 480 ^{o}C. The Vickers micro-hardness of both the SWNT/nano-Al composites and nano-Al was measured on the next parameters F=0.245 N, v=3 μm/s, t=10s. The hardness of the SWNT/nano-Al composites and nano-Al at different consolidating temperatures is shown in Fig. 3. As the consolidation temperature increased, the hardness of the nano-Al increased from 1.36 GPa at room temperature to a peak value of 1.69 GPa at 320^{o}C,

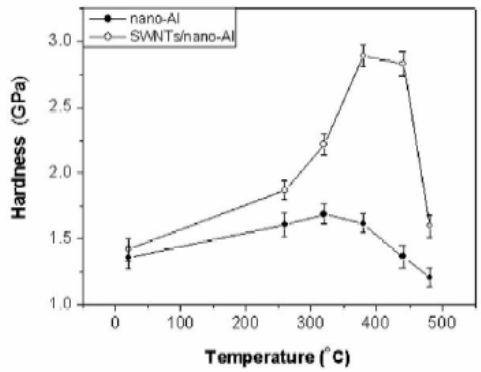

Fig.3. The hardness of nano-Al and SWNT/nano-Al composite at different consolidation temperatures

and then declined to 1.21GPa at 480 ^{o}C. Meanwhile, the hardness of the SWNT/nano-Al composites increased from 1.42 GPa at room temperature to a peak value of 2.89 GPa at 380 8C, and then declined rapidly to 1.60 GPa at 480 ^{o}C. The initial hardness increase of the SWNT/nano-Al composites and nano-Al probably resulted from the increased densities, and the subsequent hardness reduction may be caused by the grain growth of the nano-Al matrix. While the nano-Al matrix grew up slightly over 320 ^{o}C, the reinforcement by SWNTs was more evident with the increasing temperature, which caused the hardness of the SWNT/nano-Al composites to reach a peak value. The highest hardness of the SWNT/nano-Al composites was 2.89 GPa after the optimum consolidation procedure, which was approximately 20 times higher than that of the coarse-grained Al (0.15 GPa) and 178% of that of the nano-Al (1.62 GPa) consolidated at the same temperature. The novel mechanical properties of the SWNT/nano-Al composites indicate that SWNTs can be used as an excellent reinforcing phase in a nano-Al matrix. In summary, SWNTs/nano-Al composites were successfully fabricated by a procedure of mixing nano-Al particles and SWNTs, cold-consolidation and hot-consolidation. The hardness of the SWNT/nano-Al composites reached a peak value of 2.89 GPa, which shows that SWNTs are a promising reinforcement for some matrices

It was also realized magnesium matrix composites with different percents of carbon nanotubes [1]. Mg-1wt%MWCNTs (fig.4) was processed by hot pressing, whereas Mg-2wt%MWCNTs (fig.5) was synthesized by hot pressing then hot isostatic pressing (HIP) under high pressure. In order to obtain high density parts, it is better to increase the sintering temperature, temperatures between 60 and 90% of the melting-point of the particular metal or alloys to temperatures which sometimes can be even higher than 90% of the melting temperature. The welding together of the particles occurs by atomic diffusion and generates the strength required for application. In the processing of Mg-2wt%MWCNTs, 0.4 g of purified MWCNTs was oxidized by heat-treatment in a furnace at 500 °C for 5 min then cooled down to room temperature in air. These heat-treated MWCNTs and 19.6 g of commercial Mg powders (99.8 % purity, average particle size 38 μm) were placed in a container (5.5 cm in diameter and 4.5 cm in height), subsequently the MWCNTs and Mg powders were mechanically mixed by dry blending for 4 h in a Turbula T2C mixer. In order to separate the MWCNTs from the agglomerate state (the purified MWCNTs were agglomerated due to the intermolecular van- vander- Waals der-interactions between the nanotubes) and to mix MWCNTs with Mg powders sufficiently, 10 ceramic (Al Al2O3) balls were added into the container. After blending of the mixture, no agglomerates of MWCNTs

were visible and this indicates that both materials were well mixed together. The blends were placed in a double-action graphite tooling consisting of a die and two cylindrical pistons. The graphite tooling containing the mixture was mounted in a Sintris 10STV hot press and hot pressed under following processes: in vacuum, the sample was heated up from room temperature to 500 °C at a heating rate of 50 °C /min then from 500 °C to 600 °C at a heating rate of 10 °C /min under a pressure of 50 MPa. After sintering at 600 °C for 30 min, the sample was cooled down to room temperature and a disk-shaped compact (Ø 53 mm x 5mm) was obtained. Finally, the compact underwent hot isostatic pressing at 600 °C for 60 min under an argon pressure of 1800 bar. The surface of compact was before the density of the sintered part was measured. For the realizing of the composite Mg-1%MWCNTs was used a similar method just that the mixture of 0.2 g of heat-treated MWCNTs and 19.8 g of Mg powders was manually wet mixed in an alcohol and acid then it was dried. The used sintering temperature and the pressure were 550 °C and 25 MPa, respectively. This case did not experience hot isostatic pressing. It was concluded that CNT are better wetted in the case of processing by hot isostatic pressing.

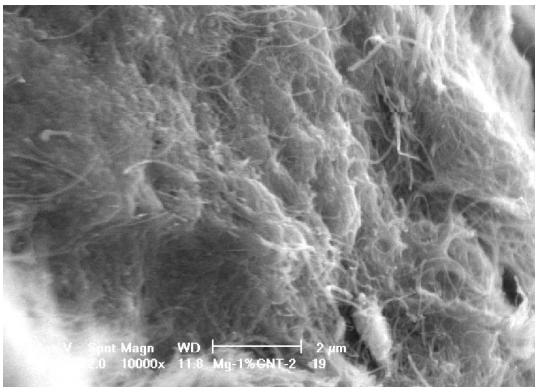

Fig.4. SEM image of fracture surface of Mg-1wt% MWCNTs

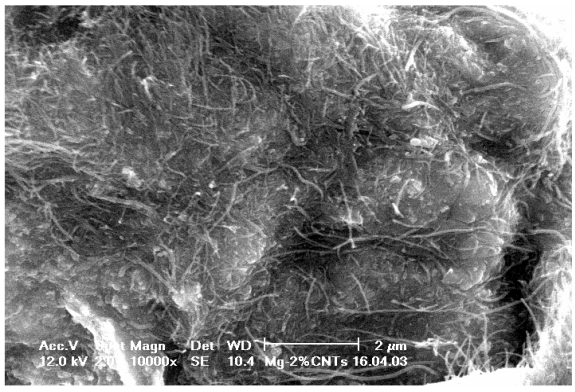

Fig.5. SEM image of fracture surface of Mg-2wt%MWCNTs. Homogeneous dispersion of MWCNTs in Mg matrix

Another method for obtaining metal matrix composites reinforced with carbon nanotubes is the usage of short fibers of alumina named SAFFIL [1] covered with carbon nanotubes and than infiltrated in molten metal. These fibers covered with carbon nanotubes are used as reinforcement materials in metal matrix composites. MWCNTs - based composites were synthesized in a gas pressure infiltration device, which allows one to infiltrate ceramic preforms with molten metals or their alloys. As matrix were used pure magnesium and aluminum alloys (Al-4%Cu-1%Mg-0.5%Ag (WFA)). Both preforms and the metals or their alloys were preheated at 720 °C in vacuum (10^{-2} mbar). A pressure of 2 MPa was applied during infiltration infiltration. Then the composites were rapidly cooled down by air circulation. WFA-25vol%SAFFIL-CNTs, WFA-25vol%SAFFIL, Mg-25vol%SAFFIL-CNTs, Mg-25vol%SAFFIL composites were obtained in this method.

Powder metallurgy is the technique used in the next experiment too [10]. Multiwalled and single-walled nanotubes were synthesized by arc evaporation method. In the case of MWNTs an electric arc was struck between a graphite anode and a copper cathode of respective diameters 7 mm and 12 mm in a helium atmosphere of

500 Torr. A cylindrical deposit grew on the copper cathode and consisted of a hard gray outer shell and a soft fibrous black core. The soft core mainly consisted of MWNTs. The graphite rod was drilled axially and densely packed with a mixture of nickel and iron 5% (1:1) and 95% graphite powder. The helium pressure is maintained at 100–200 Torr obtaining in this way SWNTs. CNTs (MWNT and SWNT) were dispersed in ethanol and sonicated for 20 min. The decanted solution was heated to vaporize ethanol and the residue was used as the reinforcement material. Commercial purity aluminum was used as the matrix material. A mixture of CNT and aluminum powder (200 mesh) were ball milled at 200 rpm for 5 min. The short duration and slower milling speed ensures that the carbon nanotubes are intact. The milled powder was compacted in a circular die with a load of 120 KN; the billets thus obtained were sintered in an inert gas environment (nitrogen) for 45 min at 580 °C and finally hot extruded at 560 °C. Some samples were also prepared with K_2ZrF_6 coated CNTs. This coating was added by first dissolving the salt in boiling distilled water, and then adding CNT powder. The water was allowed to evaporate off, leaving behind a residue, which was used in subsequent composite preparation.

Received April 20, 2007 *The Technical University from Cluj-Napoca*

REFERENCES

1. J.YANG, *Carbon Nanotubes as Reinforcements and Interface Modifiers in Metal Matrix Composites*, thèse no 3140 (2004), École Polytechnique Fédérale de Lausanne http://biblion.epfl.ch/EPFL/theses/2004/3140/EPFL_TH3140.pdf
2. S.Suresh, A.Mortensen, A.Needleman, *Fundamentals of Metal-Matrix Composites*, Butterworth-Heinemann, 1993
3. E.Flahaut, *Synthese par Voie Catalytique et Caracterisation de Composites Nanotubes de Carbone-Metal-Oxide. Poudres et Materiaux Denses*, These no 3566(1999), Universite Paul Sabatier de Toulouse
4. E.W.Wong, P.E.Sheehan, C.M.Lieber, Science, 277, (1997), **1971-1975**
5. http://physicsweb.org/articles/world/11/1/9
6. http://nanotechweb.org/articles/news/5/1/12/1
7. C.L. Xu, B.Q. Wei, R.Z. Ma, J. Liang, X.K. Ma, D.H. Wu, *Fabrication of aluminum /carbon nanotubes composites and their electrical properties*, **Carbon, 37** (5), 855(1999)
8. C.Y. Min ,X.B. Zhang*, Z.P. Ding,S.M.Zhou,X.Y.Tao,H.Zhang, G.L. XU,W.M.Zhu, F. Liu, *CNTs-reinforced Aluminium Composite Fabricated by Pressureless Infiltration Process and its Tribological Properties*, Department of Materials Science and Engineering, Zhejiang University
9. R.Zhong, H.Cong, *Fabrication of nano-Al based composites reinforced by single-walled carbon nanotubes*, ***Carbon*, v 41, n 4**, 2003, **848-851**
10. R. George, K.T. Kashyap, R. Rahul and S. Yamdagni, *Strengthening in carbon nanotube/aluminium (CNT/Al) composites*, **Scripta Mat**., **Vol 53**, Issue 10, Nov. 2005, 1159-1163

STUDIU PRIVIND OBTINEREA COMPOZITELOR CU MATRICE METALICA ARMATE CU NANOTUBURI DE CARBON

Rezumat: Lucrarea prezinta un studiu stiintific ale celor mai noi tehnologii pe plan mondial privind obtinerea compozitelor cu matrice metalica armate cu nanotuburi de carbon. Majoritatea cercetatorilor au abordat metodologia de obtinere a compozitelor utilizand metalurgia pulberilor si infiltrarea de metal topit. Materialele obtinute prezinta diferite caracteristici care depind de procesul si bineinteles de matricea folosita. Studiul se doreste a fi o prezentare a datelor din literatura de specialitate si este baza pentru experimente ulterioare in scopul obtinerii compozitelor cu matrice metalica armate cu nanotuburi de carbon.

BULETINUL INSTITUTULUI POLITEHNIC DIN IAŞI
Tomul LIII (LVII), Fasc. 1, 2007
Secția
ŞTIINȚA ŞI INGINERIA MATERIALELOR

CERAMIC NANOSTRUCTURES PRODUCED ON TITANIUM AND TITANIUM ALLOYS

BY

CORNEL FRĂȚILĂ[(1)], IOAN ROMAN[(2)], EUGENIU VASILE[(2)], ROXANA TRUŞCĂ[(2)], FLORENTIN STOICIU[(1)] and PETRU NIȚĂ[(2)]

Abstract: The anodizing is the process that a coating oxide layer is grown on a metal by an electrochemical way, by anodic oxidation. The paper describes the experiments regarding titanium and TA6V4 titanium alloy anodic oxidation aiming their corrosion rate decrease as implants and the minimization of corrosion products release into the human body. The samples surfaces are covered with adherent and uniform coloured coatings, by special preparation operations. Some water electrolytes with phosphate ions content were used. The layers grown on titanium and TA6V4 titanium alloy contain titanium oxides and phosphorus compounds; they are adherents, homogeneous and elastic. The coated samples were thermally treated at 600, 770^0C. The proposed surface treatment enables an excellent electrochemical stability at the interface implant/biological environment, minimizing the local and general toxic specific effects. The samples were characterized using: cyclic voltametry in Ringer solution, X-ray diffraction analysis, high resolution electron microscopy (HRTEM), and selected area electrons diffraction (SAED).

Key words: nanostructure, anodizing, coatings, ceramic, implants.

1. Introduction

The paper presents the results of the laboratory experiments regarding implant materials, like titanium and TA6V4 alloy oxidation, by electrochemical, controlled technology, using compatibles electrolytes with the structure and physical-chemical characteristics of the supports. The titanium electrochemical oxidation, that is it anodization, represents a procedure to artificial growth on the titanium surface of oxides layers, having higher thickness than the natural, spontaneous one.

This procedure has as purpose to increase the corrosion resistance in different environments and also to improve the plastic deformation conditions of both titanium and titanium alloys. This titanium and titanium alloys processing has long time concerned the electrochemists [1÷10] but we estimate that the resources are not yet exhausted. In this process the titanium is the anode and the cathode consists of metals such as lead, aluminium, titanium, platinum, stable metals in the used electrolytes. The anodic reaction is an oxidation process developed at the sample (titanium anode)/electrolyte interface:

$$Ti + 2H_2O \rightarrow TiO_2 + 4H + 4e^- \quad (1)$$

The cathodic reaction is a water reduction process:

$$4H_2O + 4e^- \rightarrow 2H_{2(g)} + 4OH^- \quad (2)$$

The hydrogen gives off at the cathode as bubbles during the anodizing process.

2. Experimental results

Pure titanium and TA6V4 titanium alloy, having chemical compositions given in table 1 were used. Titanium and TA6V4 alloy anodic oxidation experiments were carried according to the technological schedule in figure 1. The samples with the size of 28 x 20 x 0.5 mm were prepared according to the technological schedule. The samples were anodized in compatibles electrolytes (E3-E4), to realize on the titanium and titanium alloy surface oxidic layers with phosphorus content (named here „phosphating"): E3: H_3PO_4 0,5N + $NaHCO_3$ 10% phosphating electrolyte; E4: H_3PO_4 1N : citric acid 20g/l 1:1 phosphating electrolyte.

Table 1. Experimental results. Samples chemical composition (base material)

Symbol	Chemical composition [% weight]												
	Ti	O	H	N	C	Al	V	Fe	Si	Ni	Cr	Co	Cu
Ti	Bal.	0.12	0,012	0,04	0,06			0,15					
TA6V4	Bal.			0,005	0,03	5,53	3,9	0,13	0,05-0,1	0,01-0,05	0,005-0,01	<0,005	0,001

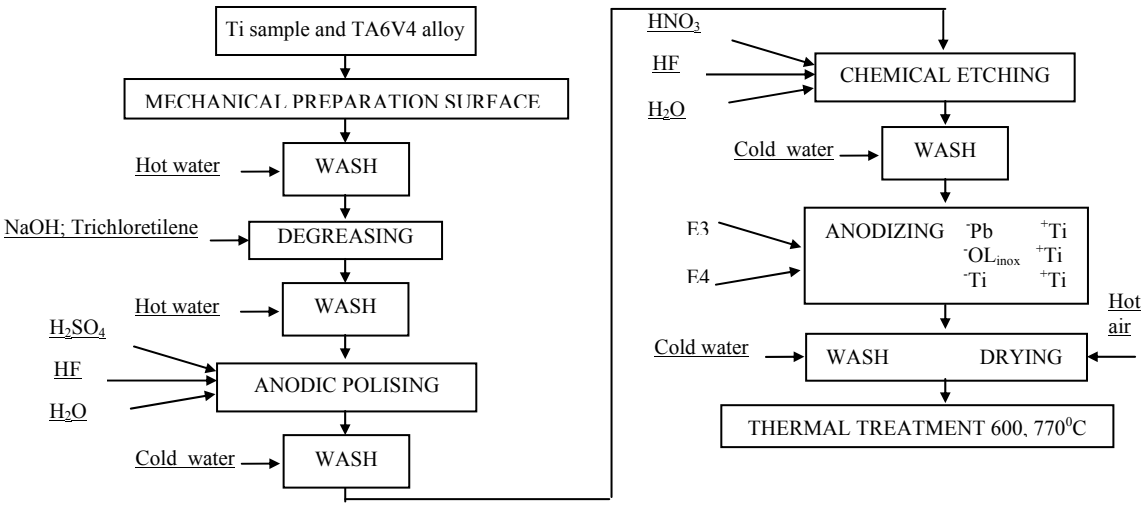

Figure 1 Titanium and titanium alloys anodic oxidation schedule

Several technological parameters were studied in order to accurately reveal the titanium and titanium alloy behaviour during the whole anodizing process. A special unit cathode – anode device was used, the cathodes plates being made of stainless steel or titanium, as shown in figure 2 (Experimental anode/cathode unit device).

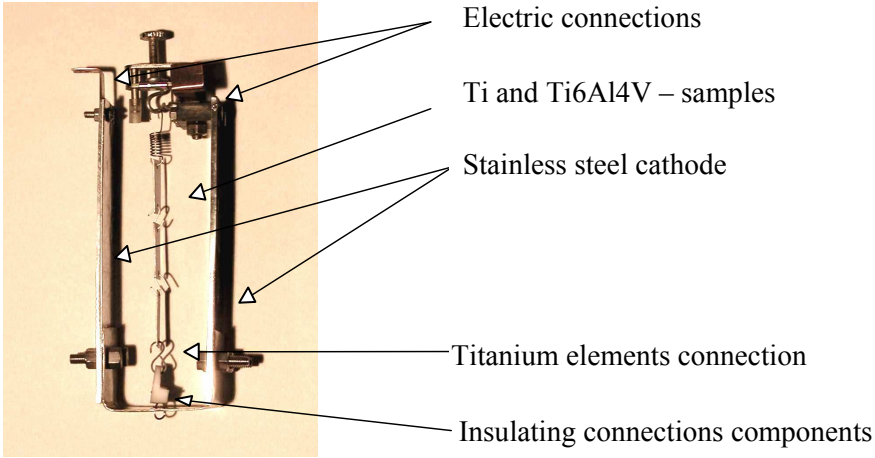

The experimental conditions are presented in the tables 2, 3. Both titanium (index „T") and TA6V4 alloy (index „A") samples were used.

Table 2 Anodizing titanium

Sample Code	Anodic oxidation				Thermal Treatment	
	Electrolyte	$U_{max.}$ [V]	Time min	T °C	Time min	T °C
T-AF4	E3	100	25	25	-	-
T-AF4-350	E3	100	25	25	60	350
T-AF4-600	E3	100	25	25	60	600
T-AF4-770	E3	100	25	25	60	770
T-AF5	E3	75	20	25	-	-
T-AF5-350	E3	75	20	25	60	350
T-AF5-600	E3	75	20	25	60	600
T-AF5-770	E3	75	20	25	60	770
T-TEG	E4	50	180	25	-	-
T-TEG-350	E4	50	180	25	60	350
T-TEG-600	E4	50	180	25	60	600
T-TEG-770	E4	50	180	25	60	770

Table 3 Anodizing TAl6V4 alloy

Sample Code	Anodic oxidation				Thermal Treatment	
	Electrolyte	$U_{max.}$ [V]	Time min	T °C	Time min	T °C
AF4	E3	100	25	25	-	-
AF4-350	E3	100	25	25	60	350
AF4-600	E3	100	25	25	60	600
AF4-770	E3	100	25	25	60	770
AF5	E3	75	20	25	-	-
AF5-350	E3	75	20	25	60	350
AF5-600	E3	75	20	25	60	600
AF5-770	E3	75	20	25	60	770
TEG	E4	50	180	25	-	-
TEG-350	E4	50	180	25	60	350
TEG-600	E4	50	180	25	60	600
TEG-770	E4	50	180	25	60	770

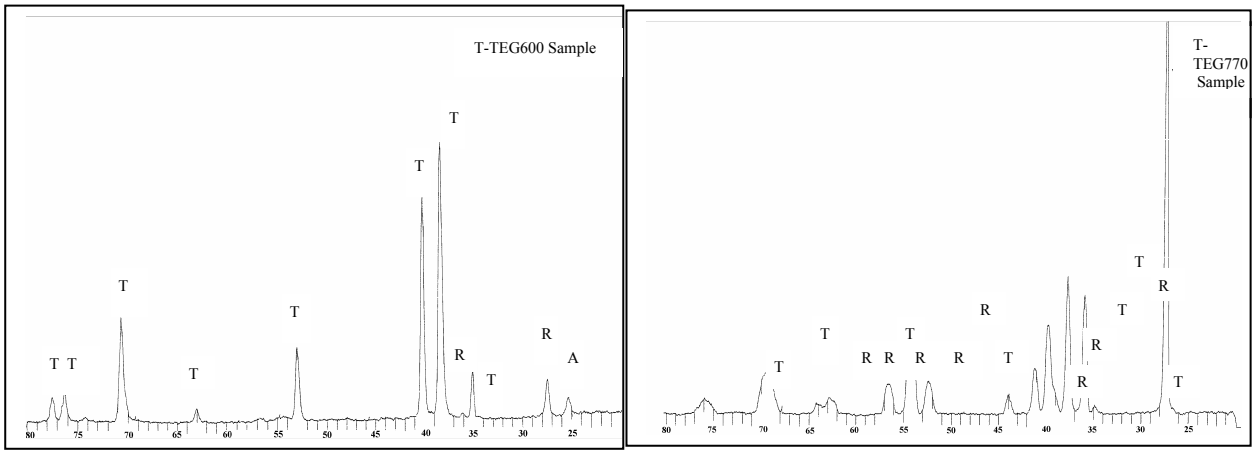

Figure 3. T- α titan; A- TiO_2 (anatase); R- TiO_2 (rutile)
X-ray diffraction analysis T-TEG600 sample and T-TEG770 sample

The samples were characterized using: X-ray diffraction analysis, high-resolution electron microscopy (HRTEM), selected area electrons diffraction (SAED) and cyclic voltametry in Ringer solution. X-ray diffraction (figure 3) for T-TEG600 sample revealed α–titanium TiO_2 (anatase) compound but also TiO_2 (rutile) with well defined peaks according of interplanar distance of 3.24 Å (angle $2\theta = 27.45^0$) and interplanar distance of 2.48 Å (angle $2\theta = 36.10^0$). Figure 4 presents high resolution electron microscopy (HRTEM) images for TTEG 600 sample structure characterization. The granular aspect of this sample heat treated at 600^0C is clearly revealed in TEMBF image figure 4a. Diffraction electrons image (SAED)- figure 4b- associated to the micro area from 4a figure revealed by diffraction rings the polycrystalline character of the sample. High resolution electron microscopy (HRTEM), from 4c and 4d figures reveals sample nanocrystalline structure by the existence of 10 Å size nanocrystals. The 4e and 4f figures show nanocrystals anatase and rutile presence –anatase interplanar distance 3.52 Å (101) and rutile interplanar distance – 3.24 Å (110).

The X -ray diffraction for T-TEG 770 sample (figure 3) revealed other diffraction peaks besides α–titanium, TiO_2 (rutile) compound, with well defined main peak of 3.24 Å (angle $2\theta=27.45^0$) of maxim intensity. It is noticed the absence of main peak of anatase compound suggesting its disappearance from oxide layer, as a result of heat treatment at 770^0C.

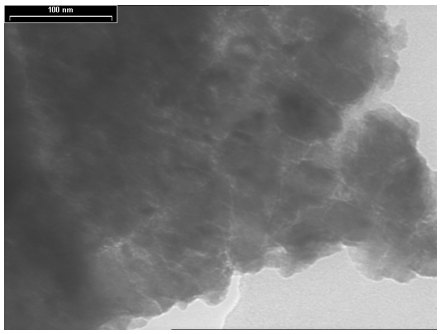

4a TEMBF Image

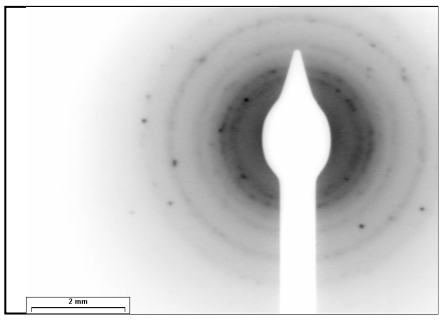

4b SAED Image

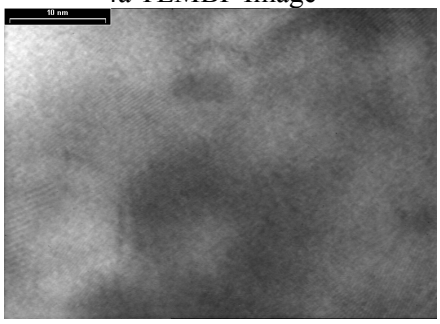

4c HRTEM Image

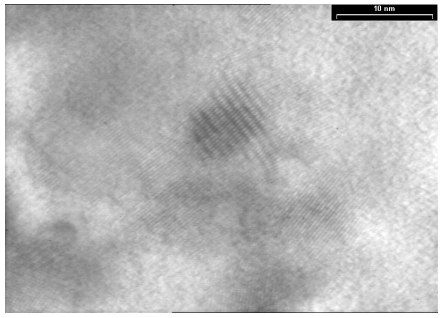

4d HRTEM Image

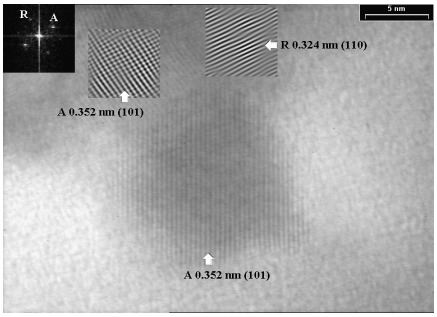

4e HRTEM Image

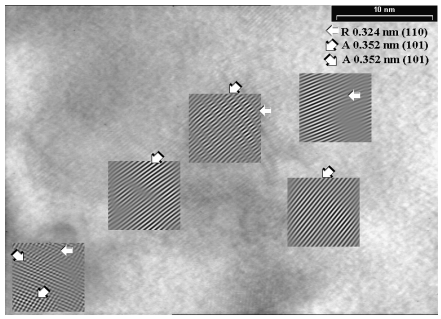

4f HRTEM Image

Figure 4 T-TEG 600 Sample

Figure 5 presents high-resolution electron microscopy images for structure characterizing of TTEG 770 sample. TEMBF images figure 5a show relative homogeneous aspect of sample at a medium magnification.

The electrons diffraction image figure 5b associated with micro area 5a figure, revealed the polycrystalline character of sample and index image shows that in sample TiO_2 (rutile) compound exists, pointed out by diffraction rings according to interplanar distances of de 3.3Å (110), 2.5 Å (101), 2.2 Å (111), 1.7 Å (211).

High resolution electron microscopy (HRTEM), from 5c, 5d , 5e and 5f figures show rutile nanocrystals existence by reticular aspect, interplanar distances of 3.24 Å, and 2.49 Å

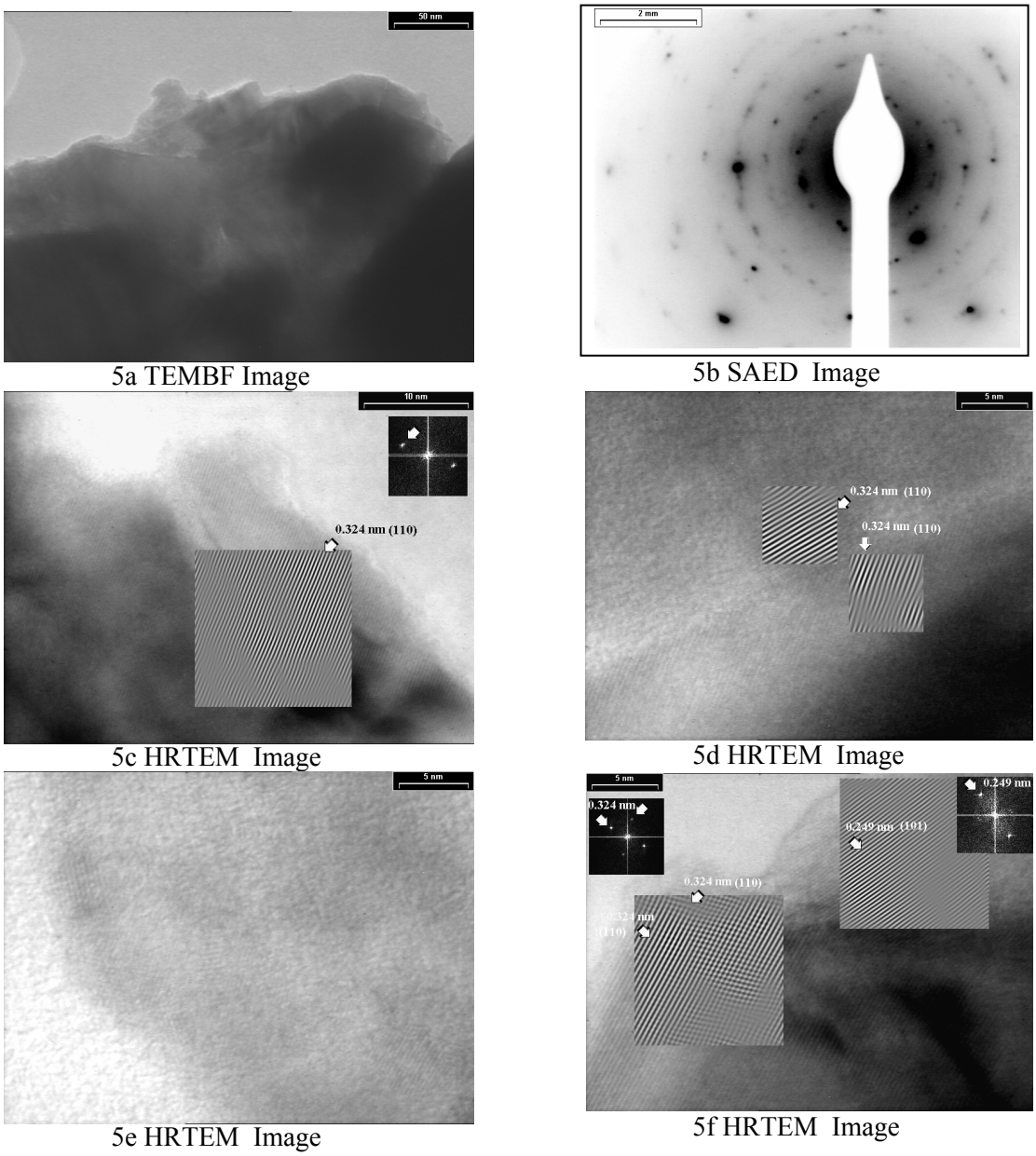

5a TEMBF Image

5b SAED Image

5c HRTEM Image

5d HRTEM Image

5e HRTEM Image

5f HRTEM Image

Figure 5 T-TEG 770 Sample

The samples were electrochemically investigated regarding the influence of heat treatment on the anticorrosive performance of the anodic oxidation layers achieved on titanium and on the TA6V4 alloy. The experimental technique was cyclic voltametry. Electrolyte used was Ringer solution, with pH 2.5. Investigated potential area was between -1000÷4000 mV e.s.c. Polarization rate was 1000 mv/sec. For titanium anodic oxidized samples TEG the heat treatment in air at 770^{o}C produces an electrochemical inert surface, at electrochemical polarization no oxidation process was identified in the field of -1000÷4000mVe.s.c. Electrochemical investigations show that heat treatments increase the stability and chemical inertness of the layers.

It is especially proved that rutil presence considerably increases the corrosion resistance of the samples.

3. Conclusions

The paper presents a notable and complex technology for the improvement of the biocompatibility and quick osteointegration properties, in comparison with living organisms, of dental and body implants made up of titanium and TA6V4 alloy. This is achieved by the growth on the metallic substrate of ceramic nanostructures made up of ceramic oxide on the basis of anatase, brookite and rutile. Experiments have been performed for the acquirement of the ceramic nanostructures on titanium and TA6V4 alloy, by an electrochemical controlling anodizing process in electrolytes on the basis of phosphorus, followed by consolidation of thermochemically processed layers that took place in the air at 600 and 770^0C. The obtained samples have been characterised by X-ray diffraction analysis, high-resolution electron microscopy (HRTEM), selected area electrons diffraction (SAED) and cyclic voltametry in Ringer solution.

The changes that take place at the level of layer microstructure resulting from heat treatments applied in various conditions, in air, have been particularly studied. The layers contain titanium oxides with nanocrystalline structure and present special performances in synthetic Ringer solution.

Received April 23, 2007

(1) National Institute for Nonferrous and Rare Metals,Romania
(2) METAV CD SA Romania

REFERENCES

1. A.Aladjem *"Anodic oxidation of titanium and its alloys"* Journal of Materials Science 8 (1973), p.688/704;
2. J.L.Delplancke, M.Degrez, A.Fontana, R.Winand *"Self-colour anodizing of titanium";*
3. F.Climent Montoliu, R.Capellades Font *"Die anodische Oxidation von Titan"*;
4. H.Yamaguchi, K.Miki,H.Satoh, K.Shimogori "*Characteristics of anodized titanium and its application"* Societe Francaise de Metallurgie, Vol.4, P1817/22 Proceedings of the Sixth World Conference on Titanium Cannes, June 6-9,1988 Edited by P.Lacombe, R.Tricot, G.Beranger Published by les editions de phisique;
5. A.K.Sharma, H.Bhojaraj "Anodizing Titanium for Space Applications" Titanium 1990-Products and Applications, Vol.1,p.282/89 Proceedings of the Technical Program from the 1990 Conference Published by Titanium Development Association;
6. C.D.Hall and N.Hackerman, J.Phys.Chem., 57,262(1953);
7. M.Stern and H.Wissenberg, This Journal, 106,755 (1959);
8. J.F.Dewald, This Journal, 102,1 (1955);
9. A.Charlesby, Proc.Phys.Soc., B66,317 (1953);
10.T.Koizumi et al., "*Structure of Oxide Films Formed On Ti in Boiling Dilute acid* „Corrosion Sci., 1968, 8: 195-196.

NANOSTRUCTURI CERAMICE PRODUSE PE TITAN ŞI ALIAJELE SALE

Rezumat Anodizarea este procesul prin care un strat de oxid este crescut pe un metal pe cale electrochimică, prin oxidare anodică. Lucrarea descrie experimentări privind oxidarea anodică a titanului şi aliajului de titan TA6V4, în scopul scăderii vitezei de coroziune a implantelor şi pentru minimalizarea eliberării produşilor de coroziune în organismul uman. Suprafaţa probelor este acoperită cu straturi colorate uniforme şi aderente prin operaţii speciale de preparare. S-au utilizat electroliţi apoşi cu conţinut de ioni de fosfor. Straturile crescute pe titan şi aliaj de titan TA6V4 conţin oxizi de titan şi compuşi de fosfor; ele sunt aderente, omogene şi elastice. Probele acoperite sunt tratate termic la: 600, 770^0C.Tratamentele de suprafaţă realizate asigură o excelentă stabilitate electrochimică la interfaţa implant-mediu biologic, minimalizând efectele toxice locale şi generale. Probele au fost caracterizate utilizând: voltametria ciclica în soluţie Ringer, difracţia de raze X, microscopia de înaltă rezoluţie (HRTEM) şi difracţia de electroni (SAED).

BULETINUL INSTITUTULUI POLITEHNIC DIN IAŞI
Tomul LIII (LVII), Fasc. 1, 2007
Secția
ŞTIINȚA ŞI INGINERIA MATERIALELOR

KINETICS OF ALUMINUM CVD ON STAINLESS STEEL SUPPORTS CHARACTERISATION

BY

BRANDUSA GHIBAN[(1)], GEORGE ANGELOPOULOS [(2)] and CORNELIA LUPU [(1)]

Abstract: Present paper presents the experimental results concerning deposition of aluminum on stainless steel supports by fluidized bed chemical vapor deposition process. Parameters used for the deposition were: temperatures about 530, 540, 550, 580 and 610 °C and maintaining periods between 15 minutes up to 180 minutes. Equations, optical and x-ray diffraction measurements were presented, in order to establish kinetics of the aluminum deposition on stainless steels supports.

Keywords: FBCVD method, aluminum deposition, stainless steel

1. Introduction

Stainless steel's oxidation/corrosion resistance at high temperatures can be improved using aluminum coatings on the surface, because the high near surface content of aluminium increases the ability of forming an Al_2O_3 protective film. The coatings were obtained using the Fluidised Bed Chemical Vapour Deposition Technique which is characterised by the following features: uniform temperature distribution over the whole reactor volume; uniform concentration of the reactive gases, which prevents the development of localized coating growths; higher mass transfer rates at the substrate surface; an easier introduction and extraction of the specimens, the furnace being at the treating temperature.

Present paper's aim is to put in evidence the behaviour of aluminum deposition by FBCVD method on stainless steel 316.

2. Experimental procedure

The experimental apparatus is presented in figure 1. It consists of a cylindrical fluidized bed (FB) quartz tube, 270mm length and 36mm inner diameter, heated by electrical resistance. Activators: A. I_2(s) or B. HCl (aq) 37 %.

FBCVD procedures according to the activator used may consist in:

a) A gas mixture of Ar (99.999 %) gas and iodine vapours is used for the fluidisation of the Al powder bed (99.8 %, grain size: 63-160μm). The iodine vapours are provided by means of an I_2 (> 99.8 %) evaporation device where the iodine crystals are being heated. The Ar gas is led through this device and serves as a carrier gas of the iodine vapours. For a set velocity of the Ar gas determined by the fluidization needs, the quantity of the iodine vapours is controlled by the temperature of the

evaporation device. In the present case, the fluidization velocity was set at $8x10^{-3}$ m/s and the temperature of the device at 100 °C. The iodine containing precursor vapours are formed *in situ* the reactor by the reaction of iodine and aluminium. White-violet coloured off-gases are preferable as they indicate that most of the iodine reacts with Al, while violet ones indicate a possible corrosion of the specimens as excess of iodine exists.

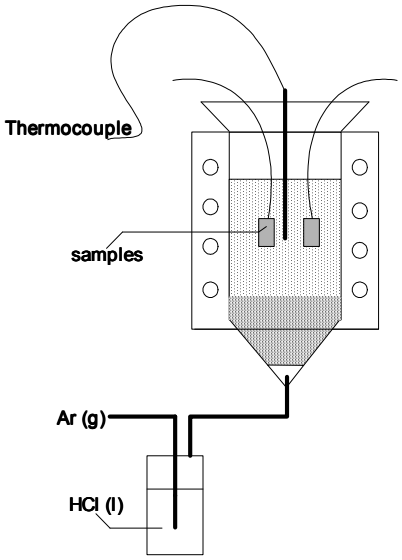

Fig. 1 FBCVD experimental device

b) Ar (99.999 %) gas is led through 37 % HCl (aq), subsequently entering the FB from the bottom, serving as a carrier for the chlorine gases and the fluidization. The quantity of the chlorine vapors is controlled by the velocity of the Ar gas. The chlorine containing precursor vapors are again formed *in situ* the reactor by the reaction of HCl and Al. Excess HCl vapors exit the reactor from its top rapidly enough to avoid corrosion of the test specimens. Presence of white off–gases indicates that the reaction between HCl and Al takes place. Following, the Al_xCl_y vapors result in Al deposition on the test specimen's surface. The liquid activator has to be renewed periodically because the vol. % of HCl in the aqueous solution decreases significantly.

The samples were inserted from the top into the Al filled reactor. Prior processing, the samples were polished up to 400 grids SiC paper, rinsed with dry alcohol, cleaned with acetone in an ultrasonic bath and blasted with Ar gas. After treatment, the samples were cleaned and treated with saturated aqueous solution of Na_2CO_3 for the removal of remnant traces of the activator, segmented, mounted in resin and polished up to 1μm diamond paste for the metallographic observation and SEM–EDX analysis.

3. Experimental results and discussion

The coatings were deposited on stainless steel 316, at 600°C for a treatment time of 30, 60, 120 and 180 minutes, with HCl activator. At this temperature the obtained coating has a dark-gray colour and is dense and homogeneous. The average thickness after 30 minutes of treatment is 7.463 μm, after 60 minutes 8.63 μm, after

120 minutes is 17.687 μm, and after 180 minutes it is 20.737. The variation of the treatment temperature was about ±10°C leading to the obtaining of a more uniform substrate.

Considering the obtained average values the variation of the substrate thickness graphic was drawn as a function of the treatment time and as a function of the root square of the time. One can see that the variation of the substrate thickness as a function of the treatment time has a smaller error value than the one given by the variation of the substrate thickness as a function of the root square of time, meaning that the mechanism of the substrate growing is given by the chemical reaction.

Some black spots can be seen in the picture representing the cross section of the Al coating. These spots results from either inconvenient metallographic preparation, either from electro-deposition. These spots may cause cracking in the substrate and even its breakdown.

Fig. 2 Cross section of the Al coating on a stainless steel 316, treatment time 30 minutes at 600°C, with HCl activator

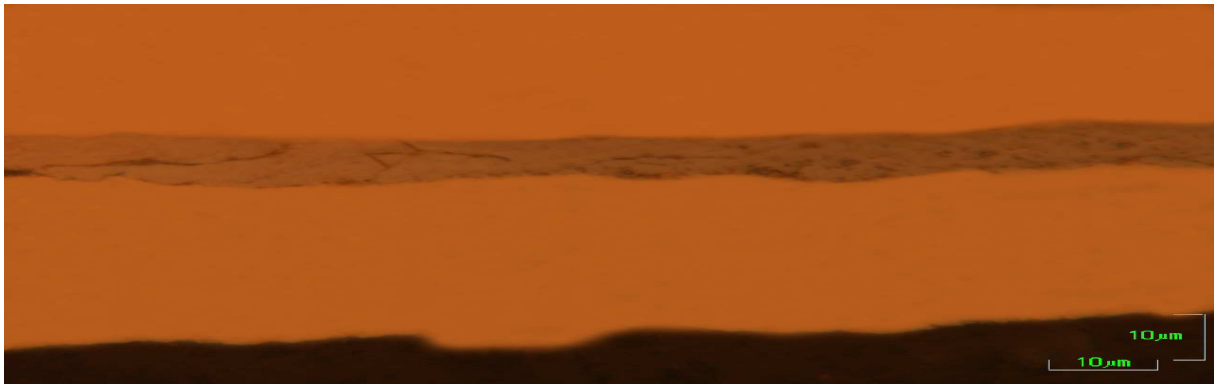

Fig. 3 Cross section of the Al coating on a stainless steel 316, treatment time 60 minutes at 600°C, with HCl activator

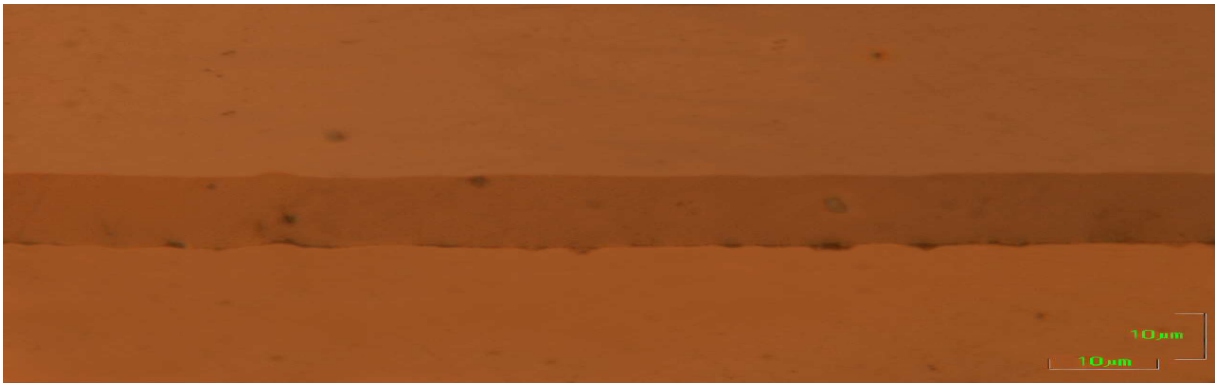

Fig. 4 Cross section of the Al coating on a stainless steel 316, treatment time 120 minutes at 600°C, with HCl activator

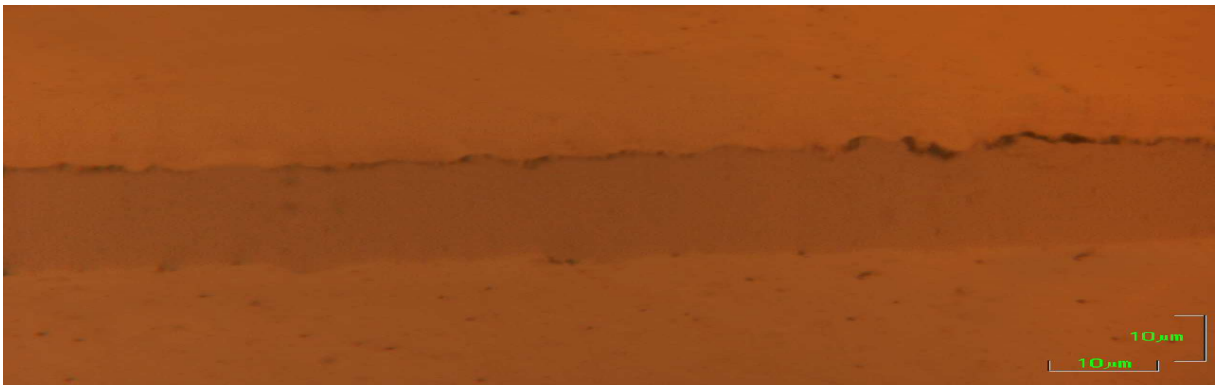

Fig. 5 Cross section of the Al coating on a stainless steel 316, treatment time 180 minutes at 600°C, with HCl activator

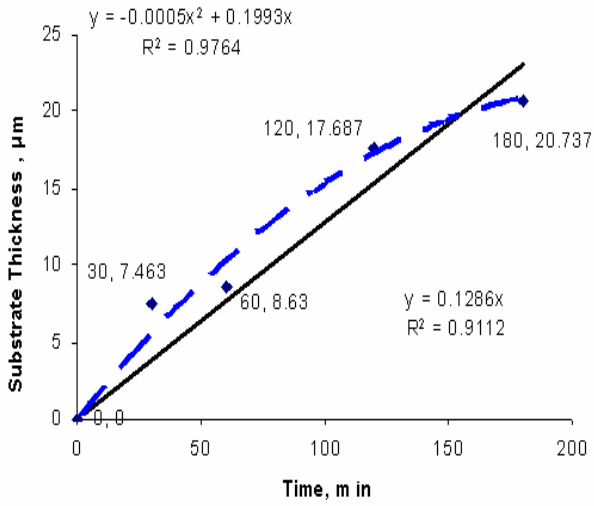

Fig. 6 The thickness of the substrate as a function of time

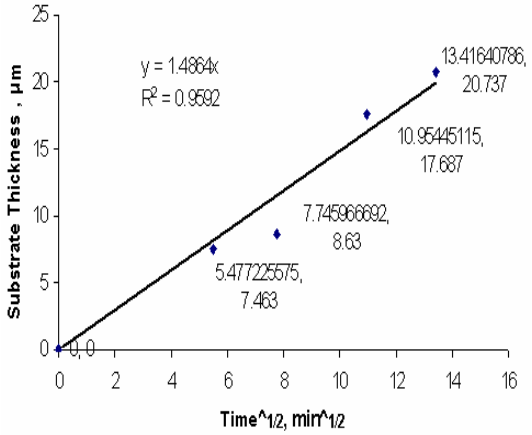

Fig. 7 The thickness of the substrate as a function of the square root of the treatment time

During another experiment, the deposited coating on stainless steel 316, at 610°C for a treatment time of 15, 30, 45 and 60 minutes, with HCl activator, has a dark-gray colour and is dense and homogeneous. The average thickness after 15 minutes of treatment is 6.42375 µm, after 30 minutes 9.18866 µm, after 45 minutes is 11.3575 µm, and after 60 minutes it is 14.575. The variation of the treatment temperature was about ±10°C leading to the obtaining of a more uniform substrate.

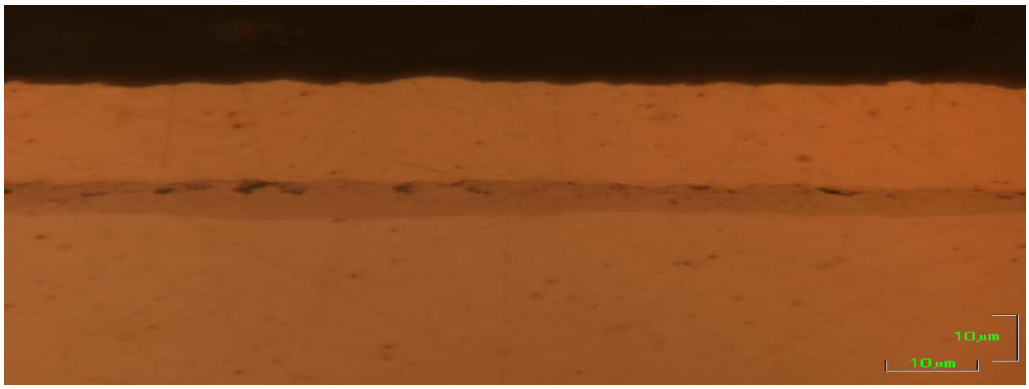

Fig. 8 Cross section of the Al coating on a stainless steel 316, treatment time 15 minutes at 610°C, with HCl activator

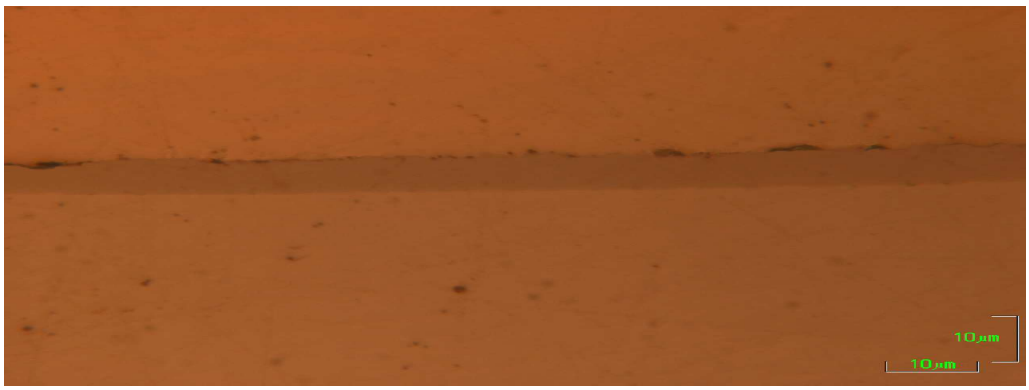

Fig. 9 Cross section of the Al coating on a stainless steel 316, treatment time 30 minutes at 610°C, with HCl activator

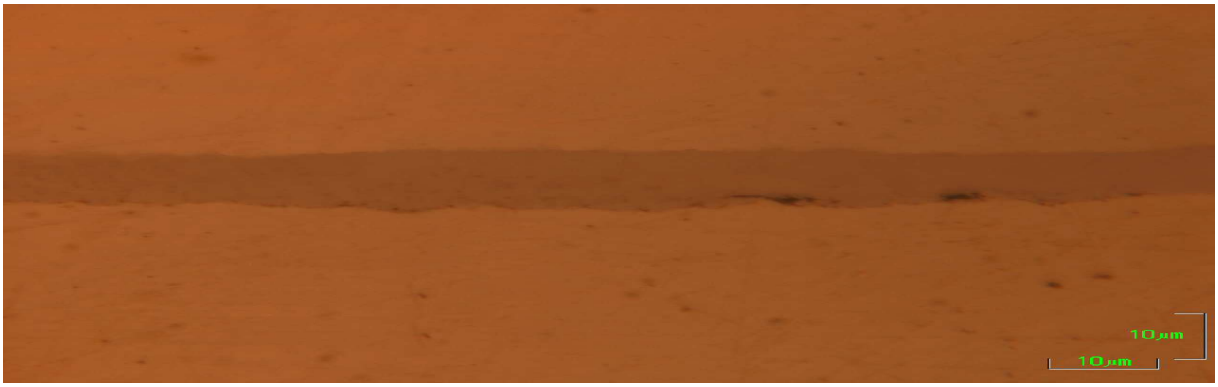

Fig. 10 Cross section of the Al coating on a stainless steel 316, treatment time 45 minutes at 610°C, with HCl activator

Fig. 11 Cross section of the Al coating on a stainless steel 316, treatment time 60 minutes at 610°C, with HCl activator

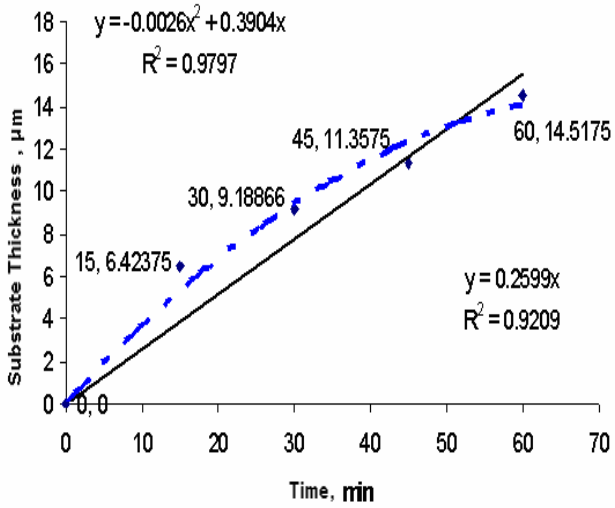

Fig. 12 The thickness of the substrate as a function of time

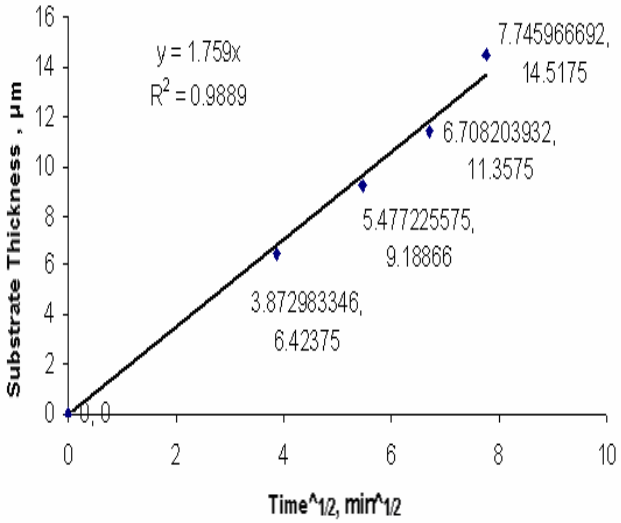

Fig. 13 The thickness of the substrate as a function of the square root of the treatment time

The fluidized bed is used for further experiments for the aluminium deposition on stainless steel supports at different temperatures: 530, 540, 550 and 580 °C and for different time of treatment, from 15 minutes up to 180 minutes.

4. Conclusions

From the present paper the following conclusions can be drawn:

- At the same treatment conditions the thickness of the deposited substrate is increasing with the temperature,
- through deposition at a certain temperature but at different maintaining time, the growth of the deposited substrate increases with the deposition time;
- the deposition rate in 60-120 minutes domain, is greater than in 120-180 minutes domain, meaning that after 120 minutes the deposition rate tends to decrease;

The treatment parameters must be carefully observed in order to avoid local temperature growth which may cause local growth of the substrate.

Table 1. Characterisation of the substrate and the deposition parameters

No.	Parameters		Substrate Description		Deposition Mechanism Characterisation	Kinetic Equation of the Deposition
	Temperature (°C)	Time (min)	Thickness (µm)	Observation		
1	530±15	15	6.867	Homogeneous, dark-grey, uniform, dense	Chemical Reaction	$y = -0.0004x^2 + 0.3657x$
		30	9.18763	Homogeneous, dark-grey, uniform, dense		
		45	15.93318	Homogeneous, dark-grey, uniform, dense		
		60	20.40391	Inhomogeneous, dark-grey, uniform, dense		

No.	Parameters		Substrate Description		Deposition Mechanism Characterisation	Kinetic Equation of the Deposition
	Temperature (°C)	Time (min)	Thickness (μm)	Observation		
2	540±25	15	11.99	Homogeneous, dark-grey, dense	Diffusion	$y = -0.0076x^2 + 0.8508x$
		30	19.836	Homogeneous, dark-grey, dense		
		45	20.55	Homogeneous, dark-grey, dense		
		60	24.84762	Homogeneous, dark-grey, dense		
3	550±8	30	2.0865	Homogeneous, black, dense	Diffusion	$y = -0.0002x^2 + 0.0689x$
		60	3.3775	Homogeneous, grey, dense		
		120	5.6658	Homogeneous, black, dense		
		180	6.575	Homogeneous, grey, dense		
4	550±10	15	1.15	Homogeneous, dark-grey, dense	Chemical Reaction	$y = -0.0005x^2 + 0.0633x$
		45	3.87	Homogeneous, dark-grey, dense		
		60	5.81	Homogeneous, dark-grey, dense		
5	610±10	15	6.42375	Homogeneous, dark-grey, uniform, dense	Diffusion	$y = 0.0026x^2 + 0.3904x$
		30	9.18866	Homogeneous, dark-grey, uniform, dense		
		45	11.3575	Homogeneous, dark-grey, uniform, dense		
		60	14.5175	Homogeneous, dark-grey, uniform, dense		
6	610±15	15	12.727	Homogeneous, dark-grey, uniform, dense	Diffusion	$y = -0.008x^2 + 0.7801x$
		30	14.8095	Homogeneous, dark-grey, uniform, dense		
		60	17.81	Homogeneous, dark-grey, uniform, dense		
		120	18.1625	Homogeneous, dark-grey, uniform, dense		

No.	Parameters		Substrate Description		Deposition Mechanism Characterisation	Kinetic Equation of the Deposition
	Temperature (°C)	Time (min)	Thickness (μm)	Observation		
7	610±25	30	13.91857	Homogeneous, dark-grey, uniform, dense	Diffusion	$y = -0.0011x^2 + 0.4396x$
		60	22.64	Homogeneous, dark-grey, uniform, dense		
		120	34.85	Homogeneous, dark-grey, uniform, dense		
		180	42.72421	Homogeneous, dark-grey, uniform, dense		
8	580±10	60	10.2266	Homogeneous, dark-grey, uniform, dense	Diffusion	$y = -0.0007x^2 + 0.2029x$
		120	13.491	Homogeneous, dark-grey		
		180	13.674	Homogeneous, dark-grey, dense		
9	540±10	30	4.068	Homogeneous, dark-grey, uniform	Chemical Reaction	$y = -0.0004x^2 + 0.1402x$
		60	7.222	Homogeneous, dark-grey, uniform, dense		
		120	10.0711	Homogeneous, dark-grey, uniform		
		180	11.411	Homogeneous, dark-grey, uniform, dense		

The table given above contains data about the deposited substrate of Al on stainless steel supports by FBVCD technique using different parameters.

Received April 24, 2007

(1) University Politehnica of Bucharest – ROMANIA
(2) University of Patras - GREECE

REFERENCES

[1].C. Gomez, M.C. Carpintero, M.P. Hierro, F.J. Perez, F.Pedraza –"**On the aluminisation of stainless steel by CVD in fluidised beds**", Surf. Coat. Technol. (2004)
[2].S.R. Levine, R.M. Caves, J. Electrochem. Soc. 121 8 (1974) 1051
[3]. H.M. Soliman, K.E. Mohamed, M.E.A. El-Azim, F.H. Hammad, J. Mater. Sci. Technol. 13 5 (1997) **383**
[4].A. Bahadur, T.L. Sharma, N. Parida, A.N. Mukherjee, O.N. Mohanty, J. Mater. Sci. 28 (1993) **5375**
[5].B. Ghiban, C.E. Dinescu, M. Zaharia –"**Surface Analysis of Aluminum Powders on Magnesium Substrates deposed by Fluidized Bed CVD Process**", International Conference on Advanced Materials and Technologies, 21-22 oct. Bucharest, ROMAT 2004, p.**155-162**
[6].B. Ghiban, G. Cosmeleata – "**Aluminum Deposition by CVD Method on Stainless Steel Supports**", BRAMAT 2005, ISBN 973-635-454-1, Brasov 24-26 February 2005.
[7].C.Lupu, B. Ghiban, G. Angelopoulos – "**Kinetic characteristics of aluminum CVD on stainless steel supports**", BRAMAT 2007, ISSN 1223-9631, Brasov 22-24 February 2007.

CARACTERIZAREA CINETICII DEPUNERII ALUMINIULUI PRIN METODA CVD PE SUPORTURI DIN OȚEL INOXIDABIL

Rezumat: Lucrarea de față prezintă rezultatele experimentale referitoare la depunerea aluminiului pe suport din oțel inoxidabil, prin intermediul procesului de depunere chimică de vapori în pat fluidizat. Parametrii utilizați pentru depunere au fost: temperature în jur de 530, 540, 550, 580 şi 610°C şi perioade de menținere între 15 şi 180 de minute. Au fost prezentate ecuații şi măsurători optice şi prin difracție de raze X, pentru a stabili cinetica depunerii aluminiului pe suporturi din oțel inoxidabil.

BULETINUL INSTITUTULUI POLITEHNIC DIN IAŞI
Tomul LIII (LVII), Fasc. 1, 2007
Secția
ŞTIINȚA ŞI INGINERIA MATERIALELOR

SYNTHESIS, STRUCTURAL ANALYSIS AND MAGNETIC PROPERTIES OF $La_{0.54}Ho_{0.11}Ca_{0.35}Mn_{1-X}Cr_XMnO_3$ MANGANITES

BY

CARMEN MITA[(1)], NICOLETA CORNEI[(1)], MIHAIL-LIVIU CRAUS[(2, 3)] AND MIHAI LOZOVAN[(2)]

Abstract: We have synthesized by sol-gel method $La_{0.54}Ho_{0.11}Ca_{0.35}Mn_{1-x}Cr_xMnO_3$ magnetoresistive bulk manganites. The samples contain only a perovskite phase, with Pnma orthorhombic structure. The substitution of Mn with Cr leads to the hipsochromic shift of the Mn-O frequencies, due to the decrease of MnO_6 octahedra symmetry. The magnetic properties of electron-doped manganite $La_{0.54}Ho_{0.11}Ca_{0.35}Mn_{1-x}Cr_xMnO_3$ polycrystalline samples have been investigated between 77 and 300K. The metal-insulator transition temperatures decrease from 98 K to 78 K with the increase of Cr concentration.

Keywords: manganites substituted with chrome, FT-IR, magnetic properties, magnetoresistance

1. Introduction

The phenomena of ‘‘colossal’’ magnetoresistance (CMR), observed in doped manganites ($La_{1-x}A_xMnO_3$, A = Ca, Sr, Ba), will likely find technological applications in devices involving magnetic heterostructures [1, 2]. This effect results from the application of a magnetic field driving a phase transition from a paramagnet insulator to a ferromagnetic metal in these manganites. The simultaneous presence of Mn^{4+} and Mn^{3+} ions in these compounds leads to the double exchange mechanism for the Mn^{4+}–O– Mn^{3+} coupling, which can account for the appearance of the ferromagnetism as well as the phase transition [3]. However, several reports have pointed out that the role played by the electron–phonon interaction mediated mainly by the Jahn–Teller distortion around the Mn^{3+} environment should not be neglected [4]. Substitution of La by Ca in antiferromagnetic (AFM) $LaMnO_3$ results in stable $La_{1-x}Ca_xMnO3$ systems, in which ferromagnetic (FM) double exchange: Mn^{3+}–O–Mn^{4+} competes with AFM super exchange: Mn^{3+}–O–Mn^{3+} [5]. In particular, A. Maignan et al. have shown that the CMR effect is maximum in $Sm_{0.2}Ca_{0.8}Mn_{1-y}T_yO_3$, only for T=Cr (y = 0.06) and not for T=Co(y = 0.06) and Ni(y =0.06) [6]. Furthermore, Raveau et al. [7] have found that Cr and Co substitution on the charge-ordered insulator $Pr_{0.5}Ca_{0.5}MnO_3$ can induce a semiconductor-to-metal transition (SMT) in the absence of any applied magnetic field as well as a CMR. Among the 3d-elements, Cr substitution is particularly interesting as Cr^{3+} is isoelectronic with Mn^{4+} and is a non-Jahn–Teller ion. In addition, the nature of the magnetic interaction between Cr^{3+}–O–Mn^{3+} is known to favour ferromagnetism through superexchange interaction. Hence, one might expect to induce a ferromagnetic phase in an otherwise

antiferromagnetic, charge-ordered ground state for the electron-doped manganites depending upon the Mn^{3+}/Mn^{4+} ratio [8, 9].

The purpose of present paper is to study the influence of the substitution of Mn with Cr on the magnetic and crystalline structure of $La_{0.54}Ho_{0.11}Ca_{0.35}Mn_{1-x}Cr_xO_3$ manganites.

2. Experimental procedure

Polycrystalline samples of nominal $La_{0.54}Ho_{0.11}Ca_{0.35}Mn_{1-x}Cr_xO_{3-\delta}$ (x=0.0, 0.05, 0.10, 0.15 and 0.20) composition were prepared by a sol–gel technology. Stoichiometric amounts of La_2O_3, Nd_2O_3 and Ho_2O_3 (purity: 99.99%) $CaCO_3$ (99.5%), $Cr(NO_3)_3 \cdot 9H_2O$ (97%), and $Mn(CH_3COO)_2 \cdot 4H_2O$ (99%) were dissolved in a dilute HNO_3 solution with citric acid used as the chelating agents. The mixed solution was then heated until a dark brown- colored resin material was formed. The resin was subsequently fired at 673 and 1073K in air to decompose the organic residual. The resultant powder was then ground, palletized, and sintered at 1473K for 10 h in air atmosphere. To determine the decomposition temperature of the gel treated at 673 K, few samples were subjected to a thermal analysis (Fig.1). The decompose process takes place in four stages. The loss masse depends by the initial composition of samples: the increase of Cr/Mn ratio determined the increases of conversion degree.

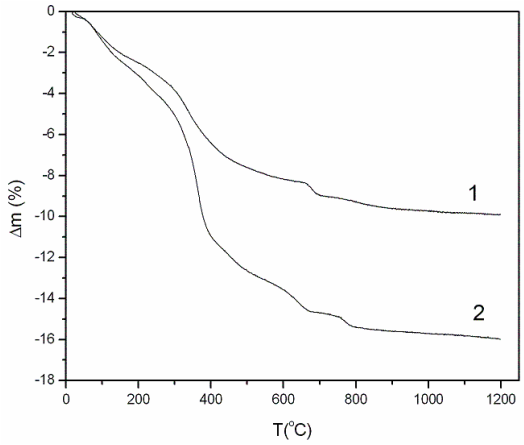

Figure 1. TG for $La_{0.54}Ho_{0.11}Ca_{0.35}Mn_{1-x}Cr_xO_3$ manganites (1-x = 0.0; 2- x = 0.2): sol-gel decomposition

The phase composition, structure, and lattice parameters were determined by powder X-ray diffraction using a diffractometer, equipped with a Cu X-ray tube and a data acquisition system. The precision of the interplanar distances was better as 0.001 Å. The magnetic measurements were performed with a vibrating sample magnetometer between 77 and 600 K. The measuring systems were previewed with a data acquisition system. The infrared (FT-IR) transmission spectrum was collected on powder samples with a JASCO 660 Plus spectrophotometer, in which KBr was used as a carrier. The FT-IR spectrum was taken in the frequency range from 1000 to 300 cm^{-1}. The electronic spectra were determined using a VSU-2P spectrophotometer.

3. Experimental results and discussion

The sintered samples contain only a phase, which have an orthorhombic structure (SG 62 – Pnma) in agreement with the literature [9]. These patterns are indexed to the perovskite structure with the space subgroup Pbnm and do not show the presence of any other phases or precipitates of unreacted oxides. Further analysis by the Rietveld method using the FULLPROF program [10] resulted in lattice parameters of a = 5.5296 Å, b = 7.8559 Å, c = 5.5190 Å (V =239.745Å^3) for the $La_{0.54}Ho_{0.11}Ca_{0.35}MnO_3$ sample (Fig. 2). We expected of a decrease of the volume the unit cell with the increase of the Cr concentration in the sample. On Sudyoadsuk et al. the unit cell parameters should decrease with the increase of the Cr concentration in the samples [9]. The decrease in the unit cell volume with the Cr substitution can be attributed to the presence of Cr^{3+} since the ionic radius of Cr^{3+} (0.755 Å) is smaller than that of Mn^{3+} (0.785 Å) [11].

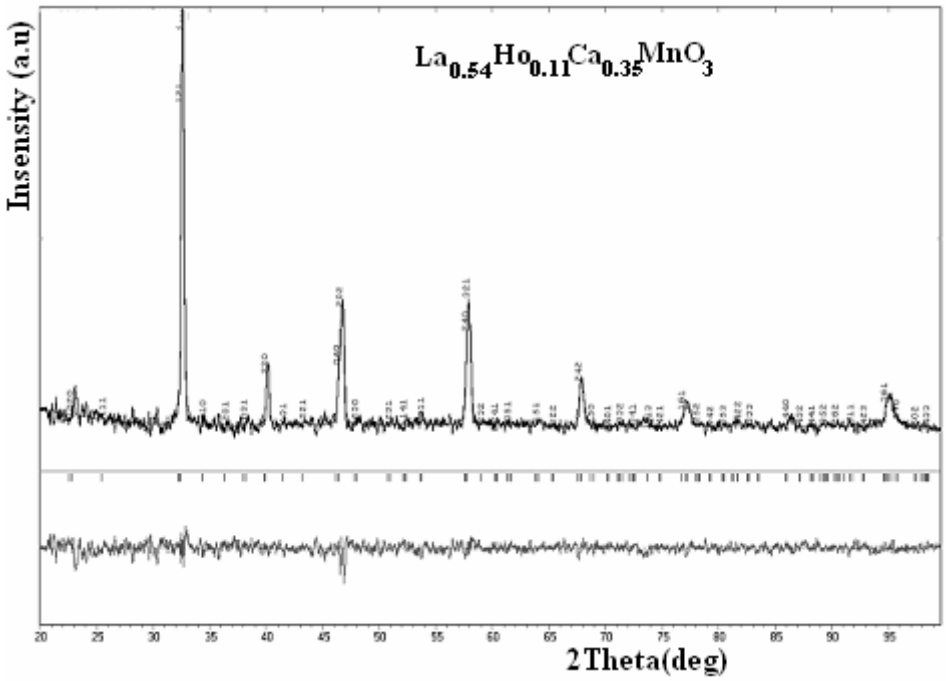

Figure 2. X-ray diffraction spectra of $La_{0.54}Ho_{0.11}Ca_{0.35}MnO_3$. Data points are indicated with solid circles, while the calculated patterns are shown as a continuous line. The positions of the reflections are indicated with the vertical lines below the patterns.

The study of the manganites by FT-IR spectroscopy is determined from the effect of covalent degree of Mn-O bond and of the grain boundaries on the magnetic properties and charge transport. The vibrational spectra of perovskites have been described as the internal vibration of the octahedron containing highly charged and small B ion because of relatively weak A-O bonds [11]. The group analysis predicts that there are two infrared active vibrations modes for the MnO_6 octahedra, regarded as a molecular unity. The absorption peaks around 350 cm^{-1} correspond to the bending mode of O-Mn(Cr)-O and Mn(Cr)-O-Mn(Cr) bonds angle and the other peak around 600 cm^{-1} corresponds to the stretching mode which is sensitive to the Mn(Cr)-O bond

length [12]. The experimental infrared plot of the $Ho_{0.11}La_{0.54}Ca_{0.35}Cr_xMn_{1-x}O_3$ manganites shows the expected main peaks in both regions (Fig. 3).

The symmetry of MnO_6 groups is correlated with the existence of manganese ions into a mixture of two valence states, $Mn^{3+}$and Mn^{4+} and the Jahn-Teller effects (partly related to the average ionic radius and electronegativity of ions on the A sites)

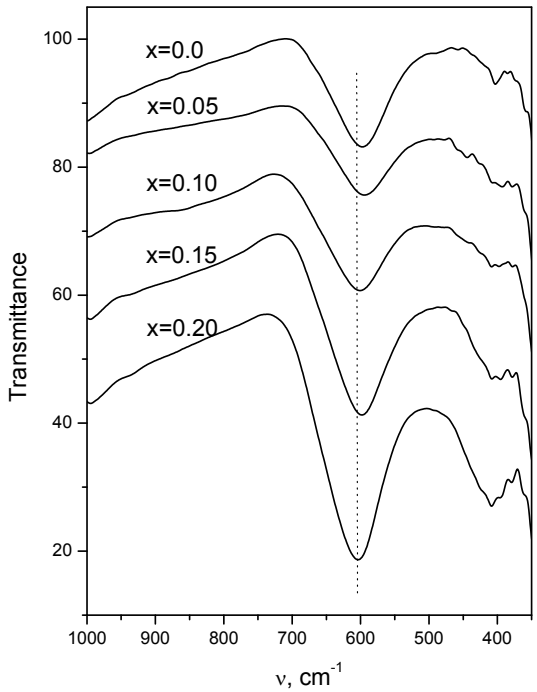

Figure 3. The FT-IR spectra of $La_{0.54}Ho_{0.11}Ca_{0.35}Cr_xMn_{1-x}O_3$ manganites.

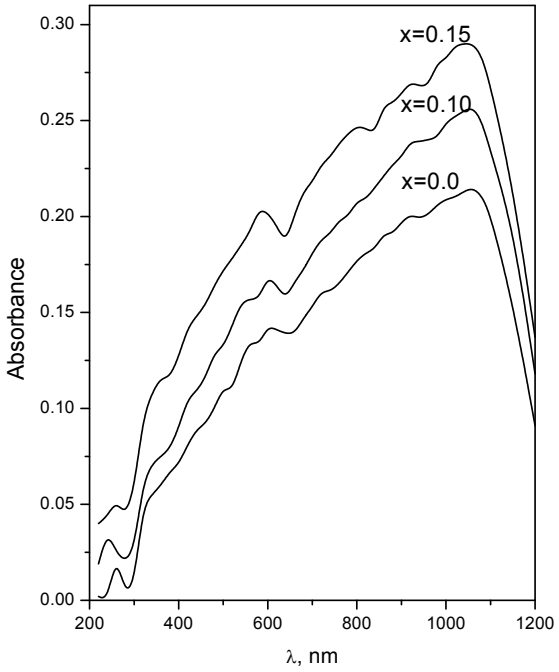

Figure 4. Diffuse reflection spectra of $La_{0.54}Ho_{0.11}Ca_{0.35}Cr_xMn_{1-x}O_3$ samples.

The maximum absorption bands of the stretching mode (ν_1) shift slow to higher frequency and the intensity of peaks increase with the increase of Cr content (Fig. 3 and Tab. 1). This increase may be, partially, ascribed to the size and electronegativity effects of Cr^{3+} ion on B places (Cr^{3+} = 0.755 Å for coordination number = 6) and decrease of local symmetry of crystalline lattice of manganites. This effect of Cr ions is counterbalanced by the increases of polarity of Mn-O bonds which can be determined by the increase of Mn^{4+} concentration and/or the supplementary polarization (dipole moment) due to local distortion of the the lattice near the grain boundary.

Table 1. The FT-IR values of $\Delta\nu_{Mn\text{-}O}$ (cm^{-1}) for the $Ho_{0.11}La_{0.54}Ca_{0.35}Cr_xMn_{1-x}O_3$ perovskites.

Samples	x	ν_1, cm^{-1}	$\Delta\nu_1$, cm^{-1}
$Ho_{0.11}La_{0.54}Ca_{0.35}Cr_xMn_{1-x}O_3$	0	594	201
	0.05	597	194
	0.10	598	198
	0.15	600	218
	0.20	603	219

The presence of Cr atoms into crystalline lattice of manganites determined the increase of peaks symmetry and the range of broad frequencies ($\Delta\nu_{Mn\text{-}O}$) with the

increase of Cr/Mn ratio. These processes are due to the increase of the homogeneity of average grain size and, respectively, to a light increase of crystallites concentration on unit volume.

Diffuse reflectance spectra were measured to know variation of the maximum bands in compounds and the d-d transition energy of Mn^{3+}, Mn^{4+}, Cr^{3+}, respectively, Cr^{4+}. The intensity of band depends on ionicity of bonding in solid. The fundamental term of Mn^{4+} (d^3 configuration) is $^4A_{2g}$, which is associated with minimum 3 d-d electronic transitions. The effect of spin-orbital coupling and the distortion of MnO_6 octahedra lead to the increase of the number of observed electronic transition (bands) into UV and near IR range [13]. The Mn^{4+} cation is associated with a decrease of Jahn-Teller effect and its influences on the splitting of the spectral terms. The Mn^{3+} cation – high spin at room temperature (d^4), in octahedric symmetry, presents an E_g fundamental term and a strong Jahn-Teller effect. For $Mn^{III}O_6$ chromophors were observed minimum two electronic transitions attributed the splitting of $^5T_{2g}$ ($^5B_{2g}$ and ^5E_g) and ^5E_g terms. For the strong distorted octahedra the transition energies of ^5E_g terms are enough high to have values in near IR range. Mn^{3+} ions present maximum 4 d-d electronic transitions.

In general, the hexacoordinated Cr^{3+} (d^3) and Cr^{4+} (d^2) spectra present three transition bands, in the same range of wavelength with Mn^{4+} [13]. The existence of Cr into more oxidation stage, non-equivalence of second coordination sphere and of the crystalline lattice determined the complexity of UV-VIS spectrum of chromium compounds.

The diffuse reflectance spectra of $La_{0.54}Ho_{0.11}Ca_{0.35}Cr_xMn_{1-x}O_3$ ($0 \leq x \leq 0.2$) manganites are shown in Fig. 4.

The $La_{0.54}Ho_{0.11}Ca_{0.35}Cr_xMn_{1-x}O_3$ manganites show between 200 and 300 nm a band attributed to the Ln-O and Ca-O charge transfer (CT_{A-O}). The Mn-O and Cr-O CT transitions should be observed in 300-600 nm, more intense for the Mn-O due to more oxidative character of $Mn^{4+/3+}$ than Ln^{3+} and Cr^{3+}. For these reasons the intensities of VIS and near IR bands are much higher than the d-d pure transitions.

The partial substitution of manganese ions with chromium determines a hipsochromic shift of CT_{A-O} and CT_{B-O} transitions. The increase of CT energy could be explained by the decrease of covalent contribution of A-O and B-O induced to the the increase of oxidized character of ions on the B places (the increase of Mn^{4+} concentration). This is confirmed to the increase of relatively intensities of absorbance values in UV near IR range. The processes is accompanied to the batochromic shift and the supplementary splitting of chromium d-d transition due to the increase of asymmetry contribution of O-Cr-O bond angles (confirmed to the FT-IR spectrum for x=0.2).

The Curie temperature have a minimum with Cr/Mn ratio, except the sample with x=0.2 (Fig. 5 and Tab.2).

The specific/molar magnetization decreases monotonously with the increase of the Cr concentration in the samples (Fig.5 and Tab.2).

To determine the concentration of Mn^{3+}, Mn^{4+}, Cr^{3+} and Cr^{4+} we will suppose that the magnetic moment per molecule is due only to the Mn^{3+} and Mn^{4+} pars and the oxygen concentration corresponds to the nominal chemical formula of the investigated manganites. If the cations distribution on A and B places is:

$$(La_{0.54}^{3+}Ho_{0.11}^{3+}Ca_{0.35}^{2+})_A(Mn_y^{4+}Mn_{1-x-y}^{3+}Cr_{x-z}^{3+}Cr_z^{4+})_B O_3 \quad (1)$$

the concentrations of Mn^{4+} (y) and Cr^{4+}(z) decrease and, respectively, increase with the total Cr concentration in the samples (Tab.2). The concentration of the Mn^{3+} which does not participate to the magnetic moment (1-x-2y) remains practically constant with the increase of Cr concentration (Tab.2). Concerning the molar magnetization variation with Cr concentration, we observed a good agreement with our previous hypotheses.

In the samples coexist more bonds types: Mn^{3+} - O – Mn^{4+}, Mn^{3+} - O- Mn^{3+}, Mn^{3+} - O – Cr^{3+}, Cr^{3+} - O – Cr^{3+}, Cr^{3+} - O – Cr^{4+}, Cr^{4+} - O – Cr^{4+}. Only first type can participate to the magnetic moment of the investigated samples, in agreement with the data of magnetic moment and the chemical composition. A part of the rest of the B cations form antiferromagnetic bonds characterized by a superexchange interaction (Mn^{3+} - O- Mn^{3+}, Cr^{3+} - O – Cr^{3+}, Cr^{4+} - O – Cr^{4+}). Two of these superexchange interactions, type Mn^{3+} - O – Cr^{3+} or Cr^{3+} - O – Cr^{4+}, should lead to the appearance of a net contribution to the total magnetic moment of the samples. A suplimentary contribution could be interpreted as a new magnetic phase, which its own Curie temperature and specific magnetization. This hypothesis is not confirmed by the variation of the specific magnetization/molar magnetization with the temperature.

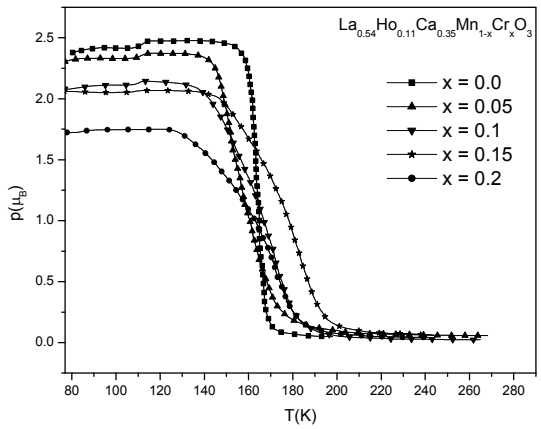

Figure 5 Variation of the specific magnetization vs. temperature and Cr concentration

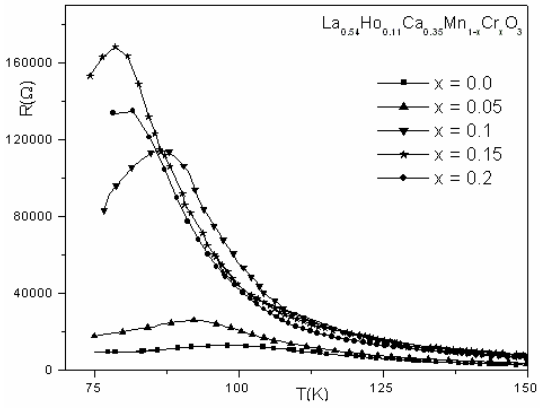

Figure 6. The variation of resistance vs. temperature at H=0 T.

The decrease of the specific/molar magnetization is due the decrease of the Mn^{3+}-O-Mn^{4+} pars, between which a Zener type interaction (double exchange interaction) takes place. The concentration of Mn^{3+} cations, which do not participate to the Mn^{3+}-O-Mn^{4+} bonds (1-x-2y, col.7, Tab.2) have a non-monotonous variation cu Cr concentration.

Preliminary investigations were performed concerning the transport properties. From the curves of variation of resistance with the temperature it was determined the transition temperature from metallic to insulator (semiconductor) temperature(T_{M-I}) (s. Fig.6). The transition temperature decrease with the increase of the Cr concentration in the samples.

In an intermediate range of temperatures the samples behave as pure semiconductors. Supplementary tests for variation of the resistivity with the temperature will be made to establish the nature of the transport mechanisms for other ranges of temperature. A difference appears between the variation of the Curie and transition temperatures with the Cr concentration in the samples.

Table 2 The variation of Curie temperature (T_C), the molar magnetization (p), transition temperature (T_{M-I}), Mn^{4+} and Cr^{4+} concentrations (y, respectively, z) with the chrome concentration (x)

x	T_C (K)	p (μ_B/fu)	T_{M-I} (K)	y	z	1-x-2y
0.00	164	2.48	98.8	0.35	0.0	0.30
0.05	152	2.38	92.0	0.34	0.01	0.27
0.10	172	2.15	86.4	0.31	0.04	0.28
0.15	182	2.07	78.6	0.29	0.06	0.27
0.20	173	1.75	-	0.25	0.10	0.30

The Curie and the transition temperatures have a non-monotonous variation, respectively, a decrease with the Cr concentration in the samples. The transport properties in present samples are due not only Zener mechanism by to the Mn^{3+}-O-Mn^{4+} bonds; it can be influenced by the presence of the crystalline defaults, which determine an increase of the extrinsic component of the magnetoresistance as comparing with the intrinsic magnetoresistance. The extrinsic component of magnetoresistance are determined by the regions with defaults from the crystallites (as boundaries layers), while the intrinsic component are connected with the inner, without defaults, core of the crystallites. The boundaries layers are characterized by a strong deformed Mn-O-Mn bonds, that means an associated Curie temperature lower than the Curie temperature corresponding to the inner core of the crystallite. The resistance of the boundaries layers can be much higher as the resistance due to the crystalline core and depends of the thickness of the boundaries layers. The investigations will be performed to determine the microstrain level with the Cr concentration in the samples, implicitly the correlation between the defaults concentration and the extrinsic component of the magnetoresistance.

4. Conclusions

The $La_{0.54}Ho_{0.11}Ca_{0.35}Mn_{1-x}Cr_xO_3$ orthorhombic manganites were obtained by sol–gel technology.

The presence of Cr cations on the B places induce a supplementary polarisation of Mn-O bonds due to the local distortion of lattice near the grain boundaries and the increase of Mn^{IV} concentration.

The variation of the molar magnetization confirms that the Cr cations do not participate to the magnetic moment of the samples. The samples can be considered as formed by a mixture between two phases: a magnetic phase, due to the double exchange interaction between Mn^{3+} and Mn^{4+} cations (via oxygen anions), and a matrix, where superexchange interactions between Mn^{3+} - O - Mn^{3+} or similar, predominate.

The extrinsic component of the magnetoresistance becomes stronger with the increase of the Cr concentration in the samples.

Received April 3, 2007

(1) "Al.I.Cuza" Technical University Iaşi
(2)National Institute Of Research&Development for Technical Physics Iasi
(3)Joint Institute for Nuclear Research, Dubna, Russia

REFERENCES

1. von Helmolt, R., Wecker, J., Holzapfel, B., Schultz and L., Samwer ,K.- *Gianegative magnetoresistance in perovskite like $La_{2/3}Ba_{1/3}MnO_x$ ferromagnetic films,* **Phys. Rev. Lett**,. **71**, 1993, **2331-2333**
2. Barnabe, A., Maignan, A., Hervieu, M., Damay, F., Martin, C. and Raveau, B. - *Extension of colossal magnetoresistance properties to small A site cations by chromium doping in $Ln_{0.5}Ca_{0.5}MnO_3$ manganites,* **Appl. Phys. Lett., 71**, 1997, **3907-3909**
3. Millis, A.J., Shraiman, B.I. and Mueller, R- *Fermi – liquid to polaron crossover. I. General results,* **Phys. Rev. B 54**, 1996, **5389-5404**
4. Biotteau, G., Hennion, M., Moussa, F., Rodrıguez-Carvajal, J., Pinsard, L., Revcolevschi, A., Mukovskii, Y.M. and Shulyatev, D. - *Approach to the metal-insulator transition in $La_{1-x}Ca_xMnO_3$ (0<~x<~0.2): Magnetic inhomogeneity and spin-wave anomaly*, **Phys. Rev. B 64, 10**, 2001, **104421-104435**
5. Maignan, A., Martin, C. and Raveau, B. – *Cobalt and nickel indiced ferromagnetisms and metallicity in $Co_{1-x}Sm_xMnO_3$ influence upon colossal megnetoresistivite (CMR) properties,* **Mater. Res. Bull., 34**, 1999, **345-354**
6. Raveau, B., Maignan, A. and Martin, C. – *Insulator –metal transition induced by Cr and co doping in $Pr_{0.5}Ca_{0.5}MnO_3$*, **J. Solid State Chem., 130** (1), 1997, **162-166**
7. Shames, A.I., Auslender, M., Rozenberg, E., Gorodetsky, G., Sominski, E., Gedanken, A. and Mukovski, Ya. M. – *Magnetic resonance in crystalline $La_{0.9}Ca_{0.1}MnO_3$. Comparative study of bulk and nanometer – sized samples*, **J. Magnetism and Magnetic Materials**, **300**, 2006, **12–15**
8. Sudyoadsuk, T., Suryanarayanan, R., Winotai, P.and Wenger, L.E. – *Suppression of charge ordering and appearanceof magnetoresistance in a spin-cluster glass manganites,* **J. Magnetism and Magnetic Materials**, **278**, 2004, **96–106**
9. Rodriguez-Carvajal, J.- *Recent advances in magnetic structure determination by neutron powder diffraction,* **Physica B 192,** 1994, **55-69**
10. Huheey, J.E., Keiter, E.A. and Keiter, K.I.- **Chemistry principles of structure and reactivity,** Harper Collins, Coliege Publishers, 1993, **114-117**
11. Nakamoto, K. - **Infrared and Raman Spectra of Inorganic and Coordination Compounds,** Wiley-Interscience, New-York, 1997, **214-220**
12. Petzelt, J., and Ostapchuk, T. - *Infrared and Raman spectroscopy of some ferroelectric perovskite films and ceramics*, **J.Opt.Adv.Mat., 5**, 2003, **725-733**
13. Lever, A. B. P.- **Inorganic Electronic Spectroscopy**, 2nd edition, Elsevier, Amsterdam ,1984, **414-444**

SINTEZA, STRUCTURA LOCALĂ SI PROPRIETAŢILE MAGNETICE ALE MANGANIŢILOR $La_{0.54}Ho_{0.11}Ca_{0.35}Mn_{1-X}Cr_XMnO_3$

Rezumat: Manganiţii magnetorezistivi de tip $La_{0.54}Ho_{0.11}Ca_{0.35}Mn_{1-x}Cr_xMnO_3$ s-au sintetizat prin metoda sol-gel. Probele sunt monofazice, cu structura ortorombica Pnma. Substituirea parţiala a Mn cu Cr duce la deplasarea hipsocroma a frecventei de alungire a legăturii Mn-O, datorată scăderii simetriei octaedrelor MnO_6. Proprietăţile magnetice ale manganiţilor policristalini $La_{0.54}Ho_{0.11}Ca_{0.35}Mn_{1-x}Cr_xMnO_3$ au fost determinate in domeniul 77 – 300 K. Temperaturile de tranziţie metal – izolator scad odata cu creşterea concentraţiei cromului de la 98 K la 78 K

BULETINUL INSTITUTULUI POLITEHNIC DIN IAŞI
Tomul LIII (LVII), Fasc. 1, 2007
Secția
ŞTIINȚA ŞI INGINERIA MATERIALELOR

EVALUATION OF THE RESULTS REGARDING THE MECHANICAL BEHAVIOR OF ADHESIVE JOINTS WITH COMPOSITE MATERIALS

BY

FLORENTINA MOCANU

Abstract: The present paper discusses the results of some investigations, which had in view the establishment the mechanical behaviour of the adhesive joints, with composite supports, made with epoxy and urethane adhesives. The structural response of various configurations of bonded composite joint is analyzed with experimental results.

Keywords: composite substrate, adhesive joints, mechanical behaviour, adhesive strength, epoxy, urethane.

1. Introduction

In the last 30 years many composite materials offer a combination of strength and modulus that either comparable to or better than many traditional metallic materials. The principal advantages of this new class of materials are: low weight and density, noncorroding behavior, moderate cost compared to metallic materials, high internal damping, good durability, high strength and high stiffness to weight ratio. The major structural applications for composite materials are in the field of military and civil aircrafts.

The composite material properties are usually determined by conducting mechanical tests under controlled laboratory conditions. The orthotropic nature of fiber-reinforced composites has led to the development of test methods that are often different from those used for traditional isotropic materials. The standard test methods, which are used for adhesive joints with composite materials, are following:

- tensile test: ASTM D3039-76;
- compressive test: ASTM D3410-87;
- flexural test: ASTM D790-81;
- shear test: ASTM D3518-76;
- interlaminar shear test: ASTM D2344-84;
- fatigue test: ASTM D3479-76;
- impact test: for metallic matrix - ASTM E23-81, for polymeric matrix - ASTM D256-78.

The results of the mechanical tests depend generally on: 1) the adhesive's nature, 2) application mode of adhesive and its cure cycle, 3) the adhesive layer's thickness and polymerisation cycle, 4) the support's material, 5) mode of surfaces' preparation, 6) thickness, mechanical characteristics and length of the supports'

superposing, 7) the geometry of the adherends, 8) the geometry of the joint, 9) the surface pre-treatment.

2. Strength of adhesive joints

Adhesive bonding of composite components is a joining method, which is attractive as an alternative or as a complement to more conventional methods like spot welding, riveting or bolting. Bonded joints use an adhesive interlayer between the supports in the joint region [1,2].

The strength of an adhesive joint depends, however, not only on the strength of the adhesive, but also on the geometry of the joint. This is because the stress distribution in the adhesive depends highly on the geometry of the joint. The maximum strength in achieved if the joint is designed so that the stress distribution in the adhesive is uniform. The performances of the composite adhesive joints depend by the following factors:

- the dimensions of the adherents;
- the non-linear mechanical properties of adhesive and of composite material;
- the thermal properties of the adhesive and adherent;
- the residual thermal stress generated due the coefficient of the thermal expansion difference between the composite adherent and adhesive;
- the environmental temperature at which the adhesive joint is used [3].

In order to design and dimension an adhesive bonded joint for a critical load application it is necessary to have a detailed knowledge of the strength behavior of the joint. Generally adhesive strengths are measured using a single lap-shear test specimen. The most simple strength evaluation method of this test specimen is given by the average shearing stress at fracture. In this case the stress concentrates at the bonding edges and this concentration differs depending on the specimen's shape [4].

For increasing the joint strength the following points are important in designing an adhesive joint: 1) increasing the ratio of lap length to substrate thickness; 2) tapering the substrate ends at the ends of the overlap reduce the high normal stresses at these locations; 3) fiber orientation in the laminate surface layers adjacent to the lap joints should be parallel to the loading direction; 4) equal axial stiffness for the substrates are highly desirable for achieving the maximum joint strength. Since stiffness is product of modulus E and thickness t, it is important to select the proper thickness of each substrate so that $E_1 \cdot t_1 = E_2 \cdot t_2$; 5) the important characteristic of a good adhesive are high shear tensile strengths but low shear and tensile modulus.

3. Experimental results, discussion

The purpose of the current work is to determine the variation mode of the strength of adhesive joints under static loading. The strength is investigated experimentally. On consider that: 1) the thickness of the adhesive layer is constant, 2) the stress are uniformly distributed on the adhesive layer thickness, 3) the adhesive layer thickness is small as compared with the supports, 4) the stress in both the adhesive and supports are uniformly distributed on the joint width, 5) the adhesive is

more flexible than the support material, 6) the adhesive layer is assumed to be isotropic and homogeneous, 7) the adherents of the specimen are deform elastically.

All tests have been developed at normal conditions of the temperature and humidity (23°C±2°C and 50%±5% relativ humidity). The joints used in this study consist of composite material adherents, joined with epoxy and urethane adhesives [5,6,7].

The material properties for all configurations are listed in Table 1.

Table 1. Material properties

Material properties	Substrate	Epoxy adhesive	Urethane adhesive
E_1 [MPa]	$1.82 \cdot 10^7$	$3.2 \cdot 10^5$	$4.5 \cdot 10^5$
E_2 [MPa]	$1.18 \cdot 10^6$	$3.2 \cdot 10^5$	$4.5 \cdot 10^5$
E_3 [MPa]	$1.18 \cdot 10^6$	$3.2 \cdot 10^5$	$4.5 \cdot 10^5$
ν_{12}	0.37	0.38	0.34
ν_{23}	0.3	0.38	0.34
ν_{13}	0.3	0.38	0.34

where:
E - Young's modulus;
ν - Poisson's ratio.

Adhesive shear strength is measured using a single lap-shear test specimen [8]. The supports have 25±0.25mm width and the superposition length is 12.5mm for all joints. For T-peel tests have been realised adhesives samples between the composite supports, joints through simple superposition. Adhesion was estimated from T-peel strength measurements of 150mmx20mm adhesive joints. On used samples with 30mm overlap length. The bond length used fixed at 20mm because the load capability of the adhesive joints satured in the vicinity of this value. The thickness of substrate was 5mm.

Thickness of adhesive layer is one of the significant design parameters for adhesive joints [9]. Adhesive joints between composite adherends with adhesive layer of various thicknesses were employed (adhesive layer between 0.2mm-5mm). The T-peel strength was measured in a test instrument (peel rate =0.1m/min). Variation of the shear and T-peel strengths as a function of thickness of adhesive layer is presented in Table 2. Results represent the average of ten specimens.

Table 2. Influence of thickness of adhesive layer

t	T[kN/m]		τ[MPa]	
[mm]	E	P	E	P
0.2	8.1	5.9	42.3	35.2
0.4	8.9	6.4	43.1	38.6
0.6	8.7	5.5	42.7	37
0.8	8.4	4.9	38.1	28.2
1	7.5	4.2	34.4	24.5
2	6.6	3.4	30	19.7
4	5.9	3.1	21,7	10.5
5	5.1	2.5	9.6	5.2

where:
E – epoxy adhesive;
P – urethane adhesive;
T – peel strength;
τ - breaking resistance to shear;
t - thickness of adhesive layer.

In general failure takes in the adhesive (cohesive failure) rather that between the adhesive and adherent or substrate (adhesive failure). The decrease in the breaking resistance to shear and T-peel strength of the adhesive joints with increasing adhesive layer thickness may be due to the presence of the residual internal stresses or defects in the adhesive bond-line.

The influence of the supports' thickness on the breaking resistance to shear and on T-peel strength has been established [10]. The thickness value of the two supports was selected between 1÷6mm. The thickness of the adhesive layer was 0.4mm for all adhesive joints. The effect of the thickness of supports on the strengths of adhesive joints is illustrated in Table 3.

Table 3. Influence of thickness of supports

s [mm]	T[kN/m]		τ[MPa]	
	E	P	E	P
1	5.1	4.3	27.3	17.5
1.5	5.9	4.9	34.1	22.6
2	6.7	5.3	36.8	27.1
4	7.5	5.8	39.7	33.7
5	8.9	6.4	43.1	38.6
6	8.1	5.9	49.5	40.9

s - thickness of composite supports.

Variation of the shear strength as a function of the superposition length is presented in Table 4 [11,12]. The superposition lengths have been selected between 8÷60 mm (s = 5mm, t = 0.4mm for all joints).

Table 4. Influence of the superposition length

l [mm]	τ[MPa]	
	E	U
8	42.4	37.9
12,5	43.1	38,6
20	39.7	33.8
30	33.1	27.7
40	28.2	23.4
60	17.1	15.5

l - superposition length of single lap-shear test specimen.

Processing of the obtained results permitted to establish establishment the variation mode of the T-peel strength of the adhesive joints with composite supports, made with epoxy and urethane adhesives as a function of peel rate. This influence is shown in Table 5.

Tabelul 5. Influence of peel rate

Peel rate [m/min]	T[kN/m]	
	E	U
0.05	8.2	5.9
0.1	8.9	6.4
0.2	8.6	6.1
0,4	7.7	5.6
0.5	6.8	4.8

4. Conclusions

The strength of the joints with urethane adhesive is always lower than that from epoxy adhesive.

In general failure takes in the adhesive (cohesive failure) rather that between the adhesive and adherent or substrate (adhesive failure).

The shear and T-peel strengths of the adhesive joints with composite materials increases to a maximum at an adhesive layer thickness of about 0.4mm and subsequently decrease. The decrease of these strengths of the adhesive joints with increasing adhesive layer thickness may be due to the presence of the residual internal stresses or defects in the adhesive bond-line.

A considerable influence on the strength of joints realised with epoxy and urethane adhesives is exercised by the support's thickness. With the increase of supports' thickness the whole adhesive layer becomes more actively involved in the load's taking over, while the joint's strength is improved.

For structural applications joints with low superposition lengths are preferred. The joints with relatively high superposition lengths and small thickness values of the supports should be avoided. That is justified firstly if considering the law of tangential stress distribution in the adhesive layer and respectively, the mathematical relation for the calculation of nominal stress. Decrease of the shear strength with the increase of superposition length may be explained, too by the fact that, with the increase of the adhesive amount in a joint, these also increases the possibility that it should contain air bubbles, impurities, generally plans with defects, which form effort concentrators that may weaken the joint's resistance.

The T-peel strength of the adhesive joints with composite substrates decreases with increasing peel rate, independent of the adhesive.

The result of these investigations does provide the strength data on adhesive joints available for engineering design purposes.

Received February 20, 2007 *The "Gh. Asachi" Technical University Iaşi*

REFERENCES

1. Mocanu, F., - **Adezivi, îmbinări adezive***,* Editura Gh. Asachi, Iaşi, 2001, ISBN 973-8292-43-3
2. Lilleheden L., - *Mechanical Properties of Adhesives "in situ" and in Bulk,* **Journal of Adhesion and Adhesives**, no. 13, 2005, **31-37**
3. Mocanu, F., Barsanescu, - *Some Aspects Concerning the Durability of Adhesive Joints,* **Bulletin of Polytechnic Institute of Iasi,** Supliment, Fasc. 3, 2005, **187-192**
4. Adams R. D., Harris J. A., - *The influence of local geometry on the strength of adhesive joints,* **Journal of Adhesion and Adhesives**, no. 2, 2002, **69-80**
5. Luhowiak W., - *L'étude de la résistance au cisaillement d'assemblage des matériaux collés par l'intermediaire d'une résine epoxidique,* **Informations Chemie**, no. 287, 1999, **19-27**
6. Mocanu F., Popa S. C., Bârsănescu P.D., - *The influence of the structure upon the breaking resistance to shear of the adhesive*, **Bulletin of Polytechnic Institute of Iasi,** Fasc. 3-4, Secția V, 1999, **333-337**
7. Mocanu F., - *Considerations on the elaboration of an epoxide adhesive*, **Bulletin of Polytechnic Institute of Iasi**, Fasc 3-4, Secția V, 1999, **107-112**
8. Mocanu F., Curtu I., - *Study of shearing resistance of adhesive joints*, **The Fifth World Conference on Timber Engineering**, Montreux, Switzerland, vol. 1, 1998, **850-851**
9 Mocanu, F., - *Fracture Behaviour in Adhesive Joint with Various Bond Thicknesses,* **Bulletin of Polytechnic Institute of Iasi**, Supliment, Fasc. 3, 2005, **199-202**
10. Kyogoku H., Sugibayashi T., - *Strength Evaluation of Single Lap Joints (Effects of the Adherent Thickness),* **J.S.M.E. International Journal**, vol. 49, no. 307, 1994, **160-167**
11. Mocanu F., Bârsănescu P.D., - *Strength evaluation of single lap joints bonded with an epoxide adhesive*, **The 27th. Israel Conference on Mechanical Engineering**, Haifa, 1998, **623-625**
12. Mocanu, F., - *Some observation on stress state in a simple overlapping adhesive joints,* **Bulletin of Polytechnic Institute of Iasi**, Fasc. 3-4, Secția V, 2003, **63-70**

EVALUAREA REZULTATELOR PRIVIND COMPORTAREA MECANICĂ A ÎMBINĂRILOR ADEZIVE AVÂND SUPORȚI MATERIALE COMPOZITE

Rezumat: Lucrarea prezintă rezultatele unor cercetări care au urmărit stabilirea modului în care se comportă, din punct de vedere mecanic, îmbinările adezive având suporți materiale composite. Pe baza rezultatelor experimentale, s-a stabilit variația rezistenței la forfecare şi la jupuire pentru diferite configurații de îmbinări realizate cu un adeziv epoxidic şi respectiv unul uretanic.

BULETINUL INSTITUTULUI POLITEHNIC DIN IAŞI
Tomul LIII (LVII), Fasc. 1, 2007
Secția
ŞTIINȚA ŞI INGINERIA MATERIALELOR

STRENGTH EVALUATION OF ADHESIVE JOINT WITH COMPOSITE MATERIALS UNDER SHEAR LOADING

BY

FLORENTINA MOCANU

Abstract: The mechanical performances of adhesive joints are closely linked to the stress distribution in the adhesive layer, and then a good understanding of this distribution is essential. The shearing resistance of some samples obtained by single lap joints represents the most widely applied method of testing for adhesive joints. In this paper the influence of the superposition length and the supports' thickness on the breaking resistance has been established.

Keywords: shearing resistance, adhesive strength, single lap joints, geometric parameters, experimental results

1. Mechanics of composite materials

Fiber-reinforced composite materials consist of fibers of high strength and modulus embedded in or bonded to a matrix with distinct interfaces between them. Most fiber-reinforced composites are elastic in their tensile stress-strain characteristics. The heterogeneous nature of the composite materials provides mechanisms for high-energy absorption on a microscopic scale comparable to the yielding process. Depending on the type and severity of external loads, a composite material may exhibit gradual deterioration in properties but usually would not fail a catastrophic manner. Coefficients of thermal expansion of many composite materials are much lower than those for metals. As a result, composite structures may exhibit a better dimensional stability over a wide temperature range. However, the differences in thermal expansion between metals and composite materials may create undue thermal stresses when are used in joint.

Due to its superior properties composites have been one of the materials used for applications in many different engineering sectors. However, a major drawback which limits the utilization of their full capabilities in the accumulation of residual stresses within the layers of the composite during the cure process at high temperatures. These residual stresses arise from the differential thermal expansion between layers oriented at different angles within the laminate and can be high as sixty percent of the material's transverse strength [1].

The mechanics of composite materials are far more complex than that of conventional materials and are studied at two levels: micromechanics and macromechanics.

In the micromechanics levels the interaction of the constituent materials is examined on a microscopic scale. Equations describing the elastic and thermal characteristic of a lamina are based on micromechanics formulations. For example the micromechanical behavior of fiber-matrix interactions in a unidirectional lamina is studied in following assumptions:

- fibers are uniformly distributed throughout the matrix;
- perfect bonding exists between fibers and matrix;
- the matrix is free of voids;
- applied loads are either parallel to or normal to the fiber direction;
- no residual stresses are present in the lamina;
- both fibers and matrix behave as linearly elastic materials [2].

In the macromechanics level the response of a composite material to mechanical and thermal loads is examined on a macroscopic scale. The composite material is assumed to be homogeneous and equations of orthotropic elasticity are used to calculate stresses, strains and deflections. In the macromechanics level the performance of a composite material is judged by its properties and behavior under tensile, compressive, shear and other static or dynamic loading conditions in both normal and adverse test environments. This information is essential for selecting the proper material for an application as well as designing a structure with the selected composite material [1, 2].

2. Adhesive joints

The therm adhesion is used when referring to the attraction between substrates. The level of adhesion forces, which are operating across an interface, cannot usually be measured by mechanical tests. The science of technology of adhesion and adhesives are multidisciplined subjected: surface chemists, polymers chemists, physicists, materials engineering, and mechanical engineering.

Because of their weight penalty and their unavoidable stress concentration, bolted and riveted joints are advantageously replaced by adhesive bonded joints. The principal attribute of adhesive is their ability to form strong bonds with surfaces of a wide range of materials and to retain bond strength under expected use conditions.

Several test techniques for assessing the mechanical performance of adhesive joints under uniaxial tension, tensile-shear, compressive-shear loading have been specified. For determine adhesive strength are commonly used the guidelines published by the American Society for Testing and Materials (ASTM) [3].

Extensive studies have been devoted to the stress analysis of adhesively bonded joints, both analytically and numerically, forming the basis for design and durability assessment of joints [4]. In order to design and dimension a composite/composite adhesive bonded joint for a critical load application it is necessary to have a detailed knowledge of the strength behaviour of the joint [5].

The results of the shearing tests, to which the adhesive joints with composite supports, joints obtained by single lap, represents the most widely applied method of testing for adhesive joints [6].

The present paper discusses the results of some investigations which had in view the establishment the variation mode of the adhesive strength as a function of the substrate' thickness for various superposition lengths.

3. Experimental results

Generally adhesive strengths are measured using a single lap-shear test specimen as shown in Fig. 1. The single lap joint is most commonly used for assessing the shear strength of adhesive-bonded joints in practice because of its simplicity. The most simple strength evaluation method of this test specimen is given by the average shearing stress at fracture. In this case the stress concentrates at the bonding edges and this concentration differs depending on the specimen's shape. Thus, this strength evaluation method cannot be applied to other shape adhesive structures. In this paper on confirm the adhesive strength of single -lap joints with various lap lengths and substrate thickness can be jointly expressed [7,8].

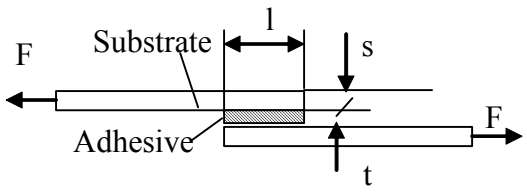

l - lap length;
t - adhesive layer thickness;
s - substrate thickness.

Fig. 1. Schematic shape and dimension parameters of adhesive single-lap joints.

A urethane adhesive is chosen in this study. The supports have 25±0.25mm width and for all joints, the superposition lengths have been selected between 8÷40 mm. The thickness values of the two supports are 0.8mm, 1.6mm, 2mm and 4mm. respectively. All tests have been developed at a temperature of (22 ±3)°C.

Variation of the shear strength as a function of the superposition length, for the four values of the thickness is presented in Fig. 2.

The variation curves indicate pronounced decrease of strength of the joint at higher superposition lengths. That can be justified firstly if considering the law of tangential stress distribution in the adhesive layer and respectively, the mathematical relation for the calculation of nominal stress. On the other hand, decrease of the breaking stress with the increase of superposition length may be explained, too by the fact that, with the increase of the adhesive amount in a joint, these also increases the possibility that it should contain air bubbles, impurities, generally plans with defects, which form effort concentrators that may weaken the joint's resistance [9].

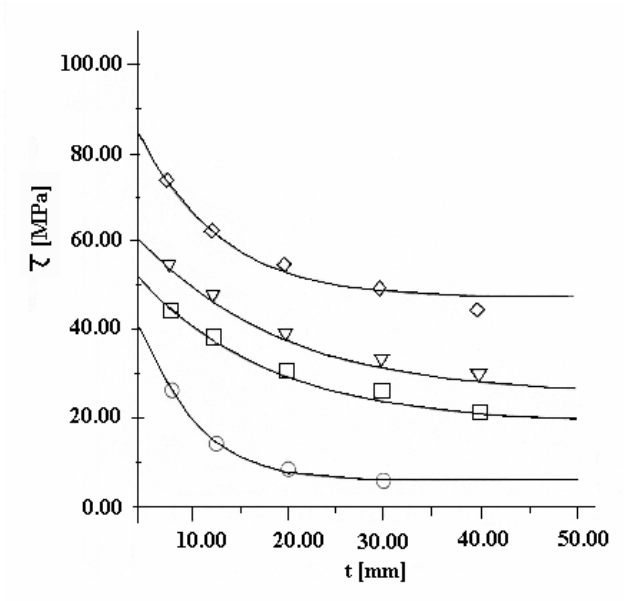

Fig. 2 Influence of the superposition length and of the support' thickness.

Influence of the superposition length on the shear strength of the urethane adhesive under study, for superposition lengths of the joints ranging between 5÷40mm is expressed through the following exponential variation law:

$$\tau = a \bullet exp(-b \bullet l) + c \quad (1)$$

Further on, the functional dependence $\tau = f(l, s)$ was established. The procedure applied was the following:

- establishment of the variation of coefficient ***a*** from equation (1) as a function of the support's thickness:

$$a = 15.2\, s^2 - 55.8\, s + 147 \quad (2)$$

- establishment of the variation of coefficient ***b*** from equation (1), as a function of s:

$$b = 0.0679\, s^2 - 0.293 s + 0.681 \quad (3)$$

- establishment of the variation of free term ***c*** as a function of the same variable:

$$c = 14.9 s - 7.13 \quad (4)$$

By means of an original program the three variation laws resulted for the three coefficients in equation (1) have been introduced and thus the surface representing the variation of shear strength was obtained as a function of the superposition length and thickness of the two supports (see Fig. 3).

The following relation gives such variation:

$$\tau = (15.2 \cdot s^2 - 55.8 \cdot s + 147) \cdot exp(-0.0679 \cdot s^2 + 0.293\, s - 0.681) \cdot l + 14.9 \cdot s - 7.13 \quad (5)$$

The relation (5) may be easily applied for fracture load prediction of some adhesive joints, in the concrete situation taken into consideration. The estimated results of the adhesive joint strengths using the maximum stress can express the experimental results concerning the influence of lap length and substrate thickness on adhesive joint strength [10].

The values listed in Table 1 indicate small differences between the values calculated with relation (5) and those established as a result of tests, which confirms the relation's precision.

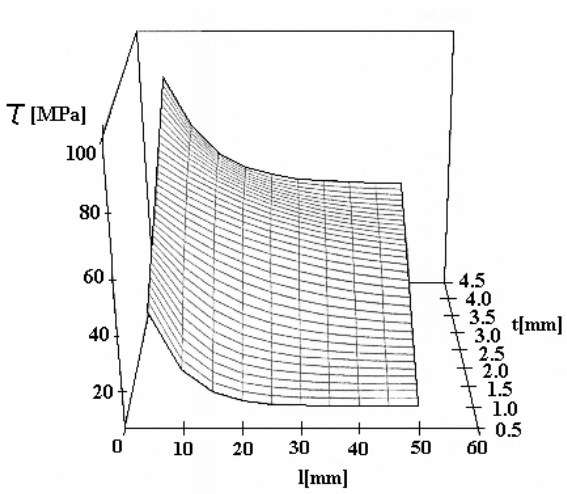

Fig. 3 Variation $\tau = f(l, s)$.

Table 1 Values calculated and the experimental results

l [mm]	Shear strength [MPa]							
	s=0.8mm		s=1.6mm		s=2mm		s=4mm	
	exp.	calc.	exp.	calc.	exp.	calc.	exp.	calc
8	20.5	21.1	34.5	34.8	39.8	40.2	47.9	48.5
12.5	14.9	15.2	28	28.3	30.6	31	36.6	36.9
20	10.6	11.3	18.8	19.5	26	26.8	32.4	31.8
30	4.8	5	15.9	16.4	22.8	23	28.7	28.9
40	-	-	10.1	10.8	17.5	18.1	23.8	24

4. Conclusions

The following conclusions were obtained:

A considerable influence on the strength of joints realised with adhesives is exercised by the support's thickness.

With the increase of supports' thickness the whole adhesive layer becomes more actively involved in the load's taking over, while the joint's strength is improved.

The estimated results show that the shearing strength increases in accordance with the increase of substrate thickness.

The shearing strength of single-lap joints decreases when the lap length increases to more than the substrate thickness.

For structural applications joints with low superposition lengths are preferred.

The estimated results coincide well with the experimental results.

Received February 20, 2007 *The "Gh. Asachi" Technical University Iaşi*

REFERENCES

1. Kelley A., Rabotnov Y.N., - **Handbook of Composites,** vol. 3, Elsevier, 1985
2. Sih G.C., Skudra A.M., - **Handbook of Composites**, *Failure Mechanics of Composites,* vol. 3, North-Holland, Amsterdam, 1985

3. Mocanu, F., - **Adezivi, îmbinări adezive***,* Editura Gh. Asachi, Iaşi, 2001, ISBN 973-8292-43-3
4. Mocanu, F., Barsanescu, - *Some Aspects Concerning the Durability of Adhesive Joints,* **Bulletin of Polytechnic Institute of Iasi,** Supliment, Fasc. 3, 2005, **187-192**
5. Lilleheden L., - *Mechanical Properties of Adhesives "in situ" and in Bulk,* **Journal of Adhesion and Adhesives**, no. 13, 2005, **31-37**
6. Adams R. D., Harris J. A., - *The influence of local geometry on the strength of adhesive joints,* **Journal of Adhesion and Adhesives**, no. 2, 2002, **69-80**
7. Mocanu F., Curtu I., - *Study of shearing resistance of adhesive joints*, **The Fifth World Conference on Timber Engineering**, Montreux, Switzerland, vol. 1, 1998, **850-851**
8 Mocanu, F., - *Fracture Behaviour in Adhesive Joint with Various Bond Thicknesses,* **Bulletin of Polytechnic Institute of Iasi**, Supliment, Fasc. 3, 2005, **199-202**
9. Mocanu, F., - *Some observation on stress state in a simple overlapping adhesive joints,* **Bulletin of Polytechnic Institute of Iasi**, Fasc. 3-4, Secția V, 2003, **63-70**
10. Bigwood D. A., Crocombe A. D., - *Elastic analyses and engineering design formulae for bonded joints*, **Journal of Adhesion and Adhesives**, no. 4, 1997, **229÷242**.

EVALUAREA REZISTENȚEI LA FORFECARE A ÎMBINĂRILOR ADEZIVE AVÂND SUPORȚI MATERIALE COMPOZITE

Rezumat: Performanțele mecanice ale îmbinărilor adezive sunt strâns legate de repartiția tensiunilor în stratul de adeziv. Ca urmare, cunoaşterea şi interpretarea corespunzătoare a acestei repartiții sunt esențiale. Încercarea la forfecare a îmbinărilor adezive realizate prin simplă suprapunere reprezintă cea mai folosită metodă de caracterizare a acestui tip de îmbinare. În această lucrare se prezintă rezultatele unor studii privind influența lungimii de suprapunere a suporților şi a grosimii acestora asupra rezistenței de rupere la forfecare.

BULETINUL INSTITUTULUI POLITEHNIC DIN IAŞI
Tomul LIII (LVII), Fasc. 1, 2007
Secția
ŞTIINȚA ŞI INGINERIA MATERIALELOR

STUDY OF COMPOSITE MATERIAL FOR HARDFACING TO COUNTERACT THE TOOLING DAMAGE

BY

PETRA MOTOIU[(1)], CORNELIU MUNTEANU[(2)] DANIELA VIOLETA DUMITRESCU[(1)], GABRIELA POPESCU[(3)] and HORIA BINCHICIU[(4)]

Abstract: The paper deals with the methods of wear prevention and/or repairing of tools and dies employed for many and different manufacturing processes: rolling mills, forging dies and punches, dies for die casting processes, dies for plastic injection moulding. The continuous increase of the applications of thermal sprayed coatings together with the demand for layers having always more and more enhanced performances and properties stimulates the research activity toward the development of new coating materials and alloys. To meet this goal, new complex alloys, based on the Fe, Si, B, Mo, Cu, W system, are here considered, through the development of new and innovative powders to be used, as powders directly or as a wire form, for thermal sprayed coatings to improve wear and corrosion resistance, as well as thermal fatigue properties of the coated parts, highlighting the materials performances and attaining economical and environmental advantages.

Keywords: composite, tubular electrodes, thermal sprayed coatings

1. Introduction

Abrasion fatigue is a degradation phenomenon of the friction surfaces, usually encountered in machines' and gears' functioning; it's a mechanical process which consists in softer surfaces wear by tougher particles, which may accidentally occur between two metallic surfaces in contact with hard mineral materials, [1].

Abrasion may occur through micro splintering by the sharpened parts of the hard particle or asperities, but also by plastic deformation. The volume of worn material obtained in such situations differs by 10 ÷ 20 % and depends on different factors. So, if the ratio between the roughness of a metal, H_m and that of a rougher, H_a has the value $H_m/H_a = 0.8 \div 1.3$ the rougher diminishes its cutting power; if the form is sharp, splinting prevails; if the abrasive particles roll between the surfaces, the wear is reduced compared to sliding. Situations like these happen especially to some agricultural machine organs, construction gear, diving strip gear, etc.

There are situations when abrasion happens on tough particles impact, for example foundry, throwing paddles and sand transporters, which is dried abrasive erosion. Similar cases, action with kinetic energy towards a surface in abrasive medium, happen to break up gear (eg. jaw crusher, hammer mill).

Advantages in using tubular electrodes for hardfacing abrasion surfaces

The main advantages of tubular electrodes consist in their constructive draft: tubular rod made out of steel belt/strap field with powdered core, which contains allied elements and graphitic or graphitic-basic layer, applied through immersion, [2]. The most important advantages of the tubular electrodes compared to conventional

electrodes are presented below:

- simpler and cheaper feasible technology;
- proxy; 1/3 welding/loading currents;
- reduced distortions of the machine parts;
- allow thin layers deposits;
- no burns through piercing of the thin parts;
- very small amounts of slag;
- bigger deposit yields;
- reduced losses in fabrication and using;
- easy use and accessibility, SMEs.

2. Experiments

Raw matters and materials

Raw matters are used under powder form and the sodium silicate under liquid form. Wolfram carbon is provided in granulation classes from 0.07 to 3.0 mm. For ferrous alloys (FeMn, FeCr etc) which are provided as balls, they are grinded and sieved under 0.3 mm, [3].

To obtain the tubes, cold laminated steel belt/strap made in Romania was used.

The dimensions of the steel belt/strap, used to obtain tubular electrodes, are presented below in *Table 1*.

Table 1. The dimensions of the steel belt/strap

Electrode's Diameter, [mm]	Breadth, [mm]	Thickness, [mm]
4.8 (5.0)	15	0.4
6.4 (6.0)	20	0.5

The chemical composition and the mechanical characteristics of the cold laminated steel belt/strap used to obtain tubular electrodes are presented below in *Table 2*.

Table 2. The chemical composition and the mechanical characteristics of the cold laminated steel belt/strap

Chemical Composition, [%]						Mechanical Characteristics			Type
C	Mn	Si	P	S	Al	R_m [N/mm²]	$R_{p0,2}$ [N/mm²]	A_{80} [%]	A3K04M SF 558/96
0.08	0.45	0.03	0.023	0.01	0.05	329	237	37.2	15 mm x 0.5 mm
0.05	0.29	0.02	0.015	0.019	0.04	322	202.5	40,3	20 mm x 0.5 mm

Wolfram carbon used to obtain different tubular electrodes has the following technical characteristics presented in *Table 3*.

Table 3. The technical characteristics of the wolfram carbon

Chemical Composition, [%]				Granulation, [mm]			Hardness
C_{free}	C_{total}	other	W				
max. 0.08	3.9	0.25	rest	< 0.05	0.5 ÷ 1.0	1.0 ÷ 2.0	1800 ÷ 2000 $HV_{0.05}$

The elaboration of the core recipes

In order to elaborate the core recipes, different allying levels for the two types of alloys which will form the tubular electrodes, were taken into consideration.

For the Wolfram Carbon electrodes, 4 different WC concentrations were elaborated: 40 %; 50 %; 55 % and 60 %WC, [4].

For Mn – austenitic tubular electrodes, 3 core variations were used.

One's component (element) concentration calculus, from the powder core, was made with the next formula:

$$C_{elem.core} = \frac{C_{elem.MD} + (1 \quad K_f) C_{elem.rod}}{K_f} \tag{1}$$

where: $C_{elem.core}$ – element's concentration, in the powder core [%]

$C_{elem.MD}$ - element's concentration, in the pure deposited metal [%]

$C_{elem.\ rod}$ - element's concentration, in the tubular rod [%]

K_f – filling coefficient

In the case of tubular electrodes, based on Wolfram Carbon, a 40 ÷ 70 % filling coefficient (function of particles granulation and rod's diameter) was taken into account.

In the case of manganese – austenitic tubular electrodes, a 55 % filling coefficient was taken into account for a 4.8 mm rod's diameter.

The compounds introduced into the powder core and their dosage limits are presented in *Table 4*.

Table 4. The compounds introduced into the powder core and their dosage limits

Nr. crt.	Component in the powder core	Dosage Limits, [%]	
		WC alloy	Mn-Ni alloy
1	Wolfram Carbon	70 ÷ 100	-
2	Ferrochrome	0 ÷ 5	2 ÷10
3	Metallic Chrome	-	0 ÷ 3
4	Metallic Nickel	0 ÷ 5	6 ÷ 12
5	Loose Ferromanganese	-	25 ÷ 50
6	Metallic Iron	0 ÷ 30	10 ÷ 50

K_f – the filling coefficient represents the ratio between the powder core mass and the tubular electrode mass. The values were obtained both through documentation and our own research and experimentation. Thus, it has resulted that, for the tubular electrodes, based on Wolfram Carbon, the K_f coefficients varied from 40 to 70 %, function of the rod's diameter and the WC granulation.

For the Mn-Ni type austenitic tubular electrodes with a larger diameter than 4 mm, the K_f coefficient has to be more than 55 %; a smaller K_f does not insure the

requested alloy level. The morphological study of the powder particles was accomplished with a Citoval type stereo-microscope, produced by Carl Zeiss Jena ltd, [5].

The metallographic determinations dwell on solidification structures' study, referring to both the particles' shape and dimensions, as to the quantitative determinations regarding the distribution of the crystalline grains of a certain phase.

The powder is formed of frosted particles (*Figure 1*), their shape varying from angular to irregular - polygonal. The particles have an apparent bi-phased structure, being formed out of rough grains of WC and a softer Co or W matrix.

In *Figure 2*, one can notice that the powder particles have spherical form. From time to time, particle dispersing appear due to atomization specific phenomena through the method of the two fluids, [6].

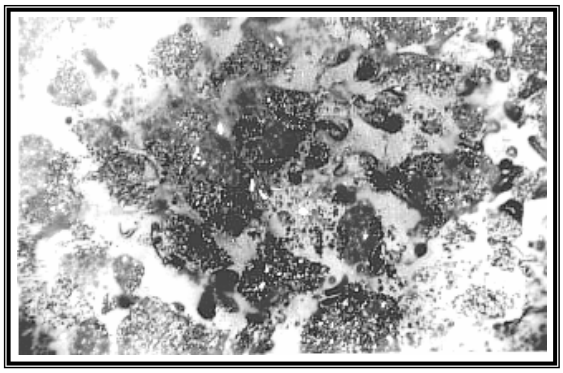

Fig.1 Alloy powder based on WC x 250

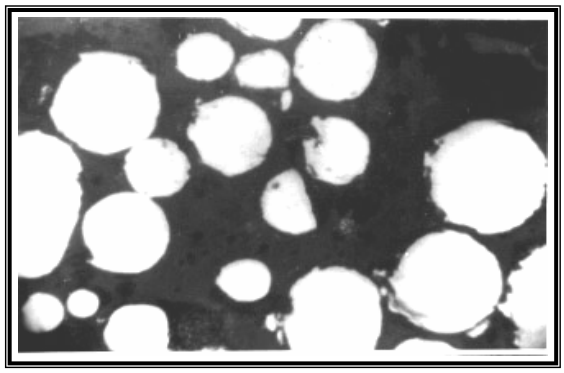

Fig.2 Mn – Ni type powder

The elaboration of the layer recipes

The research on reference electrodes underlined, that the most used tubular electrodes layers are the graphite type, basic or semi-basic. The graphite type layer insures a good protection for the electric arch, stability, easy kindling and very small amounts of slag, which are easily removed. The basic layers insure high purity metals, low content of non-metal inclusions and reduced tendency to crack.

The elaboration of the layer recipes pursued obtaining layers, which insure a good protection for the electric arch, a good welding behavior under loading manganese-austenitic steels, which are hard to weld.

In order to obtain an electrode with superior metallurgical and welding behavior characteristics, the layer must have a basic or semi-basic character, which provides a higher purity to the deposited metal, respectively low nonmetallic inclusions content.

To determine the layers' basicity, the Boniszewski basicity formula was used, as it contains all layer components effects:

$$BB = \frac{\%CaO + \%MgO + \%BaO + \%Na_2O + \%K_2O + \%CaF_2 + \%1/2(\%MnO + \%FeO)}{\%SiO_2 + 1/2(\%Al_2O_3 + \%TiO_2 + \%ZrO_2)} \quad (2)$$

In this basicity formula, the numerator is the sum (in %) of the acidic oxides and the denominator is the sum (in %) of the basic oxides, which form the layer.

The value of the BB ratio, calculated with this formula, defines the character of the layer as follows:

- acidic layer, for BB<1;
- basic layer, for BB =1÷ 1.5;

- semi-basic layer, for BB =1.5 ÷ 2.5;
- strong basic layer, for BB >2.5.

For tubular electrodes, interesting are the basic and semi-basic layers, [7] which have the following properties:

- provide suitable arch protection due to the substances that are introduced into the layer and produce gases, like: marble and calcium carbonate;
- eliminate possible nonmetallic inclusions appearance into the deposited metal, dew to small amounts of silica dioxide, introduced into the layer;
- enable a high transfer coefficient for the allied elements.

Besides these properties, the basic layers insure a low solidification time and a viscous increase during cooling process, in comparison with other types of layers. Also, these layers are recommended for high Carbon content steels welding, frequently met in loadings.

Based on the study of the slag systems, in order to elaborate layer recipes for the electrode coating, there were chosen two slag systems: CaO-BaO-CaF_2 (basic) and CaO-CaF_2-TiO_2 (semi-basic).

For the tubular electrodes based on WC, there were manufactured coating recipes with graphite-semi-basic, which insure a good welding behavior, considering their use in alternative current too, [8]. For the manganese-austenitic electrodes (Mn-Ni type), there were made basic coating recipes, which insure a higher purity for the deposited metal.

This is an important fact, because they are supposed to be used as buffer layers.

The structure of the coating recipes and the powder components of the electrodes are presented in *Table 5*.

Table 5. Layer Option for Layer Component

Nr. crt.	Layer Component	Layer Option, %	
		Basic (B)	Semi basic-graphitic (G)
1	Marble	20 ÷ 50	15 ÷ 35
2	Fluorine	20 ÷ 50	20 ÷ 40
3	Barium Carbonate	15 ÷ 20	0 ÷ 10
4	Strontium Carbonate	5 ÷ 10	5 ÷10
5	Feldspar	0 ÷ 10	0 ÷ 5
6	Aluminum Fluoride	0 ÷ 12	0 ÷ 5
7	Ruthile	0 ÷ 5	30 ÷ 50
8	Mica	0 ÷ 3	0 ÷ 3
9	Graphite	-	2 ÷10
10	Aluminum	0 ÷ 3	0 ÷ 3
11	Sodium silica (liquid)	10 ÷ 20	10 ÷ 20

Based on these recipes structure three options have been elaborated for each type of the layer: B1, B2, B3 and G1, G2, G3 respective.

Prime matters preparing and dosage

For tubular rods and electrodes based on WC, there was used carbide with grain size between 0.2 ÷ 2.0 mm, rallied into granular classes: 0.2 ÷ 0.5 mm; 0.5 ÷ 1.0 mm

and 1.0 ÷ 2.0 mm.

The powder raw matters used to obtain the core for the manganese-austenitic electrodes had the grain size of max. 0.3 mm. To obtain the layers, the powder prime matters had a grain size of max. 0.2 mm. The component dosage was made by hand in 2 kg lab batches, complying with the recipes for the powder core and layer. The weighing was made with technical scale (precision ± 5g).

Homogenizing core and layer mixtures process

The dried homogenizing process of the dosed prime matters takes place in porcelain mills with balls. In order to obtain homogenous mixtures, a pre-homogenizing process has been introduced. The process is mandatory because of the great differences in the specific weights of the prime matters, [9].

The specific weight of the powder core (γ) is given by the sum of the percentage contributions of each component:

$$\gamma = \sum a_i \times \gamma_i \tag{3}$$

where: a_i – recipes components' contents (%);

γ_i – recipes components' specific weights [g/cm³].

In *Table 6* are presented the specific weights of some powder prime matters, currently used to obtain welding and loading materials:

Table 6. The specific weights of some powder prime matters, currently used

Nr crt.	Prime Matter Powder	Specific Weight [g/cm³]
1	Wolfram Carbon	11÷16.7
2	Marble	2.70
3	Fluorine	1.70
4	Barium Carbonate	3.82
5	Ferromanganese	6.51
6	Ferrochrome	6.80
7	Ferrovanadium	6.62
8	Metallic Chrome	8.50
9	Metallic Nickel	8.56
10	Metallic Iron	7.11
11	Graphite	1.65

For the variants of elaborated electrodes, there were obtained specific weights of the powder mixtures as it follows:

- WC core: 11 ÷ 14 [g/cm³];
- powder core: 6.6 ÷ 7.0 [g/cm³];
- layer: 2.0 ÷ 2.6 [g/cm³].

These obtained values are specific to the tubular electrodes for allying loading through core and with thin layers applied through immersion.

Grouping prime matters by close specific weights and introducing the pre-homogenizing process, decreases the danger of non-homogenous mixtures appearance, dew to the segregation phenomena.

The tube forming, filling and cutting

In order to obtain the tubes, a strap of cold laminated steel A3K04M type with

15 mm x 0.5 mm and 20 mm x 0.5 mm has been used; the obtained tubular rods had 4.8 mm and 6.4 mm diameter.

The rods filling was made with a band batcher, thus allowing the simultaneously filling/dosage of two core mixtures with quite different granulation classes.

The batcher's band is activated by a continuous current engine (Fronius type) and allows to continuously regulating the band's speed, thus the filling flow. Also the thickness of the mixture layer may be taken by the band and may be regulated.

The obtained average coefficients were 40 %, 52 %, 60 % and 69 % for the WC rods. For the tubular rods with a core mixture of Mn-Ni type, the obtained average coefficients were between 56 ÷ 60 %. The tube cutting into rods at a 350 ± 5 mm length was made with a knife gear assembled on a pair of rolls.

3. Conclusions

The accomplished experiments and research led to new loading materials as tubular electrodes, whose main characteristics are compatible to the usual loading materials;

The new loading materials fit into the category of high-performance materials, which are mainly used to protect against the two most known types of wear: severe abrasion wear and abrasion wear combined with strong impact;

Types of loading alloys were elaborated: alloys based on WC for the severe abrasion wear and alloys based on austenitic-manganese steel for abrasion and strong impact;

The accomplished experiments and research led to obtain a new alloying system: 40 ÷ 70 % WC + Iron based matrix and the max. 1.2 %C, 11 ÷ 15 % Mn and 2 ÷ 5 % Ni one;

Slagging systems were studied, researched and elaborated:

- CaO-CaF2-TiO_2 for WC type electrodes and
- CaO-BaO-CaF_2 for austenitic-manganese type electrodes;

Based on the allying and slagging systems, recipes for the core and layer were elaborated.

Received April 20, 2007

(1) R&D Institute for Nonferrous and Rare Metals, 102 Blvd. Biruinței, Bucharest – Romania
(2) Technical University "Gh. Asachi" Iasi, Faculty of Materials Science and Engineering
(3) University "POLITEHNICA" of Bucharest, Materials Science and Engineering Faculty, 313 Splaiul Independentei, Bucharest – Romania
(4) SC SUDOTIM AS SRL, 30 M.Viteazul, Timisoara – Romania

REFERENCES

[1] Metal Handbook-Powder Systems and Applications (p.569)
[2] Ronald W. Smith, Advances and Applications in US Thermal Spray Technology (II The Market and R&D), p. m. i, vol 23, nr. 4, 1991,(pp. 231)

[3] N. J. Grant, Powder and particulate production of metallic alloys- -Dep. of Materials Science and Engineering Massachusetts Institute of Technology Cambridge
[4] Metals Handbook, Ninth Edition, vol. 7, Powder Metallurgy-American Society for Metals-Ohio,-1984.(pp. 25-51)
[5] J. K. Beddow, The Production of Metals Powders by Atomization, Heiden, London, 1978
[6] K. M. Kulkarni, IBID 10 (pp. 142). Production of Nickel Alloy Powders by Atomization-
[7] K.M.Kulkarni, IBID 10 (pp. 824). Metal Powders Used for Hardfacing
[8] IBID 10 (pp. 827) Carbides
[9] S.W.H.Yih, Tungsten-; Plenum Press; 1981-Tungsten Carbides and the Hard Industry, (pp. 386).

STUDIUL MATERIALELOR COMPOZITE PENTRU DURIFICAREA SUPRAFETELOR ÎN SCOPUL CONTRACARĂRII DETERIORĂRII ELEMENTELOR ACTIVE ALE UTILAJELOR

Rezumat: Lucrarea se ocupă de metodele pentru prevenirea uzurii şi/sau repararea elementelor active şi a poansoanelor utilizate în procesele de prelucrare: bile de moară, matrițe de forjare, perforatoare, forme de turnare, matrițe pentru pulverizarea materialelor plastice prin injecție. Creşterea continuă a aplicațiilor pentru acoperiri termice împreună cu creşterea continuă a cererii de straturi cu proprietăți şi performanțe îmbunătățite continuu, stimuleaza activitatea de cercetare în direcția dezvoltării de noi materiale şi aliaje de acoperire. Pentru realizarea acestui deziderat, au fost luate în considerare aici noi aliaje complexe bazate pe sisteme cu Fe, Si, B, Mo, Cu, W, prin intermediul dezvoltării unor noi şi inovative pulberi, utilizate ca atare sau sub formă de electrod pentru acoperiri termice în scopul îmbunătățirii rezistenței la uzură şi coroziune ca şi a creşterii proprietăților de rezistență la oboseala termică a subansamblelor acoperite, punând în evidență performanțele materialelor şi avantajele economice şi de mediu.

BULETINUL INSTITUTULUI POLITEHNIC DIN IAŞI
Tomul LIII (LVII), Fasc. 1, 2007
Secția
ŞTIINȚA ŞI INGINERIA MATERIALELOR

EVALUATION OF THE DYNAMIC PARAMETERS OF THE FLEXIBLE CAM-FOLLOWER SYSTEMS

BY

CEZAR OPRISAN and ELENA DRAGAN

Abstract: The paper presents a method for of kinetoelastodynamics analysis of the mechanism with cams and elastic follower. It is studied the influence of the combined motion laws on the functionality of the mechanism with the follower being in translation movement. There are discussed the behavior of the following motion laws trapezoidal velocity. The motion equation is determined from the condition of the dynamic equilibrium applied to the reduced mass of the follower. The dynamic response of the mechanism is obtained with the help of the Laplace transformation in the hypothesis of neglecting the dumping.

Key words: Dynamic, Cam, Flexible follower, Combined motion

1. INTRODUCTION

The researches regarding the dynamic simulation of the cam follower systems, taking into consideration the elastic follower, led to the development of physical and mathematical models, which are used in the analysis of the real motion of these mechanisms. The choosing of the law of motion represents an important element in the design of the cam profile. Generally, the choosing of the follower's motion law is made on the basis of three criterions: function, dynamic and technological [4], [8].

The first criterion recommends a motion law, which must meet certain kinematics, conditions specific to the technologic operation executed by the follower directly, or by using transmission mechanisms. The technologic criterion characterizes the motion law from the point of view of the possibilities of processing of the profile in economic conditions.

The dynamic criterion becomes dominant especially in the establishment of the motion law for the cam mechanisms, which work at high velocity. Concordant to this criterion, the motion law must assure a working without shocks or vibrations and with requests of the links as reduced as possible.

The mathematical model, which describes the behavior of the physical model, is made of motion equations, which can be differential.

The number of freedom degree of the physical model gives the complexity of the mathematical model the number of the generalized coordinates. The solution of the mathematical model representing the motion law of the system is named the system response. The cam mechanism may be conceived (by approximation) as an oscillating system with a freedom degree.

The paper presents a way of elaboration of the mathematical model having on the basis of the Laplace transformation for the combined motion laws with trapezoidal velocity. This is an elegant method for the solving of the differential equation, which

represents the follower's motion law [2], [6], [9].

2.DYNAMIC MODEL

The dynamic model of the cam and flexible follower mechanism is presented in Fig. 1. The parameters, which define this model, are:

m – the reduced mass of the follower;
k – the resulted rigidity corresponding to the series system;
c_1 - the damping coefficient specific to the external damping;
c_2 - the damping coefficient specific to the internal damping of the follower;
F_0 - the preloading force of the compression spring;
F_t - technological force which drives on the mass m.

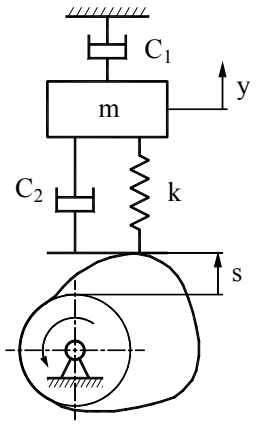

Fig. 1. Dynamic model of the cam mechanism

The displacement of the flexible follower is noted with y and the displacement due to the cam profile is s (Fig. 1).
The equation determined by applying the dynamic equilibrium to the mass m, has the following form:

$$m \cdot \ddot{y} + \left(c_1 + c_2\right) + k \cdot y = c_2 \cdot \dot{s} + k \cdot s - F\left(t\right) \tag{1}$$

where $F\left(t\right) = F_0 + F_t$.

Using the generalized coordinates Lagrange, $q = y - s$, $\dot{q} = \dot{y} - \dot{s}$, $\ddot{q} = \ddot{y} - \ddot{s}$ the relation (1) becomes:

$$\ddot{q} + 2 \cdot \left(n_1 + n_2\right) \cdot \dot{q} + \omega_n^2 \cdot q = -\ddot{s} - 2 \cdot n_1 \cdot \dot{s} - \frac{F\left(t\right)}{m} \tag{2}$$

where:

$\omega_n = \sqrt{\frac{k}{m}}$ - natural frequency of the linkage, [radians / sec];

$n_1 = \frac{c_1}{2 \cdot m}$ - external damping factor;

$n_2 = \frac{c_2}{2 \cdot m}$ - internal damping factor.

In the hypothesis of neglecting the friction forces and considering $F\left(t\right) = 0$, the equation (2) becomes:

$$\ddot{q} + \omega_n^2 \cdot q = -\ddot{s} \tag{3}$$

This equation will be used next for the dynamic analysis of the cam mechanisms designed on the basis of the combined motion laws.

3. METHOD FOR SOLVING THE MATHEMATICAL MODEL

The mathematic model represented with the differential equation (3) applies to the motion law trapezoidal velocity. For the establishment of the solution it is used the

Laplace transformation. Using this solving method it is obtained an analytic solution for the differential equation (3). The analytic solution offers superior possibilities of analysis compared with the numeric solution. As it follows there are presented the solutions for the differential equations corresponding to the three motion laws.

The differential equations of the motion are determined for the intervals $[0,t_s]$, $[t_s,t_1-t_s]$ and $[t_1-t_s,t_1]$ (Fig. A1, Appendix A). The relations (A_1) and (A_2) from

Appendix A define from the kinematics point of view the kinematics parameters of the respective motion law.

For the interval [0, t_S] (Fig. A1, Appendix A) the differential equation (3) has the following form:

$$\ddot{q}+\omega_n^2\cdot q=-A_1 \tag{4}$$

Appling the Laplace transformation for the equation (4) with the initial condition $q(0)=0$, $\dot{q}(0)=0$ results the following algebraic equation in the complex variable s_0 and the image function Lq: $s_0^2\cdot Lq+\omega_n^2\cdot Lq=-\dfrac{A_1}{s_0}$,

from the above relation it is determined the image function $Lq(s_0)$:

$$Lq=-A_1\cdot\frac{1}{s_0\cdot\left(s_0^2+\omega_n^2\right)}$$

The original function $q(t)$ it is obtained by applying the reverse Laplace transformation for the image function *Lq(s0)* [2]:

$$q(t)=-\frac{A_1}{\omega_n^2}\cdot\left(1-\cos\omega_n\cdot t\right) \tag{5}$$

In the interval $[t_s,t_1-t_s]$ (Fig. A1, Appendix A) the differential equation has the form:

$$\ddot{q}+\omega_n^2\cdot q=A_2. \tag{6}$$

with the initial conditions $q_{20}=q(t_s)$, $\dot{q}_{20}=\dot{q}(t_s)$ specific to the interval $[t_s,t_1-t_s]$.

Applying the Laplace transformation, in the same way, as in (4) it is obtained the following solution:

$$q(t)=q_{20}\cdot\cos\omega_n\cdot t+\frac{q_{20}}{\omega_n}\cdot\sin\omega_n\cdot t \tag{7}$$

For this interval, the relation (7) becomes:

$$q(t)=q_{20}\cdot\cos\omega_n\cdot\left(t-t_s\right)+\frac{q_{20}}{\omega_n}\cdot\sin\omega_n\cdot\left(t-t_s\right) \tag{8}$$

The interval $[t_1-t_s,\ t_1]$ (Fig. A1, Appendix A) is characterized by the following differential equation of motion:

$$\ddot{q}+\omega_n^2\cdot q=A_1. \tag{9}$$

The initial conditions are $q_{30}=q(t_1-t_s)$, $\dot{q}_{30}=\dot{q}(t_1-t_s)$. Determination of the solution with Laplace transformation is made in the same way as in relation (9). So, the solution equation (9) is:

$$q(t)=\frac{A_1}{\omega_n^2}\cdot\left(1-\cos\omega_n\cdot\left(t-t_1+t_s\right)\right)+q_{30}\cdot\cos\omega_n\cdot\left(t-t_1+t_s\right)+\frac{\dot{q}_{30}}{\omega_n}\cdot\sin\omega_n\cdot\left(t-t_1+t_s\right) \tag{10}$$

As it followers, parameters A_1 is computed with the relation presented in Appendix A. The real motion of the follower y for both intervals it is obtained with the relations:

$$y=s+q;\quad \dot{y}=\dot{s}+\dot{q};\quad \ddot{y}=\ddot{s}+\ddot{q}. \tag{11}$$

The functions $s(t)$, $\dot{s}(t)$, $\ddot{s}(t)$ are presented in Appendix A, and the functions $\dot{q}(t)$ and $\ddot{q}(t)$ are obtained by successive derivations in relation with time of the relation (8) and (10).

4. DISCUSSIONS OF THE NUMERIC RESULTS

The initial data on which were made the diagrams form Fig. 2 are:

- the follower's course $h=0{,}025$ [m];
- the time period for the rising phase $t_1=0{,}022$ [s];
- the natural frequency $\omega_n=1570{,}7963$ [rad/s];
- the time periods for the connecting intervals $t_s=0{,}0055$ [s].

In figure 2 are presented the variation diagrams of the dynamic and kinematics parameters specific to the trapezoidal velocity motion law.

Analyzing the diagrams from Fig. 2 it is observed that the vibration's acceleration has two discontinuities (Fig. 2, f) at the passing from the positive acceleration to zero acceleration and as the passing from zero acceleration to negative acceleration.These discontinuities do not stop the obtaining a continue signal for the elastic follower's acceleration ($\ddot{y}$) (Fig. 2, f). The maximum values of the acceleration modulus were modified in the rising direction at the passing from an interval to another.

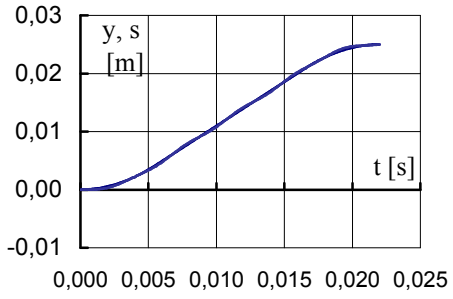

a)

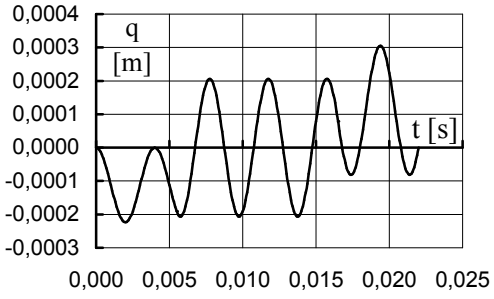

b)

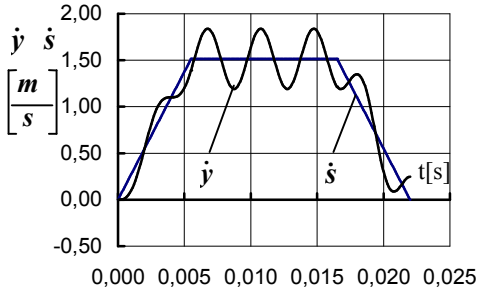

c)

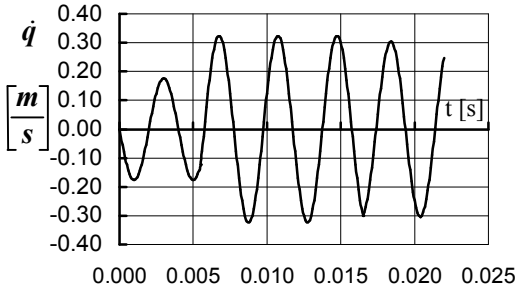

d)

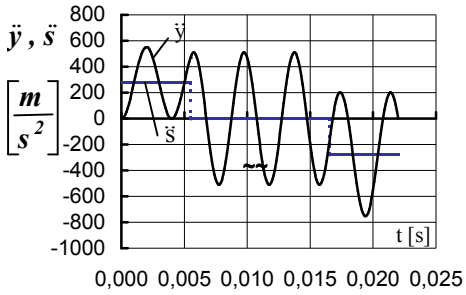

e)

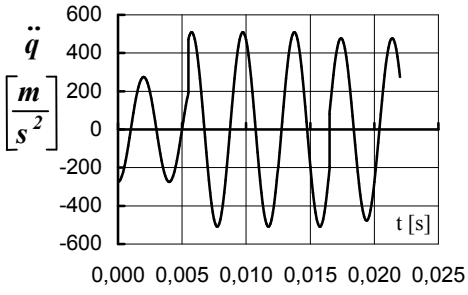

f)

Fig. 2 The variation of the parameters of the trapezoidal velocity motion law

5. CONCLUSIONS

The dynamic model without damping can be easily used in the characterization from the dynamic point of view of the motion laws with constant acceleration, trapezoidal velocity and sinusoidal modified trapezoidal velocity.

The Laplace transformation leads to the obtaining of an analytical solution for the differential equation of the motion, with superior possibilities in the dynamic analysis rather then numeric analysis.

Received April, 23 2007

Technical University of Iassy
Department of Theory of Mechanisms and Robotics

REFERENCES

1. Benson, H.T., *Principles of Vibration*, Oxford University Press, 1996.
2. Brown, F.T., *Engineering System Dynamics*, Marcel Dekker, Inc. New York, Basel 2001.
3. Dubowsky, S., Deck, J.F. and Costello, H., *The dynamic modeling of flexible spatial machine systems with clearance connections*, ASME – Transmissions and Automation in Design, vol. 109, pp. 87-94, 1987.
4. Duca, C., Popovici, A., Oprisan, C., *The basis of the cam mechanisms design* (in Romanian), Gh. Asachi, Iasi, 1999.
5. Grewall, P.S., Newcombe, W.R., *A comparative study of cam motions for high – speed semi – rigid follower cam systems*, Transaction of the ASME, vol. 12, No. 3, pp. 121 – 128, 1988.
6. Leviskii, N.I., *The vibrations of the mechanisms* (in Russian), Nauka, Moskva, 1988.
7. Mahyuddin, A.I., Midha, A., *Influence of varying cam profile and follower motion event types on parametric vibration and stability of flexible cam follower systems*, Transaction of the ASME, vol. 116, pp. 298 – 305, 1994.
8. Oprisan, C., Leohchi, D., *Specific Problems of the Cam Mechanisms Kineto-Elastodynamics*, COBEM – 2001, Brazil, 2001.
9. Redheffer, R., Port, D., *Differential Equations*, Jones and Bartlett Publishers, Boston, 1991.
10. Rothbart, H.A, *Cams,* John Wiley & Sons, Inc., New York, 1956.
11. Sigley, H.A., *Dynamic Analysis of Machines*, McGraw – Hill Book Company Inc, 1961.
12. Yu Wang, Zaiping Wang, „Dynamic analysis of flexible mechanisms with clearances”, Transactions of the ASME, vol. 118, pp. 592 – 594, 1996.

EVALUAREA PARAMETRILOR DINAMICI AI SISTEMULUI ELASTIC CAMĂ –TACHET

Rezumat Lucrarea prezinta o metoda privind analiza cinetoelastodinamica a mecanismelor cu cama si tachet elastic.Este studiata influenta legilor de miscare combinate asupra functionarii mecanismelor cu cama si tachet in miscare de translatie.In acest scop ,este folosit ca exemplu legea de miscare cu viteza trapezoidala. Raspunsul dinamic al mecanismului este obtinut cu ajutorul transformatei Laplace, in ipoteza neglijarii amortizarii.

APPENDIX A

The motion law with trapezoidal velocity

The time of the rising phase is shared in three intervals: one centered, $t \in \lfloor t_s, t_1 - t_s \rfloor$ with constant velocity and two laterals with $t \in \lfloor 0, t_s \rfloor$ and $t \in \lfloor t_1 - t_s, t_1 \rfloor$ with constant acceleration (Fig. A1).

$$t \in \lfloor 0, t_s \rfloor$$

$$A_1 = \frac{h}{t_s \cdot (t_1 - t_s)}$$

$$\text{(A1)} \qquad \begin{cases} s = \dfrac{A_1 \cdot t^2}{2} \\ \dot{s} = A_1 \cdot t \\ \ddot{s} = A_1 \end{cases}$$

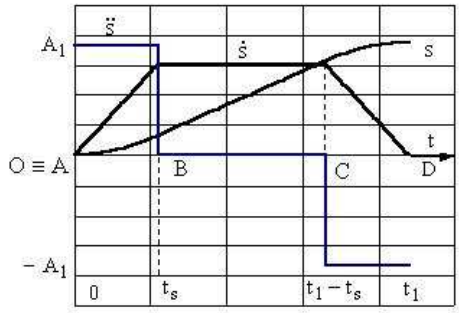

Fig. A1. Variation diagrams of the kinematics parameters

$$t \in \lfloor t_s, t_1 - t_s \rfloor \qquad t \in \lfloor t_1 - t_s, t_1 \rfloor;$$

$$\text{(A2)} \qquad \begin{cases} s = A_1 \cdot t_s \cdot t - \dfrac{A_1 \cdot t_s^2}{2} \\ \dot{s} = A_1 \cdot t_s \\ \ddot{s} = 0 \end{cases} \qquad B_3 = A_1 \cdot t_1;$$

$$C_3 = -A_1 \cdot \frac{t_1^2}{2} - A_1 \cdot t_s^2 + A_1 \cdot t_1 \cdot t_s$$

$$\text{(A3)} \qquad \begin{cases} s = -\dfrac{A_1 \cdot t^2}{2} + B_3 \cdot t + C_3 \\ \dot{s} = -A_1 \cdot t + B_3 \\ \ddot{s} = -A_1 \end{cases}$$

where; h–follower's course; t_s - time period of the interval [*A, B*]; t_1 - time period of the rising phase.

There are discontinuities at the acceleration in points B and C (Fig. A1).

BULETINUL INSTITUTULUI POLITEHNIC DIN IAŞI
Tomul LIII (LVII), Fasc. 1, 2007
Secția
ŞTIINȚA ŞI INGINERIA MATERIALELOR

THE ELECTROPHORETIC DEPOSIT OF THE HYDROXYAPATITE

BY

NĂSTACA TIMOFTE, BODGAN NICOLAU and ŞTEFAN TOMA

Abstract: The present paper aims to establish the conditions of electrohoretic deposit of hydrohyapatite on titan. We present schemas that comprise sequences and work conditions. We presented the scheme of the electrophoretic deposit on a electrochemically activated surface and in another work scheme we opted for the use of a metallic sample etched with acids and activated with sodium hydrate . We presented images of the titan surface after the electrophoretic surface according to scheme I, where we can observe a uniform coverage with hydroxyapatite, of white mat color. The aspect of the sample surface after activation according to the scheme II shows an accentuated and non-uniform etching. We can claim that the electrophoretic deposit is less dependent upon the manner in which the activation takes place, but we must take into account the surface roughness.

Keywords: hydroxyapatite, electrophoretic, roughness, sand-blasting

1. Introduction

The coverage of metallic implants through the eletrophoretic methods presents the advantage of a very short time of coverage and a very good reproducibility : there are still disadvantages of the hydroapatite adhesion to the metallic layer if a previous sand-blasting is not executed , helping the increase of roughness and a calcination for the adhesion improvement.

The electropholic method ensures the coverage using hydroxyapatite previously synthesized which is deposited on the metallic support under the action of a great intensity electric field.

Under the experimental aspect, the study of the deposit of hydroxyapatite through the electrophoretic method supposes two distinctive methods:

- the synthesis and characterization of the hydroxyapatite
- the proper electrophoretic deposit

The main object is the preparation of a hydroxyapatite under the form of fine, synthesized dust. Several methods for obtaining the hydroxyapatite can be used, the best being the precipitation methods.

No matter the precipitation method used, a chemical and structural characterization of some synthetic hydroxyapatites is necessary for the purpose of choosing the most adequate product for coverage through the electrophoretic method. For the analysis, we used four hydroxyapatite samples noted HA1…HA4 that were obtained through precipitation from solutions in the system Ca^{2}+/H PO_4 $^{2-}$ using different reagents and modifying the reaction conditions.

After the synthesis and the characterization of the four samples, we reached the following conclusion: the hydroxyapatite with stoichiometric and well crystallized

composition is obtained starting from CaCl2 and (NH4) PO4, working at 75^{o} C for pH= 11…12 and ensuring a time of maturation of the precipitate of over 90 hours at the room temperature. For the coverage studies through the electrophoretic method, we used hydroxyapatite HA1C2, this having the report Ca/P= 1.67 and the best crystallinity.

2. The proper electrophoretic deposit of hydroxyapatite on the titanium

This was achieved through a fine suspension of hydroxyapatite in isopropyl alcohol. 4g of HA were introduced in 100 ml isopropyl alcohol and 5 ml HCL were added as a dispersion agent in an ultra-stirrer (30.000 rotations/minute) for 10 minutes.

Before the introduction in the electrochemical cell, this suspension was ultrasounded for 10 minutes for uniformity. The titan sample (the cathode) etched and previously activated was connected to the negative pole of a tension source, to the other pole being connected the platinum electrode (the anode). The distance between the electrodes was 4 cm.

After the deposit, the samples were washed with water, then dried at 110^{0} C, microscopically analyzed and roasted. In the 1st schema we present the work sequences and conditions in the case of electrochemical activation of the surface.

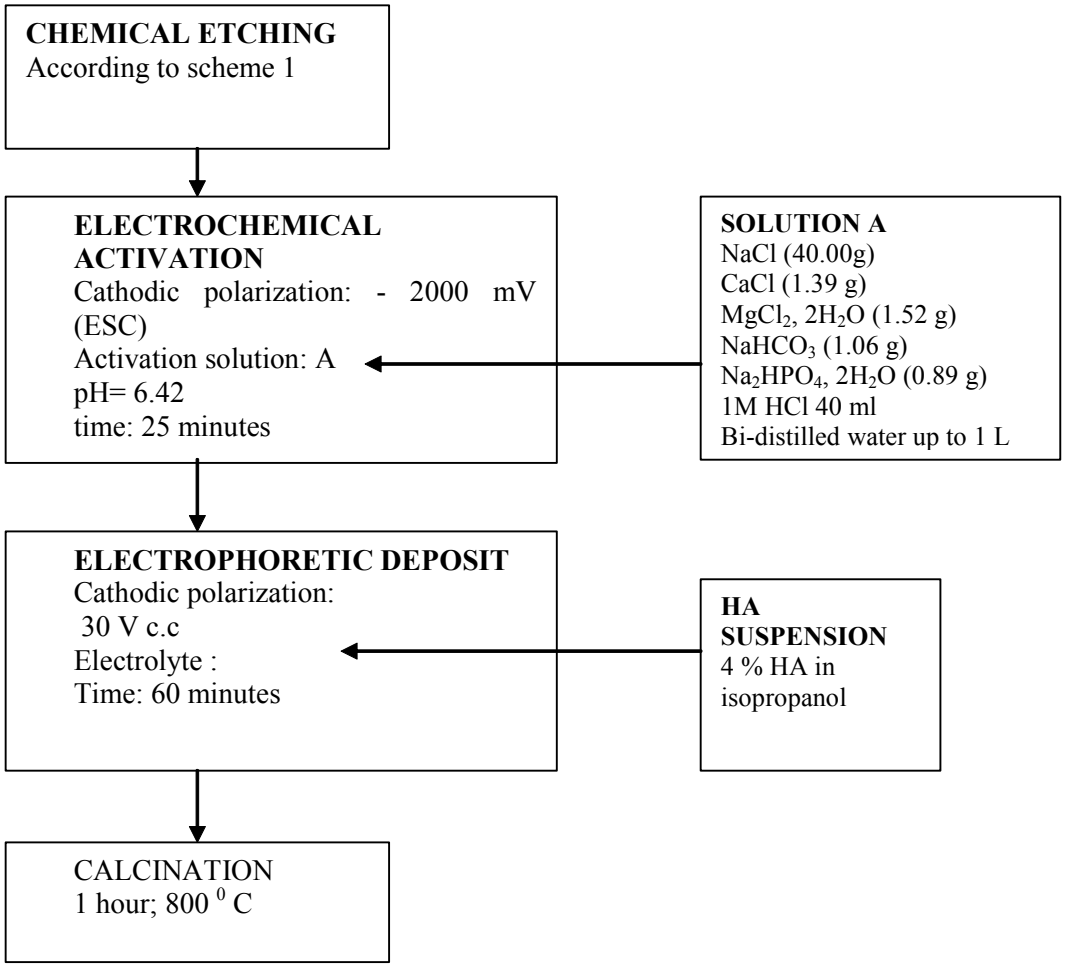

Scheme 1. The electro-phoretic deposit on the electrochemically activated surface.

Qualitatively, with the naked eye you can notice a uniform coverage with hydroxyapatite of white mat color. The microscopic analysis also emphasizes a consistent, relatively uniform deposit, figure 1

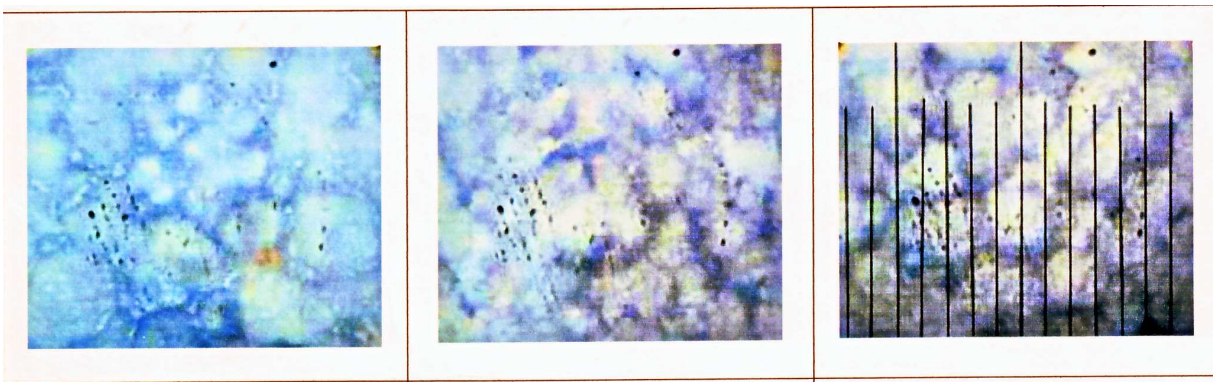

Figure 1. Images of the titan surface after the electrophoretic deposit according to scheme 1

We can still distinguish the micro particles of hydroxyapatite with dimensions of 40…60μm, rather uniform. The calcination of the sample covered was carried out only at 800° C since the hydroxyapatite used was already synthesized at 1200° C and the sample was warmed at 800° C for the fixation and compacting of the deposited layer, figure 2.

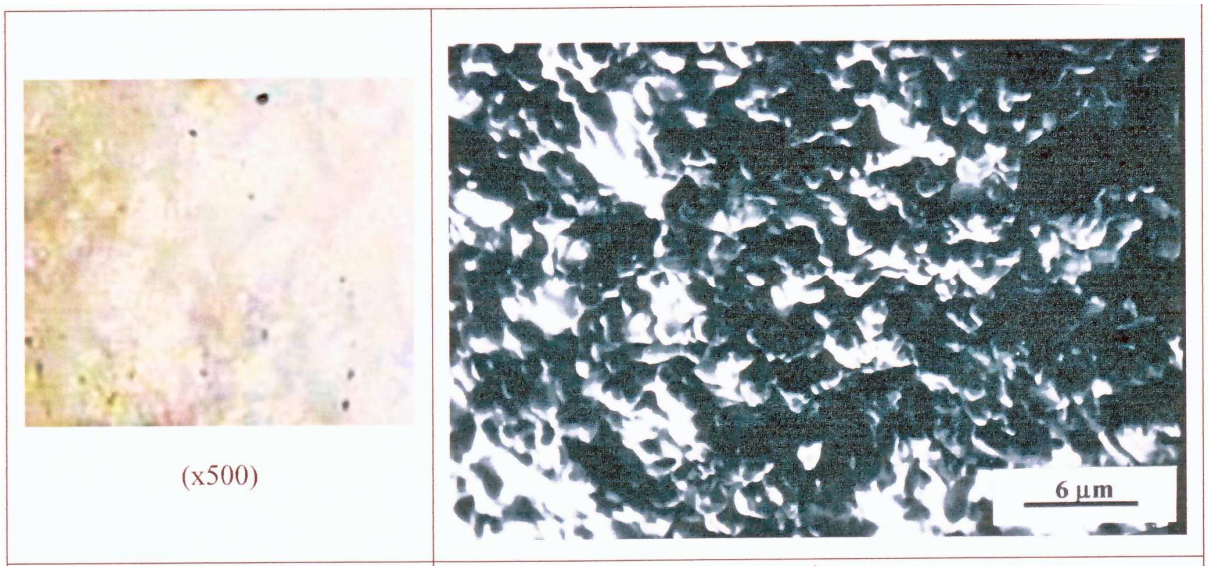

Figure 2. The surface of the sample covered after calcinations at 800 ^{0}C

We can ascertain that through the electrophoretic deposit, the morphology of hydroxyapatite was not essentially modified and the adherence at the surface of the metal is very good.

The use of a metallic sample etched with acids and activated with sodium hydrate is presented in scheme II. In this case we opted for a fast alkaline activation (60 min) using a very concentrated solution of sodium hydrate (10 mol/l) and the temperature of 75 ^{o} C.

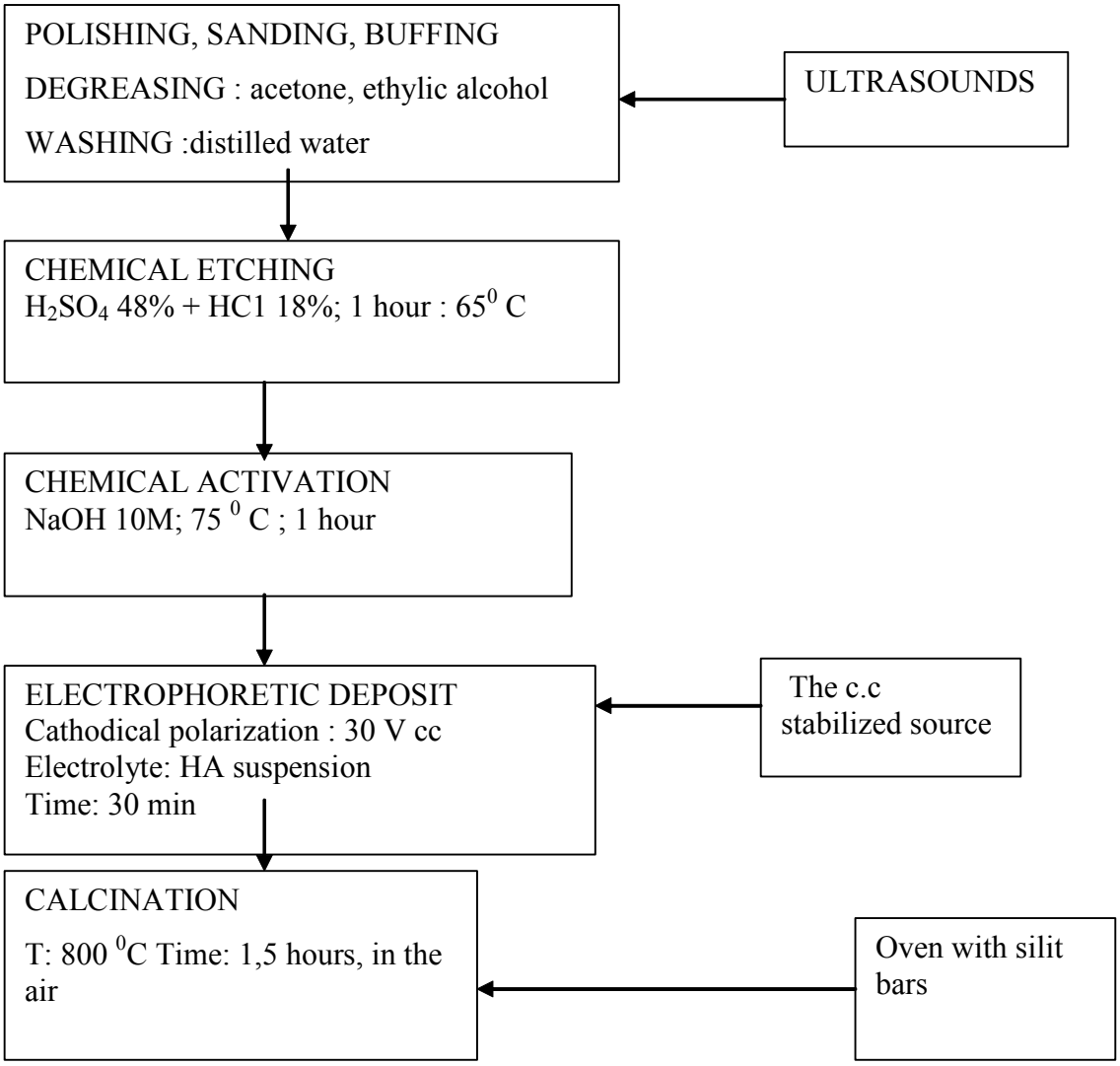

Scheme 2

The electrophoretic deposit took place at 30 V for a period of 30 minutes using the same suspension of HA as in the scheme I. The aspect of the sample surface is illustrated in figure 3.

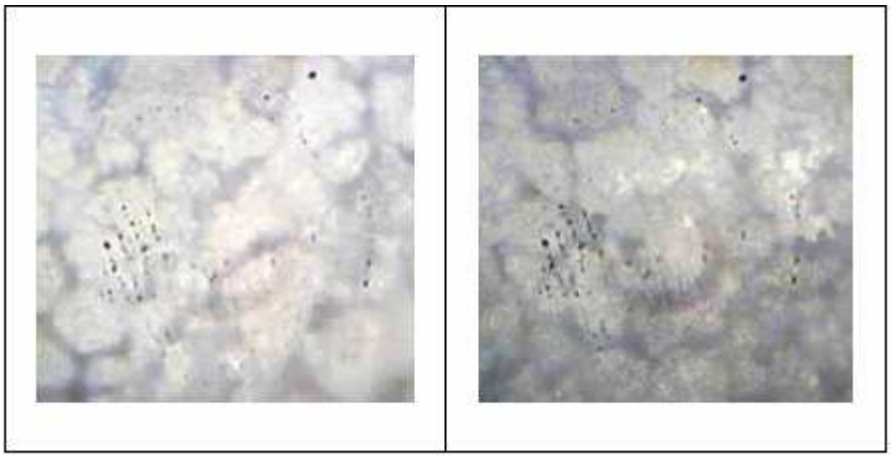

Figure 3 . The structure of the sample surface after the electrophoretic deposit

Thus we confirm the fact that the electrophoretic deposit is less dependent upon the manner in which the activation is made, but the roughness of the surface must not be neglected. The analysis through electronic microscopy emphasizes the same structure as in the case of the deposit according to the scheme I. the image obtained for this sample is presented in figure 4.

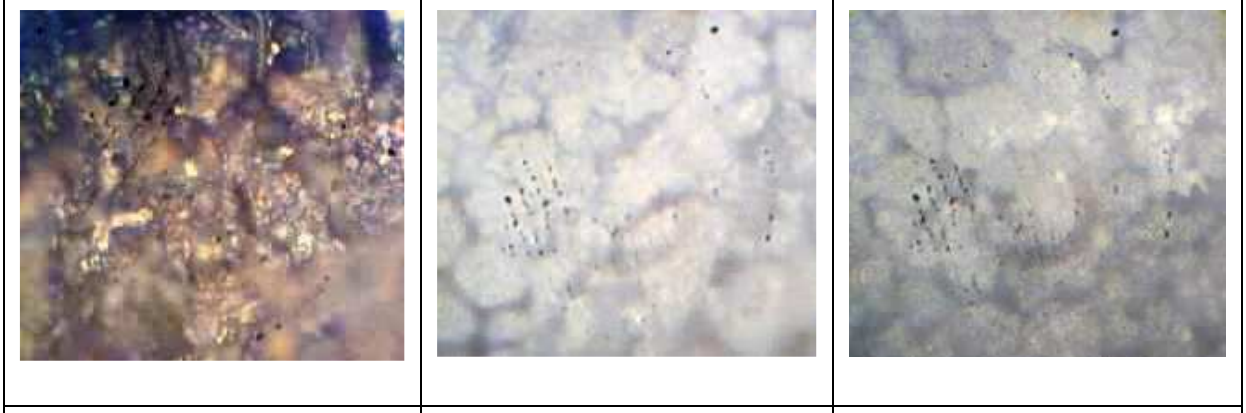

(a) (b) (c)

Figure 4: The surface structure after the chemical engraving and the activation with NaOH (a) and after the electrophoretic deposit. (b,c)

We can still notice the more accentuated dislevelment of the deposits due especially to the irregular roughness.

The X ray specter figure 5 obtained for this sample and SEM micrography, figure 6 shows that the material deposited is hydroxyapatite and its purity were not affected through the coverage process; the crystallinity of this sample is better especially because of the supplementary calcinations.

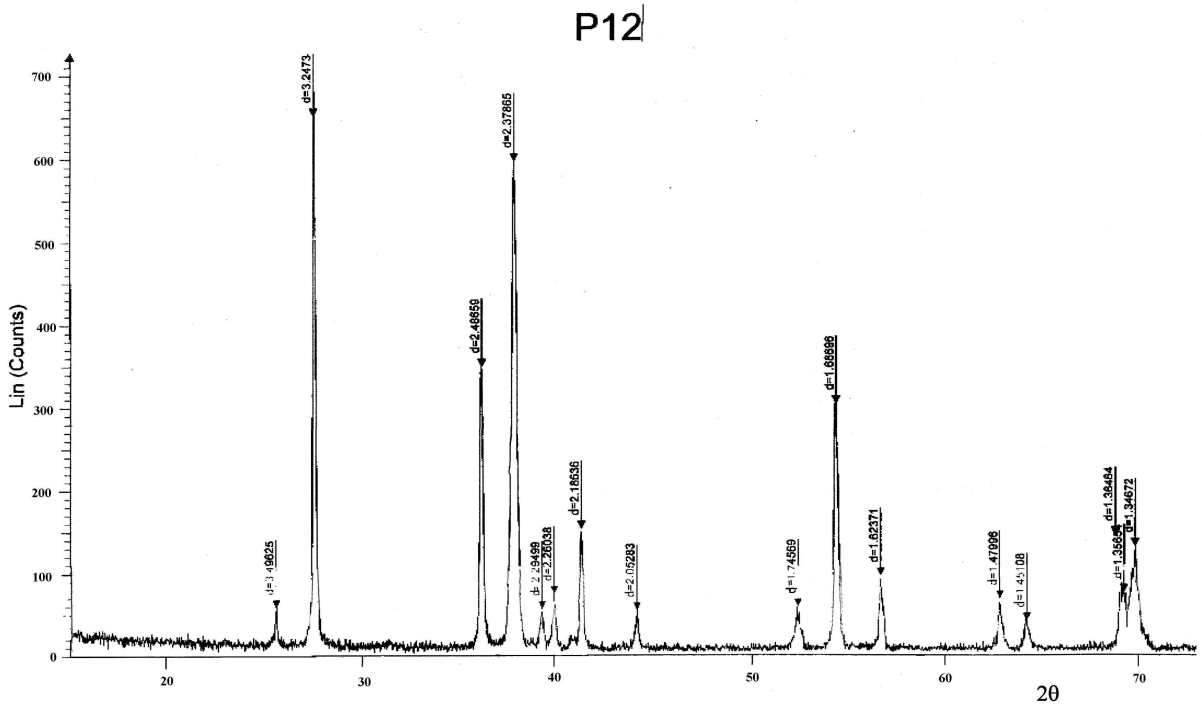

Figure 5: The X ray specter of the chemically activated sample and covered through electrophoresis

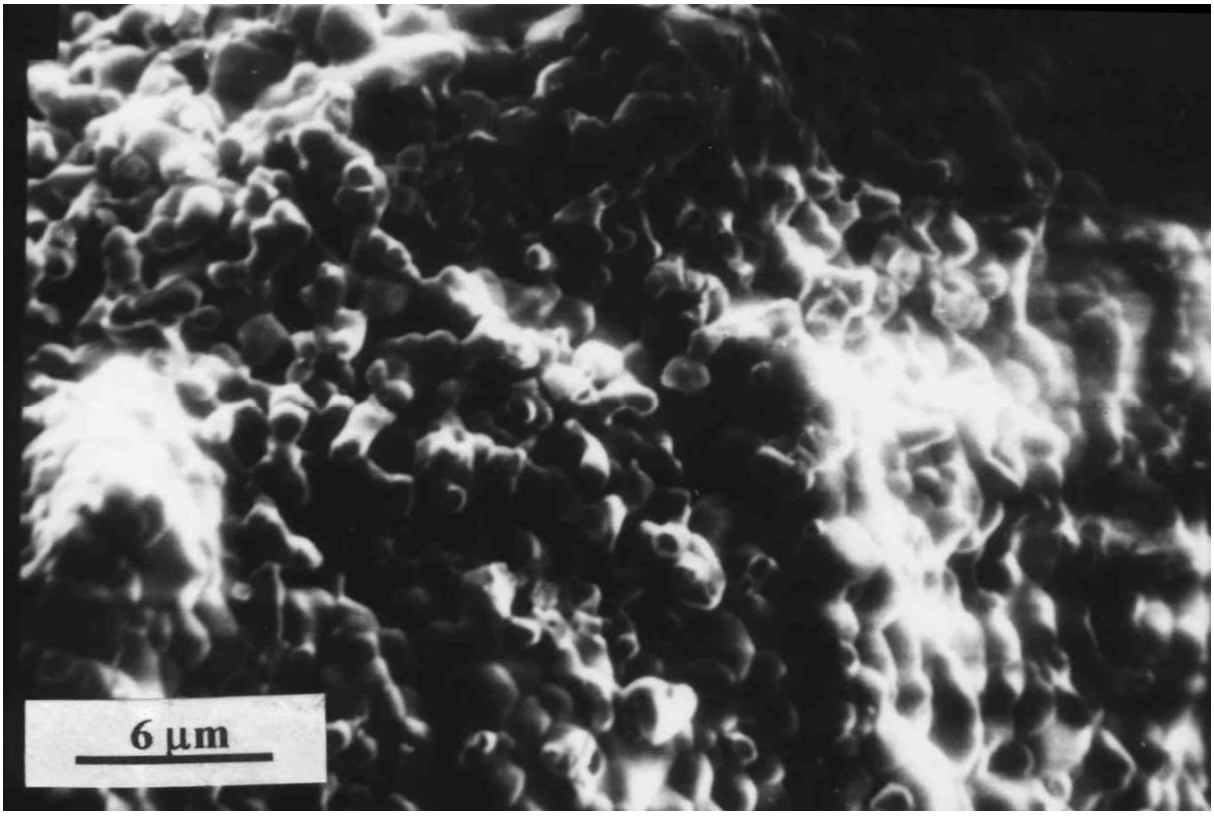

Figure 6. The SEM microforography for the chemically activated sample and covered through electrophoresis

3. Conclusions

The electrophoretic method uses the hydroxyapatite previously synthesized that is deposited on a metallic support under the action of an electric field of great intensity.

Although the method of spaying in the plasma is also used in the synthetic hydroxyapatite, because of the very high temperature, this can suffer serious alterations; so that from this point of view, the electrophoretic method seems more advantageous and more economical.

The electrophoretic method seems the most advantageous for the coverage of titan implants, being fast, non-polluting, requiring a reduced energy consume, which is very well fixed on the implant after calcinations.

Received April 23, 2007 *The "Gh.Asachi" Technical University Iaşi*

REFERENCES

1. Zhang Qiyi, Leng Yang, Renlong Xin, A comparative study of electrochemical deposition and biomimetic deposition of calcium phosphate on porous titanium, *Biomaterials,***26,** 2005, p. 2857-2865
2. Muller F A, Jonasova L, Helebrant A, Strnad J and Greil P, *Biomaterials,* **23,** 2002, p. 3095
3. Hata K, Ozawa N, Kokubo T and Nakamura T, *J. Ceram. Soc. Jap.*, **109,** 2001, p. 461
4. Muller F A, Jonasova L, Helebrant A, Strnad J and Greil P, *Biomaterials,* **25,** 2004, p.1187

DEPUNEREA ELECTROFORETICĂ A HIDROXYAPATITEI

Rezumat: Lucrarea de față isi propune stabilirea condițiilor de depunere electroforetică a hidroxiapatitei pe titan. Sunt prezentate scheme ce cuprind secvențe şi condiții de lucru. A fost prezentată schema depunerii electroforetice pe suprafața activată electrochimic, iar intr-o altă schema de lucru s-a optat pentru utilizarea unei probe metalice gravată cu acizi şi activată cu hidroxid de sodiu. S-au prezentat imagini ale suprafeței titanului după depunerea electroforetică conform schemei I, unde se poate observa o acoperire uniformă cu hidroxiapatita, de culoare alb mat. Aspectul suprafeței probei dupa activare conform schemei II arată o gravare accentuată şi neuniformă. Se poate spune că depunerea electroforetică este mai puțin dependentă de modul în care se face activarea, trebuie ținut seama însă de rugozarea suprafeței.

BULETINUL INSTITUTULUI POLITEHNIC DIN IAŞI
Tomul LIII (LVII), Fasc. 1, 2007
Secția
ŞTIINȚA ŞI INGINERIA MATERIALELOR

NEW HEAT TREATMENTS APPLIED TO ALUMINIUM ALLOYS AlCu2.5Mg

BY

R. M. POPESCU, V.N. CÂNDEA and D. SENCHETRU

Abstract: This work describes a model of thermal treatment for the aluminium alloy AlCu-2.5Mg with the advisable use of the equipment and the thermal treatment appliances.

Keywords: materials, thermal treatment

1. Introduction

A recent tendency in the industrial hot processing development is the application of computer aided heat treatment processes and tooling in combination with the reduction of the energetic consumptions. The work methodology suggested for studying the improvement of the heat treatment technologies to be applied to the AlCu2.5Mg aluminium alloy comprise the following phases:

- adapting the heat treatment process to the said aluminium alloy;
- choosing the tooling and the installations required for carrying out the heat treatment cycles for the said aluminium alloy;
- choosing the installations and the devices to be used in the study of the mechanical characteristics and in the structural analysis of the said aluminium alloy;
- carrying out the experiment and analytical interpretation of the results.

Mention must be done that this methodology is an original one and has been conceived for enabling the establishment of the final heat treatment opportunities at high accuracy rates.

Thus, in order to improve heat treatment technologies for this aluminium alloy, there have been taken into account as follows:

- application of methods and techniques to eliminate the physical human labour;
- elimination of manual control manoeuvres by applying automated control systems, capable to maintain the proper operation of the tooling without any intervention on behalf of the process operator, no matter the external or internal actions;
- reduction of heat losses due to the lack of air-tightness, by using a proper insulation;

To this respect, components and semi-manufactured parts made of the said aluminium alloy shall be heated in electric ovens featuring a forced air circulation. The temperature of the heating mechanisms shall be set and controlled using automatic self-registration devices with a precision class as high as possible, so that the

measuring accuracy be within ±3°C. Control and adjustment devices shall be checked as soon as the operational area reaches the maximum temperature.

In order to perform treatment cycles as set forth, there has been chosen a SUPERTHERM oven manufactured by the Nabertherm company in Germany. This equipment is available in the endowment of the S.C. Compania Apa S.A. Joint stock trading company in Sibiu. The utilized heating installation is in accordance with the ISO 9001 standard requirements.

The heating oven meets all requirements of a final heat treatment applicable to such aluminium alloys. By means of this equipment, some heat treatment diagrams have been successfully accomplished and also, some heating – holding curves have been successfully maintained. [1]

By programming the desired temperature or a treatment cycle can be performed by the instrumentality of the 903 P controller. Using the same controller, several programs can be interconnected or the same cycle repeated under identical circumstances, for several times.

Typical μR1000-Yokogawa registration devices are fitted in addition in the oven, thus enabling, in parallel, the measurement of the heating / cooling temperature and speed, as well as the registration of the temperature – time diagrams and printing the main treatment cycle parameters onto the same.

With a view to modelling the final heat treatment process for the AlCu2.5Mg aluminium alloy [2], a minimum number of 9 experiments are necessary according to the 3^k factorial experiment theory; in this specific case k = 2, i.e. there are two variation factors: the quenching heat treatment temperature for putting into solution (T_c) and the heating temperature for ageing (T_r)

2. Performing the experiment and providing the analytical interpretation of the results

In order to optimize the heat treatment process for the chosen aluminium alloy, it is necessary to settle some heat treatment versions within the limits set forth in the standards as well as to research the mechanical, technological and structural properties of the test pieces to be obtained under differently directed heating, holding and cooling conditions.

In order to be able to perform mathematical modelling as desired, this experiment has to be programmed. This involves as follows:

- establishing the necessary and sufficient number of experiences and the accomplishment conditions thereof;
- establishing the regression equation representing the model of the process;
- establishing the conditions to attain the optimum value in terms of the accomplished process performance

Therefore, for each variable basic levels as well as variation intervals shall be determined. By adding the variation level to the basic level, the superior level of the variable, and by subtracting it, the inferior variable level is obtained. Variation intervals shall be chosen so that possibly most accurate values be involved in terms of a functional viewpoint. As a first step, basic levels and variation intervals shall be obtained.

For modelling the AlCu2.5Mg aluminum alloy final heat treatment process, the quenching and aging temperatures available as variables over the different physical or technological parameters obtained by way of experience.

Table 1 shows the variation interval and the basic level for programming the experiment in order to establish the optimum final heat treatment technology.
Table 2 shows the experiments that are necessary in order to obtain the mathematical model. Mention must be done that each test piece has been pressed and labelled using a code number so that it can be properly pursued during the experiment.

Table 1

Factor	Quenching temperature, T_c [°C]	Aging temperature, T_r [°C]
Basic level	515	160
Variation interval	10°C	10°C
Superior level (+)	525	150
Inferior level (-)	505	170

Table 2

Experiment	Test piece code number	Quenching temperature, T_c [°C]	Aging temperature, T_r [°C]
1	1.1.1	505	150
2	1.2.1	505	160
3	1.1.2	505	170
4	2.1.1	515	150
5	2.2.1	515	160
6	2.1.2	515	170
7	3.1.1	525	150
8	3.2.1	525	160
9	3.1.2	525	170

Using the obtained experimental results, it will be determined which are the ones yielding the most advantageous mechanical and technological properties among the proposed versions. Mention must be done that the holding times and the cooling conditions are the same for each experiment, and that the variables are only the heating temperatures used for the purpose of the heat treatment.

4. Conclusions

We deem that the chosen original research methodology enables carrying out experiments for the purpose of the improvement of heat treatment technologies applicable to aluminium alloys due to the following considerations:

- proper adoption of the heat treatment technology for the AlCu2.5Mg aluminium alloy taken into consideration;

- choosing a high-performance heating equipment by means of which the heating and holding process can be monitored for the performed heat treatment operations;
- choosing an up-to-date equipment for establishing the exact chemical composition;
- using the MTS 810 tooling for establishing the tensile strength values, the elasticity module, as well as other mechanical parameters. This is tooling of last generation equipment and provides failure diagrams as well as the registered parameters using a computer software.
- employing a more accurate apparatus for establishing hardness, at a 1 mm spacing over the parts diameter;
- using a proper and up-to-date method for analyzing material structures;
- experiment management and possibility to analytically analyze the results

Received April 26, 2007

REFERENCES

1. Brăgaru, A., and others: *Optimizarea produselor şi echipamentelor tehnologice (Optimization of technological processes and equipment)*, Bucureşti, Editura Didactică şi Pedagogică, 1996
2. Giacomelli, I., *et al.*: *Tratament termice (Heat treatments)*, Ed. Universitatea Transilvania, 1980
3. Zgură, G., and others: *Tehnologia sudării prin topire (Welding Engineering by Melting)*, Bucureşti, Editura Didactică şi Pedagogică, 1983

NOI TRATAMENTE TERMICE APLICATE ALIAJELOR DE ALUMINU AlCu2,5Mg

Rezumat: Această lucrare descrie un model de trament termic aplicat aliajului de aluminiu AlCu2,5 Mg, împreună cu recomandări de utilizare a echipamentului şi aparatelor de tratament termic.

BULETINUL INSTITUTULUI POLITEHNIC DIN IAŞI
Tomul LIII (LVII), Fasc. 1, 2007
Secția
ŞTIINȚA ŞI INGINERIA MATERIALELOR

RESEARCHES ON MECHANICAL PROPERTIES FOR STEELS SINTERED WITH NICKEL AND MOLYBDENUM

BY

N.V. CÂNDEA, R. M. POPESCU and D. SENCHETRU

Abstract: This work describes the metallurgy of poor alloyed steel obtained from powders containing Ni and Mo, for producing sintered elements of high mechanical resistance.

Keywords: sintered materials

Low alloy steels obtained using Ni and Mo content powders are used for producing sintered components featuring high strength values.

Nickel influences iron powder compressibility which decreases as the nickel content decreases due to its ferrite hardening effect (Fig. 1). [1]

Nowadays, the tendency in obtaining low Ni, Cu, Mo alloy steels is to use partially alloyed powder obtained by diffusion. This is especially intended to avoid direct handling of nickel powders by the users, since it is well known that nickel has a noxious effect as to the human organism.

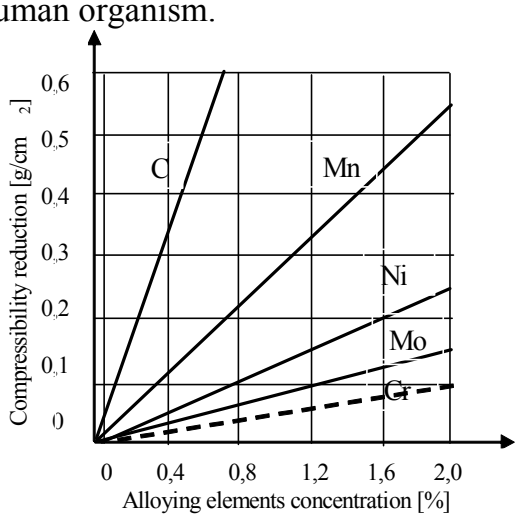

Fig. 1 The effect of the alloying elements onto the iron powder compressibility

The advantages of using partially alloyed powders include, among others, the avoidance of the component segregation during handling (for instance copper in Fe-Cu-C powder mixtures), increasing the homogeneity of the sintered material alloyed with a relatively low diffusion coefficient in Fe such as Cu, Ni, or Mo, providing some inter-diffusion as early as the treatment phase, the increase of the dimensional stability due to the sinter process.

Steels obtained from partially alloyed powders through diffusion feature a higher strength than the ones obtained using mixtures having the same composition. Strength in this latter case is subject to the carbon content (Fig. 2).

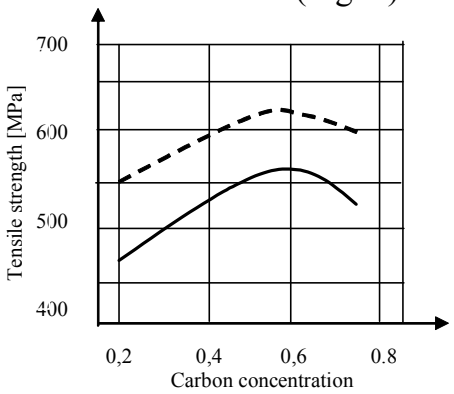

Fig. 2 Tensile strength variation depending on the Fe-4Ni-0.5Mo-1.5Cu steel carbon content obtained from 1) powder mixture; 2) partially alloyed powder through diffusion with additions of alloying elements

Table 1 and Table 2 show, by way of example, the most important chemical compositions and engineering properties featured by partially alloyed powders through diffusion. Such typical copper, nickel and molybdenum powder alloys can be regarded as being representative for partially allied powders through diffusion.

Typically, Fe-1.75Ni-1.5Cu-0.5Mo alloys (Distaloy SA) are the most recommended ones.

Table 1

Powder type	Iron powder used as a base	Concentration [%] of the alloying elements		
		Cu	Ni	Mo
Distaloy SA	SC 100.26	1.50	1,75	0.50
Distaloy AB	ASC 100.29	1.50	1,75	0.50
Distaloy SE	SC 100.29	1.50	4.00	0.50
Distaloy AE	ASC 100.29	1.50	4.00	0.50
Distaloy DC-1*	Astaloy Mo	-	2.00	1.50
Distaloy DH-1*	Astaloy Mo	2.00	-	1.50
Distaloy HP-1**	Astaloy Mo	2.00	4.00	1.50

* DC – dimensional control
** HP – high performance

The same simple compacting – sinter process, tensile strength can be increased to values as high as 650-700 MPa in typical Fe-4Ni-1.5Cu-0.5Mo steels obtained using atomized ASC 100.29 powder as a base and increasing the Ni concentration from 1.75 to 4.0% (Distaloy AE) in a mixture with 0.5% C. Such powders can be used for manufacturing large parts. In order to obtain Ni, Cu and Mo alloy steels, pre-alloyed powders can be used, just in the same way.

Table 2

Typical powder	Maximum particle size [μm]	Apparent density [g/cm^3]	Fluidity [s/50g]	Density at 600 MPa [g/cm^3]	O_2 (loss in hydrogen) [%]	C [%]
Distaloy SA	20-150	2.8	27	7.15	0.10	<0.01
Distaloy AB	20-180	3.05	24	7.15	0.10	<0.01
Distaloy SE	20-150	2.8	27	6.90	0.10	<0.01
Distaloy AE	20-180	3.05	24	7.14	0.10	<0.01
Distaloy DH-1*	20-250	3.15	25	7.09	0.10	<0.01
Distaloy DC-1*	20-250	3.10	25	7.10	0.10	<0.01
Distaloy HP-1**	20-250	3.15	25	7.09	0.10	<0.01

* DC – dimensional control
** HP – high performance

In the pre-alloyed powder particles the alloy elements are evenly distributed in the solid solution or available under the shape of other phases. This is due to the fact that they are obtained by spraying the already melted alloys. Compressibility in such alloys is, however, somewhat lower. Such typical powders are preferred no matter their high costs, in cases where higher structural homogeneity is required for the material in order to obtain higher properties. Table 3 shows the chemical compositions of some typically representative, slightly pre-alloyed powders to be used in sintered steels for constructions. It has been demonstrated that oil sprayed powders feature the best quality for a low oxygen content. The apparent oxygen content of these powders lies within 3.0 – 3.1 g/cm^3 while the particle size in this case is lower than 0.15 mm.

Table 3

Typical powder	O_2 (loss in hydrogen)	Concentration of the alloy elements [%]					Spraying environment	Producer
		C	Ni	Mo	Cr	Mn		
Astaloy A	0.1	0.05	1.90	0.50	0.08	0.25	water	Höganäs
Astaloy D	0.15	0.10	0.25	0.50	0.18	0.35	water	Höganäs
Sumiron 4600	0.1	0.05	1.90	0.50	-	0.15	oil	Sumitomo
HF 4	0.2	0.02	1.90	0.55	-	0.25	water	Mannesmann

The highest raw strength is attained in compacts made of oil sprayed powders (Sumiron 4600), due to the optimum morphology of the particle. The oxygen content of water sprayed Ni-Mo powders subsequently submitted to H_2 reduction treatments (Astaloy A, Astaloy D, HF 4) does not exceed 0.2% and that of the oil sprayed and treated powder does not exceed 0.1%.

The compressibility of such pre-alloyed powders is subject to the chemical composition and to the purity. The relevant values for the qualities given in Table 3, are shown in Fig. 3.

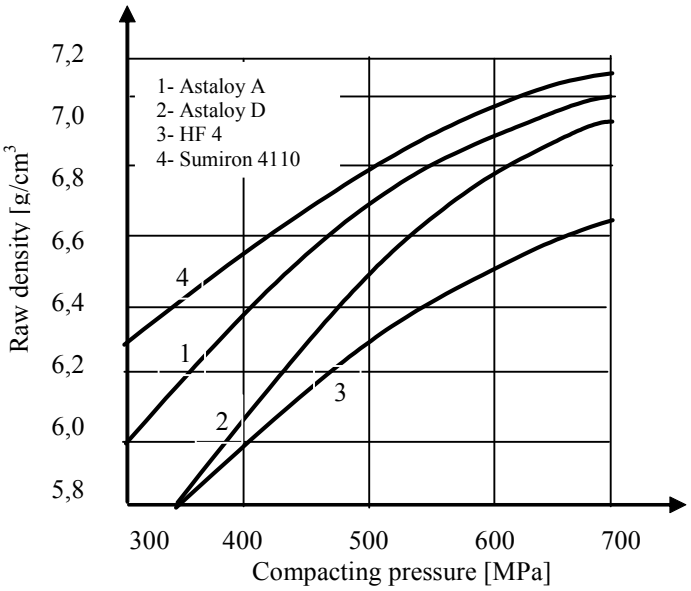

Fig. 3 Raw density variation in compacts obtained using different pre-alloyed iron powders according to the compacting pressure

The highest compressibility is featured by the Sumiron 4600 powder as a result of the oil spraying operation and the subsequent hydrogen reduction treatment. The lowest compressibility is shown by water sprayed HF 4 which, therefore, has a high oxygen content. Table 4 compares the mechanical properties of the sintered steel and, respectively, of the sintered and forged steel of the Fe2Ni-0.5Mo type including 0.3 and 0,8% graphite obtained using a mixture of iron powders with a powder made up of the alloy elements and, respectively, of pre-alloyed powder. Mention must be done that the considered mechanical properties in steels obtained using powder mixtures are higher in both conditions as compared to those obtained using pre-alloyed powder.

Table 4

Typical powder	C [%]	Density [g/cm^3]	Tensile strength [MPa]	HB hardness	Conditions
A1	0.15	6.55	330	72	sinter at 1200°C for 30 minutes in dissociated ammonia
A2	0.57	6.55	400	137	
B1	0.52	6.58	250	85	
B2	0.60	6.59	330	128	
A1	0.17	7.70	750	141	forging
A2	0.54	7.68	1120	211	
B1	0.14	7.70	675	156	
B2	0.47	7.72	925	159	

In Table 4 the mechanical properties in typical Fe-2Ni-0.5Mo sintered steels were obtained using A – powder mixture; B – Astaloy A pre-alloyed powder with additions of: 0.3% graphite – 1 and 0.8% graphite - 2.

Another method to obtain high strength alloy steels is to add to the pre-alloyed Ni and Mo powder another alloy element (Cu) in an elementary form. The effect of the copper addition to two types of pre-alloyed powders as to the mechanical properties under sinter and forging conditions are shown in Table 5. Copper enables that the system be sintered in the presence of the liquid phase. The effect of the copper addition as to the mechanical properties featured by sintered steels (6.5% density). Graphite addition: 0.3%. sintered at 1,200°C, 30 minutes. Atmosphere: dissociated ammonia; forging at 1,060°C in table 5.

Table 5

Typical powder	C [%]	Tensile strength [MPa]	Elongation [%]	HV 10 hardness	Conditions
A*	1.00	314	2.6	104	sinter at 1200°C for 30 minutes in dissociated ammonia
	1.50	325	3.3	118	
	2.00	312	2.3	121	
D**	1.50	256	3.5	87	
	2.00	294	3.0	87	
	2.50	308	2.8	95	
A*	1.00	765	16.5	204	forging
	1.50	882	11.9	215	
	2.00	903	12.5	222	
D**	1.50	650	20.5	221	
	2.00	685	17.3	227	
	2.50	708	16.7	247	

Conclusions

The compressibility of such pre-alloyed powders is subject to the chemical composition and to the purity.

The considered mechanical properties in steels obtained using powder mixtures are higher in both conditions as compared to those obtained using pre-alloyed powder.

By adding Cu in an elementary form, to pre-alloyed Ni and Mo powder, high strength alloy steels were obtained. The effect of the copper addition to two types of pre-alloyed powders as to the mechanical properties under sinter and forging conditions were shown. Copper enables that the system be sintered in the presence of the liquid phase.

Received April 26, 2007

REFERENCES

1. Popescu, R.: *Tehnologia materialelor* (Technology of materials), Bucharest, Editura Lux Libris, 2000
2. Brăgaru, A., and others: *Optimizarea proceselor şi echipamentelor tehnologice* (Optimization of engineering processes and equipment, Bucharest, Editura Didactică şi Pedagogică, 1996

CERCETĂRI ASUPRA PROPRIETĂȚILOR MECANICE ALE OȚELURILOR SINTERIZATE CU NICHEL ŞI MOLIBDEN

Rezumat: Această lucrare descrie metalurgia oțelurilor slab aliate, obținute din pulberi care conțin Ni şi Mo, pentru a produce elemente sinterizate de înaltă rezistență mecanică.

BULETINUL INSTITUTULUI POLITEHNIC DIN IAŞI
Tomul LIII (LVII), Fasc. 1, 2007
Secția
ŞTIINȚA ŞI INGINERIA MATERIALELOR

THE FISSURING MECHANISMS IN WELDED JOINTS

BY

N.V. CÂNDEA, R. M. POPESCU and D. SENCHETRU

Abstract: This work describes the looseness gearing of the welded conjunction due to thermal and structural stresses, by expansion, contraction, and phase transformations, that influences the technological and exploitation characteristics of metallic materials.

Keywords: materials, welding

When joining parts through welding, internal stresses might occur in the resulting products to be balanced within their volume, fully or partially remaining there as residual stresses. Stresses incurred by the welding process may be residual stresses and reaction stresses. The presence of the residual stresses sensibly influences product behaviour during the subsequent processing operations and during exploitation.

According to the cause which gives rise to them, internal stresses are of two kinds: *thermal*, i.e. due to the non-uniformity of the dilatations and the contractions further to the non-simultaneity of heating and cooling in different micro-volumes of the metallic body, and *structural*, i.e. due to the unevenness of the dilatations and contractions accompanying the phase transformations subject to the non-simultaneous heating and cooling in different micro-volumes of the metallic body.

The presence of the internal stresses sensibly influences the technological and operational characteristics of metallic materials, that is the metal products behaviour during the processing operations in service or even during storage.

From among the consequences that result in damages due to the presence of internal stresses in metal products, the most important ones are as follows:

1. alteration in shape and size further to subsequent processing and operation or during storage, in certain parts of the product, changes in the stress values which result in a disturbance of the forces and moments equilibrium and thus, in shape and size changes.

2. failure at much lower loads that the ones which would normally be withstood by the product in the absence of internal stresses. As these add up to the resulting stresses with the external loads, they may be increased or decreased. It is well known that if external tensile stresses overlap the remanent tensile stresses, cracks or failure can occur.

Internal stresses sensibly affect product behaviour under the chemical action of the environment combined or not with a mechanical action.

As to the extent and the distribution of remanent stresses, beyond uneven deformations due to the changes in the material volume while cooling, a certain

influence is also due to the volume changes occurring under the austenite decomposition temperature.

With different steel qualities, changes are subject to the carbon concentration and to the alloying elements. [1].

On grounds of the data shown in Table 1, assessments can be made as to the role of the composition on the occurrence of remanent stresses in welded joints.

Table 1

Steel quality	Austenite transfor-mation start temperature [°C]	Internal deformation before transfor-mation starts [%]	Stress before transfor-mation starts [daN/mm^2]	Temperature interval of compression stress availability [°C]	Internal deformation after cooling down to 200°C [%]	Stresses after cooling down to 200°C [daN/mm^2]
OL 370	680	+0.78	+1.7	670-550	0.33	+29
OLT 45K OLC 20	670	+0.72	+1.5	630-480	+0.30	+22
40Cr10	430	+1.4	+4.0	430-220	-0.22	+10
10TiNiCr180	-	+	+	none	+1.65	+24

In cross-section, heating is strong on the welding side and less strong on the opposite side. Over the entire length of the weld, heating is maximum next to the electric arc; in front of the arc components are cold and behind the arc they are under cooling process. Another source of stress is represented by possible expansions or contractions in welded structures.

The total amount of stress in welded parts is zero. The extent of the remanent stress further to this and to the deformations is subject to the heat quantity delivered during the unit time. This can vary much according to the applied welding procedure. Thus, at electric arc welding 50% lower heat quantity is transmitted during the unit time than in gas welding. The greater the melted metal volume the greater the contraction during the solidification period. The respective stress will occur in the same direction as the contractions, changing the steel structure and resulting in additional stress. Intense cooling of the welded area (or if using addition materials that can be welded in the air), welding structures such as bainite or martensite can build up. Alongside with these transformations a volume increase takes place accompanied by an internal stress generation.

Hydrogen penetration is intense both in the melted metal and in the basic material heated above 994°K which diffuses from the wet of the electrodes sheath. On cooling, as soon as structural transformations are completed, hydrogen, which is less soluble in ferrite and pearlite, agglomerates in the imperfection areas of the crystal lattice, thus giving rise to high local stresses. Therefore, it is necessary to observe the electrodes drying recommendations as well as to clean the joints, removing any trace of grease, rust, etc.

Welding under a 5°C temperature shall be avoided or performed by *protecting the welding spot* since steel contraction takes place more rapidly thus shortening $t_{8/5}$ and there is the risk to obtain welds with welding constituents. The great thickness featured by the parts to be welded results in high remanent stresses since inn addition

to the longitudinal and transversal stresses, thermal stresses occur over the weld thickness, as well. In this way spatial stresses occur, which are highly dangerous in terms of the welded construction security.

With steels showing no phase transformations within the welding temperature range, the arising issues are the grain size increase, carbide precipitations, and, in steels including much chromium, the occurrence of the σ_F phase [2] in the area influences by the heat. At high temperatures, some alloying elements such as chromium, build up carbides and get deposited in inter-grain layers making the steel to become fragile. In order to avoid this phenomenon, a rapid cooling is performed within the 500°C – 700°C range, by alloying with tantalum, niobium or titanium as well as by reducing the carbon content of steel.

The σ phase is an iron carbide at a 50% ratio each. It is hard and brittle. At the beginning it precipitates into inter-grain layers but as soon as it covers the layers, it occurs inside the austenite grains. Consequently, steel hardness is increased while its plasticity decreases.

The explanation of the structural fragility mechanism of the heat affected zone (HAZ), in weldable carbon and low alloy steels, shall also take into account the specific undulations imposed by the heat cycle on welding. Thus in HAZ favourable conditions are created for the occurrence of hard acicular welding structures, of high internal stresses and, finally, of micro-fissures and cracks.

Specific to such fissures is the fact that in the mechanism of their formation the main role is played by the concentration of the internal stresses, due to the *countersinking* phenomenon. This phenomenon is characterized by the crowding of the force lines in the vicinity of some discontinuities in the material or is due to other causes of geometrical nature. Thus, the countersinking phenomenon results in the transition of the material from the tenacious into a fragile condition.

As far as the countersinking phenomenon is concerned, this is due to the tensile stress level, required both for the development of the fissuring germs, and for the fissure propagation up to breaking (Griffith – Orowoan).

The fissures built up in the HAZ can be explained by the micro-model of dislocation agglomerations at the intersection of two sliding planes (Fig. 1) provoked by the deviation of the force lines next to the internal stress concentrators. [3].

The essence of the dislocation agglomeration mechanism resides in the idea that the sliding provoked by the movement of the dislocations from one source (Frank – Read source) is blocked by certain obstacles, such as, for example, grain boundaries. Internal stresses around the group head might reach the value of the steel cohesion resistance which, under certain load conditions, can result in local creeping phenomena and, implicitly, to the occurrence of micro-fissures. Then this micro-fissure propagates provided that Griffith's condition is met. Have not produced any prior sliding process whatsoever, since due to such processes stresses get relaxed. Any micro-fissure can propagate if the energy released thereby is at least equal to the one delivered from outside and if due to such increase and to the excess of released energy, the fissure propagation process is continued.

There are several methods for reducing the level of residual stresses in welded joints, which might result in fragility – fissures, but the most widely known is the application of a stress relieving heat treatment (TTD) after welding.

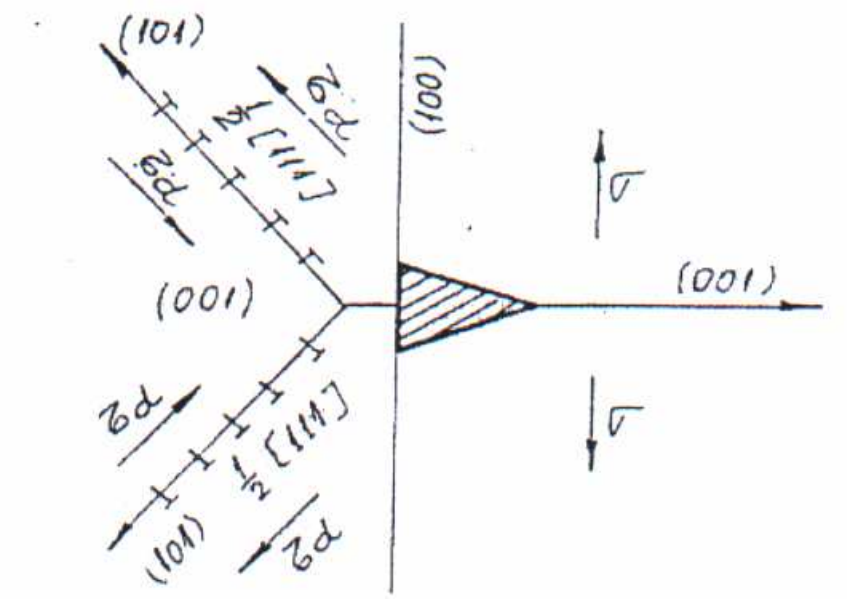

Fig. 1 Fissure formation due to the dislocations agglomeration mechanism according to Cottrell's theory

Such treatments feature multiple metallurgical implications, such as:

- restoring deformed crystal lattices;
- rearranging dislocations, carbide coalescence;
- providing some finely dispersed precipitates in the basic mass, as established during the TTD;
- blocking the sliding phenomena and the grain boundaries by a fine dispersion of stable particles (this dispersion is necessary for avoiding some uncontrolled structural transformations in cases where discontinuous precipitates occur, as well.

The above implications influence favourably or not certain mechanical characteristics (R_m, R_{p02}, A, Z, R_{cor}, KV, etc.) and structural features (shape and distribution of carbides, typical structures, etc.), onto which the welded structures behaviour in operation depends.

However, under these sophisticated circumstances, stress relieving heat treatments shall provide for the optimum reduction of the residual stress level, the restoration of the ductility in areas that got fragile, and the minimum degradation of the mechanical characteristics of the basic aim, unaffected by the thermal cycles on welding.

Beyond the effects that are favourable from the viewpoint of the reduction or the avoidance of fragile or inter-grain breaking, of dimensional stability or of corrosion under tension, the application of the stress relieving heat treatment after welding might result under certain circumstances in the degradation of the thermally influenced area, further to the fragility – fissuring phenomena.

Research carried out for the elucidation of damages in welded structures made of non-alloy (carbon) steels and alloy (low Cr-Mo alloy) steels submitted to stress relieving heat treatments highlighted the presence of some fine fissures, featuring a reduced (as low as 225μm) size, which are not noticeable by macroscopic analysis nor by X-rays.

Conclusions

Thus, in HAZ favourable conditions are created for the occurrence of hard acicular welding structures, of high internal stress and finally of micro-fissures and cracks.

The above implications influence favourably or not certain mechanical characteristics (R_m, R_{p02}, A, Z, R_{cor}, KV, etc.) and structural features (shape and distribution of carbides, typical structures, etc.), onto which the welded structures behaviour in operation depends.

For reducing the level of residual tensions in welded joints, which might result in fragility – fissures, there are several methods, but the most widely known is the application of a stress relieving heat treatment (TTD) after welding.

Received April 26, 2007

REFERENCES

1. Zgură, G., and others, *Tehnologia sudării prin topire (Welding engineering by melting)*, Bucharest, Ed. Facla, 1983
2. Voicu, S., *Controlul îmbinărilor şi produselor sudate (Control of welded joints and products)*, Timişoara, Ed. Facla, 1984
3. Pascu, D. R., *Influența factorilor structurali asupra caracteristicilor tehnologice şi proprietăților mecanice ale oțelurilor slab aliate pentru construcții sudate supuse tratamentelor termice post-sudare (Structural factor influences onto the engineering characteristics and mechanical properties in low alloy steels for welde dconstructions submitted to heat treatments after welding)*, Doctorate thesis, Bucharest, Institutul Politehnice, 1982

MECANISME DE FISURARE ALE ÎMBINĂRILOR SUDATE

Rezumat: Această lucrare descrie mecanismul de creare a jocului în îmbinările sudate din caza tensiunilor termice şi structurale, prin dilatare, contracție şi transformări de fază, care influențează caracteristicile tehnologice şi de exploatare ale materialelor metalice

BULETINUL INSTITUTULUI POLITEHNIC DIN IAŞI
Tomul LIII (LVII), Fasc. 1, 2007
Secția
ŞTIINȚA ŞI INGINERIA MATERIALELOR

METHODS FOR DETERMINING THE RELIABILITY OF SERVICE PIPES FOR TRANSPORTING CINDER IN POWER PLANTS

BY

N.V. CÂNDEA, R. M. POPESCU and D. SENCHETRU

Abstract: This work describes researches concerning the reliability of steel pipes, used for transporting cinder derived from thermo-electrical power stations and the problems that intervene of their consequent action.

Keywords: materials, reliability

Reliability represents the totality of features providing for the proper operation of a product in keeping with the prescribed norms, even beyond the warranty period. Reliability is defined as:

a) the entirety of the qualitative characteristics featured by a technical system which establishes the capacity thereof to be used under given conditions for the longest possible while according to its intended use;

b) a measure characterizing the safe operation of a technical system;

c) a measure of the probability of the safe operation of a technical system in keeping with the prescribed norms.

Reliability means "quality in time", the concept of reliability being closely related to the one referring to breakdown.

Breakdowns (failures) represent ceasing of the aptitude of a device to meet its intended use.

Also, reliability may be defined as being the aptitude of a device to meet its intended use under given circumstances and over a pre-set period of time.

Another component part of the concept of reliability is the ambient environment, the actual environmental conditions under which the product is operated. Environment strongly influences product performances as well as the actual life time / period of utilization thereof.

Should the product be utilized under environmental conditions other than those taken into account during its design and manufacturing phase, its operation might be seriously disturbed.

Reliability is a basic characteristic of any technical system or element, strictly depending on the quality of the given product or assembly, on the sale-purchase costs thereof, and, since it defines the behaviour during the entire lifetime of such technical systems or elements, also on the actual operating costs of the technological engineering. The general expression of correlation is given in Fig. 1.

In order to assess the reliability parameters the procedure to be used is pursuing the piping behaviour throughout its operation. Let's suppose that the piping is used

after a prior run-in (removal of the initial breakdowns/ failures) and before wear occurs (defects due to ageing), i.e. that the product is in its useful lifetime.

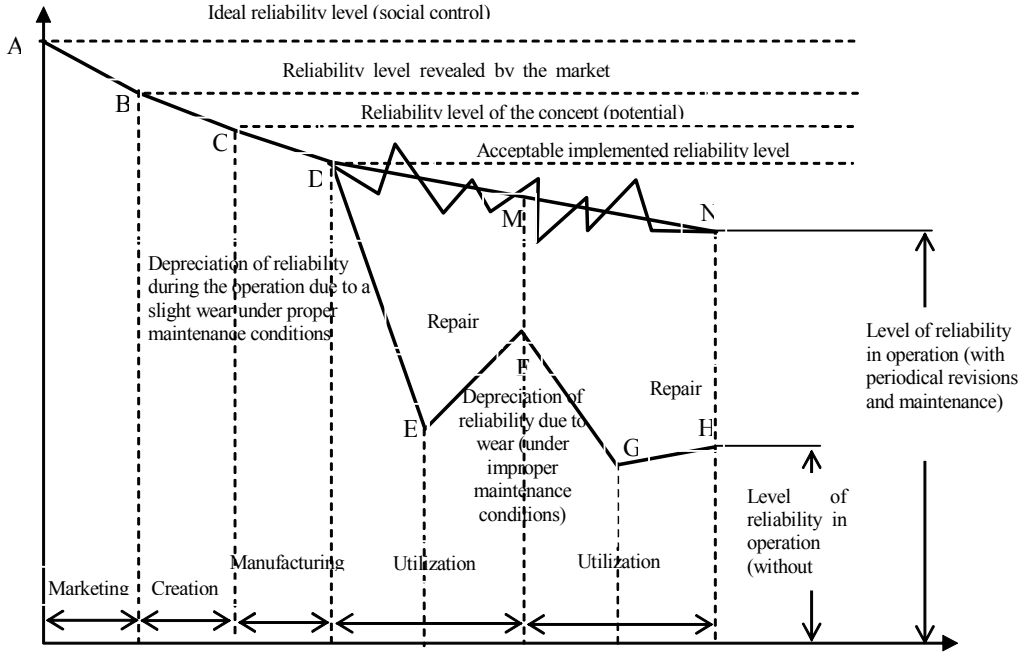

Fig. 1 Depreciation of reliability from its design phase to its operation

Statistical methods of reliability calculus on grounds of failure intensities (λ) feature a widespread, requiring, however, a longer period of time for the collection of statistic data. Probability methods are realistic and result in rational manufacturing output since they remove the shortcomings of the determinist methods introducing the value dispersion of input and output measures about the rated values, thus each and every input measure can be weighed against the output value.

Table 1 shows the lifetime of 10 ducts included in this study.

Table 1

Pipe no.	Operating time [h]	Pipe no.	Operating time [h]
1	228694	6	270605
2	242302	7	258605
3	242408	8	261308
4	258605	9	235986
5	264332	10	239794

The average operating time is:

$$t = \frac{\sum_{i=1}^{n} ti}{N} = \frac{12037353}{44} = 273576,2 \quad (1)$$

The main square deviation of the operating time is calculated using:

$$s = \sqrt{\frac{\sum_{i=1}^{N} ti \quad t}{N \quad 1}} = \sqrt{\frac{1}{N \quad 1} \sum_{i=1}^{N} ti^2 \quad \frac{\left(\sum_{i=1}^{N} ti\right)^2}{N}} = 32776,7 \qquad (2)$$

The calculation algorithm is initiated at a t= 250,500 hours and a c = 275,400 hours value. The average operating time, in another calculation version, results in:

$$t = a \quad \frac{\sum_{i=1}^{N} ti^1 \quad ki}{N} + c = 296863,6 \qquad (3)$$

The main square deviation of the operating time is determined using:

$$s = a \quad \sqrt{\frac{1}{(N \quad 1)} \sum_{i=1}^{N} ti^{1\,2} \quad ki \quad \frac{1}{(N \quad 1)} \sum_{i=1}^{N} \frac{\left(ti^1 \quad ki\right)^2}{N}} = 32802,5 \qquad (4)$$

Piping in steam power plants shall operate without failures whatsoever during a certain time interval, usually for a long while, under given operating conditions. In the power supply industry, sizing relies on codes and calculation norms. Establishing permissible theoretical strength values is an important issue. Some norms confine themselves only to showing the way how permissible strength values are calculated, while others provide actual values for each acceptable material. Both ways, when establishing permissible strength values, the starting point is to find values that are guaranteed by norms for the strength characteristics of materials. All these characteristics are static measures. Piping elements in steam power plants feature an acceptable breaking probability even in their design phase. The breaking probability is lower in the design phase and increases in time, while the safety coefficient decreases down to a minimum value established for the calculated operating time.

Metallurgical degradation is mainly due to the structural deteriorations and especially to the fluctuations of the precipitates as well as of the alloy elements in the metal matrix. Structural degradations are difficult to be detected in operation from a quantitative point of view. Such degradations result in inter-grain erosions by cavitation, which determine the fragile rupture at high temperatures in steels. Mechanical degradation takes place due to cavity and micro-fissure forming processes, which are more easily detectable parameters in making estimates as far as the operating time is concerned.

Micro-structural research works related to the steels covered by this study highlight that further to a prolonged operation at normal parameters, irreversible changes occur therein, ferrite grains increase in size, pearlite areas get dispersed, carbides get precipitated and coalescence thereof takes place. The incurred structural modifications are the reason for changes in mechanical characteristics. Thus, the precipitation of some very fine carbides results at the beginning in increased mechanical strengths, and the quantity increase in precipitated carbides on the limit in between the grains as well as the coalescence thereof result in a decrease of the strength properties and ultimately, of the strength reserve. The mechanical characteristics of the piping materials, as established by static tests (R_m, R_{p02}, δ_5, Z),

show values that are greater than the ones prescribed for the material in delivery condition. The same holds true for resilience, too, i.e. shows values greater than the ones prescribed by the norms.

Studying the reliability curve is based upon the survival curve of the piping. An operation to be carried out prior to establishing the theoretical law is to remove from among the multitude of collected data, the non-homogeneous ones, which, being gross errors, are not included in the given repair.

Reliability, as a modern concept with technical, economical and social reverberations imposed by the industrial development, succeeds to define and characterize from a qualitative viewpoint the constructive concept adopted by the designer, the manufacturing method, the technical security in operation, the level of acceptance and maintenance expenditures, as well as production losses due to the frequency and the duration of breakdowns (failures).

There is no 100% reliability nor technical security since practically one must take into account the occurrence of the so called force major events. It is necessary to be aware of the optimum reliability or, respectively, technical security levels, and also, of the fact that about 95% of the piping failures are due to technological engineering activities and only about 5% are due to the working personnel.

On grounds of the professional knowledge concerning the manifestation logics of the piping behaviour in steam power plants, the hypothesis concerning the theoretical law of reliability is formulated to be followed by the experimental data. Non-homogeneous data (gross errors) are removed on grounds of the known tests. If reliability is high, failure rates are low. The reliability, the strength reserve as compared to the yielding limit and the strength reserve as compared to the breaking limit provide full information as far as steam power plant piping behaviour is concerned.

Conclusions

The mechanical characteristics of the piping materials as established by static tests (R_m, R_{p02}, δ_5, Z) show values that are greater than those prescribed for the material in delivery condition. The same holds true for resilience, too, i.e. shows values greater than the ones prescribed by the norms.

Received April 26, 2007

REFERENCES

1. Dima, A., *et al*, *Cuptoare şi instalaţii de încălzire - elemente de încălzire şi proiectare constructiv-funcţionale* (Heating ovens and installations – heating elements and constructive – functional designs), Iaşi, Ed. Gh. Asachi, 1993

2. Mitelea, I. *et al*, *Selectarea şi utilizarea materialelor metalice* (Selecting and using metal materials), Timişoara, Ed. Politehnica, 1998

METODE DE DETERMINARE A FIABILITĂŢII CONDUCTELOR DE TRANSPORT AL ZGUREI ÎN CENTRALELE TERMICE

Rezumat: Această lucrare descrie cercetările referitoare la fiabilitatea conductelor de oţel, utilizate pentru transportul zgurei provenite din centralele termice şi a problemelor ce intervin din acţiunea lor.

BULETINUL INSTITUTULUI POLITEHNIC DIN IAŞI
Tomul LIII (LVII), Fasc. 1, 2007
Secția
ŞTIINȚA ŞI INGINERIA MATERIALELOR

THE INFLUENCE OF ALLOYING ELEMENTS ON STEELS USED IN STEAM POWER PLANTS

BY

R. M. POPESCU, V.N. CÂNDEA and D. SENCHETRU

Abstract: This work describes the influence of alloying elements Ni, Mn, Cr, Si, P, S and Mo on the structure and mechanical properties of steel used in thermo power stations.

Keywords: metallurgy, materials

Steels used in steam power plants shall feature good mechanical properties, stability and withstanding to corrosion, as well as heat conductivity, dilatation and elasticity module of acceptable values.

Subject to the working pressure and the operating temperature, either carbon steels or especially Cr, Mo or Cr-Ni alloy steels are used.

In cases where the working pressure does not exceed P_{max} = 6 MPa and the operating temperature T_{max} = 400°C, OLT 35K and OLT 45K (STAS 8148-87) carbon steels and 16Mo3, 14CrMo10, K410, K460, K510 (STAS 2883/3-88) alloy steels are used. [1]

For a p_{min} = 15 MPa working pressure and a T = 550°C operating temperature ferrite and martensite steels are used. Such steels feature the following characteristics:

- a good creeping / yielding limit and fatigue strength at the operating temperature;
- tenacity both at ambient temperatures and at high temperatures;
- phase transformation spots occur at temperatures higher than the ones at which they are used;
- withstanding corrosions due to chemical substances, and wears due to erosion

Austenite steels are used for piping operated at T = 800°C in cases of short operating times and at a T = 700°C in cases of long operating times. There are alloy steels including 14÷ 30% Cr and 8÷35% Ni and elements such as Mo, W, Ti, Nb, V, Cu, Si, Mn, N in a smaller quantity and a C content under 0.1%. Austenite structures in these steels are hardened due t the precipitation of certain secondary phases (carbides, carbonates, inter-metallic compounds).

The mechanical properties featured by steels used in steam power plants at high temperatures are influenced by the chemical composition, by micro-structures and by the size of the grain. Breaking strength, creeping / yielding limits in these steels can be improved by Mo, Ti and Nb additions.

In Cr-Ni Austenite steels carbides are instable in the 427÷870°C temperature range, precipitated at the grain limits and decrease the withstanding to corrosion, however do not decrease the breaking strength or tenacity at ambient temperatures.

Cr-Ni austenitic steels can undergo an ageing during operation, thus resulting in fragility. This is decreased in cases where the steel includes Ti or Al additions.

Ni influences.

Alloy steels including Ni are more expensive, since the Ni is obtainable at a price of conjuncture. Ni alloy steels (Fig. 1) having a pearlitic structure, feature an elongation and an entirely special resiliency as well as a high breaking strength.

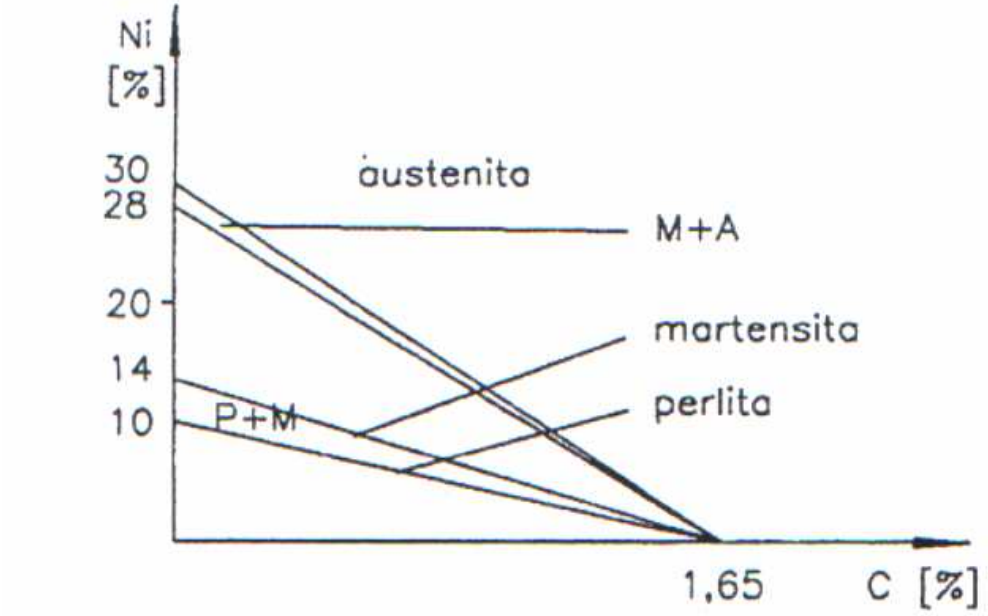

Fig. 1 Structural diagram of Ni alloy steels

Martensitic steels (Fig. 2) feature a very high breaking strength and limit of elasticity. However, the maxim strain to failure is low and therefore these steels have not much practical use, since they are fragile and difficult to be processed.

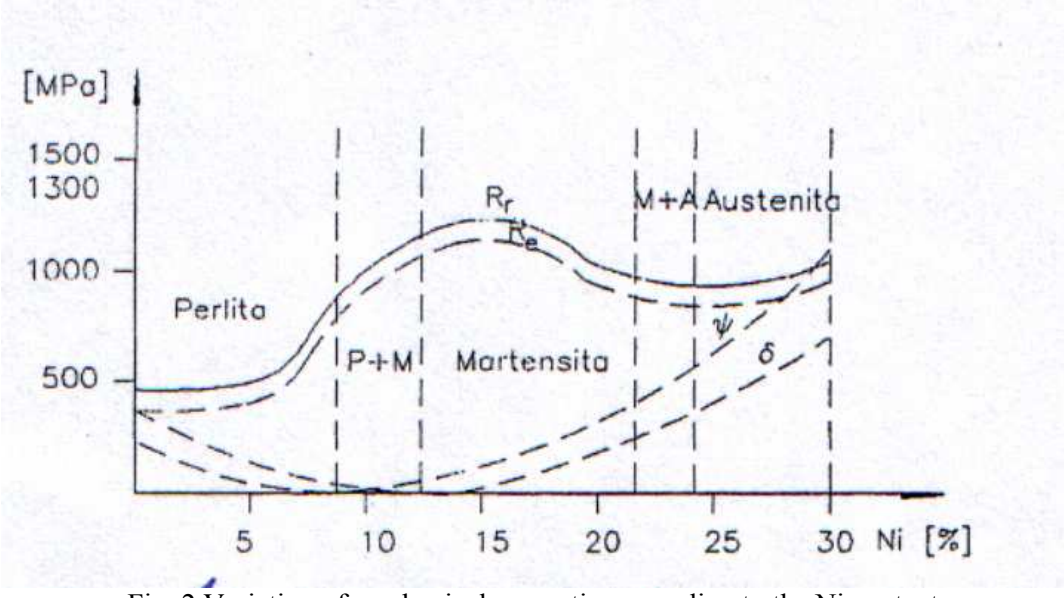

Fig. 2 Variation of mechanical properties according to the Ni content

Austenitic steels feature a breaking strength and elastic limit of low values, but their elongation and specific constriction are high. Since nickel does not form carbides, it has no influence on the steel hardness in annealed condition. Ni is associated with elements which form carbides (Cr, W, Mo), thus obtaining steels with obviously superior mechanical properties

Mn influences

.Manganese does not build special carbides, but a Mn_xC, which is totally miscible in cementite. Mn alloy steels (Fig. 3) feature the same patterns as the Ni alloy steels, but a smaller quantity is needed for changing the structures. A 0.2% C and 12% Mn steel is austenitic, while the same steel in a Ni alloy features a pearlitic structure. Mn incurs a breaking strength increase in annealed condition.

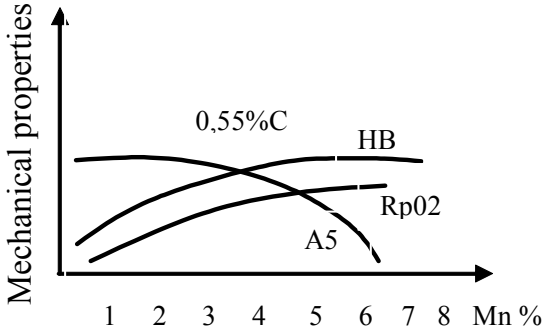

Fig. 3 Variation of mechanical properties according to the Mn content

For a 055% carbon content and a proper heat treatment, Mn produces a R_m, R_{p02} and HB increase and a decrease in elongation. Austenitic Mn alloy steels feature a pronounced tendency towards cold-hardening. Therefore their tensioning curve is a constantly ascending one. This high tendency towards cold-hardening featured by austenitic Mn alloy steels is the very reason why are they so difficult to be processed. Mn additions in small quantities result in significant hardening capacity increases. Manganese does not confer good magnetic properties to steels

Chromium influences

. Low carbon and 18% Cr content steels are ferritic at any temperature. As the carbon content increases, the steel can be austenitized and therefore, also hardened. Depending on the C and Cr content, steels can be pearlitic (1.67% C and 0 ÷ 8% Cr), martensitic (0 ÷ 1.66% C and 8 ÷ 18% Cr) which is characterized by its high hardness values due to the stable carbides that are built up to confer to the steel a high withstanding capacity to wear and qualities that make it suitable for undergoing chip removing processes. Hardening steels using Cr is accompanied by a decrease in resiliency and elongation. In order to cancel this effect, Ni quantities are added.

The steel hardening capacity increases as Cr content increases:

- a Cr content of at most 1% favours steel hardening capacity;
- a Cr content of 1 ÷ 3% increases withstanding to hydrogen under pressure and favours steel nitriding;

- as the Cr content increases, steels turn to be more withstanding to oxidization and corrosion;
- Cr contents over 30% make steels refractory;
- Chromium increases hardness, withstanding capacity to wear, decreasing however resiliency

Si influences

When smelting some steel qualities, Si is added to bind oxygen and reduce ferrous oxide (FeO) formed during the refining process. Should steels be rich in C, the Si can form carbides, too, and when Si is present in great quantities (over 3.5%), then it can graphitize the steel. Since Si features a great affinity to O_2, it forms silicate oxydes $(FeO)_2SiO_2$, $(MnO)SiO_2$, which persist as inclusions and might result in fibrous patterns during plastic deformations.

Si increases R_r and R_e with about 100 MPa for each 1% Si. Specific elongation is slightly decreased when the content does not exceed 2.2% Si; also, Si increases the strength to wear of the steel. When steels include Cr and Al, then the additions result in an increase in terms of the withstanding capacity to oxidation at high temperatures.

P influences

Phosphor can reduce weldability, favouring the occurrence of fragile breaking. Weldability of steels featuring a low (max. 0.17%) C content is not affected by the presence of the phosphor.

Phosphor dissolved in ferrite results in increasing the capacity to withstand corrosion in slightly corrosive atmosphere (industrial environment in metallurgical plants, glassware factories, building workshops). Thus, phosphor is one of the main impurities and brittles steel, so that its content is limited (to as low as 0.03÷0.06%).

S influences.

At high temperatures, sulphur produces brittleness and also, decreases steel tenacity, so that the S content thereof is set to 0.02% at most. Sulphur is an element which is suitable for chip removing processes due to the manganese sulphur which acts as a lubricant. Sulphur does not influence steel weldability unless participating in great quantities, and it decreases corrosion withstanding, as well.

Mo influences

Molybdenum influences the increase of the mechanical properties maintaining the steel tenacity. At high temperatures, it builds up with C and the compounds thereof Mo carbides (Mo_2C), which are fragile and very hard.

Introducing too much molybdenum induces in steels some tendency towards fragility. The influence of the molybdenum is shown by very small contents, i.e. of as low as 0.1% and progressively increases as this small content increases. Usually, molybdenum is added to steels in 0.4÷1% quantities, and only in cases of exception

this exceeds 2%. Molybdenum rises the re-crystallization temperature and favours the occurrence of stable carbides and some intermetallic compounds thus resulting in a breaking limit increase.

Pipes tubes in steam power plants are made of low alloy steels according to STAS -2883-88 and STAS 8184-87, in lamination sizes according to STAS-404-59.

Technical conditions for steam pipes shall meet the requirements given in the STAS-2478-82 standard. For ducts operated at temperatures above 450°C, the technical conditions shall be supplemented accordingly, with the conditions set forth for high temperatures, i.e. with the hot mechanical characteristics and with the micro-structure analysis; for temperatures in excess of 550°C, these technical conditions shall the supplemented with the inter-crystalline resistance to corrosion. Romanian low alloy steels shall meet the technical conditions set forth in STAS-8184-87 and STAS 2883/3-88 (see Tables 1, 2). [1].

Table 1

Quality	C [%]	Si [%]	Mn [%]	Cr [%]	Mo [%]	Other elements [%]
16Mo3	0.12÷0.2	0.15÷0.35	0.5÷0.8	-	0.25÷0.4	Al 0.01÷0.03
14MoCr10	0.1÷0.18	0.15÷0.35	0.4÷0.7	0.7÷1.1	0.4÷0.55	Al 0.015÷0.045
12MoCr22	0.08÷0.15	0.15÷0.5	0.4÷0.7	2÷2.5	0.9÷1.1	Al 0.015÷0.045

Table 2

Quality	R_c [MPa]				
	200°C	300°C	400°C	450°C	500°C
16Mo3	225	180	160	155	150
14MoCr10	240	215	190	180	175
12MoCr22	245	230	205	195	185

At temperatures over 250°C, steel oxidizes so quickly, that it gets covered with magnetite (Fe_3O_4) in a very short while under favorable conditions building up a compact and adherent layer that acts as a protection layer for the metal.

The subsequent evolution of the corrosion is mainly defined by diffusion, since iron and water cannot react in between themselves unless and to the extent iron diffuses through the protective layer. However, the diffusion process is very slow so that there is no metal loss to be mentioned. Should the protection layer be destroyed, a rapid oxidation takes place. When this phenomenon occurs repeatedly in the same place, then the pipe is destructed. The magnetite layer built up by the overheated steam is not free from strains, since its volume is twice bigger than the oxidized iron quantity.

At temperatures over 570°C, Fig. 4, instead of magnetite (Fe_3O_4), ferrous oxide can be built up, which no longer features protective properties. It builds up rapidly and damages the pipe in a short while. The chemical reaction that takes place with this type of corrosion is:

$$3Fe + 4H_2O \rightarrow Fe_3O_4\, 4H_2 \quad (1)$$

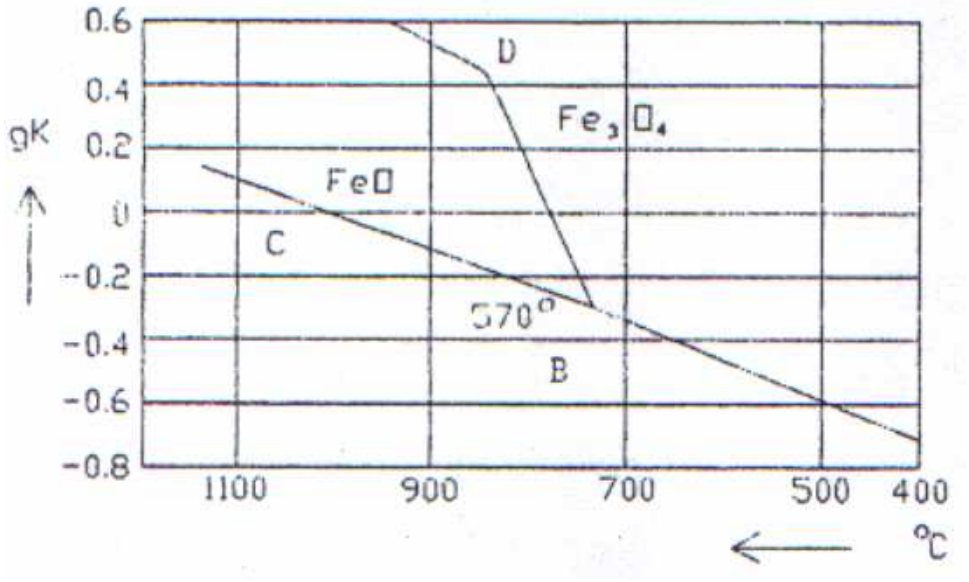

Fig. 4: Corrosion variation according to temperature

Usually, the reaction starts at a 450°C steam temperature. Speed is significant for the reaction progress: over 15 m/s no corrosion occurs, at 4 m/s there occurs H_2 and at 0.12 m/s corrosions are severe. Steam decomposition and its reaction with the steel has been studied by Chaudron. Steam action can be reduced almost entirely if a Fe_3O_4 protective layer is provided before

4. Conclusions

For ducts operated at temperatures, the technical conditions shall be supplemented accordingly, with the conditions set forth for high temperatures, i.e. with the hot mechanical characteristics and with the micro-structure analysis; for temperatures in excess, these technical conditions shall the supplemented with the inter-crystalline resistance to corrosion. The subsequent evolution of the corrosion is mainly defined by diffusion, since iron and water cannot react in between themselves unless and to the extent iron diffuses through the protective layer.

Received April 26, 2007

REFERENCES

1. Dima, A., *et al.*, *Cuptoare şi instalaţii de încălzire - elemente de încălzire şi proiectare constructive -funcţionale* (Heating ovens and installations – heating elements and constructive – functional designs), Iaşi, Ed. Gh. Asachi, 1993
2. Mitelea, I. and others, *Selectarea şi utilizarea materialelor metalice* (Selecting and using metal materials), Timişoara, Ed. Politehnica, 1998

INFLUENȚA ELEMENTELOR DE ALIERE ASUPRA OȚELURILOR UTILIZATE LA COINDUCTELE CENTRALELOR TERMICE

Rezumat: Această lucrare descrie influenţa elementelor de aliere Ni, Mn, Cr, Si, P, S şi Mo asupra structurii şi proprităţilor mecanice ale oţelurilor utilizate pentru conductele din centralele termice.

BULETINUL INSTITUTULUI POLITEHNIC DIN IAŞI
Tomul LIII (LVII), Fasc. 1, 2007
Secția
ŞTIINȚA ŞI INGINERIA MATERIALELOR

THE BEHAVIOUR OF PLASTIC DEFORMATION SLIM BANDS WITH HIGH MECHANICAL PROPERTIES

BY

R. M. POPESCU, V.N. CÂNDEA and D. SENCHETRU

Abstract: This work describes the technology for obtaining metallic straps with high mechanical properties, and the heat treatments used for reducing the level of plastic yielding and obtaining some reduced grain size.

Keywords: materials, plastic yielding

The behaviour during a plastic deformation of a metallic material as well as the effect of the deformation in terms of the material structure and properties differ depending on the ratio between the temperature at which the said deformation took place as compared to a certain characteristic temperature known as re-crystallization temperature. Cold plastic deformations incur in metallic materials three main types of structural alterations:

- in the shape and the dimensions of the crystal grain;
- in the spatial orientation of the crystal grains;
- a fine modification in the grain

As the extent of the cold deformation increases, grains get more and more elongated in the direction of the lamination getting the aspect of a fiber, the corresponding structure being named fibrous structure or cold plastic deformation fibering.

Along with the alteration of the crystal grain structure a change in their spatial orientation by the rotation of the crystal lattice takes place, too. Thus certain crystallographic elements are prone to be directed towards the direction of the deformation. The structure of such materials is called texture. The deformation texture mainly depends on the processing method. Cold plastic deformations result in significant alterations of the physical and mechanical properties. Thus, the tensile strength, yielding / creeping limit, hardness are increased as the deformation degree increases, while plasticity properties, just as the elongation and the constriction, decreases. The material becomes harder, stronger, less plastic – and this phenomenon is called hardening by deformation or cold-hardening. The cold-hardening capacity of a material is characterized by the cold-hardening coefficient. During the cold deformation process alterations of the physical properties occur, as well: the electric resistivity and the coercive field increase as the deformation degree increases. The condition attained by cold plastic deformation is a condition featuring a higher internal energy than the one of the non-deformed material. So, cold-hardened materials feature a spontaneous tendency to reach a condition of equilibrium. Applying a thermal

activation (heating), cold-hardened metallic materials can get a condition of equilibrium.

The heat treatment [1] i.e. heating the cold-hardened material for getting into the condition of equilibrium is called re-crystallization tempering. Subject to the temperature and the heating duration, inside the cold-hardened material there take place the following phenomena: restoring or re-establishing, re-crystallization and the increase of the grains.

Restoration involves two stages: expansion or detent and polygonizing.

Expansion is the phase where physical properties are restored without any possibility whatsoever to notice changes in the cold-deformed metal micro-structure During restoration, electric conductibility increases rapidly, heading towards a value corresponding to the annealed material. Restoration takes place at temperatures under the re-crystallization temperature, since in this phase there take place the diffusion process of the punctual defects, the annihilation of some punctual defects and of some dislocations featuring a contrary sign, located on the same sliding plan.

In the final restoration phase, in the vicinity of the re-crystallization temperature, dislocation structures are re-arranged into configurations of equilibrium.

The *actual re-crystallization* or primary re-crystallization is the process through which cold plastic deformation structures are replaced by a new generation of non-deformed grains. Actual re-crystallization takes places at a temperature above the re-crystallization temperature and is achieved through a germination and increase process. The motive force of the re-crystallization process is the elastic deformation energy of the crystal lattice.

Grain increase represents the last phase of the re-crystallization process and takes place as the temperature rises (beyond the re-crystallization temperature) and of the temperature hold period. Grain increase is determined by the high superficial energy featured by the small and uneven grains obtained by re-crystallization.

Mainly, re-crystallization is influenced by the following factors: the size of the deformation degree, the deformation temperature, the initial dimension of the grain, the chemical composition, and, respectively, the purity degree of the material.

The starting re-crystallization temperature decreases as the deformation degree increases up to a value known as re-crystallization threshold. Temperature, as a factor, is more important than the time factor. Doubling the annealing time is approximately equivalent to a 10°C increase in terms of the annealing temperature. During the re-crystallization process, all properties are changed reversely to the variation of the cold plastic deformation.

The continuous increase in of the user requirements and exigencies as far as product quality is concerned, as well as the high technical level attained due to the upgrading works carried out in production units, resulted in the accomplishment of a new and efficient system for steel bands lamination process monitoring. Such upgrading works involve the following:

1.- Utilization of high-performance control and measuring equipment [2], band speed measuring device using the laser technology, band profile measuring device using a measuring roll provided with piezoelectric sensors, numeric systems intended for the adjustment of the working cylinders speed, high-performance hydraulic systems for the cylinders displacement, high-accuracy apparatuses for measuring the

band thickness deviations, etc.

2. -Using high-performance hierarchic calculation systems to provide for the management of the lamination process according to different priority levels;

level 0, accomplished by the instrumentality of micro-controllers intended for the management of the electric actuating systems;

level 1, represented by automatic systems intended for the adjustment of the band thickness and profile;

level 2, represented by artificial intelligence (neuro-fuzzy) interfaces for modelling and general management purposes in the lamination process.

Up-to-date industrial management systems are mainly based on the experience gained by the human operators. Laminating tensions, and especially the tension distribution subsequently applied to the band, affect both the smoothness thereof and the control of the band shape according to its width in cold lamination processes. As the band smoothness decreases during lamination, an uneven subsequent tension distribution builds up in the deformation area of the band. The presence of the subsequent tension influences the transversal yield in metals, improving the band smoothness.

Nickel/iron alloys featuring high nickel contents, show special magnetic, thermal or elastic properties. Nickel strongly influences the linear expansion coefficient in iron; the Fe-Ni alloys expansion coefficient passing through a value near zero with 36% Ni. Changing the nickel content in iron-carbon alloys, steels featuring the expansion coefficient of some materials can be achieved, so that they can be welded with those very materials. Thus, 40% Ni steels have the same expansion coefficient as porcelain, 0.2%C and 46% Ni have te same expansion coefficient as platinum and glass. Nickel exerts an especially strong influence on the magnetic properties of the iron. The initial magnetic permeability (μ_a) highly increases with 78.5% Ni. Cold plastic deformation results in a reduction in terms of the magnetic permeability. However, if followed by a crystallization annealing, it results in the formation of a crystal texture that improves the magnetic permeability.

The applied subsequent tension influences smoothness in cold laminated bands by the intensity of the lateral creeping. The value of the subsequent tension is the one to [provide for and make even the band smoothness. It is mandatory to take this into account in calculi accompanying smoothness control band laminations. Entering the shape altering coefficient (α_j), the evenness of the subsequent tension applied to the laminated band can be quantitatively assessed.

Roll mills are up-graded according to the following directions: increasing the cylinder strength (reduction of wear and of the specific consumption), reducing the roll mill rotary parts as well as the weight thereof, increasing the laminating accuracy and improving the laminate quality; automation of the engineering processes and reducing the power consumption used in the manufacturing process. Roll mills will further be developed as lamination units according to the increase of the customers' exigencies, with the possibility to directly increase the referenced characteristics. Such exigencies shall especially result in reduced thicknesses, in combination with an increase in terms of the mechanical characteristics. Nowadays, lamination is no longer a simple method to get the final geometry of the product in the metallurgical industry, since managing the lamination process in a certain way, it becomes possible to obtain a given structure

to endow laminated products with the desired mechanical characteristics. When choosing the technological characteristics for lamination purposes, there shall be taken into account of the influence exerted thereby onto the structural transformations occurring during deformation (re-crystallization, phase transformation). Reviewing the measures playing a role of influence and on which material properties depend, technological measures can be defined for obtaining steel aspect and structure. Up-to-date roll mills enable now to meet close tolerances and, in addition, up-to-date lamination engineering enables the exertion of certain influences on the material properties, as well. Modern roll stands feature high laminating forces and high-performance measuring and adjusting installations.

Moreover, in addition to high productivity rates, recent band roll mills are provided with the most up-to-date improvements for accomplishing high quality products. A special importance is given to providing close tolerances for thicknesses over the width and the length of the band. Therefore, the most recent roll stands feature a very high rigidity (given by the big diameter of the supporting cylinders and the great weight of the frames), an automatic thickness control (gage-meter AGC) function to be operated during lamination, cylinder counter-curving devices and thickness measuring installations for providing the most suitable transversal profiles in bands.

4. Conclusions

The temperature and the heating duration, inside the cold-hardened material there take place the following phenomena: restoring or re-establishing, re-crystallization and the increase of the grains. Restoration involves two stages: expansion or detent and polygonizing.

Primary re-crystallization is the process through which cold plastic deformation structures are replaced by a new generation of non-deformed grains. Grain increase represents the last phase of the re-crystallization process and takes place as the temperature rises (beyond the re-crystallization temperature) and of the temperature hold period. The continuous increase in of the user requirements and exigencies as far as product quality is concerned, as well as the high technical level attained due to the upgrading works carried out in production units, resulted in the accomplishment of a new and efficient system for steel bands lamination process monitoring.

Received April 26, 2007

REFERENCES

1. Cazimirovici, E.: *Teoria deformării plastice (Theory of plastic deformations)*, Bucharest, Editura Academiei, 1995

2 Crivineanu, C.: Referat teză de doctorat: Aliaje Fe – Ni şi obținerea acestora *(Doctorate thesis reference: Fe-Ni alloys and production thereof*

COMPORTAREA BENZILOR SUBȚIRI, CU PROPRIETĂȚI MECANICE RIDICATE, OBȚINUTE PRIN DEFORMARE PĂLASTICĂ

Rezumat: Această lucrare descrie tehnologia de obținere a benzilor metalice, cu proprități mecanice ridicate, tratamentele termice folosite pentru a reduce nivelul curgerii plastice şi a obține o granulație scăzută.

BULETINUL INSTITUTULUI POLITEHNIC DIN IAŞI
Tomul LIII (LVII), Fasc. 1, 2007
Secția
ŞTIINȚA ŞI INGINERIA MATERIALELOR

THE MODIFICATION OF TITANIUM SURFACE STRUCTURE BY PHYSICAL AND CHEMICAL METHODS

BY

NĂSTACA TIMOFTE, BODGAN NICOLAU and VIOREL MOLDOVAN

Abstract: Because of mechanical properties and biocompatibility, the titanium is used in dental applications and in orthopedics. For the improvement of the biocompatibility of the pure commercial titanium's surface, were used some methods, which could be classified in: (i) physical methods; (ii) chemical methods; (iii) combined methods. This study attacks physical and chemical methods of changing the structure of the titanium's surface, which has as the purpose to accelerate the osteointegration. This is made by covering with hydroxiapatite or other phospho-calcium materials, by mechanical spraying, by anodic oxidation, or acids etching. For changing the titanium's surface, were used the following physical and chemical methods: (a) etching of the titanium's surface in acid medium; (b) biomimetical deposit of hydroxiapatite from solution; (c) activation of surface by alkaline treatment; (d) biomimetical deposit after alkaline activation..

Keywords: biomimetical, the immersion, osteointegration, biocompatibility

1. General aspects

The titanium is intensive used in orthopedic and dental applications, because of his mechanical properties and biocompatibility. The deficiencies appeared at the contact of the bone with titanium implant need a change of its surface, which is realized by covering with hydroxiapatite or some other phospho-calcium materials or by mechanical spraying, by anodic oxidation, or etching with acids.

The preparing of the titanium surface needs the removal of damaged superficial ledges, named in this case "carving by polarizing".

The etching techniques are:

- the immersion (the most often used);
- continuous sprinkling with solution;
- electrolytic etching;
- etching with gas**.**

2. The etching of titanium surface in acid medium

The etching process in order to create a rugged surface was effectuated according to scheme I.

The image of the titanium surface before the chemical etching and after the treatment with acid is presented in fig. 1.

The images have shown the obtaining of an uniform attack of surface with the 5…15 μm cavity alternating with equal irregular proeminences. The proofs' color has

been changed into dark grey and the surface has got a rugged, matte aspect.

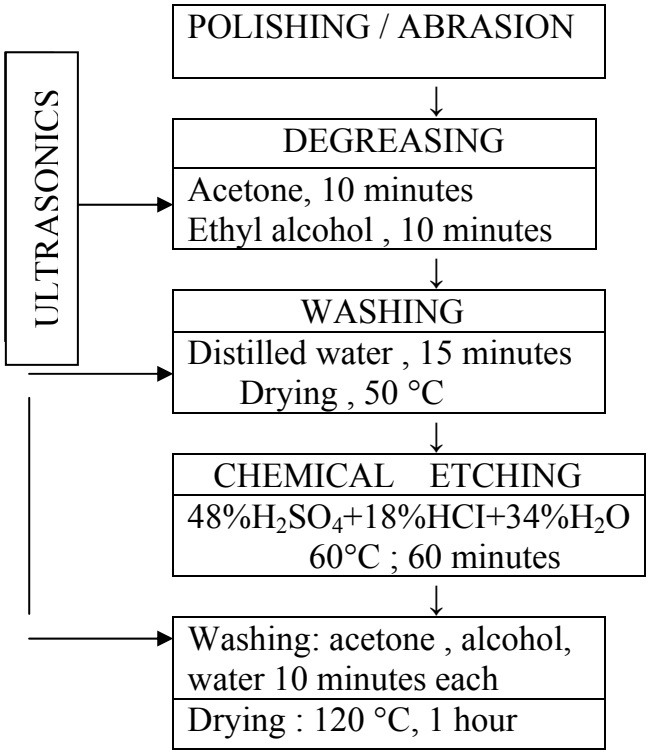

Scheme I. The chemical etching of the titanium samples through acid treatment

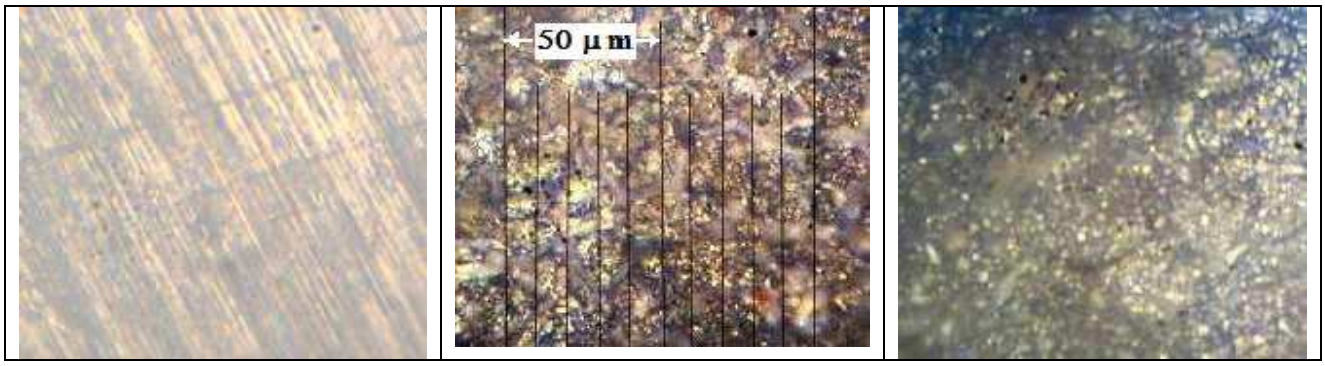

Fig.1 The image of the titanium surface before and after the chemical etching (x 500)

Due to this treatment the contact surface between the implant and tissues increases, improving the adherence at the implant's surface as well as the quality of some hydroxiapatite or other phospho-calcium materials deposits (biomimetical electrophoresis method 2).

3. The biomimetic deposit of hydroxiapatite in solution

The covering with hydroxiapatite by spraying in plasma has some inconvenient. This process can't assure an uniform covering on metallic porous surfaces. Using this method, the biological active apatite layer formed on a certain layer, after the immersion into a phospho-calcium supersaturated solution artificially prepared, which

contains organic components as in the human plasma, but in larger concentrations. This kind of solution is named **simulated body fluid (SBF)**.

The process is based on heterogeneous nucleation of the calcium phosphate from SBF, which is supersaturated in hydroxiapatite at pH=7,4 and 37^o C, (in biological conditions). The classical biomimetical covering with Ca-P needs an immersion period of 14-28 days, with a repetitive change of the solution. The global process is illustrated in scheme nr Π. The solution's composition is indicated in table 1.

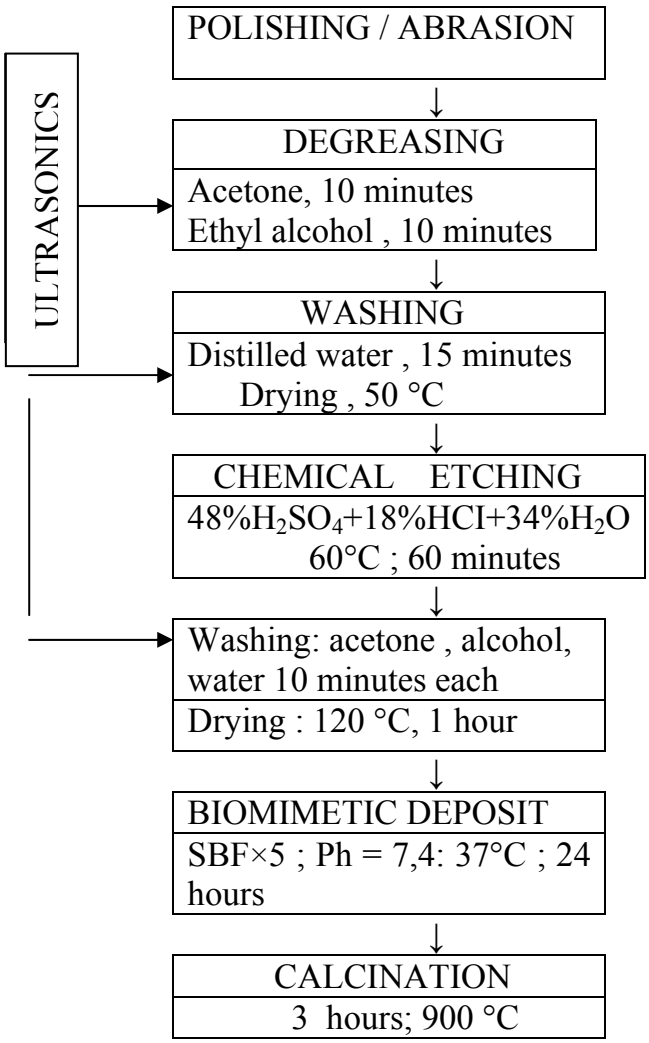

Scheme II. The biomimetic deposit of the hydroxyapatite from the super-concentrated simulated human plasma

Table I. The human plasma composition and some simulated fluids (m mol/l)

Solution	NaCl	$MgCl_2.6H_2O$	$CaCl_2.2H_2O$	Na_2HPO_4	$NaHCO_3$
Plasma	146,7	1,5	2,5	1,0	27,0
SBF	146,7	1,5	2,5	1,0	4,2
SBFx1,5	220.1	2.3	3.8	1.5	6.3.
SBFx5	733.5	1.5	12.5	5.0	21.0

In the experiment it was realized the modification of the surface by quick biomimetical deposal from the SBFx5 solution, on rugged surface, without any kind of

previous activation.

The microscopically analysis of the proofs is presented in fig.2, for the rugged proofs biomimetical deposit and calcinated.

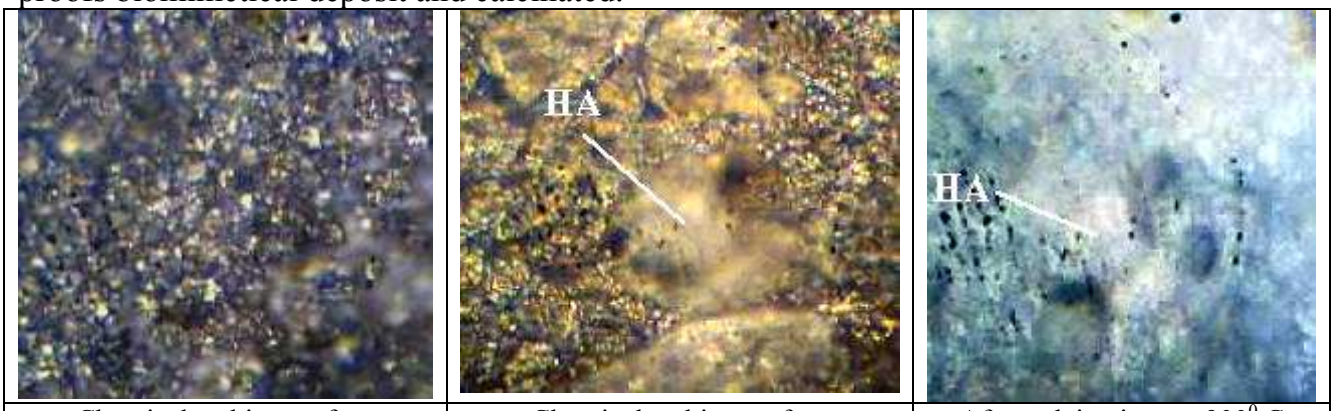

Chemical etching surface	Chemical etching surface	After calcinations at 900^0 C

Fig.2 The micro photos of the titan proof with biomimetical modification of the surface (x500)

It can be observed that the surface of the proof treated 24 hours in super concentrated simulated plasma (SBFx5), an insignificant quantity of phospho-calcium has deposit. After the calcinations of the proof, the ruggedness created by chemical etching with acids reduces, as a result of the advanced oxidation of the titan, on the surface appearing apatite traces.

The superficial distribution of the deposits on the titanium surfaces is illustrated by electronically microscopy in fig.3.

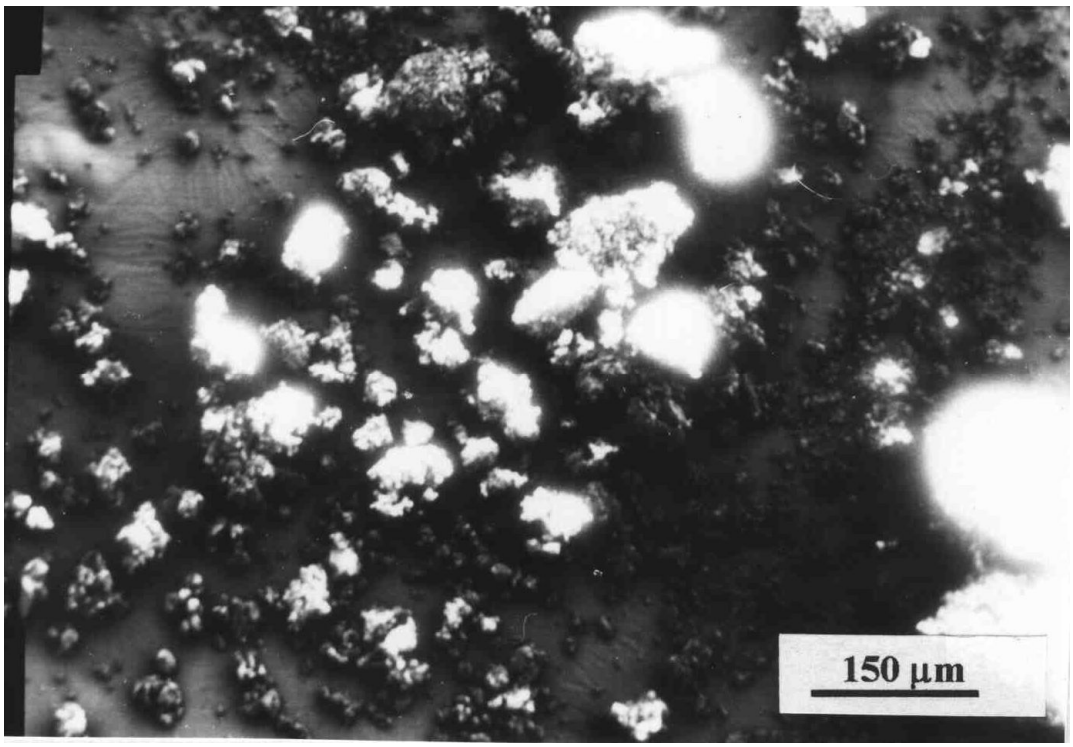

Fig.3 The micro photos of the calcinated proof at 1050 ^oC

In the figure it can observe a small density of phospho-calcium material and the agglomeration of the spherical granules in aggregates of a variety of dimensions.

4. The intensification of surface by alkaline treatment

It was proved that the treatment of titanium's surface with hydroxide after acids etching improves Ca-P deposit process in biomimetical procedure. The procedure of alkaline treatment used in this experiment is synthesized in scheme III. After NaOH treatment, the proof was washed with water jet, with distilled water and it was dried at 120 °C. The effect of chemical treatment with NaOH of rugged proofs is presented in fig. 4.

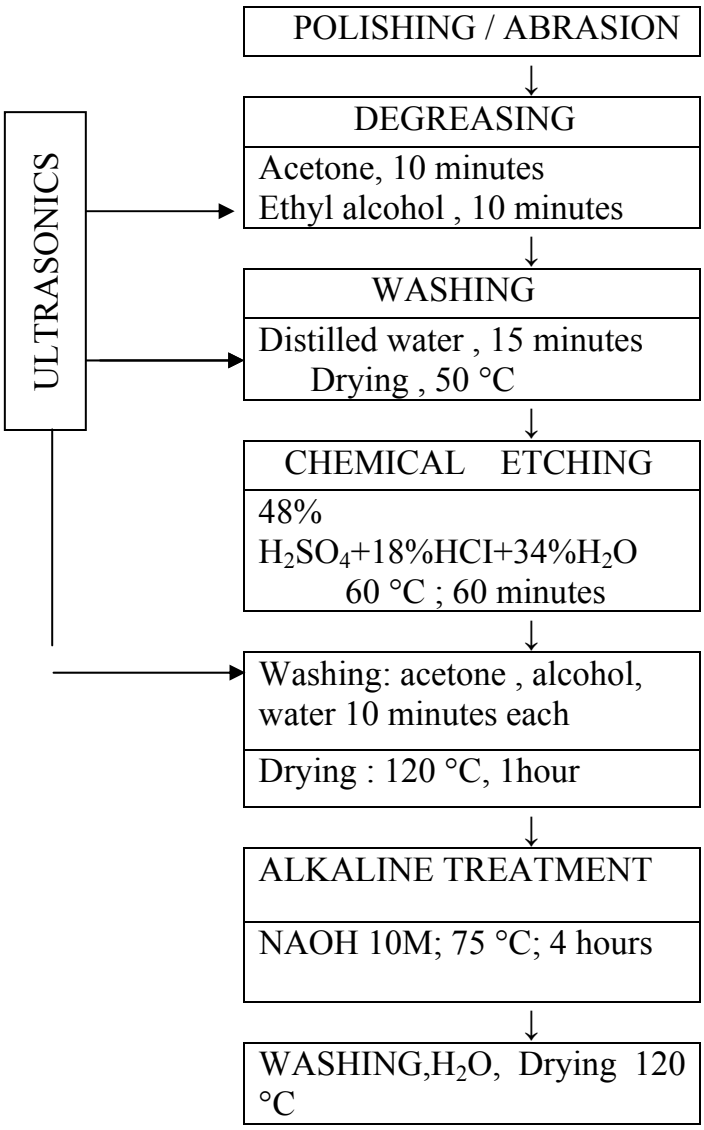

Scheme III- Etching with acids and the alkaline activation of the titanium samples

5. The biomimetical deposit after alkaline intensification

The quantity and the quality of biomimetical deposits of hydroxiapatite grow by surface activation in alkaline medium, which goes to the nucleation speed growth of nuclear speed of phospho-calcium components. The work conditions and the succession of operations are presented in scheme IV.

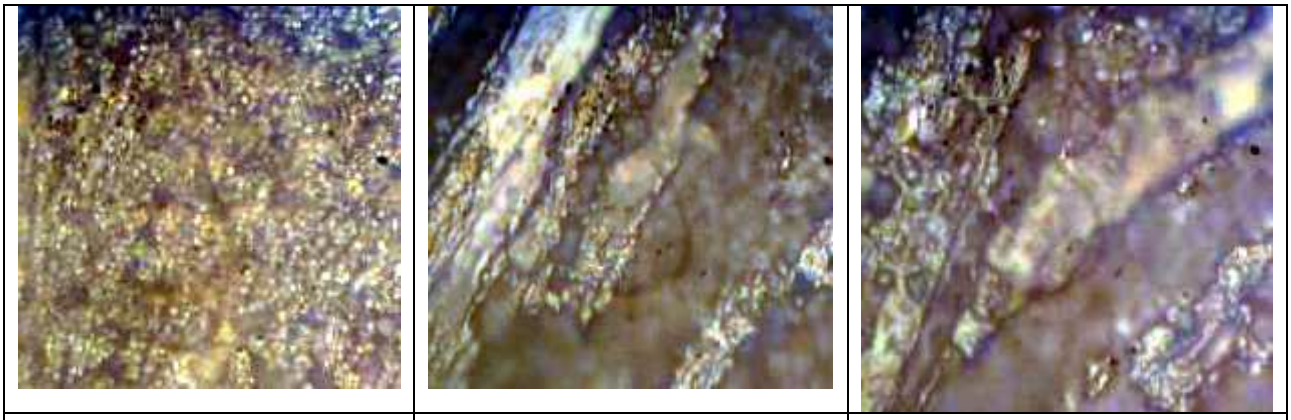

Acid etching proof	After NaOH treatment	After NaOH treatment

Fig.4 The effect of chemical treatment with NaOH of rugged proofs in acids (x500)

CHEMICAL ETCHING
ACCORDING TO SCHEMA 1
↓
CHEMICAL ACTIVATION TO NaOH
NaOH 5M; 60 °C;20 hours
↓
BIOMIMETIC DEPOSIT
Solution SBS×10; 37 °C; 20 hours
↓
Washing: acetone , alcohol, water 10 minutes each
Drying : 120 °C, 1 hour
Calcination , 3 hours ;900 °C

Scheme IV. Biomimetic deposit on a surface roughed with acids and activated in alkaline medium

The micro photos of the proof's surface are presented in fig. 5. Contrary to the deposit on inactivated surface, in this case we find an intensification of deposits under compact globular shape. The structure of phospho-calcium deposits is more evident at calcinated proof, fig.5.

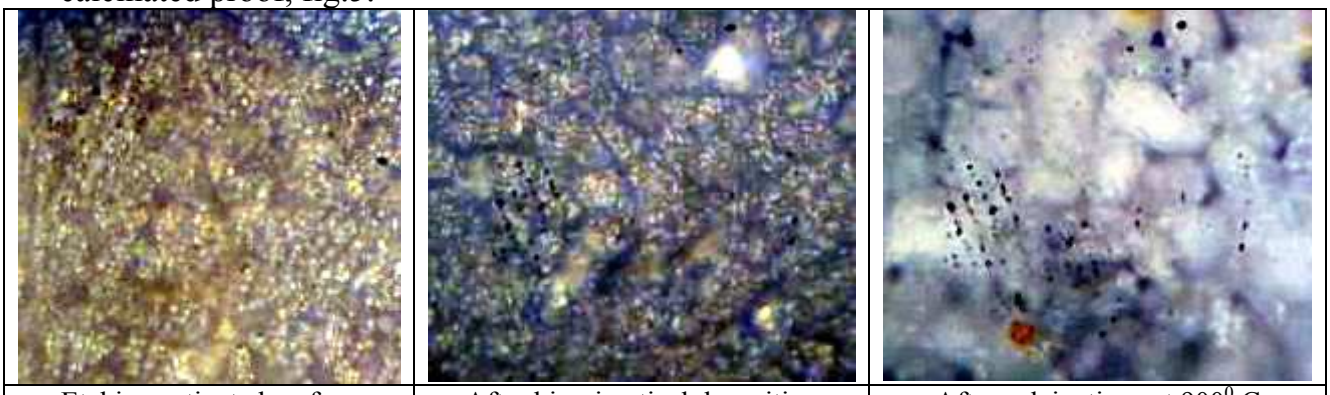

Etching activated surface	After biomimetical deposition	After calcinations at 900^0 C

Fig.5 The micro photos of the proof 'surface in biomimetical deposition cases on activated surfaces in alkaline medium (x500)

The micro photos of the surface after deposit and calcination are presented in fig. 6. We also find in this case globular deposits of 15…30μm diameter at non calcinated proof and after calcinations.

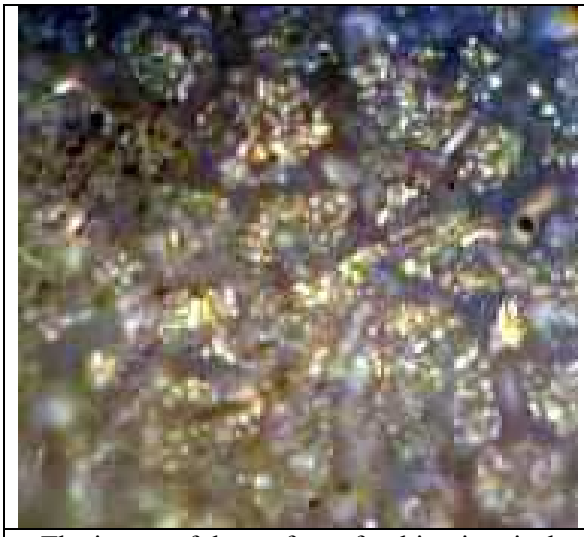

The image of the surface after biomimetical deposition

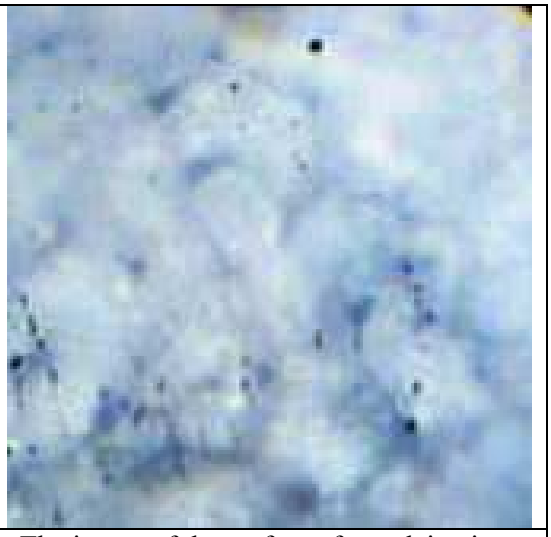

The image of the surface after calcinations at 900^0 C

Fig.6 The micro photos of implant surface obtained in second experiment

The SEM image of proof after biomimetical deposit on chemical etched and activated with NaOH surface is presented in fig. 7. Looking at the image, we find an intensification of the deposits in the same time with the reduction of spheroids dimensions, which are agglomerating.

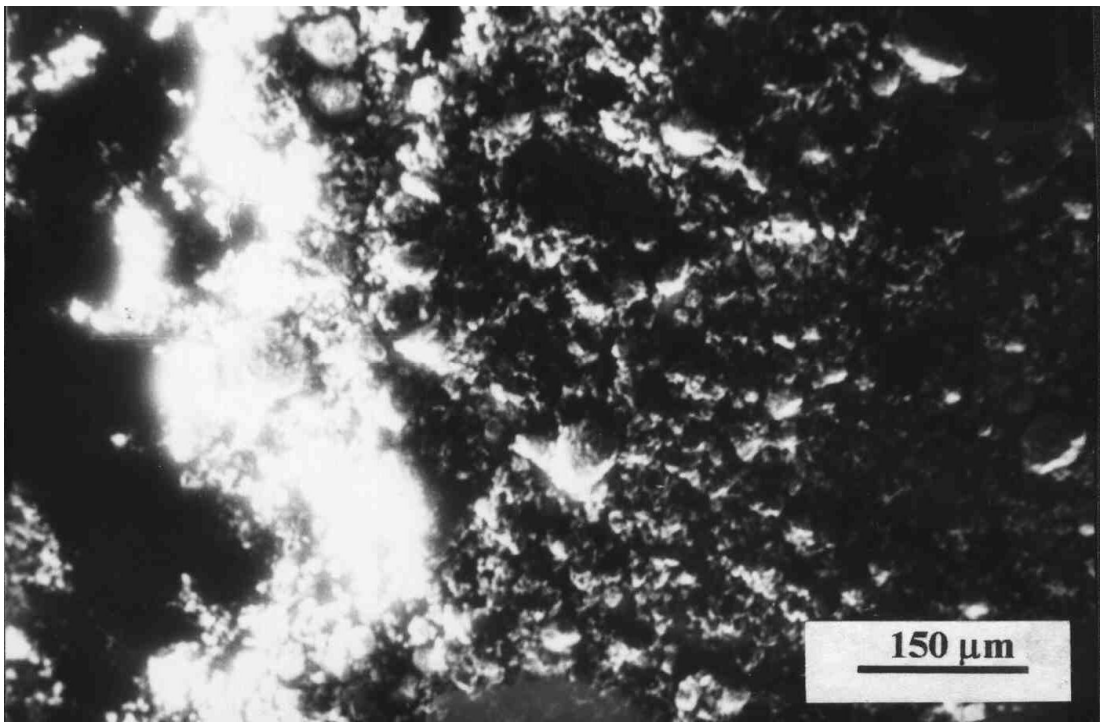

Fig. 7 The SEM image of proof after biomimetical deposit on chemical etched surface and activated with NaOH (after 900 ^{o}C calcinationn

6. Conclusions

In this study we tried different schemes for changing the surface of pure commercial titanium, to improve biocompatibility and activity in osteointegration process. The experimental results make evident that:

- the chemical etching, with mixture of strong acids at a high temperature can be a good method to obtain advanced ruggedness of the surface's titanium implant to grow the osteointegration and to facilitate the deposit of some biocomparable materials, like hydroxiapatite and some other physical and chemical materials.
- the activating process of surface's implant, rugged or not, is essential for the deposit of phospho-calcium materials. Doing this, on the metal's surface are created negative loads which are initiation centers of the crystallization process of some ingredients from solution.
- the biomimetical deposit from the solution which simulate interstitial fluid or human plasma, is a method which permits improving of integration implant/bone through creation of some nucleus by hydroxiapatite on the rugged surface of the implant.

Received April 23, 2007 *The "Gh.Asachi" Technical University Iaşi*

REFERENCES

1. Feng B,Chen J, Zhang XD. Surface modi.cation of titanium by acid-etching. In: Zhang XD,Ikada Y,editors. *Biomedical Materials Research in Asian (IV). Kyoto,Japan* Kobunshi Kankokai,2000. p. 138.
2. Sato K, Kumagai Y, Tanaka J. Apatite formation on organic monolayers in simulated body environment. *J Biomed Mater Res*;***50***: 2000, p. 16–20.
3. Yang BC, Uchida M, Kim HM, Zhang XD, Kokubo T. Preparation of bioactive titanium metal via anodic oxidation treatment. *Biomaterials*;**25:** 2004, p 1003–10
4. Sena L.A., Andrade M.C., Rossi A.M., Soares G.A., Hydroxyapatite deposition by electrophoresis on titanium sheets with different surface finishing, *J Biomed Mater Res.,***60** 2002, p. 1-7;

MODIFICAREA STRUCTURII SUPRAFEȚEI TITANULUI PRIN METODE FIZICO-CHIMICE

Rezumat Datorită proprietăților mecanice şi a biocompatibilității titanul este utilizat atât în aplicațiile dentare cât şi în ortopedie. Pentru a putea îmbunătăți biocompatibilitatea suprafeței titanului comercial pur au fost utilizate mai multe metode, care pot fi clasificate în: (i) metode fizice, (ii) metode chimice, (iii) metode combinate. Lucrarea de față abordează metodele fizico-chimice de modificare a structurii suprafeței titanului care au ca scop accelerarea osteointegrării. Aceasta se face fie prin acoperirea cu hidroxiapatită sau alte materiale fosfo-calcice, fie prin spray-ere mecanică sau prin oxidare anodică sau rugozare cu acizi. Pentru modificarea suprafeței titanului s-au folosit urmatoarele metode fizico-chimice: (a) rugozarea suprafeței titanului în mediu acid: (b) depunerea biomimtică de hidroxiapatită din soluție ; (c) activarea suprafeței prin tratament alcalin ; (d) depunerea biomimetică după activarea alcalină.

BULETINUL INSTITUTULUI POLITEHNIC DIN IAŞI
Tomul LIII (LVII), Fasc. 1, 2007
Secția
ŞTIINȚA ŞI INGINERIA MATERIALELOR

THE MATHEMATICAL SIMULATION OF RETAIN PROCESS OF SULPHUR DIOXIDE FROM THE BURNT GASES FOR ECOLOGICAL HEATING FURNACES

BY

NECULAI SCANTEIANU

Abstract: In the case of gases desulphurization from the heating furnaces caused to the high cost of the wet desulphurization installations, through absorption, the dry desulphurization process, through adsorption or reactive adsorption, is more economic if the desulphurization degree must not be bigger than 20%. A desulphurization degree of the burnt gases until 90% correspond to the imposed restrictions of ecological standards.

Keywords: modeling, desulphurization, ecology, micrograins

1. Introduction

Through *adsorption* or *reactive adsorption* the sulphur dioxide is removed from the burnt gases by direct injection in the fire-place of the calcium sorbents. The sorbent is first transformed in anhydrous lime which reacts with sulphur dioxide forming the stable sulphate of lime according to the reactions:

$$CaCO_3 \rightarrow CaO + CO_2 \quad (1)$$

$$CaO + SO_2 \rightarrow CaSO_3 \quad (2)$$

$$CaSO_3 + {}^{1}\!/\!_{2}\, O_2 = CaSO_4 \quad (3)$$

Making the sum of the relations 1, 2 and 3, it results:

$$CaCO_3 + SO_2 + {}^{1}\!/\!_{2}\, O_2 = CaSO_4 + CO_2 \quad (4)$$

The fixation of sulphur dioxide by the anhydrous lime resulted through the decomposition of the limestone in the fire-place or on the eviction way of the burnt gases is a viable cleaning solution.

2. Theoretical considerations

The rate of use of the limestone increases by diminishing the diameter of the particle. The diminish of the diameter of the limestone particle leads to the entrainment of the particle in the gas channel before reaching the transformation degree so that the excessive diminish of the particle diameter is not considered as solving the problem of increasing the rate of use of the limestone.

The precipitated limestone resulted from the growth and joining of the calcium single crystal, with the initial porosity bigger than calcareous stone could generate,

after calcinations, a porous particle similar as structure with synthetic particles respectively the model of the porous wall made of porous grains also named as subgrain model.

3. Models based on porous particles made of porous grainss

According to this model, elaborated by Akse s.a. and presented in figure 1, the solid particle surrounded by gaseous phase (A) presents a series of macropores that make accessible the interior porous grains to the reaction with sulphur dioxide.

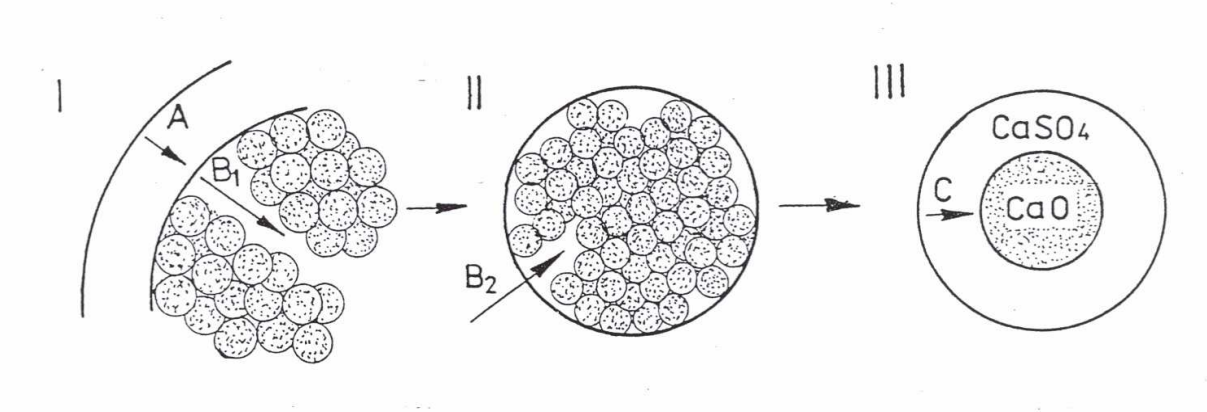

Figure 1. The geometric model of the primary particle formed of porous grainss of anhydrous lime: I – particle; II – grains; III – subgrains; A – the resistance of the exterior gas film; B_1 – the diffusion of gaseous phase towards macropores; B_2 – the diffusion of gaseous phase through micropores; C – the diffusion of gaseous phase through the formed product crust.

After the appearance of an infinitesimal crust around the micrograins of the anhydrous lime the diffusion of the sulphur dioxide through its pores becomes extremely slow so that the concentration of sulphur dioxide will be uniform in the volume of the particle because of the diffusion through macro and micropores inter and granular.

Other simplifying hypotheses are:

- the micrograins are spherical, homogenous and contain anhydrous lime (CaO);
- the free volume between the micrograins is proportional with their size;
- the sulphate of lime crust is pure and homogenous;
- the formation of the sulphate crust on a side of the grains will not affect its formation in another part;
- the sulphating stops at zero porosity;
- the radius of the particle and of the grains remain constant during the process, while the micrograins increases its diameter;
- the sulphating process is isothermal.

Along with the increase of the dimension of the micrograins it also modifies the dimensions of the pores, the radius of the micrograins can calculate according to the radius of the pores with the relation:

$$R_{sg} = r_p \cdot f \qquad (5)$$

where:

f – conversion factor that depends on the N radius intervals of the pores. The volume of the pores for a V_p interval will be equal with the volume of the micrograins, in free volume fraction for the same interval of the micrograins dimension:

$$x_i = \frac{V_{sg}}{\sum_{i=1}^{N} V_{sg}} \tag{6}$$

To calculate the conversion in each micrograins interval it is used the following model:

$$\left(\frac{\delta C}{\delta r}\right)_{R_{sg}} = \frac{C}{\frac{R_{sg}}{R_c}\left(R_{sg} - R_c\right) + \frac{D_{ef_{SO_2}}}{k_{T_{SO_2[g]}}}} \tag{7}$$

$$\frac{\delta V_{sg}}{\delta \tau} = 4\pi R^2{}_{sg}\frac{\delta R_{sg}}{\delta t} = 4\pi R^2{}_{sg} \cdot D_{ef_{SO_2}}\left(\frac{\delta C}{\delta c}\right)_{R_{sg}} \cdot \left(V_{M_{CaSO_4}} - V_{M_{CaO}}\right) \tag{8}$$

$$\frac{\delta V_c}{V_t} = 4\pi R^2{}_c\left(\frac{\delta R_c}{\delta t}\right) = 4\pi R^2{}_{sg} \cdot D_{ef_{SO_2}}\left(\frac{\delta C}{\delta r}\right)_{R_{sg}} \cdot \left(-V_{M_{CaO}}\right) \tag{9}$$

Where:

C – the concentration of SO_2 in gaseous phase;

r – the radius of the microgranule at a certain moment;

R_{sg} – the initial radius of the microgranule;

D – the diffusion coefficient of SO_2 through sulphate crust;

$k_{T_{SO_2[g]}}$ - the diffusion coefficient of SO_2 through gaseous phase;

V_{sg} – the volume of the granule;

V_c – the volume of the unreacted core.

The total transformation degree can be obtained with the relation:

$$\eta = \sum_{i=1}^{N} x_i \cdot \eta_i \tag{10}$$

The value of the transformation degree of the micrograins determines by solving the model in relations 7 and 8.

4. Conclusions

According to the presented model each micrograins has a proper transformation degree. Thus the smaller micrograins, which has a bigger specific surface, it reacts faster first reaching the limit of permissive porosity and stopping the transformation. The bigger micrograins, which confers a bigger volume of the pores, slowly closes the access of sulphur dioxide at the surface of the unreacted core, but even here the evolution of the reaction is blocked caused the advanced toughness of the crust. So in both cases the micrograins consists of an unreacted core (having a certain radius) surrounded of a crust with a constant thickness confirming the fact that anhydrous of lime with smaller pores faster lose the porosity than the one with smaller pores.

Received April 23, 2007 *The "Gh.Asachi" Technical University Iaşi*

REFERENCES

1. Akse, H., A., s.a. – Development of a regenerative sulphur dioxide sorbent system "Final Report for the Commission of the European Communities", University of Twente, the Nederland, 1990;
2. Ataman, E. - Consideratii asupra reducerii poluarii cu SO_2, Energetica, seria A, nr. 5, 1992, p. 213-217;
3. Ataman, E. – Reducerea poluarii cu SO_2, Energetica, seria A, nr. 5, 1994;
4. Barbu, H., C., - Cercetari privind separarea dioxidului de sulf din gaze industriale diluate, Universitatea Al. I. Cuza Iasi, 1999;
5. Scanteianu, N., s.a. – The modernization of a thermal plant in Romania by equipping it with desoulphouration installations using the precipitated calcium carbonate ($CaCO_3$) as a reactive, KRAFT-WERKSTECHNISCHES KOLLOQUIUM DRESDEN – GERMANY, 2000;
6. Tutuianu, O., s.a. – Premize si solutii privind o abordare globala a emisiilor de poluanti gazosi pe ansamblul termocentralelor RENEL, Sesiunea Stiintifica ICEMENERG, Bucuresti, 1995.

MODELAREA MATEMATICA A PROCESULUI DE RETINERE A DIOXIDULUI DE SULF DIN GAZELE ARSE IN VEDEREA ECOLOGIZARII CUPTOARELOR DE INCALZIRE

Rezumat: În cazul desulfurării gazelor arse de la cuptoarele de încălzire, datorită costului mare a instalațiilor de desulfurare pe cale umedă, adică prin adsorbție, procesul de desulfurare pe cale uscată, prin adsorbție sau adsorbție reactivă este mai economic dacă gradul de desulfurare nu trebuie să fie mai mare de 90%. Un grad de desulfurare al gazelor arse de până la 90% corespunde restricțiilor impuse de normele ecologice în vigoare.

BULETINUL INSTITUTULUI POLITEHNIC DIN IAŞI
Tomul LIII (LVII), Fasc. 1, 2007
Secția
ŞTIINȚA ŞI INGINERIA MATERIALELOR

AN ADVANCED ALUMINIUM ALLOY WITH HIGH PHYSICAL – MECHANICAL CHARACTERISTICS FOR AERONAUTICAL CONSTRUCTIONS APPLICATIONS

BY

IOAN SURCEL[1], VASILE SOARE[1], CONSTANTIN SERGHIE[2], VIOREL BADILITA[1], DAN GHEORGHE[3]

Abstract

An advanced high strength aluminium wrought alloy, of Al – 4.5Mg – 0.7Mn – 0.15Cr type, suitable for aeronautical constructions, was obtained in experimental conditions.
The alloy's lots were elaborated using micro-alloying with Be, rare earth (Ce), Ti and B; the samples' final tempers were obtained by hot and cold rolling, and also by annealing heat treatments.

In the paper are presented representative physical - mechanical characteristics, of the alloy samples, in different tempers, determined by tensile and hardness tests. The obtained Al-Mg alloys behavior study at shear stresses testing, at temperatures situated in the range from 25 ^{0}C to 400 ^{0}C, was accomplished in cooperation with IMMG – Greece using an original method and shear-testing machine belonging to the collaborator's institute. The Al-Mg studied alloy has good mechanical tensile strength, and high and stable shear characteristics, in the 25 ÷ 75 ^{0}C temperature range. The alloy's plasticity at room temperature is very high, and increases with the temperature growth.
The structural study was achieved by optical qualitative and quantitative microscopy, and by X - ray diffraction; there were put in evidence the main constituents and the phases for the studied alloy. The alloy's structure is composed from fine αAl solid solution's grains and intermetallic compounds distributed along the rolling direction.

Key words: *aluminium alloy, mechanical characteristics, shear strength, shear modulus, structural phase, intermetallic compounds.*

1. Introduction

The aluminium alloys, in semi-finished and products shapes, are used on a large scale in aerospace constructions, due to their high physical-mechanical and corrosion resistance properties; they have also good technological (manufacturing, assembling) characteristics.

The aluminium alloys are continuously improved and they constitute principal materials (70 ÷ 80 % from the commonly used materials) in civil and military planes structures.

New and advanced aluminium alloys, with superior characteristics, replace the standard usual alloys; these substitutions, compared with new materials, need reduced efforts and costs, and also involve low risks[2].

The wrought Al-Mg alloys with 2 ÷ 5 % Mg and different Mn and Cr contents have good mechanical resistance characteristics at room and low temperatures, high plasticity and raised corrosion resistance.

The Al-Mg alloys use in aerospace constructions is limited by their behavior at high temperatures; in the usual temperature range, up to 200 ÷ 300 ^{0}C, the dimensional stability is affected thanks to their raised creep deformation. The crystalline structure is not stable at relative high temperatures when the grains growth happens.

Some Al-Mg-Mn-Cr alloys with special modifying during their elaboration tend to pass over the exposed disadvantage in relation with the thermal and microstructural stability.

2. **Experimental material and procedure**

2.1 Experimental material

An advanced high strength aluminium wrought alloy of Al – 4,5Mg – 0,7Mn – 0,15Cr type was elaborated using micro-alloying with: Be – in order to eliminate or decrease the oxygen and oxides content; rare earth (Ce) – for the solid solution alloying and its re-crystallization temperature raising; Ti and B – to obtain fine, modified structure.

The chemical compositions of the elaborated alloys, determined on cast samples, by standard chemical analysis methods are presented in the table 1.

Table 1

Batch	**Chemical composition, % weight**											
	Si	**Fe**	**Cu**	**Mn**	**Mg**	**Cr**	**Zn**	**Ti**	**B**	**Be**	**Ce**	**Al**
P1	0,05	0,09	0,01	0,48	4,32	0,15	0,01	0,08	0,003	0,001	0,002	balance
P2	0,04	0,10	0,008	0,52	4,30	0,25	0,01	0,05	0,002	0,002	0,024	balance
P3	0,05	0,40	0,014	0,58	4,56	0,08	0,03	0,02	0,001	0,002	0,031	balance

The cast bars were processed by hot and cold deformation. The product shapes of the lots were as plates and strip of 10 ÷ 20 mm width and 2 ÷ 10 mm thickness. The final samples' tempers (cold or hot working, annealing) were obtained by rolling and by annealing heat treatments.

2.2**Experimental procedure**

The experimental lots from the studied Al-Mg alloy were characterized by: mechanical usual testing (tensile tests, hardness); thermal – mechanical shear testing; structural analyses by optical microscopy and X-ray diffraction. For each test or analysis kind there were prepared suitable samples.

Mechanical tests for tensile and hardness characteristics determinations were performed on adequate apparatus, using general standard methods and specific methods for the application field of the materials.

Shear thermal – mechanical testing were performed in the Institute of Mechanics of Materials and Geostructures – IMMG – Greece, in the frame of an EU international cooperation program. There were used original installations and methods (including an adequate software) developed by IMMG. There were performed: shearing tests with monotonous strain rate at room temperature at 75 ÷ 400 ^{0}C temperatures; creep and fatigue shear tests at 75 ^{0}C. The special designed test specimen [1] is shown in the figure 1.

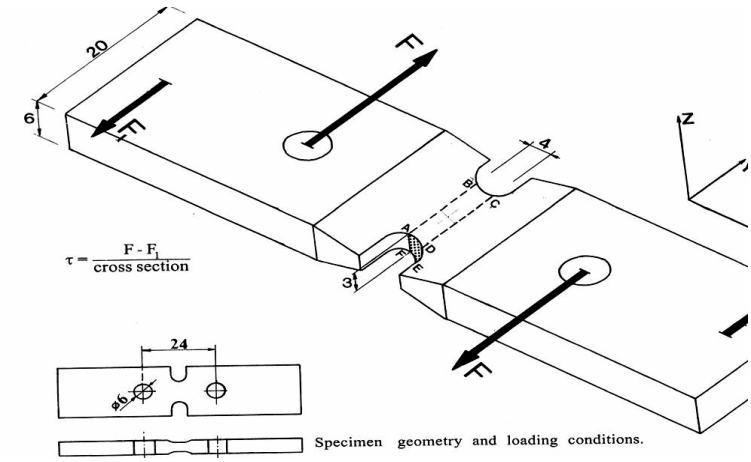

Thermal differential analyses were accomplished in order to determine the transformations' temperatures.

Figure 1 - Shear test piece.

Microscopic optical investigations included *qualitative analyses* and *quantitative analyses* using an image analysis computerized line and a Buehler – OMNIMNET soft.

Phase structural analyses were achieved by *X-ray diffraction* using Bragg-Brentano method; qualitative phase analysis was performed according to ASTM Hanawalt method.

3. Results and disscusions

The main *mechanical characteristics* (R_m-tensile strength, $R_{0.2}$-elasticity limit, A_c-elongation and HB-hardness) of the plate and strip samples, from the experimentally elaborated Al – 4,5Mg – 0,7Mn – 0,15Cr alloy, and standard characteristics [3,4] are presented in the table 2.

Table 2

SAMPLE*	**Temper****	**TENSILE TESTING**			**Brinell Hardness**
		R_m MPa	**$R_{0,2}$ MPa**	**A_c %**	**HB**
P1-PL	O	238	120	19.4	63.5
P2-PL		245	122	18.1	65.8
P3-PL		249	126	18.2	65.9
P1-S1	H 111	280	144	17.8	70.8
P2-S1		285	148	17.3	72.5
P3-S1		293	165	17.1	74.9
P1-S2	H 12	296	191	15.3	73.5
P2-S2		298	193	14.6	75.4
P2-S2		306	198	14.4	77.8
P1-S3	H 13	318	212	12.7	85.6
P2-S3		326	221	11.8	86.3
P3-S3		344	229	11.6	88.7
Standard	***H 111***	***275***	***125***	***15***	***70***

**Samples symbol*	**Tempers symbol**
PL – Plate ≠ 10 mm	H 111 – Hot rolled – as laminated.
S1– Strip ≠ 6 mm	O – Annealed
S2 – Strip ≠ 4 mm	H 11 – Strain-hardened ¼ Hard
S3 – Strip ≠ 3 mm	H 12 – Strain-hardened ½ Hard
	H 13 – Strain-hardened ¾ Hard

Micro-alloying influences upon the mechanical characteristics of the plates and strips from Al-Mg alloy. So, for the same dimensions and tempers of products, the Ti,

B and Ce additions increase the tensile and yield strength, and the elongation slowly decrease [3]. The cold work degree sharpens the mechanical strength increase.

Shear mechanical characteristics of the alloy's sample P2 in the O temper are presented in the table 2.

Table 2

Sample	**Temp.** ^{0}C	**Strain** γ maximum %	**Shear strength** at γ=4 %, τ MPa	**Shear modulus G,** GPa	**Observations**
1	25	8.5	105	25,63	tension marks use
2	75	8.05	94	22.92	tension marks use
3	75	9.8	50 (shear stress)		Fatigue test 79,000 cycles
4	150	9.2	67		in atmosphere
5	250	0.5	58		Vacuum 10^{-2} mbar
6	400	0.5	40		Vacuum 10^{-2} mbar

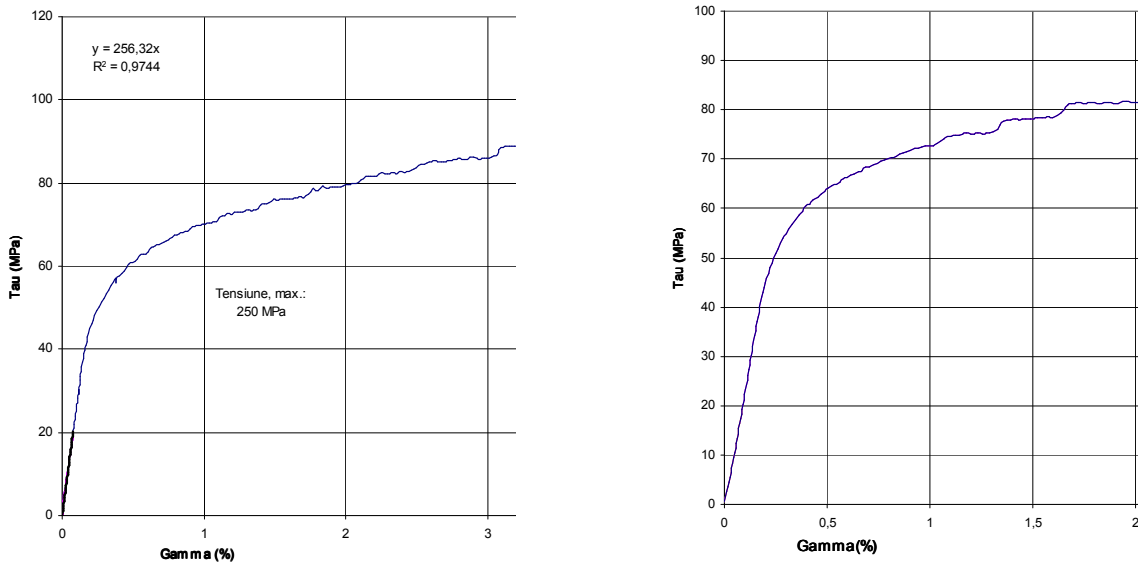

a. **b.**

Figure 3. Tension – deformation diagrams of Al-Mg alloy samples at shear testing: a. at room temperatures; b. at 75 ^{0}C

The studied alloy has high shear strength and modulus characteristics, so at room temperature as at high temperatures, up to 400 ^{0}C. At the same time the alloy has good shear fatigue strength, even at 75 ^{0}C. The high recorded values of the elongation characteristics which were revealed at all tests, demonstrate high alloy plasticity and toughness.

The transformations temperatures determined by DTA analyses are: 590 ÷ 600 ^{0}C solidus temperature; 640 ÷ 644 ^{0}C liquidus temperature [6]. A thermal effect at about 330 ^{0}C could indicate the re-crystallization point.

Microstructures –Qualitative optical analysis

In figure 4 are presented optical microstructures of a rolled strip from Al-Mg alloy.
The sample structure is constituted from αAl solid solution of light color and dark Al-Mn compounds distributed along the rolling direction.

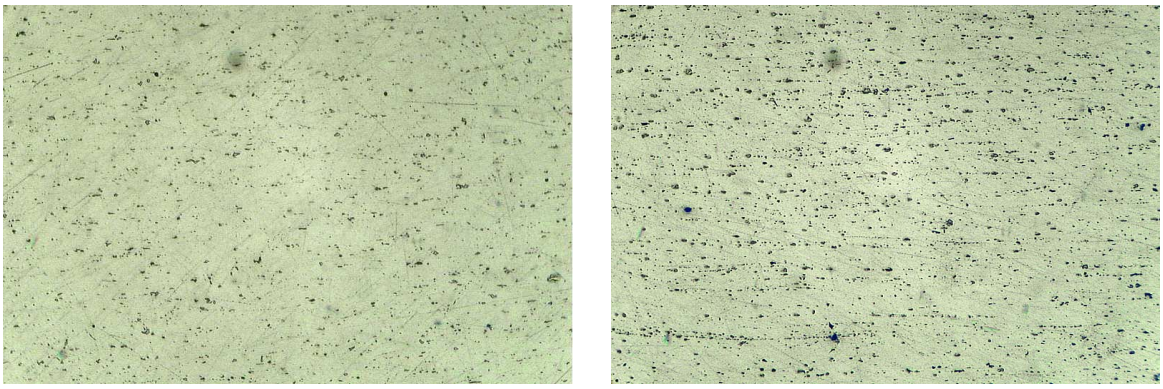

x 500 x 500

a. b.

Figure 4. Microstructure of an Al-Mg strip (≠ 3.0 mm, H13 temper) observed by qualitative analysis.
a. Transversal section; b. Longitudinal section

Quantitative optical microscopic analysis

There were determined the contents and the sizes of the main constituents – aluminium solid solution and intermetallic compounds.

The grain size is of 20 – 50 μm.

The intermetallic compounds area sizes are situated in the 5 – 20 μm^2 range; the total compounds area is of about 3 %.

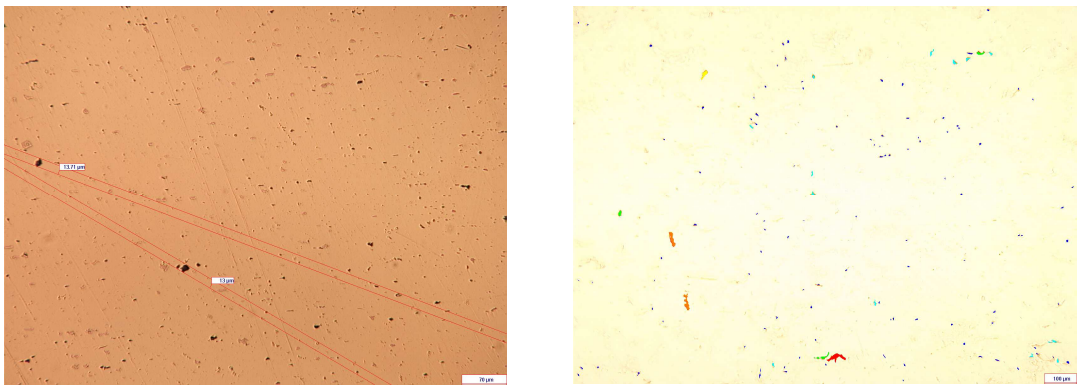

5.1. **5.2.**

Figure 5. Microstructures of an Al-Mg strip (≠ 3.0 mm, H13 temper) observed by

quantitative analysis. Figure 5.1. Measurement of 2 particles dimensions.The two of the largest particles sizes are 13.0, respectively 13.71 microns.

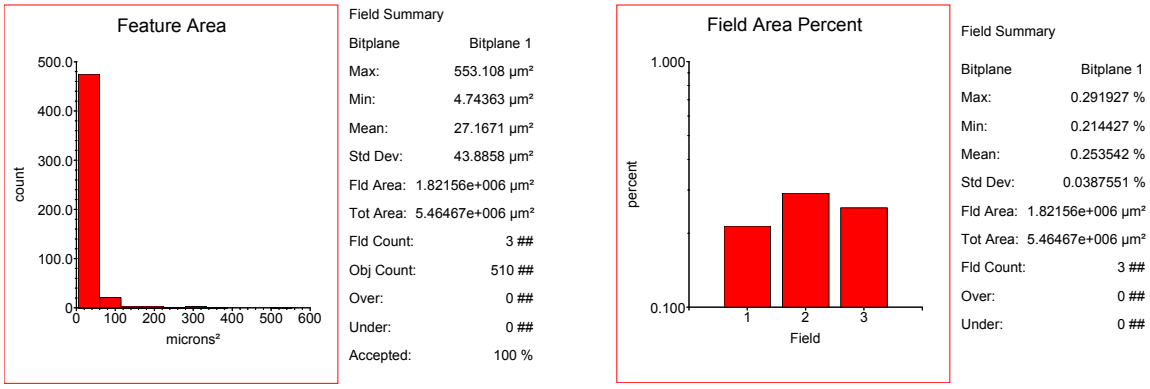

a. **b.** **c.** **d.**

Figure 5.2. Quantitative analysis of the particles' sizes and surfaces.

a. In the particles category area of 0-50 µm^2, the countered particles are 5000; in the categories containing smaller or greater particles, their number is insignificant.

b. The particles areas are: min. 4.7 µm^2 / particle; 553 µm^2 max. and 27 µm^{2}medium.

c. The surfaces occupied by particles, in the second field is max. 0.29 %.

d. The surfaces occupied by particles, in the considered fields, are: min. 0.21 %, max. 0.29 % and mean 0.25 %.

Phase structure observed by X-ray diffraction

The qualitative phase analysis and semi-quantitative evaluations for P1 and P2 samples are presented in the table 3 and the figure 6.

Table 3

No	Identified phases	P1~ % Vol.	P3~ % Vol.
1	$(Al)_{ss}$ – Al base solid solution, *c.f.c.*	z.p.	z.p.
2	$Al_{(19)}Mn_4$ or α – (AlMnSi), cubic complex,138 at / cell, which could contain Fe, Cr, $a \approx 12.66$ *Å*.	1 ÷ p.	1 ÷ p.
3	Mg_2Si – cubic, $a \approx 6.34$ *Å*.	0.1 ÷ 1	0.1 ÷ 1

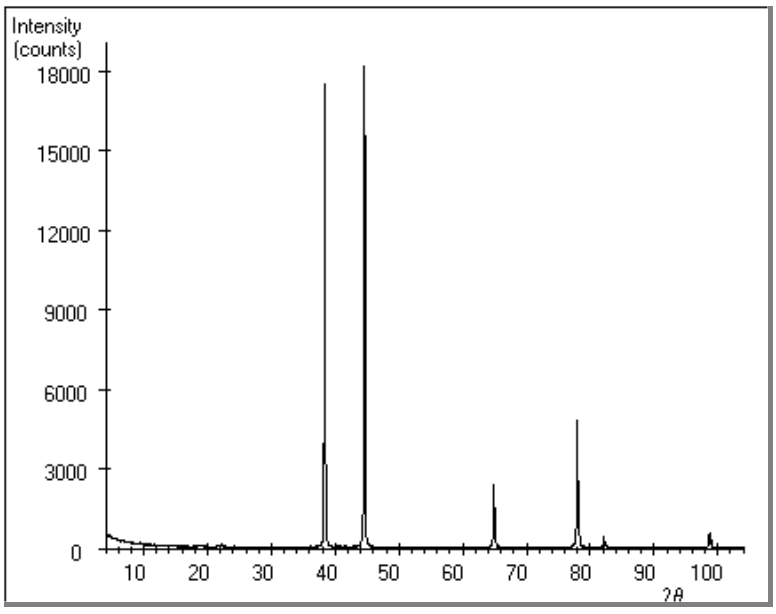

Figure 6. Diffraction diagram of the P3 alloy's sample.

The analytical representation of the analyzed profiles for the (311) and (222) lines is exposed in the table 4.

Table 4

Sample	*a, / Å*	$D_{(311)}$ / nm	$D_{(222)}$ / nm
P1 – hot rolled, annealed	*4.049 Å* (2.7 % Mg)	120	90
P3 – cold rolled	*4.060 Å* (2.4 % Mg)	40	30

By X-ray diffraction analysis were determined the main phase's components: αAl solid solution on aluminium base with magnesium; AlMn(Fe,Cr) complex compounds. There were established the lattice parameters of the phases of Al-Mg alloy samples of different compositions and products' tempers. The magnesium content of the solid solution is of about 2.7 % in the hot rolled and annealed sample (corresponding to the solubility limit of Mg in Al at ~ 100 ^{0}C), and decreases to 2.4 % in the cold rolled sample (Mg solubility in solid Al at lowered temperatures).

4. **Conclusions**

An advanced Al-4.5Mg-0.7Mn-0.15Cr wrought alloy, with high physical-mechanical characteristics, was achieved by micro-alloying using small additions of Ti, B, and rare earth (Ce), and by plastic deformations and heat treatments, performed in specific conditions.

The experimentally obtained alloy has raised shear strength characteristics at room temperature and at up to 400 ^{0}C temperatures; the alloy's plasticity is considerable.

The alloy's structure is very fine thanks to supplementary modifying and adequate processing. There were put in evidence the main phases of the alloy's structure: aluminium base solid solution and AlMn(Cr,Fe) intermetallic compounds.

Semi-finished products from this alloy with high and stable mechanical and corrosion resistance can be used in aerospace constructions and other applications.

ACKNOWLEDGEMENT

Analyzed materials and characterizing experiments were accomplished in the 31023 research project under the leadership and financial support of the Romanian AEROSPATIAL Program.

Thermo-mechanical shear characteristics study were performed in cooperation with the Institute of Mechanics of Materials and Geostructures – IMMG – Greece, the HPRI – CT – 2002 – 00185 project, in the framework of EU Program.

Received April 23, 2007

[1] National R&D Institute for Nonferrous and Rare Metals – IMNR, 102 Biruinţei Blvd., Pantelimon – Ilfov, ROMANIA
[2] National Institute for Aerospace Research "Elie Carafoli"– INCAS, 220 Iuliu Maniu Blvd., Bucharest, ROMANIA
[3] Materials Science and Engineering Faculty, "POLITEHNICA" University, 313 Independentei Ave., Bucharest, ROMANIA

REFERENCES

1. P.N. Michelis, P.D. Nicolaou, P.G. Kornezos - "Off – Axis Shear Behavior of Selected MMC's" – Low Cycle Fatigue and Elasto-Plastic Behavior of Materials, 1998 Elsevier Science Ltd., p. 480

2. E.A. Starke Jr., Aladar A.S.Csontos, "Aluminium alloys for aerospace applications", vol.4, Proceedings *of ICAA-6,* JILM, 1998, p. 2078
3. O.Roder, O.Schauerte, G.Lutjering, A.Gysler - "Correlation between Microstructure and Mechanical Properties of Al-Mg Alloys without and with Scandium", Materials Science Forum - Vols.217-222(1996), Transtec Publications, Switzerland, p. 1836
4. T.Furu, H.R.Sherclif, C.M.Sellars, M.F.Ashby – "Physically-based Modeling of Strength, Microstructure and Recrystallisation During Thermomechanical Processing of Al-Mg Alloys" - Materials Science Forum - Vols.217-222(1996), Transtec Publications, Switzerland, p. 456
5. M. Verdier, J.A. Sæter, M. Janecek - "Kinetic and Microstructural Aspects of Recovery in Al, Al-Mg and Al-Mn Alloys"- Materials Science Forum - Vols.217-222(1996), Transtec Publications, Switzerland, p. 437

ALIAJ DE ALUMINIU AVANSAT CU CARACTERISTICI FIZICO-MECANICE RIDICATE PENTRU APLICAȚII ÎN CONSTRUCȚII AERONAUTICE

Rezumat În condiții experimentale, s-a obținut un aliaj de aluminiu avansat, de înaltă rezistență, de tip Al – 4,5Mg – 0,7Mn – 0,15Cr, adecvat pentru construcții aeronautice.
S-au realizat loturi de aliaje utilizându-se microalieri cu Be, pământuri rare (Ce), Ti şi B; starea finală de prelucrare a fost obținută prin laminare la cald şi la rece, şi prin tratamente termice de recoacere.
În lucrare sunt prezentate caracteristici fizico-mecanice reprezentative ale probelor de aliaj, în diferite stări, determinate prin încercări de tracțiune şi duritate. Pentru aliajul Al-Mg obținut s-a întreprins un studiu al comportării la încercări de forfecare, la temperaturi în domeniul 25 ÷ 400 ^{0}C, realizat în cooperare cu IMMG – Grecia, utilizându-se o metodă originală şi o maşină de încercare la forfecare aparținând institutului colaborator, Aliajul Al-Mg studiat are caracteristici mecanice ridicate şi caracteristici de forfecare înalte, stabile, în intervalul de temperatură 25 ÷ 75 ^{0}C. Plasticitatea aliajului este foarte ridicată şi creşte odată cu creşterea temperaturii.
S-a realizat studiul structural prin microscopie optică calitativă şi cantitativă, şi prin difracție de raze X; s-au pus în evidență constituenții şi fazele principale ale aliajului studiat. Structura aliajului este alcătuită din grăunți fini de soluție solidă αAl şi compuşi intermetalici orientați în direcția de laminare.

BULETINUL INSTITUTULUI POLITEHNIC DIN IAŞI
Tomul LIII (LVII), Fasc. 1, 2007
Secția
ŞTIINȚA ŞI INGINERIA MATERIALELOR

Pb – Ca ALLOYS OBTAINING BY CaO ELECTROLYSIS IN MOLTEN SALTS MEDIA

BY

VASILE SOARE, IOAN SURCEL, MARIAN BURADA, VICTORIA SOARE

Abstract

Pb – Ca alloys are used to produce so called "maintenance-free lead-acid batteries", batteries which present high electrical performance, high feasibility as well as long term operational life.

In the present paper the experimental work performed for Pb – Ca alloys obtaining by electrolysis of CaO in molten salts are presented. Molten lead was used as electrolysis cell cathode; the anode was made from graphite. The electrolyte used was a mixture of calcium chloride and fluoride. The active specie in the electrochemical process was calcium oxide CaO. The duration of the process was 6 hrs. The result of the experimental works has been the obtaining of a Pb – Ca alloys with 8.2 wt.% Ca content.

Keywords: *Pb-Ca alloys, maintenance-free lead-acid batteries, electrolysis, cathode, anode, electrochemical cell.*

1.Introduction

The lead-acid batteries are extensively used in different industrial and social areas: automotive industry, electric transport, electrical enlightenment, telecommunication networks, uninterruptible power supply systems, etc.

The obtaining of new types of lead-acid batteries - the so called "maintenance-free lead-acid battery" - with high electrical and operational performances have become important, in order to eliminate some deficiencies of the classical lead-acid batteries [1]:

- Relatively short cycle life due mainly to the corrosion of the electrodes;
- Low mechanical resistance of the grids and plates;
- Environmental concerns regarding the spillage of the acid electrolyte, etc.

: Pb – Se, Pb – Sb, and specially, Pb – Ca alloys are used to produce the plates and grids of the new kind of lead-acid batteries.

The addition of only 0.2 – 0.3 wt. % of calcium to lead improves its mechanical and electrical performances as follows [1,2]:

- increases the hardness, which confers a higher mechanical resistance of the grids and plates;
- increases the electrical conductance;
- increases the corrosion resistance;
- eliminates the undesired phenomenon of electrodes passivity.

Conventional technologies for the production of Pb – Ca alloys use either a metallurgical route, involving the direct alloying of lead and calcium, or electrochemical processes.

These latter processes consist in the electro deposition of Ca on molten lead cathode pool in molten chloride or a mixed chloride/fluoride electrolyte [3].

These electrochemical technologies present the great disadvantage of Cl_2 (or F_2) evolution at the anode. Due to their noxious effect on the environment, these gases have to be collected and neutralized. For these operations expensive installation and technologies as well as specific reagents, etc. are needed.

The using of CaO as raw material in the electrolysis processes for Pb – Ca alloys obtaining can eliminate these problems. Calcium oxide is dissolved in molten calcium chloride or calcium chloride/fluoride mixture electrolyte, and calcium is electrowinned on molten lead cathode.

The electrochemical process is based on the following physical-chemical considerations:

- the solubility of CaO in molten calcium chloride is about 20 mol %, which can be compared with the negligible solubility of most oxides in their respective chlorides [4];
- the decomposition voltage of CaO is lower than that of $CaCl_2$ and CaF_2. [5, 6].

The high CaO solubility in the electrolyte (20 mol %) allows the use of high current densities during the electrolysis process with favorable effects on current and energy efficiency. Moreover, this brings an economical advantage over the classical electrochemical technologies: a lower applied voltage to the electrolysis cell has as results the decreasing of the energy consumption.

The lower decomposition voltage of CaO excludes the evolution of noxious gases Cl_2 and/or F_2 during the electrochemical process.

Another important advantage of CaO using consists in the low price of this oxide.

The half cell reaction equations, at the cathode, for the envisaged process of calcium oxide electroreducing, are shown below:

$$CaO \rightarrow Ca^{++} + O^{=}$$

$$Ca^{++} + 2e^{-} \rightarrow Ca_{\text{(on molten Pb cathode)}}$$

The reaction at the anode results in the evolving of CO_2 or CO gases, according to:

$$C + 2O^{=} \rightarrow CO_2 + 4e^{-} \quad , \quad C + O^{=} \rightarrow CO + 2e^{-}.$$

In respect to the electrolyte, a mixture of $CaCl_2$ - CaF_2 is used ,having the following advantages [4]:

- the solubility of Ca in molten calcium chloride is low, about 2 mol % ;
- the low melting point of the mixture electrolyte avoids the superheating of the electrolysis cell;
- CaF_2 decreases the viscosity of the electrolyte with favorable effect on active species movement in the electrolyte.

2. Experimental works

The experimental works consisted in the obtaining of Pb – Ca alloys by CaO electrolysis in molten chloride and fluoride mixture .

2.1 Reagents

The reagents used for experimental electrolysis works are presented in Table 1.
Tabelul 1.

Reagents	Formula	Purity	Producer
Lead	Pb	p.a.	Chimopar - Romania
Calcium oxide	CaO	p.a.	Merck – Germania
Calcium chloride	$CaCl_2$	p.a.	Chimopar - Romania
Calcium fluoride	CaF_2	p.a.	Merck – Germania

The electrolyte used in the experimental works was the eutectic mixture $CaCl_2$: 85 wt. % - CaF_2: 15 wt. %,(melting point of 650^0C). The quantity used for experiments was of.The following quantities of raw materials have been used:

- electrolyte : 350 g
- CaO : 24.5 g (7 wt. % from the total electrolyte quantity)
- molten lead cathode : 600 g.

2.2 Experimental installation

The experimental installation for Pb – Ca alloys obtaining by CaO electrolysis in molten salts media consists in the following:

- electrolytic cell
- heating furnace
- direct current power supply
- inert gas purification and drying device
- molten alloy and electrolyte siphoning device

The draft of the electrolytic cell is presented in Figure 1.

Description of the experimental installation:

Heating furnace. The experiments were carried out in an electrical resistance furnace with a power rating 4.5 kW and maximum temperature of 1200^0C : the accuracy of temperature control is 1^0C. The working area of the furnace is made from a ceramic tube. In the closed working area is mounted the electrolytic cell and an inert atmosphere (Ar) is provided.

Electrolytic cell (5) is a ceramic crucible made from a mixture of silicon and aluminum oxynitride, which resists to high temperature as well as to corrosive action of the molten electrolyte. The dimensions of the crucible are as follows: internal diameter: 68 mm, height: 100 mm, wall thickness: 5 mm. At the bottom of the crucible, a circular hole was made in order to assemble the electrical cathode contact (8) with the molten lead pool (7). This electrical contact was made from stainless steel, which presents a good corrosion resistance in the used electrolysis media. The ceramic crucible is fixed into a stainless steel crucible (2).

The *anode of the cell* (4) is made by super dense graphite and has the following dimensions: diameter: 54 mm, height: 80 mm, with a basal slope of 11^0. Two horizontal holes and one vertical hole were done in the anode in order to improve the

evacuation of the anodic evolved gases as well as the movement of the electrolyte. The anode support tube (1), which is made by stainless steel, allows the adjustment of the anode-cathode distance, the evacuation and collection of the anodic gases as well as the periodic feeding with raw materials and electrolyte.

The electrolysis cell is covered by a thermo insulator cover (3).

The electrolysis installation is fixed inside the working area of the electric furnace by means of a metallic support (9), which also permits the cathode electrical contact to power supply.

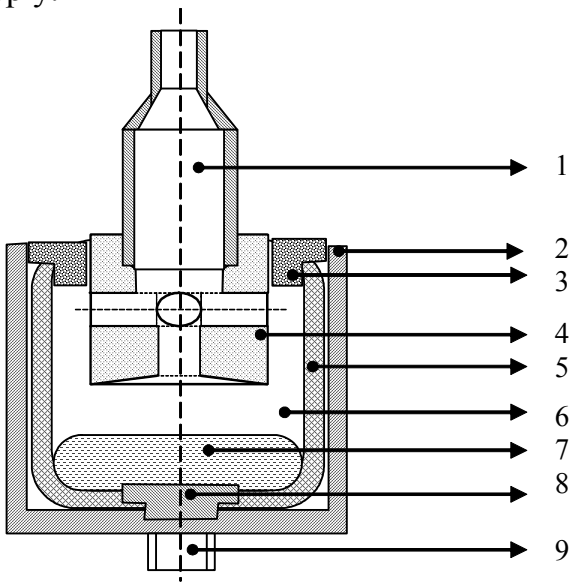

Fig.1 *The draft of the experimental electrolysis cell*

1. Anode holder tube	4. Graphite anode	7. Molten lead
2. Metallic crucible	5. Ceramic crucible	8. Cathode electric contact
3. Sindanyo cell cover	6. Molten electrolyte	9. Cell support

Experimental working

After the assembling of the components, the electrolysis cell was introduced inside the electric furnace. The operations succession was as follows: feeding of the lead into the cell in small pieces, feeding of the electrolyte and CaO mixture into the cell, fixing of the cell cover and superior furnace cover. The anode of the cell was fixed above the solid electrolyte level. Inert gas (Ar) was fed in to the furnace and the heating process was started.

After the reaching of the working temperature and approximate 30 minutes waiting period to attain equilibrium in the cell, the anode was introduced into the molten electrolyte, according to an anode – cathode distance D_{A-K} of 30 mm (from the molten lead level) , and the electrolysis process was started.

The duration of the process was 6 hrs.

During the electrochemical process, there were performed the following operations: recordings of the current and voltage values, raw material feeding as well as electrolyte feeding (when necessary) for constant electrolyte level maintaining.

At 30 minutes time interval, 6 g of CaO powder was heated and fed into the cell by means of the anode holder tube.

After the feeding of CaO, a variation of the current intensity was observed, variations which have stabilized in few minutes.

The main parameters of the process were as follows:

- Cell applied voltage: 3 V
- Current intensity: 15A
- Working temperature: 700^0C
- Anode-cathode distance: 30 mm

At the end of the process, the obtained alloy and the electrolyte were siphoned from the electrolytic cell and mechanically separated.

3. Experimental results

As a result of experimental electrolysis works, a quantity of 645,67 g Pb – Ca alloy was obtained.

The chemical analysis performed on a sample of the Pb – Ca alloy is presented in Table 2.

Table 2

Element	Pb	Ca	O	C	Si	Al	Fe	Bi
wt %	91,7	8.2	$\sim 10^{-3}$	$<5\cdot10^{-3}$	$\sim 10^{-3}$	$\sim 10^{-3}$	$\sim 10^{-3}$	0.05

The chemical analysis performed on the electrolyte, before and after the electrolysis process is presented in Table 3.

Table 3

Element wt %	Ca	Cl_2	F_2	Pb	O_2	C
IN	38.40	54.30	7.30	-	-	-
OUT	42.9	47.53	6.73	0.15	2.46	0.23

In the table 4 the mass balance of the electrolysis process is presented . From the data presented in the table, results the calcium extraction efficiency of 79 %.

Optical microscopy analysis was used to examine the structure of the Pb – Ca alloy obtained.

From the microphotography presented in Figure 2, the presence of two phases can be observed. According to the Pb – Ca phase diagram, and the composition of Pb – Ca alloy obtained, the two present phases are Pb_3Ca and PbCa respectively.

TDA analysis of the Pb – Ca alloy sample is presented in Figure 3.

Table 4. Electrolysis mass balance

IN													
	Ca		Pb		C		O_2		Cl_2		F_2		Total
	%	g	%	g	%	g	%	g	%	g	%	g	g
$CaCl_2$	36.12	107.45							63.88	190.05			297.5
CaF_2	51.33	26.95									48.67	25.55	52.5
CaO	71.47	68.6					28.53	27.4					96
Pb			100	600									600
Graphite					100	218							218
Total	203		600		218		27.4		190.05		25.55		1264

OUT													
	Ca		Pb		C		O_2		Cl_2		F_2		Total
	%	g	%	g	%	g	%	g	%	g	%	g	g
Electrolyte	42.9	147.36	0.15	0.52	0.23	0.8	2.46	8.44	47.53	163.26	6.73	23.12	343.5
Pb – Ca alloy	8.2	54.17	91.8	591.5									645.67
Graphite					100	206							206
CO_2					27.3	6.33	72.7	16.87					23.2
CO					42.9	0.14	57.1	0.19					0.33
Mechanical losses		1.47		7.98				1.9		26.49		2.43	45.63
Total	203		600		218		27.4		190.05		25.55		1264

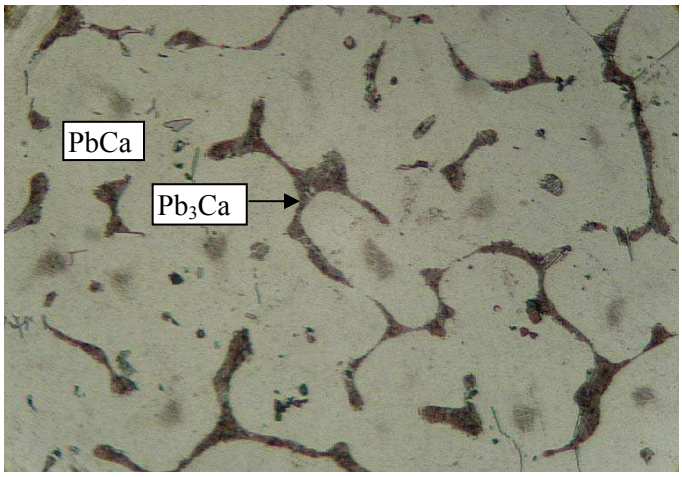

Figure 2. Microphotography of Pb – Ca alloys (x 250)

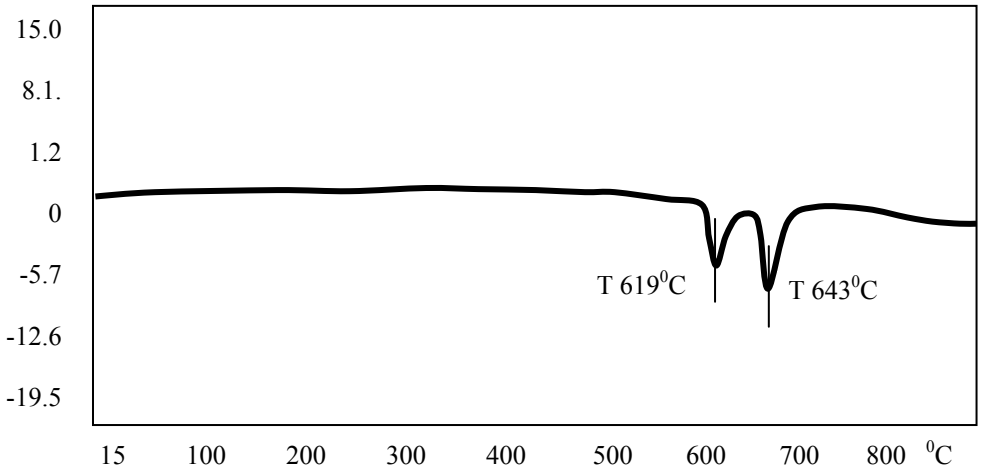

Figure 3. TDA analysis recording

Samples of anodic gases evolved during the electrochemical process were analyzed with the gas chromatograph.

The analysis confirms the presence of CO_2 and CO in proportion of 98 vol % and 2 vol % respectively.

No presence of Cl_2 and/or F_2 or their gaseous compounds were determined by gas chromatography analysis.

4. Discussion

The electrochemical process for Pb-Ca alloys obtaining by CaO electrolysis in molten $CaCl_2$-CaF_2 was carried out at a voltage of 3 V. This voltage is lower then the decomposition potentials of $CaCl_2$ and CaF_2.

In this condition, the electrolysis process consisted in the electrochemical decomposition of CaO, and in the electrodeposition of Ca ions on the molten lead cathode. This fact is also confirmed by the presence of no Cl_2 and/or F_2 or their gaseous carbon compounds in the evolved anodic gases.

From the results presented in Table 4, the current efficiency obtained for the deposition of calcium into molten lead was 79 %.

From the optical microscope analysis of the Pb-Ca alloy samples ,two phases Pb_3Ca and PbCa respectively are observed, without any salt/electrolyte inclusions (Figure 2). The intermetallic compounds are homogenously distributed in the alloy structure.

The presence of a the two phases is confirmed by the DTA analysis (Figure 3) also.

5. Conclusions

The experimental works have demonstrated that the obtaining of Pb – Ca alloys by electrolysis of CaO in molten chloride and fluoride mixture on molten lead cathode is possible.

The electrochemical process allows the **direct obtaining** of Pb-Ca alloys ; the current efficiency of the process is superior to the classical methods , having as consequence the decreasing of the production costs for Pb-Ca alloy .Also , thanks to the high Ca content in the master-alloy,(8.2%), the productivity of the Pb-Ca alloy fabrication significantly increases taking inaccount the law Ca content in the final alloy (0.2-0.3 wt %).

Furthermore, the raw materials used in this method are cheap (CaO, $CaCl_2$, CaF_2) , fact which open new horizons in the implementation of the new technology at industrial level.

In respect to the environment, this method has the great advantage to eliminate the noxious gases Cl_2 (or F_2) evolving during the process .

Received April 23, 2007

National R&D Institute for Nonferrous and Rare Metals – IMNR,
102 Biruinţei Blvd., Pantelimon – Ilfov, ROMANIA

References

[1.] Wirty I .W. Proceeding of 7th International Conference on Lead, Madrid, 1980
[2.] Muller J.J. "Energy Research Abstract", Report 1996
[3.] Delimarski, M. „Electrochemistry of fused salts", Washington DC, 1963
[4.] Levin E.M. "Phase diagrams for ceramists, 1975 Supplement" ACS, Ohio, 1975
[5.] Winard R. „Electrochimica Acta" 8 (53), 1960
[6] Mantell, C.L. „Electrochemisty" 1960

OBȚINEREA ALIAJELOR Pb-Ca PRIN ELECTROLIZA CaO ÎN SĂRURI TOPITE

Rezumat Aliajele Pb - Ca sunt utilizate la fabricarea aşa numiților „acumulatori fără întreținere”, acumulatori ce prezintă performanțe electrice ridicate, un grad înalt de fiabilitate, timp îndelungat de utilizare.

In articol sunt prezentate lucrările experimentale de obținere a aliajelor Pb - Ca prin electroliză în săruri topite. O baie de plumb topit a constituit catodul celulei de electroliză; anodul celulei a fost realizat din grafit. Drept electrolit a fost utilizat un amestec de clorură şi fluorură de calciu. Materia primă în acest proces a fost oxidul de calciu CaO. Procesul de electroliză a durat 6 ore. In urma lucrărilor experimentale s-a obținut un aliaj Pb – Ca cu 8,2 % Ca.

BULETINUL INSTITUTULUI POLITEHNIC DIN IAŞI
Tomul LIII (LVII), Fasc. 1, 2007
Secția
ŞTIINȚA ŞI INGINERIA MATERIALELOR

ALLOYED CAST IRON RESISTENT TO ABRASIVE WEAR: PROPERTIES, ALLOYING ELEMENTS AND THEIR USE, APPLICATIONS

BY

DOLORES PLOP-LUIS and VASILE PLOP-LUIS

Abstract: *The paper synthetically deals with the vast metallurgic area of white cast iron alloys and their applications.*

Key words: *wear, abrasive, white cast iron, hypoeutectic, carbides, austenitization, critical speed, martensite, austenite, solidification, matrix, solubility, fatigue strength, critical point, eutectic, inverse eutectic, heat treatment, pearlite, microstructure.*

Abrasive wear resistant alloy cast iron are white cast iron with a content of 30-40% carbides type $(FeCr)_3C$, $(CrFe)_7C$, Mo_2C, VC, $M_{23}C_6$, martensite and/or residual austenite and up to 5% pearlite.

This cast iron is special cast iron with high hardness and cold-hardening capacity. Alloying elements such as nickel, chromium, molybdenum, which reduce the critical speed of cooling on hardening, find a positive application for the cast iron brands that must undergo a heat treatment and are characterized by wear resistance and dynamic stress resistance.

This type of cast iron is used to make certain pieces employed in sandblasting and molding equipment in foundries and grinding plants.

Extremely high wear resistance under circumstances of mechanical schock on impact is secured by the hardness of alloyed martensite (600 ... 700 HV), the hardness of carbides (1100 ... 1300 HV) and the dimensions and distribution of eutectic carbides.

Ledeburitic white cast iron with pearlitic structure are used for parts of energetic machinery, grinding and sandblasting equipment: blades, disks, pump parts, balls for mills, grinding bodies.

Martensitic white cast iron are used for grinding bodies, pump parts, crushing cylinders.

Ledeburitic white cast iron with austenitic structure are used in knives, parts for the manufacture of silicon bricks, wear and mechanic shock heavily stressed parts.

White cast iron with the eutectic made of carbides M_7C_3 and $M_{23}C_6$, with martensitic and martensito-austenitic structure with M_7C_3, are used for rolls in sorting machines, slurry pumps, shielding for cement or ore mills, hydro cyclones, blades for sandblasting machines with shots and rolling cylinders.

White cast iron with austenitic and austenito-martensitic structure are used for centrifugal machine parts, sandblasting machine blades, slurry pumps, blade stirrer, impellers, etc.

White cast iron is to be used in applications which need abrasion resistance, such as the building parts of the machines for abrasive materials crushing, grinding and manipulation.

The high amount of eutectic carbides in highly alloyed white cast iron microstructures secures the hardness needed to crush and grind mineral materials. The metallic matrix which supports the carbide phase of these cast irons may be egulated both by the alloying elements content and nature and by the heat treatment applied, which allows a suitable balance between abrasion resistance and the resilience needed to face the repeated mechanical impact to be achieved.

Economically speaking, complex alloying of cast irons will be used. All highly alloyed white cast irons have chromium to stop graphite from forming on solidification and secure the stability of the carbide phase. Most cast irons also contain Ni, Mo, V, Cu or their combinations to stop pearlite from forming in the microstructure. The hardness of parts cast from alloyed parts may reach 450-800 HB; alloyed white cast irons hat contain eutectic carbides such as M_7C_3, $M_{23}C_6$ are harder than white cast iron with classical or alloyed cementite.

Cast iron alloying with chromium will increase the carbides´tendency to form and will amplify the hardening properties, it will increase mechanical resistance, wear resistance and will reduce cast iron´s structured dependence on wall thickness.

The chemical composition of chromium highly alloyed white cast iron used to build cement mills observes the following concentrations:

a) 2 ... 4,3 % C;
b) 10 ... 26 % Cr;
c) 3,5 ... 10,2 Cr/C ratio;
d) up to 4,0 % Mo.

In chromium cast irons, the most used to build parts resistent to abrasive wear by grinding, the carbide percentage is of 20-30 %, with some exceptions of the value, 40-50 % or 10-15 %.

There are cast irons alloyed with chromium and nickel (e.g. 3% C, 9% Cr, 5% Ni) whose structues include duplex carbides, made of central carbide M_7C_3 surrounded by M_3C carbide. These duplex carbides identified are due to certain solid state transformations.

In hypoeutectic cast irons, eutectic carbides solidify in the spaces between the primary austenite dendrites, with carbides having a lamellar aspect. In hypereutectic alloys, primary austenite is replaced by big primary carbides.

In a ratio CrFe > 7,2 an austenitic metallic matrix is obtained. Molybdenum reduces this ratio down to aprox. 4,5. With less than 13 % Cr in the structure, a constituent similar to pearlite appears, which is made of chromium ferrite and alloyed cementite. Ni is almost entirely found in the primary matrix. It will stop the tendency of pearlitic transformation on cooling, facilitating the production of intermediary transformations of martensitic type.

In parts cast out of chromium and nickel cast iron, a structure made of carbides, martensite and residual austenite is intented to be obtained. Nickel reduces C´s solubility in the austenite, like silicon, but to a lesser extent.

If it is well correlated with the cast iron´s content in silicon and chromium, Ni increases hardness, resistance and toughness, as well as cast iron´s wear resistance.

Molybdenum, in chromium cast iron, is distributed in three phases: Mo_2C carbide, $(Cr, Fe, Mo)_7C_3$ complex carbide and the basic metallic phase.

An adittion of up to 3,5 % Mo finishes the basic mass´s structure, leading to an improvement of wear resistance, fatigue resistance and reduces a lot the structure´s dependence on the cast part´s wall thickness.

Additions of Mo are distributed between ferrite and cementite. Complex carbide with molybdenum, which appears on big concentrations of molybdenum, is less stable than iron-chromium carbides. With more than 2,5 % Mo in cast iron, a special carbide may appear.

$\%\ Mo_{carbide} = 0{,}53\ (\%\ Mo) - 0{,}05$

$\%\ Mo_{matrix} = 0{,}23\ (\%\ Mo) - 0{,}029$

Molybdenum reduces the austenitization temperature, having a positive action on the cast iron´s heat treatment of hardening.

Vanadium is an alloying element used is the production of wear resistant white cast iron. There are:

a. vanadium cast iron → Fe-C-V;
b. chromium and vanadium cast iron → Fe-C-Cr-V.

Eutectic cementite does not form in vanadium cast iron. Primary eutectic consists of austenite and vanadium carbides at alloying degrees which define Fe-C-V cast irons.

Within the A + VC eutectic column, vanadium carbide forms a hard dendritic case laid in a softer austenite mass, at temperatures higher than the critical points or lower critical temperatures with austenite´s transformation on cooling.

A + VC eutectic, γ + VC appears at approx. 1350ºC, and eutectic transformation takes place at 810°C – (α + VC).

Such a eutectic structure is considered „inverse", the matrix being made of austenite.

Vanadium cast irons and inverse eutectic cast irons are characterized by fracture resistance, mechanic shock toughness and wear resistance. The cast iron´s content of vanadium is rectified with that of alloying elements.

Elements such as Al, Cu, Si, Ni will reduce vanadium carbides´s solubility in austenite; the critical content of vanadium needed in the eutectic structure is reduced.

Cr and Mn will reduce, in cast iron, the carbon´s thermodynamic activity; alloyed with elements that increase vanadium´s solubility in austenite induces a double influence:

- the first action of this group of elements is negative, increasing vanadium´s critical concentrations (Cr, Mn) in cast irons;
- the second action is positive and involves austenite´s cast state „destabilization" and on heat treatment. Austenite´s decomposition on slow cooling in metastable constituents secures an increase of hardness and mechanical strength.

The presence in the Cr-V cast irons´s structure of two types of eutectics ensures wear resistance and special mechanical features, including deformability and toughness.

Alloyed white cast irons resistent to abrasive wear, cast in molding mixtures reach a hardness of 400 ... 500 HV, while in those shell cast, the density reaches values of 575 ... 760 HV.

Martensitic white cast iron´s wear resistance is highly superior to that of austenitic cast iron.

The mechanical properties of alloyed white cast iron, especially hardness and wear resistance, are modified by heat treatments.

The following conditions must be met for a secure austenite-martensite transformation to take place:

1. The carbon and chromium content in the basic metallic mass, after solidification (austenite), must be reduced down to a certian limit, by precipitation of secondary globular carbides. The objective may be met depending on the alloy´s chemical composition, either by reducing the part´s cooling speed in the mold – slow cooling on balance – or by a hardening treatment.
2. Austenite poor in carbon and chromium shows martensitic transformation temperatures M_S (possibly M_F) with positive values and allows the development of martensitic transformation under the circumstances of metallic system cooling on slow speeds.

The alloy must show a certain value of the hardening property that may avoid the asutenite-pearlite transformation and the austenite-bainite transformation.

Received, April 2007 *District Inspectorate of Iasi*

REFERENCES

1. Vasile Cojocaru Filipiuc – „Fonte: obținere, proprietăți, utilizări” (Cast iron: production, properties, applications), Editura „Gh. Asachi”, Iaşi
2. Constantin Baciu, ş.a. – „Studiul materialelor metalice” (A study of metallic materials), Editura „Gh. Asachi”, Iaşi

FONTA ALIATA REZISTENTA LA ABRAZIUNE: PROPRIETATI, ELEMENTE DE ALIERE SI UTILIZAREA LOR, APLICATII

Abstract: Lucrarea tratează sintetic vastul domeniu metalurgic al aliajelor din fontă albă aliată şi domeniile lor de utilizare

BULETINUL INSTITUTULUI POLITEHNIC DIN IAŞI
Tomul LIII (LVII), Fasc. 1, 2007
Secția
ŞTIINȚA ŞI INGINERIA MATERIALELOR

ELECTRICAL RESISTIVITY VARIATION WITH TEMPERATURE IN METALLIC AMORPHOUS RIBBONS FROM $Fe_{80-X}Re_XB_{20}$ (Re = Gd, Sm) SYSTEMS

BY

CORNELIU MUNTEANU[1], LUCIA ANIŞOARA DRĂGAN[2], STELUȚA MUŞAT[2] , CIPRIAN LOHAN[1], MARIAN VASILE LOZNEANU[1]

Abstract: The paper presents a study of the electrical resistivity variation with temperature in amorphous metallic ribbons from the systems $Fe_{80-X}Gd_XB_{20}$ for X = 0, 5, 7, 10 %at. and $Fe_{80-X}Sm_XB_{20}$ for X = 0, 2, 5, 7 %at., ribbons obtained by the melt quenching method. There have been used ribbon samples with 20÷40 μm thickness and 2 mm width. The equipment used has been designed for this purpose only and have platinum ducts and the thermocouple for temperature measurements connected at a V-545 multimeter endowed with a process interface. The experiment data for the electrical resistivity variation were being taken with an HAMEG-8112 measurement system, on-line with a computer. The electrical resistivity variation has a typical shape between 20 and 250 °C, $\rho = \rho_o (1 + \delta T) + \beta T\gamma$. In the $Fe_{80-X}Sm_XB_{20}$ system the resistivity variation is relatively uniform, with a maximum *at* X = 5 %at Sm and 250 °C.

Keywords: resistivity, amorphous,

1. Introduction.

The paper presents a study of the electrical resistivity variation with temperature in amorphous metallic ribbons from the systems $Fe_{80-X}Gd_XB_{20}$ for X = 0, 5, 7, 10 %at. and $Fe_{80-X}Sm_XB_{20}$ for X = 0, 2, 5, 7 %at., ribbons obtained by the melt quenching method. There have been used amorphous ribbon samples with 20÷40 μm thickness and 2 mm width.

2. Experimental details

For the measuring of the amorphous metallic ribbons electrical resistivity as a function of temperature there have been designed and developed a special equipment (Figure 1). It has a furnace (C) into which samples are being introduced, previously fixed on a support (PP). Furnace temperature can be adjusted by means of a thermoregulator, the electrical supply being achieved by self-transformer (AT).

The sensitive element of the thermoregulator is a Chromel-Alumel thermocouple (TC). A thermocouple of the same type is used for the measuring of the sample temperature. The platinum ducts and the thermocouple for measuring the sample temperature were being connected at the V-545 multimeter (MV), endowed with a process interface. The computer dialogue with the data acquisition module (MA) was done on the basis of a serial-parallel commutation of the multimeter mode.

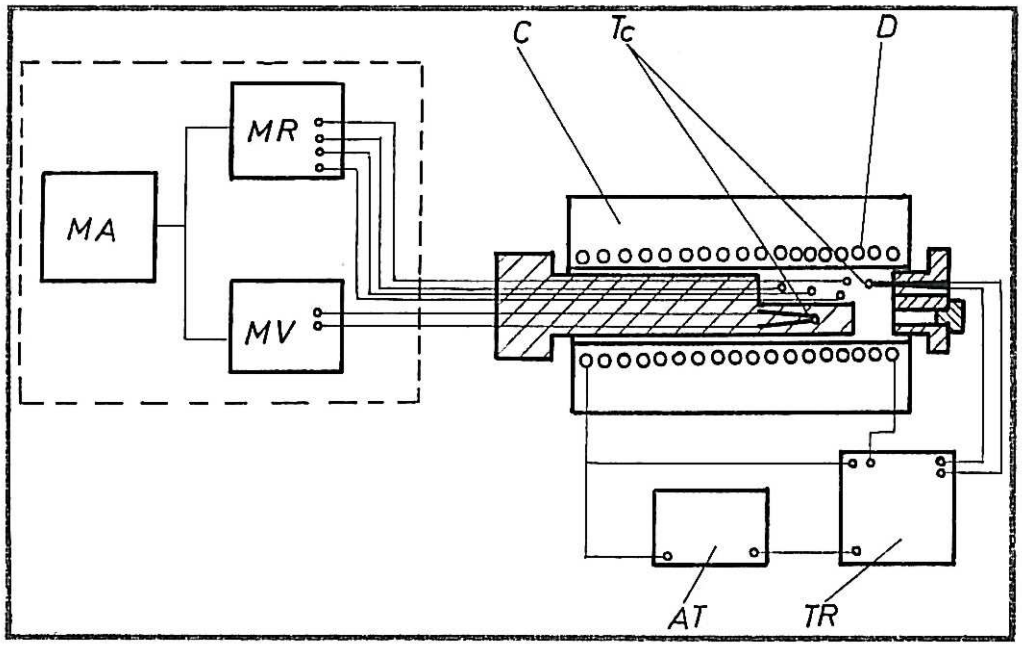

Figure 1. Electrical resistivity measurement equipement.

The experimental data for the electrical resistivity variation were taken with HAMEG-8112 measurement system, with its own interface.

The furnace has been manufactured by wrapping on a pyrolan tube of a Kantal-Al ribbon in a single layer. The furnace power is 150 W and with a maximum obtained temperature of 1200 °C.

The samples for resistivity measurements were obtained by cutting from amorphous ribbon at a length of 20 mm. We use the potential gauge method, the potential being measured with two electrodes placed at a distance **d** between them. In this case

$$V = \frac{I_d}{U_d \quad S} \tag{1}$$

where $\mathbf{I_d}$ – current, A; $\mathbf{U_d}$ – tension drop, V; **S** – cross section of the sample, m^2.

3. Results and conclusions

Measurements have been done relatively with the resistance value at 25 °C, respectively r(T)/r(25 °C). The experimental results for the obtained amorphous metallic ribbons are given in *Figure 2 and 3*.

The variation of the electrical resistivity with the temperature for the obtained amorphous metallic ribbons shows a typical shape between 20 and 250 °C, after a quasilinear law of type $\rho = \rho_o (1 + \delta T) + \beta T\gamma$, where β and γ are correction coefficients.

The system $Fe_{80-X}Sm_XB_{20}$ shows a maximum of the electrical resistivity and α coefficient at a 5 %at Sm. By comparison with the amorphous ribbons from $Fe_{37.5}Ni_{32.5-X}Cr_5Co_XB_{15}Si_{10}$ system the variation of the electrical resistivity of the Fe_{80-}

$_{X}Sm_{X}B_{20}$ system is much more uniform, fact explained by the occurring of less crystalline phases. The amorphous ribbons from this system are being recommended for X = 2 %at. Sm, for electrical use in ampermeters, precision routes for electronic measurement apparatus etc.

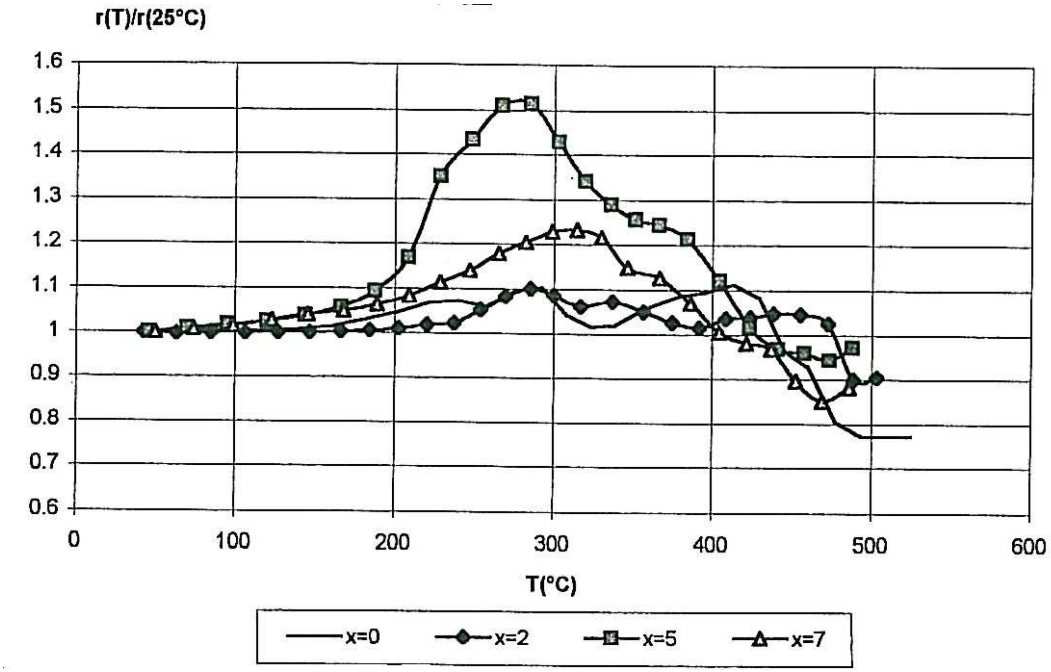

Figure 2. Electrical resistivity variation with temperature for $Fe_{80-X}Sm_XB_{20}$ system.

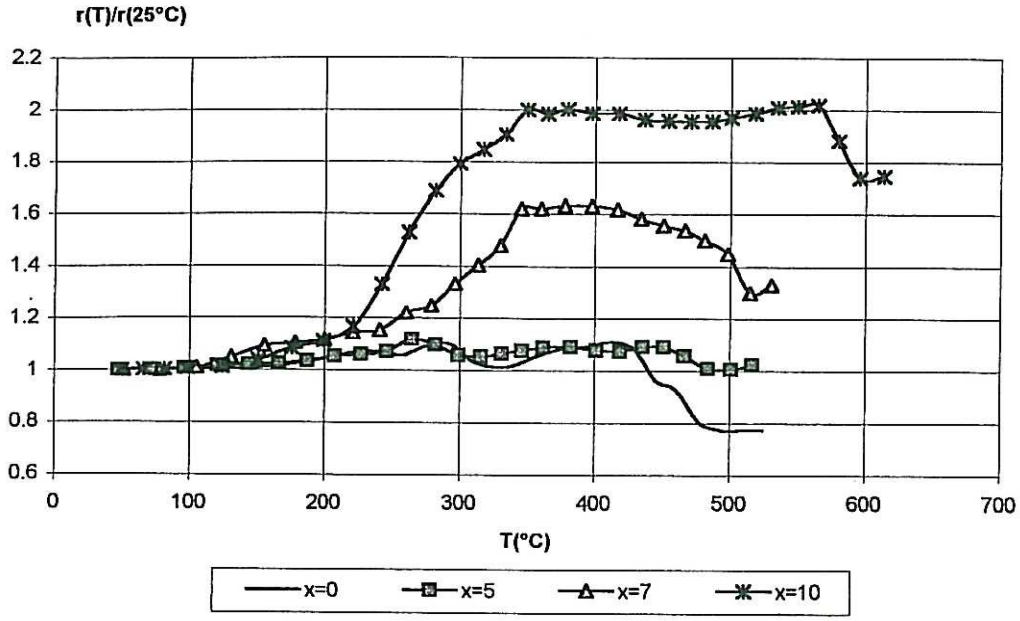

Figure 3. Electrical resistivity variation with temperature for $Fe_{80-X}Gd_XB_{20}$ system.

The variation of the resistivity with temperature in amorphous metallic ribbons from $Fe_{80-X}Gd_XB_{20}$ system shows a little increasing up to 250 °C, after which, for X = 7 and 10 %at. Gd, the resistivity (and the α coefficient) grows very much up to the

crystallisation temperature, progressively placed at higher values.

Received April 30, 2007

1.Technical University Gh. Asachi Iasi
2.Scolar Group of Services and Crafts Buzău

REFERENCES

1. **Guntherodt, H.J., Beck, H.** – *Glassy Metals I. Topics in Applied Physics*, vol. 46, Springer Verlag, Berlin-Heidelberg-New York, 1981.
2. **Herman, H.** – *Ultrarapid Quenching of Liquid Alloys*. *Treatise in Material Science and Technology*, vol. 20, Academic Press, London, 1981.
3. **Suzuki, K., Fujimori, H., Hashimoto, K.** – *Amorphous Metals*, translated from Japanese in Russian, Moscow, 1987.
4. **Munteanu, C., Rusu, I., Apachiței, I.** – *Using Properties of Metallic Amorphous Ribbons From (Fe-Co-Ni) Metalloid System Obtained by Melt Quenching*, Journal de Physique, IV, Colloque C7, nov. (1993) 139.

STUDIU COMPARATIV ASUPRA VARIAȚIEI REZISTIVITĂȚII ELECTRICE CU TEMPERATURA ÎN CAZUL BENZILOR METALICE AMORFE DIN SISTEMELE $Fe_{80-X}Re_XB_{20}$ (Re = Gd, Sm)

Rezumat: Lucrarea reprezintă un studiu asupra variației rezistivității electrice cu temperatura, în cazul benzilor metalice amorfe din sistemul $Fe_{80-X}Gd_XB_{20}$, pentru X = 0, 5, 7, 10 %at. şi sistemul de aliaje $Fe_{80-X}Sm_XB_{20}$, pentru X = 0, 2, 5, 7 %at., benzi obținute prin călire ultrarapidă din stare lichidă. S-au folosit epruvete sub formă de bandă, cu grosimea de 20÷40 μm şi lățimea de 2 mm. Echipamentul folosit a fost special proiectat în vederea realizării acestor cercetări, el având contactele de platină şi termocuplul de măsurare a temperaturii conectate la un multimetru V-545 cu interfață de proces. Datele experimentale referitoare la variația rezistivității electrice au fost obținute cu un sistem de măsură tip HAMEG-8112, on-line cu un computer. Curba de variație a rezistivității are o formă tipică între 20 şi 250 °C, după legea $\rho = \rho_o (1 + \delta T) + \beta T\gamma$. Pentru sistemul $Fe_{80-X}Sm_XB_{20}$ variația rezistivității este relativ uniformă, având un maxim la X = 5 %at Sm şi 250 °C

BULETINUL INSTITUTULUI POLITEHNIC DIN IAŞI
Tomul LIII (LVII), Fasc. 1, 2007
Secția
ŞTIINȚA ŞI INGINERIA MATERIALELOR

THE EFFECTS OF MAGNETIC NANOPARTICLES ON CANCEROUS CELLS IN MAGNETIC FLUID HYPERTHERMIA TREATMENT

BY

GIGEL NEDELCU

Abstract: The mechanism of heat-induced cell death with magnetic nanoparticles (MNPs) generates numerous cellular changes, leading to morphological changes, cell detachment, and death. Cellular alterations include, changes in the membrane, nuclear and cytoskeletal structures, cellular metabolism, macromolecular synthesis etc. In this work the purpose is to explain the main mechanisms of magnetic fluid hyperthermia (MFH), more precisely the heating mechanisms of MNPs and the effects of this heating of MNPs through extracelullar and intracellular environments.

Keywords: magnetic nanoparticles (MNPs), heating mechanism, heating effects, cell death.

1. Introduction

Magnetic fluid hyperthermia (MFH), the heating of tissue temperature [1] using magnetic nanoparticles (MNPs), is a promising tool for therapy of various cancers. This is because tumour cells are more sensitive to temperatures in the range of 42-45ºC than normal tissue cells [2]. There are several benefits to using hyperthermia. This process not only enhances the effectiveness of other cancer treatments, but it also kills tumour cells that are resistant to other forms of treatment.

There are several methods of hyperthermia that are employed in cancer therapy: whole body hyperthermia, radiofrequency hyperthermia, inductive hyperthermia using a microwave antenna, implantable needles, and nanosized magnetic particles [3].

In this work, it is described MNPs heating theory [4-6] and the effects of MNPs on extra- and intracellular level [7].

It is crucial to understand the effect that the MFH process has on a cellular level. This paper will focus on the mechanisms of cellular destruction caused by MFH.

2. Heating theory of magnetic nanoparticles (MNPs)

There exist at least three different mechanisms by which magnetic materials can generate heat in an alternating field [8]:

1. generation of eddy currents in magnetic particles with size >1μ,
2. hysteresis losses in magnetic particles >1μ and multidomain magnetic particles,
3. relaxation losses in 'superparamagnetic' single-domain magnetic particles,
4. frictional losses in viscous suspensions.

Relaxation losses in single-domain MNPs fall into two modes: rotational (Brownian) mode and Néel mode. The principle of heat generation due to each individual mode is shown in figure 1, (a) and (b). In the Néel mode, the magnetic moment originally locked along the crystal easy axis rotates away from that axis towards the external field. The Néel mechanism is analogous to the hysteresis loss in multi-domain magnetic particles whereby there is an 'internal friction' due to the movement of the magnetic moment in an external field that results in heat generation. In the Brownian mode, the whole particle oscillates towards the field with the moment locked along the crystal axis under the effect of a thermal force against a viscous drag in a suspending medium. This mechanism essentially represents the mechanical friction component in a given suspending medium.

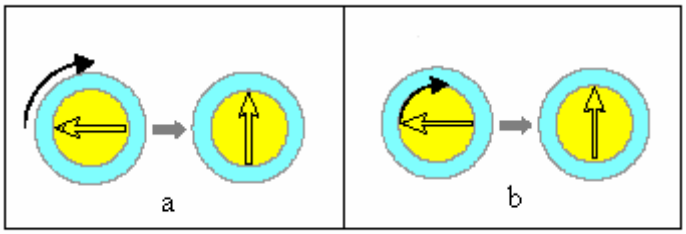

Figure 1. Relaxation mechanisms of MNP: a - Brownian relaxation, entire particle rotates in fluid; b - Néel relaxation, direction of magnetization rotates in core. The structure of MNP: core (yellow), shell (bleu). The arrow inside the core represents direction of magnetization.

The energy dissipation of MNPs in an alternating magnetic is

$$P = \pi \mu_0 \chi_0 H_0^2 f \frac{2\pi f \tau}{1 + (2\pi f \tau)^2} \tag{1}$$

where μ_0 is the permeability of free space, $4\pi \cdot 10^{-7}$ T m/A; χ_0 is the equilibrium susceptibility; H_0 and f are the amplitude and the frequency of alternating magnetic field; and τ is the effective relaxation time given by

$$\tau^{-1} = \tau_N^{-1} + \tau_B^{-1} \tag{2}$$

where τ_N and τ_B are the Néel relaxation and the Brownian relaxation time, respectively. τ_N and τ_B are written as

$$\tau_N = \frac{\sqrt{\pi}}{2} \tau_0 \frac{\exp(T)}{\sqrt{\Gamma}} \tag{3}$$

$$\tau_B = \frac{3\eta V_H}{kT} \tag{4}$$

where τ_0 is the average relaxation time in response to a thermal fluctuation; η is the viscosity of medium; V_H is the hydrodynamic volume of MNP; k is the Boltzmann

constant, 1.38×10^{-23} J/K; T is the temperature. Here, $\Gamma = KV_M/kT$ and V_M is the volume of MNP. The MNP volume V_M and the hydrodynamic volume including the ligand layer V_H are written as

$$V_M = \frac{\pi D^3}{6} \tag{5}$$

$$V_H = \frac{\pi(D+2\delta)^3}{6} \tag{6}$$

where D is the diameter of MNP; δ is the ligand layer thickness. The equilibrium susceptibility χ_0 is assumed to be the chord susceptibility corresponding to the Langevin equation, and expressed

$$\chi_0 = \chi_i \frac{3}{\xi}\left(\coth\xi - \frac{1}{\xi}\right) \tag{7}$$

where $\xi = \mu_0 M_d H V_M/kT$; $M_S = \phi M_d$; $H = H_0\cos 2\pi ft$; and ϕ is the volume fraction of MNPs. Here, M_d and M_S are the domain and saturation magnetization, respectively. The initial susceptibility is given by

$$\chi_i = \mu_0\phi M_d^2 V_M/3kT \tag{8}$$

The temperature rise is calculated as $\Delta T = P\Delta t/\rho c_P$ where ρ and c_P are the effective density and the effective specific heat calculated as $\rho = \phi\rho_1 + (1-\phi)\rho_2$ and $c_P = \phi c_{P1} + (1-\phi)c_{P2}$, where subscripts 1 and 2 represent the MNPs and the medium, respectively.

3. The effects of magnetic nanoparticles (MNPs) on tumours and cancerous cells

Majority of hyperthermic treatments not achieve uniform heating of the tumour region to the desired temperature without damaging normal tissue. Therefore, researchers have proposed intracellular hyperthermia by using nanoszed magnetic particles [3]. MFH allows the heating to be restricted to the tumour area [9]. This method, which incorporates injecting the magnetic fluids directly into the tumour body, relies on the theory that any metallic objects when placed in an alternating magnetic field will have induced currents flowing within them [10]. As this occurs, the MNPs produce heat, as a product of resisting the current flow. With the application of an external AC magnetic field [11], the particles in turn heat the malignant cells when they come into contact, thus increasing the cells sensitivity to other treatments, ex. chemotherapy and radiation.

It was discovered that MNPs concentrated by an external constant magnetic field in tumour vasculature may lead to embolic lesions and necrosis of a tumour body

and further the heat produced for thermal activation of a drug enhances the effect of chemotherapy by local hyperthermic treatment of neoplastic cells [12].

The results suggested that MNPs are potentially effective tools for the treatment of solid tumours, causing both killing of the tumour cells by heat, and the induction of an immune response [3].

Using magnetite particles, Ohno *et al.*'s strategy was based on the heat radiation associated with the physical process of hysteresis loss of magnetic substance in the alternative magnetic field [13]. Instead, though, they made a thin stick-type mingled with carboxymethylcellulose (CMC) to obtain a higher heating effect [13]. The benefit of this product was that one could much more easily direct the MNPs to their desired location. What was found was that, by using CMC, the particles did not invade the surrounding normal tissue. In addition, the tumour sizes decreased, thus obtaining satisfactory results.

3.1. Effects on tumour

The response of the tumour to hyperthermia depends on the size of the tumour, its composition, physical location within the host tissue, and its vascularity [14]. During hyperthermia, the tumour bed does not vasodilate – therefore, blood flow can't increase and heat is retained in the tumour tissue at temperatures that would have caused normal capillary beds to vasodilate [14]. The growth of solid tumours is associated with the incorporation of fluid within the tumour mass as a result of nutrient deprivation, which can constitute up to 60 percent of the tumour volume [14]. This fluid, however, is void of oxygen and glucose, and contains excessive amounts of carbon dioxide and lactic acid. Under conditions of extreme nutrient deprivation, cell death occurs rapidly at 37ºC and even quicker at higher temperatures [14]. An increase in the temperature of this fluid may lead to an increase in the hydrostatic pressure due to the increase in molecular motion [14].

3.2. Destruction and death of cancerous cells in MFH treatment

Cell death occurs in two modes, *apoptosis* and *necrosis*, that are biochemically and morphologically different [15].

Apoptosis: Apoptosis is a genetically programmed and biochemically active mode of death in which the cell actively participates in its own elimination [15]. It is required for cell life span and normal development [16]. Apoptosis aids in self-deletion of injured cells, terminal differentiation of epithelial cells, and organ and tissue shaping [15]. Abnormalities of this process are implicated in several human diseases, including cancer.

This process can be recognized by cell shrinking, condensation of the chromatin, and eventually DNA fragmentation [15]. In addition, actin is considered to play a role in several main morphological events of apoptosis, including formation of blebs, cell rounding, detachment, and final cell disintegration into apoptotic bodies [16].

Cells inducing apoptosis retain much of their membrane function and do not elicit an inflammatory response [15]. This process can be triggered by radiation,

transduced signals, DNA damage, and hyperthermia. Furthermore, hyperthermia with a temperature range of 41-45ºC induces apoptosis to varying degrees in many cell lines [15]. The mechanism behind hyperthermia-induced apoptosis, however, isn't well understood. Some postulate that the primary targets are heat liable and newly synthesized proteins. These denatured proteins and unfolded nascent peptides can be cytotoxic and lead to cell death [15]. In addition, heat shock proteins act by preventing the aggregation of the denatured proteins through interactions with the ATP pathway [15]. Targeted proteins must go through the ATP pathway before they can be recognized as substrates for proteolysis. Therefore, when hyperthermia is induced on the cells, the proteins denature before the heat shock protein response can occur. It is logical to assume, then, that by administering hyperthermia, the cell can accumulate high does of heat shock proteins [15]. Some hypothesize that by inhibiting the synthesis of the heat shock proteins, the cells is unable to build a pool of protective stress proteins, and the cell loses its capability to survive [15].

Necrosis: Cells subject to toxic insult die by necrosis [17]. In this case, metabolic functions stop, which therefore causes a lack of osmotic regulation, thereby inflicting cellular swelling [17]. In addition, necrosis causes a sharp decline in ATP production, mitochondrial swelling, and eventually cytolysis and the release of pro-inflammatory agents [15]. Unlike apoptosis, these reactions occur as a natural result of loss of cell function. Although it had been widely accepted that hyperthermia always caused necrosis, it is now clear that this isn't the case [18]. Rather, hyperthermia induces apoptosis in neoplastic cells and tissues.

4. Conclusions

This paper reviews theoretical background of MNPs used in magnetic fluid hyperthermia and some of the cellular affects resulting from MFH. To summarize, tumour cells are more susceptible to high temperatures, thus allowing MFH to actually kill the malignant cells. Apoptosis, not necrosis, is one result of hyperthermia. High heat subjected to cells drastically effects the cellular components and pH is an important determinant of tumour cell death. And lastly, MNPs are emerging as a potential substance to increase the effectiveness of hyperthermia.

The future possibilities of this anti-cancer precursor are nearly endless. For example, researchers could soon use MFH treatments to completely inactivate the symptoms of HIV, thus allowing the patients to live a longer life. Further, MFH treatments may soon cure cancers such as leukemia. Although MFH is a relatively new treatment used for cancer, it has already changed the lives of many people.

REFERENCES

1. Hori Y., Nagai R., Urabe N., Yoshikawa T., and Otsuka M., **Bioorganic & Medicinal Chemistry, 10,** 2002, **111**

2. Shinkai M., Le B., Honda H., Yoshikawa K., Shimizu K., Saga S., Wakabayashi T., YoshidaJ., and Kobayashi T., **Japan Journal of Cancer Research, 92,** 2001, **1138**

3. Yanase M., Shinkai M., Honda H., Wakabayashi T., Yoshida J., and Kobayashi T., **Japan Journal of Cancer Research, 89,** 1998, **775**

4. Venkatasubramaniam S. Kalambur, Bumsoo Han, Bruce E. Hammer, Thomas W. Shield and John C. Bischof, **Nanotechnology, 16,** 2005, **1221**
5. Hergt R., Dutz S., Muller R. and Zeisberger M., **J. Phys.: Condens. Matter 18,** 2006, **2919**
6. Maenosono S. and Saita S., **IEEE Transactions on Magnetics, 42,** 2006, **1638**
7. Rister C., **Anatomy and Physiology for Engineers,** 2004
8. Andra W., **Magnetism in Medicine,** Berlin: Wiley–VCH, 1998
9. Tartaj P., Morales M., Veintemillas-Verdaguer S., González-Carreño T., and Serna C., **Journal of Physics D: Applied Physics**, **36,** 2003, **182**
10. Berry C. and Curtis A., **Journal of Physics D: Applied Physics**, **36,** 2003, **198**
11. Šafařik I. and Šafařiková M., **Chemical Monthly**, **133,** 2002, **737**
12. Babincová M., Leszczynska D., Sourivong P., Babinec P., and Leszczynski J., **Medical Hypotheses**, **62,** 2004, **375**
13. Ohno T., Wakabayahi T., Takemura A., Yoshida J., Ito A., Shinkai M., Honda H., and Kobayashi T., **Journal of Neuro-Oncology**, **56,** 2002, **233**
14. Vertrees R., Leeth A., Girouard M., Roach J., and Zwischenberger J., **Perfusion**, **17,** 2002, **279**
15. Poe B. and O'Neill K., **Apoptosis**, **2,**1997, **510**
16. Luchetti F., Mannello F., Canonico B., Battistelli M., Burattini S., Falcieri E., and Papa S., **Apoptosis, 9,** 2004, **635**
17. Huschtscha L., Jeitner T., Andersson C., Bartier W., and Tattersall M., **Experimental Cell Research, 212,** 1994, **161**
18. Rong Y. and Mack P., **International Journal of Hyperthermia**, **16,** 2000, **19**-27.

Received March 31nd , 2007 *"Al.I.Cuza" University, Faculty of Physics,Iaşi*

EFECTELE NANOPARTICULELOR MAGNETICE ASUPRA CELULELOR CANCEROASE IN TRATAMENTUL PRIN HIPERTERMIE CU FLUIDE MAGNETICE

Rezumat: Mecanismul distrugerii celulelor canceroase prin inducerea de căldură într-o tumoură cu ajutorul hipertermiei cu nanoparticule magnetice este putin cunoscut. De aceea am descris în această lucrare nu numai mecanismul fizic prin care nanoparticulele magnetice se încălzesc sub acțiunea unui câmp magnetic alternativ exterior, ci şi efectele căldurii degajate de aceste nanoparticule magnetice asupra țesuturilor tumourale şi implicit asupra celulelor tumourale.

BULETINUL INSTITUTULUI POLITEHNIC DIN IAŞI
Tomul LIII (LVII), Fasc. 1, 2007
Secția
ŞTIINȚA ŞI INGINERIA MATERIALELOR

SIMULATION OF THE TECHNOLOGIES OF HEATING OF THE STEELS WITH HALF-WARM INITIAL CONDITION, DESIGNED IN C# LANGUAGE

BY

VASILE CAȚARSCHI[a], DAN-GELU GĂLUŞCĂ[a], MIHAI DUMITRU[a] and SMARANDA CAȚARSCHI[b]

Abstract: The biggest quantity of the forged parts of steel are achieved from ingots with the half-warm initial condition, at the introduction of these ones in the heating furnaces, when the temperature of the centre is bigger than the surface temperature. This is performed by the transport of the ingots after stripping in thermos wagons to the forging workshops or by direct transport, when the forging workshop is close to the electric steelworks. In this work three variants of the technologies of ingots heating for forging are presented, related to steel ingots equivalently cylindrical, charged in half-warm initial condition in the furnace, and a variant of the technology of heating of half-cold ingots, with the centre warmer than the surface, at which the temperature of the surface has decreased up to 400-600°C. The software's related to the regimes of heating as parts of the heating technologies are performed on PC in C# language.

Keywords: technologies of heating, C# language, half-warm initial condition, heating diagrams.

1. Introduction

The results of the mathematic modelling [1], of each heating regime, part of a heating technology for the steel half-products equivalently cylindrical, are designed in C# language taking into account the particularities of the initial and final condition of the metal.

After the introduction in the furnace of the warm ingot in the first heating regime, when the temperature of the centre is higher than the surface temperature, while the surface begins to heat, the temperature of the centre of the ingot continues to go down. This cooling takes place until the thermal flow from the surface reaches the ingot axle, moment when the centre of this one starts to heat. The time of cooling of the ingot centre named also "time of thermal inertia" (τ'), depends on the size of the ingot radius ($0 < r < R$) and on the thermal diffusivity (a_0), as per the following relation [2], [3]:

$$\tau' = \frac{r^2}{8 \cdot a_0} \qquad [h] \qquad (1)$$

After the time of thermal inertia, the centre of the ingots starts also to heat, and the thermal gradient of the ingot begins to decrease until a final value of this one is reached (ΔT_f) when the ingot is evacuated from the furnace in order to be forged on the press. If the initial thermal gradient from the ingot (ΔT_0) is very big, it is possible that the heating finish (to reach ΔT_f) in the thermal inertia interval (τ'), [4].

2. Simulation of the technologies

1. *Heating of the half-warm steel ingots with the initial thermal gradient different from zero*

The heating of the warm ingots with the initial temperature (after stripping) comprised between $T_{surf.init.}$ = 650-850°C and $T_{surf.init.} < T_{centre.init.}$ is achieved in two periods, i.e. (fig.1), [5], [6]:

- regime 1 of heating is achieved with constant increase speed (w_1) of the furnace temperature:

$$T_{furn.1} = T_{furn.in} + w_1 \sum_{i=1}^{n} \Delta\tau_i \qquad n = 1, 2, 3, \ldots, \infty \tag{2}$$

where: $T_{furn.in}$, $T_{furn.1}$ – initial temperature and respectively temperature of the first heating period;

w_1 – speed of heating of the furnace from the first heating period;

$\Delta\tau_i$ – time step;

n – number of the time steps until the final condition of the respective heating period is achieved;

- regime 2 of heating is achieved at constant furnace temperature ($T_{furn\ 2}$ = const.)

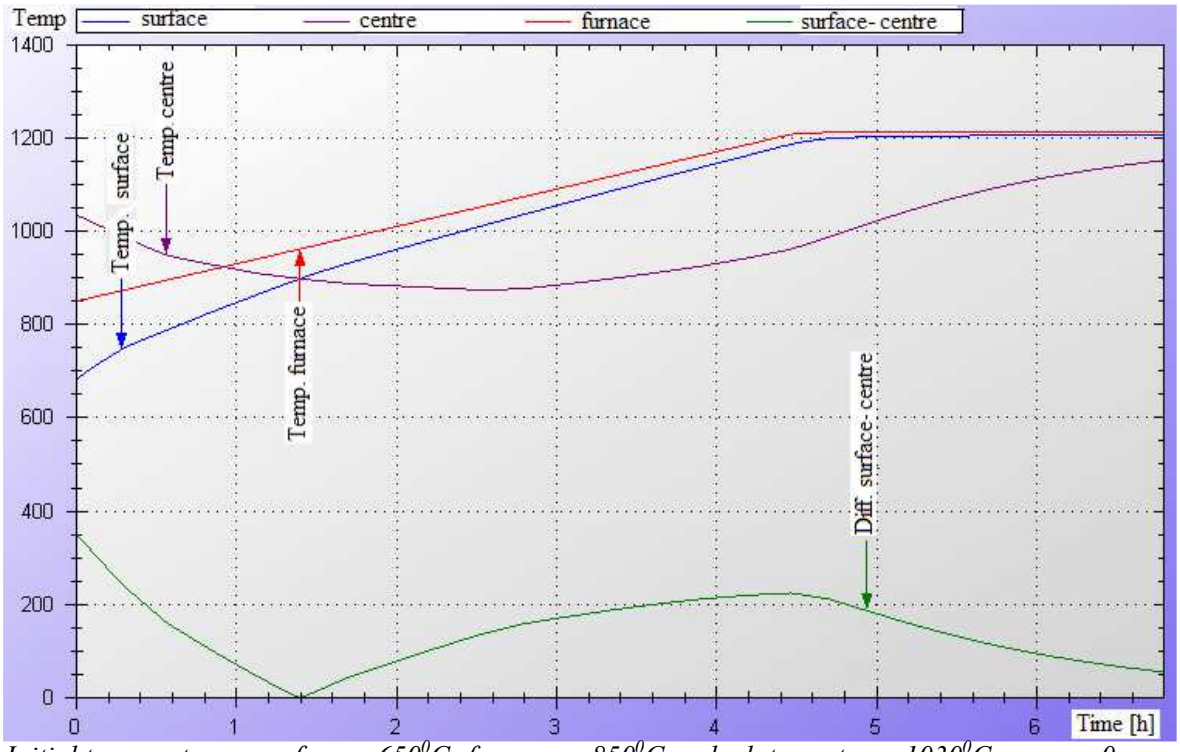

Initial temperatures: surface = 650^{0}C; furnace = 850^{0}C; calculate centre = 1030^{0}C; r_{centre} = 0 mm; Final temperatures: surface = 1207^{0}C; centre = 1154^{0}C; furnace = 1212^{0}C; Heating time [hours]: t_1 = 4.52; t_2 = 2.33; Total time = 6.85; Heating speeds [^{0}C/h]: v_1 = 59; medium diameter = 1200 mm; ingot length = 2700 mm; ingots number = 2; furnace CI = 40.0 m^2; r_{furn} = 4.414;

Fig. 1 Heating of half-warm steel ingots in 2 periods, with the initial thermal gradient different from zero, steel mark 90VMoCr18

2. *Heating of half-warm steel ingots with the initial thermal gradient zero*

A particular case is that when the temperature of the metal surface arrives to be

equal with that of the centre after the maintaining of the ingots in a furnace of thermal conservation and after that the ingots are transferred in a heating furnace in order to continue the heating up to the forging temperature.

In this case, the heating of the ingots with constant initial temperature ($T_{surf.init.} = T_{centre.init.} = 650…750°C$) occurs still in two periods as in the previous case, with the remark that the temperature of the centre maintains constant in the thermal inertia interval (τ'), (fig.2), [5], [6].

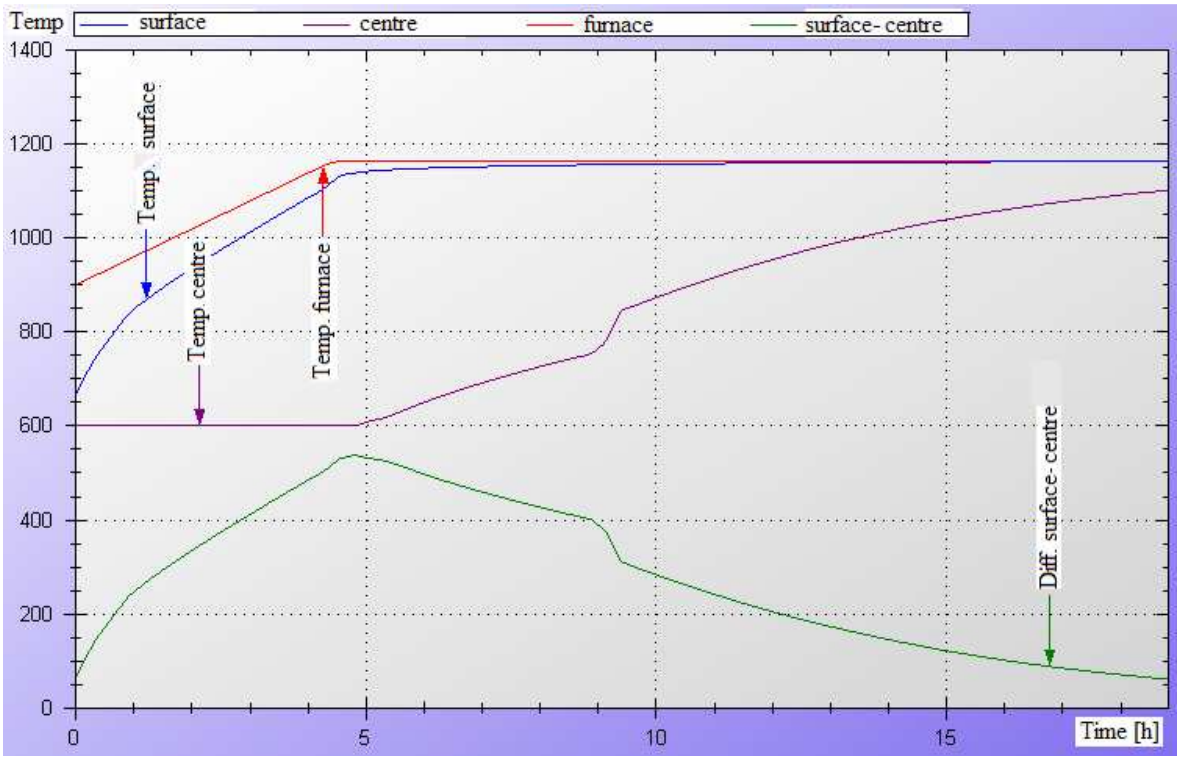

Initial temperatures: surface = 600^0C; centre = 600^0C; furnace = 900^0C; r_{centre} = 0 mm;
Final temperatures: surface = 1162^0C; centre = 1102^0C; furnace = 1164^0C;
Heating time [hours]: t_1 = 4.45; t_2 = 14.52; Total time = 18.97; Heating speeds [^{0}C/h]: v_1 = 59;
medium diameter = 1613 mm; ingot length = 4110 mm; ingots number = 2; furnace CI = 40.0 m^2;
r_{furn} = 3.99;
Fig. 2 Heating of half-warm steel ingots in 2 periods, with the initial thermal gradient zero, steel mark 34MoCrNi15

3. *Re-heating of the warm steel ingots with the initial thermal gradient different from zero*

This technology is applied for the re-heating of the ingots between the forging operations, when the temperature of the surface went down under 800…850°C and the initial temperature of the centre ($T_{centre.init.}$) is lower than the centre final temperature of the previous heating ($T_{centre.fin.}$)

$$T_{surf.init.} < T_{centre.init.} < T_{centre.fin.} \tag{3}$$

The re-heating of the ingots takes place in a single heating period with the regime (fig.3), [5], [6]:

$$T_{furn.} = const. \text{ and } \Delta T_0 \neq 0 \tag{4}$$

And in this case, in the interval of thermal inertia (τ') a cooling of the centre of the half-product equivalently cylindrical takes place and then the proper heating of this one follows. The heating is finalized when the final thermal gradient (ΔT_{fin}) has reached a prescribed value as per the condition:

$$\Delta T_{fin.} \leq \Delta T_{fin.pr.} \tag{5}$$

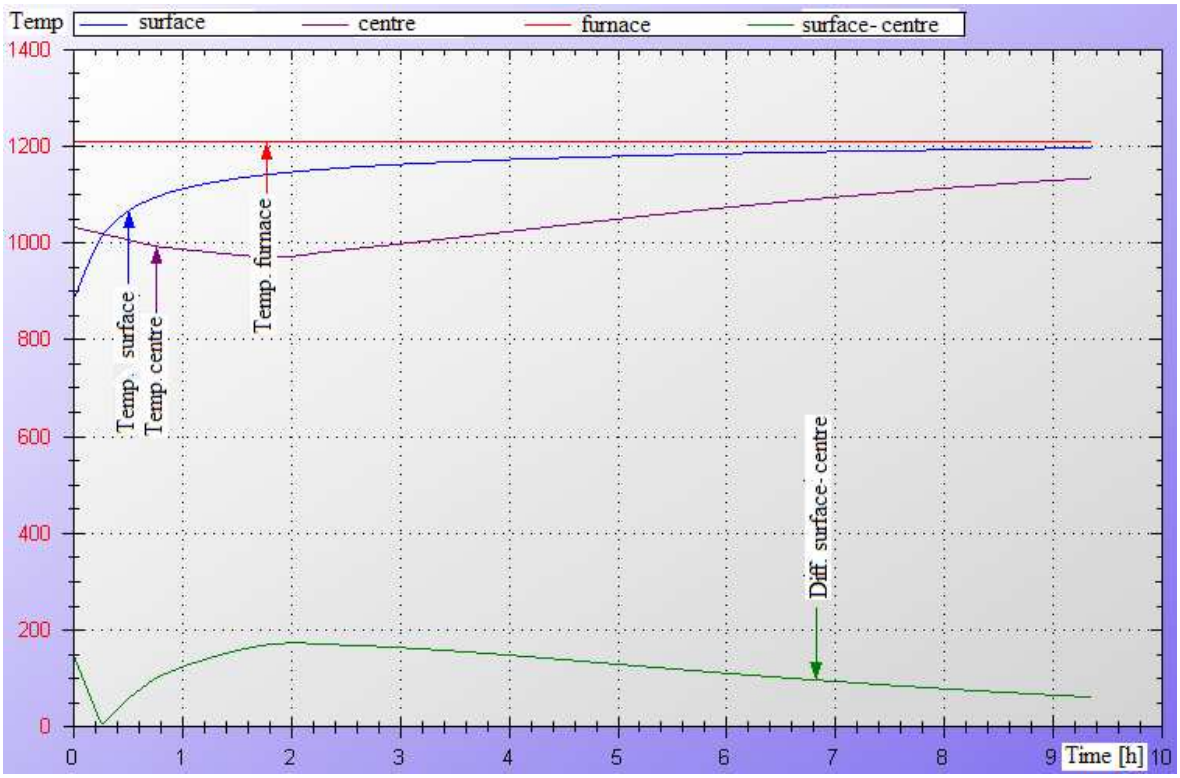

Initial temperatures: surface = 850^{0}C; furnace = 1209^{0}C; r_{centre} = 0 mm;
Final temperatures: surface = 1196^{0}C; centre = 1137^{0}C; furnace = 1209^{0}C;
Heating time [hours]: t_1 = 9.55;- r_{furn} = 3.99;
medium diameter = 1613 mm; ingot length = 4110 mm; ingots number = 2; furnace CI = 40.0 m^2;

Fig. 3 Re-heating of warm steel ingots in 2 periods, with the initial thermal gradient different from zero, steel mark 55MoCrNi15

4. *Heating of the half-cold steel ingots with the initial thermal gradient different from zero.*

The half-cold ingots are defined those that after stripping became cold at the surface up to $T_{surf.init.}$ = 400…600°C, with $T_{centre.init.} > T_{surf.init.}$ and $\Delta T_0 \neq 0$.

The heating of the half-cold ingots takes place in three heating periods, with the regimes (fig.4), [5], [6]:

- regimes 1 and 3 of heating are achieved with constant furnace temperature ($T_{furn.1}$ = const.; $T_{furn.3}$ = const.)
- regime 2 of heating is achieved with constant speed (w_1)of increase of the furnace temperature (relation 2).

The heating of the ingot centre starts after the thermal inertia interval (τ'), in which the centre continued to cool down.

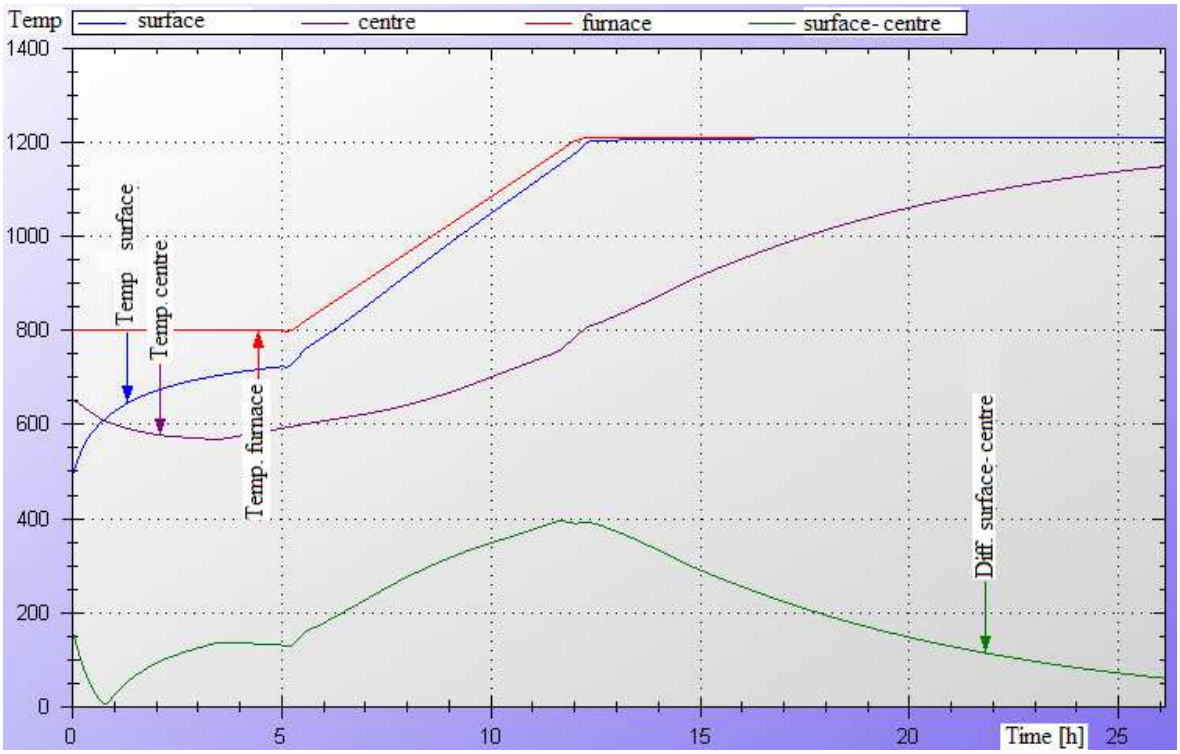

Initial temperatures: surface = 450^{0}C; furnace = 800^{0}C; r_{centre} = 0 mm;
Final temperatures: surface = 1209^{0}C; centre = 1150^{0}C; furnace = 1210^{0}C;
Heating time [hours]: t_1 = 5.22; t_2 = 6.91; t_3 = 14.11; Total time = 26.24;
Heating speeds [^{0}C/h]: v_1 = 59; - r_{furn} = 3.99;
medium diameter = 1613 mm; ingot length = 4110 mm; ingots number = 2; furnace CI = 40.0 m^2;

Figure 4: Heating of half-cold steel ingots in 3 periods, with the initial thermal gradient different from zero, steel mark 12MoCr50

3. Conclusions

The simulation of the technological heating processes on PC, presented at the numbers 1…4, determine the superior instruction of the students from the faculties in this profile (Materials Science and Engineering) as well as of the engineers from the workshops of forging on presses from the companies with hot sectors.

Heating diagrams for the concrete cases of the production workshops can be quickly obtained on a laptop, depending on the real conditions of the furnace charging with a charge of ingots of which the initial data are known (surface temperature, steel grade, dimensions of the representative ingot of the charge, type of the heating furnace and the initial temperature of this one, number of ingots etc.), [7].

Received April 25, 2007

[a] Technical University "Gh. Asachi" of Iassy,
[b] "Anghel Saligny" Technical School of Iassy

REFERENCES

1. Catarschi, V. – *Contributions to Computer Mathematical Adaptation of the Heating Technologies of Flow Susceptible Steel Ingots.* Buletinul Institutului Politehnic Iasi, Tomul XL(XLIV). Fasc.3-4/1994, Sectia IX, **704-712**.
2. Carslaw, H. S., Jaeger, J. C.- Conduction of Heat in Solids. At. the Clarendon Press, Oxford, 1964.

3. Roman, E., Maeder - *Programming in Mathematics*. Addison Wesley Publishing Company, Redwood City, California, U.S.A., 1991.
4. Samoilovici, Iu. A, Timospolskii, V. I. - *Nagrev stali:Spravocinic posobie.* Visaia scola..Minsk, 1990, **8-81**.
5. Catarschi, V. - *Contribution considering the computer designed technologies for steel ingots heating in INCFOR programs***.** METALURGIA INTERNATIONAL, nr.4/2004, ISSN 1582-2214, **8-13**.
6. Catarschi, V. - *Manufacturing Engineering of the Forged Mill Rolls for Rolled Products from SC FORTUS S.A. Iasi.* METALURGIA INTERNATIONAL**,** Nr.5/2004, ISSN 1582-2214, **27-34**.
7. Nemzer, G.G. - *Teplovie protessi proizvodstva crupnih pocovoc.* Masinostroenie, Leningrad, 1979.

SIMULAREA TEHNOLOGIILOR DE ÎNCĂLZIRE A OȚELURILOR CU STAREA INIȚIALĂ SEMICALDĂ, PROIECTATE ÎN LIMBAJUL C#

Rezumat: Cea mai mare cantitate de piese forjate din oțel se realizează din lingouri cu starea inițială semicaldă, care la introducerea lor în cuptoarele de încălzire, au temperatura centrului mai mare decât tempertura suprafeței. Acest lucru se realizează prin transportul lingourilor după stripare în vagoane termos la secția de forjă sau prin transportul direct în cazul în care secția de forjă se află la capătul oțelăriei electrice. În această lucrare se prezintă trei variante tehnologice de încălzire pentru forjare a ligourilor din oțel echivalent cilindrice încărcate cu starea inițială semicaldă in cuptor şi o variantă tehnologică de încălzire a lingourilor semireci, cu centrul mai cald decât suprafața, iar temperatura suprafeței se află între 400-600^{0}C. Softurile realizate pentru regimurile de încălzire fac parte din tehnologiile de încălzire proiectate pe PC în limbajul C#.

BULETINUL INSTITUTULUI POLITEHNIC DIN IAŞI
Tomul LIII (LVII), Fasc. 1, 2007
Secția
ŞTIINȚA ŞI INGINERIA MATERIALELOR

SIMULATION OF THE TECHNOLOGIES OF HEATING OF STEELS WITH COLD INITIAL CONDITION, DESIGNED IN C# LANGUAGE

BY

VASILE CAȚARSCHI[a], DAN-GELU GĂLUŞCĂ[a], AUREL FLORESCU[a] and SMARANDA CAȚARSCHI[b]

Abstract: The advanced technologies at international level are those assisted by PC still in the design stage of these ones and till at the obtaining of the finished product. More and more the accent is put on the nanotechnologies, while the technologies of certain products and half-products of tens or hundreds of tons advance more slowly, even if these ones are used in the metallurgical industry, nuclear-energetic industry, naval industry, petrochemical industry, etc. In the present work are shown three variants of technologies of heating for forging of the ingots equivalently cylindrical of steel, charged in cold condition in the furnace, as well as of the milling rolls forged with a view to heat treatment. The software product utilized is formed by computer software related to the heating regimes designed in C# language. Heating diagrams obtained can be used both for the simulation of the heating technological processes and for their application at industrial scale in the production workshops of hot sectors.

Keywords: advanced technologies, technologies of heating, C# language, heating diagrams

1. Introduction

The achievement of certain optimal heating technologies both for the ingots equivalently cylindrical of steel and the forged milling rolls is made by PC assisted design. In the same time, it is absolutely necessary that the application of certain advanced heating technologies be achieved by means of modern heating technologies, with high flexibility, with reduced thermal inertia, with as high degree of heat recovering, with minimum energetic losses etc.

In order to achieve these technologies, it is absolutely necessary to achieve yet in the designing stage the optimal furnaces and if the existent furnaces are used, these ones must be modernized and optimized.

In the scheme of research-design of the thermal processes in steels, with a view to achieving the mathematic modelling of these processes, an important role is occupied by the schema of the statistic components included in the designing of heating technologies for plastic deformation (fig.1), [1].

2. Simulation of the technologies

For the design in C# language (C_{Sharp}) of the heating technologies for plastic deformation, a software product is assembled, formed by computer software afferent to each technology.

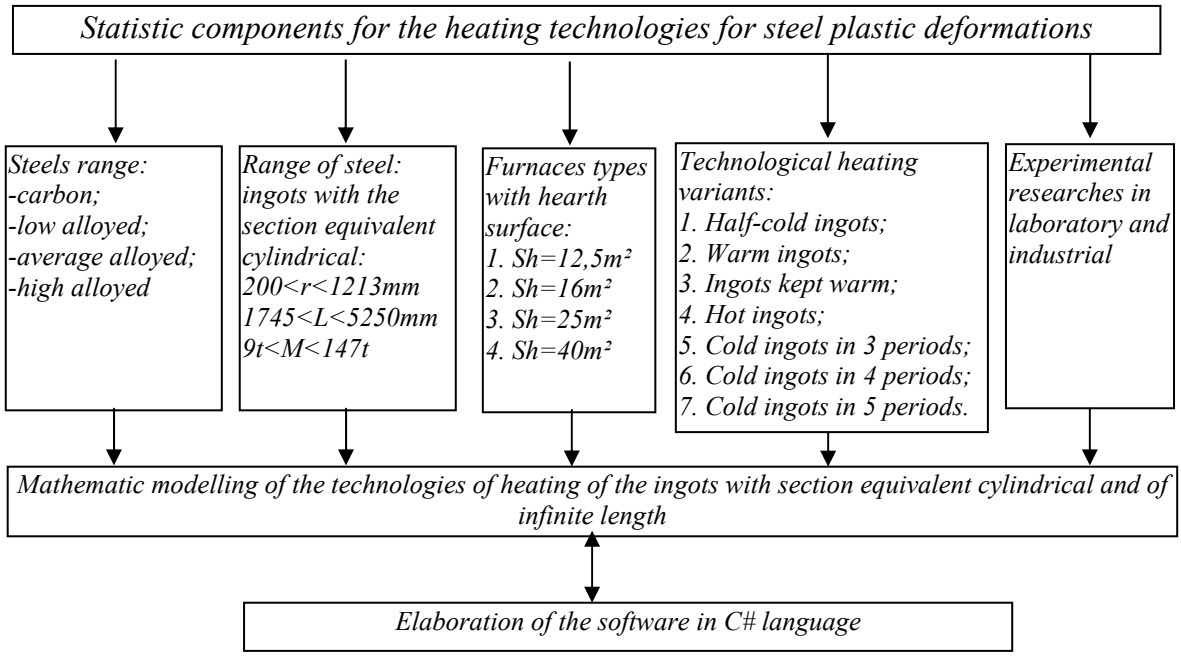

Fig. 1 Scheme of the statistic components for the heating technologies for steels plastic deformation

This computer software are performed based on mathematic modelling [1], of each heating regime related to the 3 technological variants for the steels with cold initial condition, as follows [2], [3]:

1. *Heating of cold ingots in 3 periods (fig.2) contains :*

- 1st and 2nd heating regimes are achieved with constant speed (w_1 and w_2) of furnace temperature increase:

$$T_{furn.1} = T_{furn.in} + w_1 \sum_{i=1}^{n} \Delta\tau_i \quad n = 1, 2, 3, \ldots, \infty \tag{1}$$

where: -$T_{furn.in}$, $T_{furn.1}$ – initial temperature and respectively temperature of the first heating period;

- w_1 – speed of heating of the furnace from the first heating period;
- $\Delta\tau_i$ – time step;
- n – number of the time steps until the final condition of the respective heating period is achieved;

- the 3rd heating regime is achieved with constant temperature of the furnace ($T_{furn.3}$ = constant)

2. *Heating of cold ingots in 4 periods (fig.3) contains :*

- 1st an 4th heating regimes are achieved with constant temperature of the furnace ($T_{furn.1}$ = const., $T_{furn.2}$ = const.);
- 2nd and 3rd heating regimes are achieved with constant speed of furnace temperature increase (w_2 and w_3) (similar to 1st and 2nd regimes from the case 1).

3. *Heating of cold ingots in 5 periods (fig.4) contains :*

- 1st, 3rd and 5th heating regimes are achieved with constant temperature of the furnace ($T_{furn.1}$ = const., $T_{furn.3}$ = const., $T_{furn.5}$ = const.)
- 2nd and 4th heating regimes are achieved with constant speed of furnace temperature increase (w_2 and w_4), (similar to 1st and 2nd regimes from the case 1).

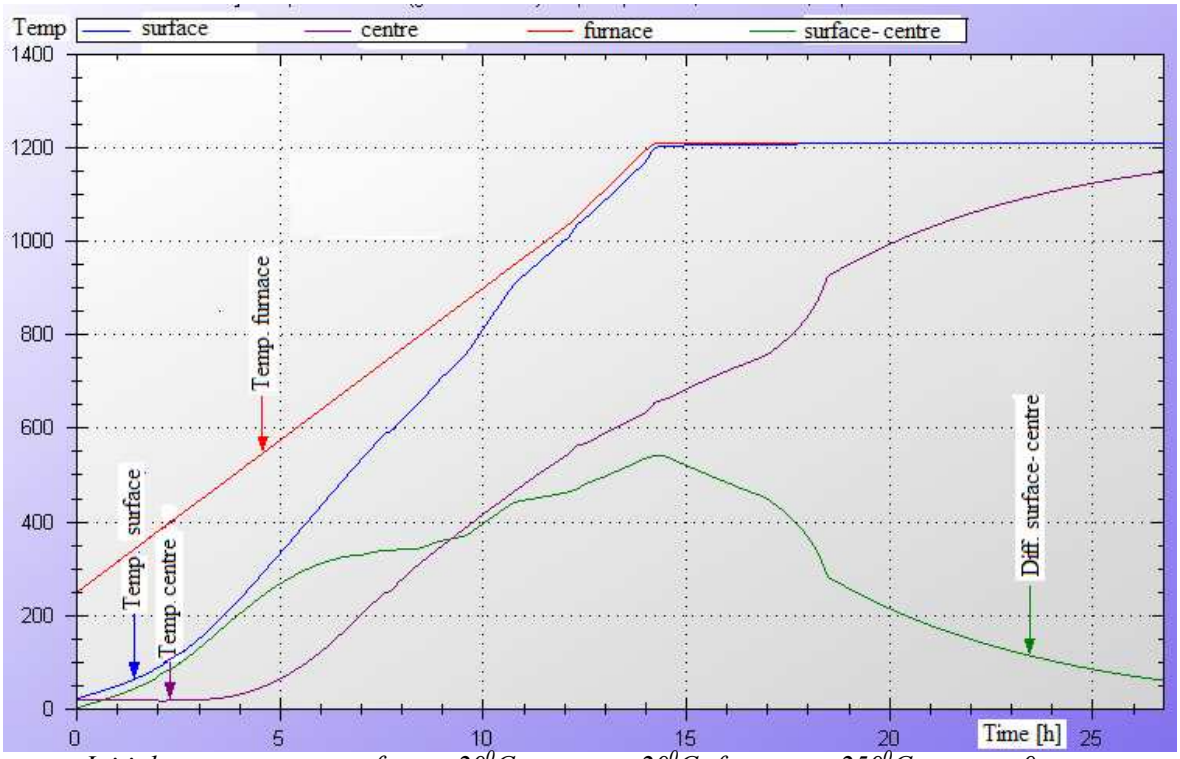

Initial temperatures: surface = 20^0C; centre = 20^0C; furnace = 250^0C; r_{centre} = 0 mm;
Final temperatures: surface = 1186^0C; centre = 1136^0C; furnace = 1210^0C;
Heating time [hours]: t_1 = 12.19; t_2 = 1.99; t3 = 12.65; Total time = 26.83;
Heating speeds [^{0}C/h]: v_1 = 84; v_2 = 100; - r_{furn} = 3.99;
medium diameter = 1613 mm; ingot length = 3200 mm; ingots number = 2; furnace CI = 40.0 m^2;

Fig. 2 Heating of cold ingots in 3 periods, steel mark 65MnCr15

Based on the statistic components scheme it is possible to effect the synthesis of the statistic information that together with the laboratory and industrial experiments can determine the particularization of certain technologies by groups of materials, groups of dimensions and the same heating furnace or different combinations between steel grades, ingots dimensional range and the types of heating furnaces [4], [5].

The development of the statistic components scheme (fig.1) needs the detailing of its components as it follows:

a) The steel grade contains: carbon steels, low alloyed steels, medium alloyed steels and high alloyed steels. The first two categories of steel can be framed in the heating cases (1) and (2) and the medium alloyed steels and high alloyed steels have to frame in the 3rd heating case (in 5 periods).

b) The range of steel ingots with the section equivalently cylindrical where the ingot radius is framed in the interval 1745…5250 mm and the ingot mass between 9 and 147 tons, must be framed depending on the ingots charge size in one of the four types of existent furnaces, in order to not exceed the maximum charging on the furnace hearth. In this range, conforming to the norms of S.C. FORTUS S.A Iasi, a number of 52 types – dimensions of ingots can be elaborated, ingots that could frame into the above dimensions and mass.

c) The types of heating furnaces like chamber with mobile hearth, heated with gas flame, have the hearth surface comprised in one of the following four cases : 1) S_v = 12.5 m²; 2) S_v = 16.0 m²; 3) S_v = 25.0 m²; 4) S_v = 40.0 m². Each type of furnace contains, into the framework of the mathematic modelling of the heat change

between the furnace chamber and the metallic charge, the three dimensions: the length and the width of the mobile hearth and the high of the furnace chamber. In these furnaces a very big variety of metallic charges can be introduced.

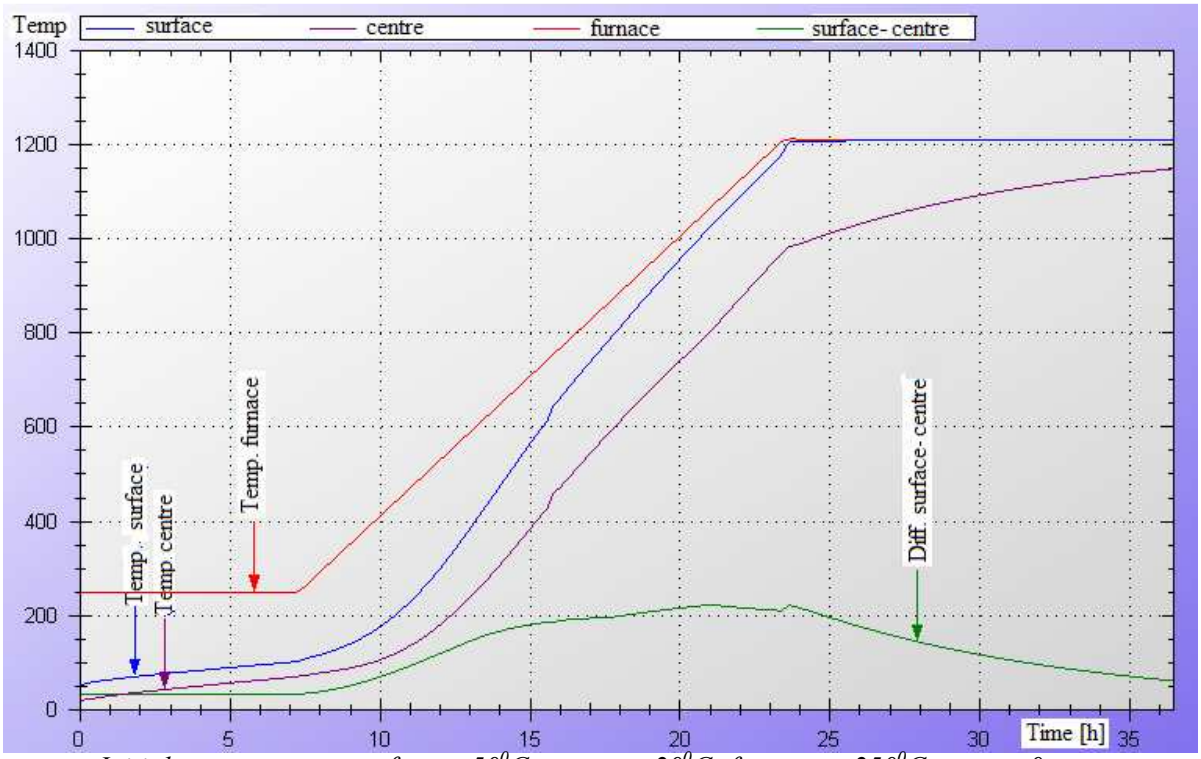

Initial temperatures: surface = 50^{0}C; centre = 20^{0}C; furnace = 250^{0}C; c_{entre} = 0 mm;
Final temperatures: surface = 1210^{0}C; centre = 1150^{0}C; furnace = 1211^{0}C;
Heating time [hours]: t_1 = 7.27; t_2 = 8.73; t_3 = 7.46; t_4 = 13.26; Total time = 36.72;
Heating speeds [^{0}C/h]: v_1 = 59; v_2 = 69; - r_{un} = 3.99;
Medium diameter = 1613 mm; ingot length = 3200 mm; ingots number = 2; furnace CI = 40.0 m^2;

Fig. 3 Heating of cold ingots in 4 periods, steel mark 13CrNi30.

d) The experimental researches, in laboratory and in industry, bring the necessary data to the introduction of checking at cracking during heating, as well as for the necessary correction applied to the theoretical heating diagrams, by respect to the experimental ones.

The determination of surface $T_{surf.n}$ ($T_{s.n.}$) and of $T_{centr.n}$ ($T_{c.n.}$) centre temperatures for a heated cylindrical ingot with equivalent radius R, for the heating mode $T_{furn.n}$ = const., in the conditions when the initial thermal gradient is $\Delta T_0 \neq 0$, the following relations are given [2], [3], [5]:

$$T_{s.n.} = T_{cupt0} + (T_{s.0.} \quad T_{cupt0}) \sum_{n=1}^{\infty} M_n J_0(z_n) e^{\ z_n^2 Fo} \tag{2}$$

$$T_{c.n} = T_{cupt.0} + (T_{s.0} \quad T_{cupt.0}) \sum_{n=1}^{\infty} M_n e^{\ z_n^2 Fo} \quad \Delta T_0 \sum_{n=1}^{\infty} W_n e^{\ z_n^2 \ Fo} \tag{3}$$

where: $M_n = \dfrac{2J_1(z_n)}{z_n[J_0^2(z_n) + J_1^2(z_n)]}$ and $W_n = \dfrac{4J_2(z_n)}{z_n^2[J_0^2(z_n) + J_1^2(z_n)]}$ (4)

$J_0(z_n)$; $J_1(z_n)$; $J_2(z_n)$ – Bessel function of 0; 1; 2 order and argument z_n;

$$\frac{J_0(z_n)}{J_1(z_n)} = \frac{z_n}{h \quad R} \tag{5}$$

$z_n = m_n R$ are the solutions of the transcendent equation (5) for $n = 1, 2, \ldots, \infty$.
R – equivalent radius of the mill roll, in mm;

$h = \frac{\alpha}{\lambda}$ - the relative coefficient of thermal transfer of the steel;

α - heat passing coefficient at the surface of the metal;

λ - thermal conductivity coefficient at the surface in the metal;

$F_0 = \frac{a \cdot \tau}{R^2}$ - Fourier's criterion of metal heating;

$a = \frac{\lambda}{c \cdot \gamma}$ - thermal diffusivity coefficient of the steel;

c – specific heat of heated steel;

$\boldsymbol{\tau}$ - heating time, in hours;

γ - specific weight of the metal, depending on its chemical composition;

$hR = Bi$ – Biot's criterion of the metal heating;

$\Delta T_0 = T_{surf.0} - T_{centr.0}$ – initial thermal gradient of metal heating.

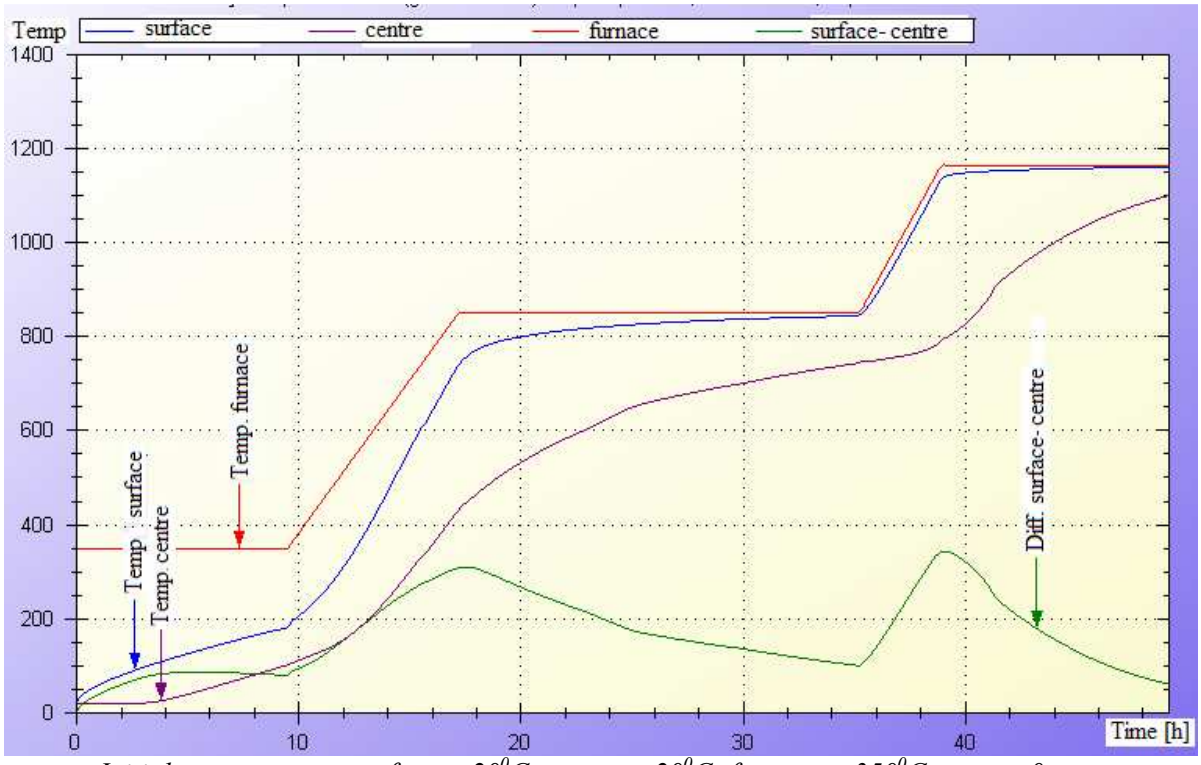

Initial temperatures: surface = 20^{0}C; centre = 20^{0}C; furnace = 350^{0}C; c_{centre} = 0 mm;
Final temperatures: surface = 1160^{0}C; centre = 1100^{0}C; furnace = 1162^{0}C;
Heating time [hours]: t_1 = 9.49; t_2 = 7.70; t_3 = 18.04; t_4 = 3.67; t_5 = 10.30; Total time = 49.20;
Heating speeds [^{0}C/h]: v_1 = 65; v_2 = 85; - r_{furn} = 3.99;
medium diameter = 1613 mm; ingot length = 3200 mm; ingots number = 2; furnace CI = 40.0 m^2;

Fig. 4 Heating of cold ingots in 5 periods, steel mark 90VMoCr18

3. Conclusions

The five statistic components introduced in the mathematic modelling of the heating technologies of the ingots with the cross section equivalently cylindrical and the designing of afferent computer software in C# language for each technology can form a software product of which both the industrial production sectors and the suppliers of industrial furnaces could benefit [6], [7].

Received April 25, 2007

[a] Technical University "Gh. Asachi" of Iassy,
[b] "Anghel Saligny" Technical Scool of Iassy

REFERENCES

1. Catarschi, V. – *Contributions to Computer Mathematical Adaptation of the Heating Technologies of Flow Susceptible Steel Ingots.* Buletinul Institutului Politehnic Iasi, Tomul XL(XLIV). Fasc.3-4/1994, Sectia IX, **704-712**.
2. Carslaw, H. S., Jaeger J. C.- Conduction of Heat in Solids. At. the Clarendon Press, Oxford, 1964.
3. Roman, E., Maeder - *Programming in Mathematics*. Addison Wesley Publishing Company, Redwood City, California, U.S.A., 1991.
4. Samoilovici, Iu. A, Timospolskii, V. I. - *Nagrev stali:Spravocinic posobie.* Visaia scola..Minsk, 1990, **8-81**.
5. Catarschi, V. - *Contribution considering the computer designed technologies for steel ingots heating in INCFOR programs***.** METALURGIA INTERNATIONAL, nr.4/2004, ISSN 1582-2214, **8-13**.
6. Catarschi, V. - *Manufacturing Engineering of the Forged Mill Rolls for Rolled Products from SC FORTUS S.A. Iasi.* METALURGIA INTERNATIONAL**,** Nr.5/2004, ISSN 1582-2214, **27-34**.
7. Nemzer, G.G. - *Teplovie protessi proizvodstva crupnih pocovoc.* Masinostroenie, Leningrad, 1979.

SIMULAREA TEHNOLOGIILOR DE ÎNCĂLZIRE A OȚELURILOR CU STAREA INIȚIALĂ RECE, PROIECTATE ÎN LIMBAJUL C#

Rezumat : Tehnologiile avansate la nivel mondial sunt cele asistate de PC, încă din faza de proiectare a acestora și până la obținerea produsului finit. Se pune accent din ce în ce mai mult pe nanotehnologii, în timp ce tehnologiile unor produse și semifabricate de zeci sau sute de tone avansează mai lent, cu toate că acestea sunt utilizate în industria metalurgică, industria nuclearo-energetică, în industria navală, petrochimică etc. În lucrare se prezintă trei variante ale tehnologiilor de încălzire pentru forjare a lingourilor echivalent cilindrice din oțel, încărcate în stare rece în cuptor, precum și a cilindrilor de laminor forjați, în vederea tratamentelor termice. Produsul soft utilizat este format din programe ale regimurilor de încălzire proiectate în limbajul C#. Diagramele de încălzire obținute pot fi utilizate atât pentru simularea proceselor tehnologice de încălzire, cât și pentru aplicarea lor la scară industrială în secțiile de producție ale sectoarelor calde.

BULETINUL INSTITUTULUI POLITEHNIC DIN IAŞI
Tomul LIII (LVII), Fasc. 1, 2007
Secția
ŞTIINȚA ŞI INGINERIA MATERIALELOR

RESEARCHES CONCERNING BIOACTIVE METAL-CERAMIC IMPLANTS

BY

GHEORGHE T. POP [(a)], LILIANA VERESTIUC[(a)], GABRIELA CIOBANU[(b)], OCTAVIAN CIOBANU[(a)], IOAN CARCEA[(c)], ROMEU CHELARIU[(c)], NICOLETA LUPU [(d)], MONICA ROSTAMI [(e)] and VASILE DIA[(f)]

Abstract: Bioactive materials are those materials which spontaneously bond to living bone. Among such materials one could mention Bioglass, Hydroxyapatite and Glass Ceramic. The Bioactive materials form a bone-like apatite layer on their surfaces in the living body and bond to bone through this apatite layer. Such properties are induced by functional groups: Si-OH, Ti-OH, Zr-OH, H_2PO_4 and – COOH. These fundamental findings provide methods for preparing new bioactive materials with improved mechanical properties such as titanium alloy, silica-ceramic and inorganic-organic composites through biomimetic process. Titanium metal and its alloys are very tough and have been widely used as orthopedic and dental implants. They are, however, non-bioactive and therefore, are usually coated with HA by using a high-temperature process, such as the plasma spraying method, which partially decomposes and melts the HA. It has been suggested that such HA coatings are liable to delaminate from the substrate and to dissolve in a short period after implantation. In view of the composition of the above functional groups effective for apatite nucleation, titanium metal and its alloys have the potential to exhibit intrinsic bioactivity by a surface modification by biomimetic processes, which has been used to deposit micronic bone like apatite, as we did in this work.

Keywords: hydroxyapatite, apatite-like bone, titanium, biomimetic process

1. Introduction

In the recent years, hydroxyapatite (HA) ceramic implants have attracted much attention as an alternative substance for autogenous free bone grafting [1-3]. It is the most prominent bioactive ceramic and is widely used and investigated. Applications include coatings of orthopaedic and dental implants, alveolar ridge augmentation, maxillofacial surgery, otolaryngology, and scaffolds for bone growth and as powders in total hip and knee surgery [4-5].

Synthetic HA is classified as polycrystalline ceramics since its material structure is derived from individual crystals that have been fused together by a high temperature sintering. Many biocompatibility studies prove that HA has a very similar chemical composition as the inorganic part of human hard tissue, such as bone and teeth. The most important advantage of HA being a bioactive material is that bone will form a direct chemical bond to HA implant without forming a collagen interface layer which is usually found in many other bioinert materials after implantation.

In view of the composition of the above functional groups effective for apatite nucleation, titanium metal and its alloys have the potential to exhibit intrinsic bioactivity by a surface modification, by biomimetic processes, which has been used to deposit micronic bone like apatite, as we did in this work.

2. Experimental

2.1. Materials

Metallic titanium and Ti_6Al_4V alloy were used as support materials and were obtained from ZIROM R.A. Giurgiu. Materials had a cylindrical bar form with a diameter of 60 mm and a high purity according to Tables 1 and 2. Metallic bars were obtained initially by casting and were worked out using a lathe and a milling machine in order to obtain plate samples of 3x10x10 mm.

Table 1. Chemical composition of raw titanium used as support material

Elements	Ti	Al	Fe	C	O	N	H
%	99.525	0.110	0.205	0.038	0.186	0.013	0.003

Table 2. Chemical composition of Ti_6Al_4V alloy used as support material

Elements	Ti	Al	V	Fe	C	N	H	O
%	88.50-90.50	5.5-6.5	3.5-4.5	max. 0.25	max. 0.08	max. 0.05	max. 0.015	max. 0.13

Diluted solutions of NaOH (5-10 M) were prepared in the UMF Iaşi laboratories and used for titanium samples oxidizing and sodium titanate superficial layer forming.

Diluted solutions of Simulated (or synthetic) body fluids SBF (Kokubo solution) were prepared in the UMF Iaşi laboratories with the chemical composition according to values presented in Table 3.

Table 3. Molarity of SBF solution

Ions	Na^+	K^+	Ca^{2+}	Mg^{2+}	Cl^-	CO_3^-	PO_4^{2-}	O_4^{2-}	pH
Mol	142.0	5.0	2.5	1.5	147.8	4.2	1.0	0.5	7.25-7.40

Supersaturated calcification solutions SCS were prepared and processed in cooperation with the Faculty of Engineering Chemistry of Technical University "Gh. Asachi" Iasi, with the chemical composition presented in Table 4.

Table 4. Ion concentration of supersaturated calcification solutions

Solution/ ion concentration	Na^+	Ca^{2+}	Cl^-	$H_2PO_4^-$	HCO_3^-
SCS-1	6,5	5	10	5	1.5
SCS-2	4	5	10	2.5	1.5
SCS-3	4	10	20	2.5	1.5

2.2. Experimental methods:

Experimental methods were developed in two directions:

a) Biomimetic treatment in Simulated Body Fluid solutions (SBF) consisting in chemical and heat treatment of titanium and titanium alloys metallic samples in three steps:

- metallic samples oxidizing in 5-10 M solutions of NaOH at 60 ^{0}C for a duration of 24 - 48 hours**.** Chemical treatment was performed in thermostated autoclaves according to formula:

$$Ti + 2\,NaOH \xrightarrow{60^0 C} TiO_2 \cdot Na_2O \quad (1)$$

- heat treatment of oxidized samples at 600 ^{0}C in order to bound $TiO_2 \cdot Na_2O$ layer to metallic surface by diffusion.

- formation and deposit of a bioactive apatite layer through a biomimetic process, in solutions of simulated body fluids *SBF,* at 36 ^{0}C, for a duration between 24 and 72 hours. During this step the chemical reactions between oxidized samples and SBF solutions can be envisaged as follows:

Ti-OH formation with negative loads on the surface of titanium after releasing of positive Na ions:

$$TiO_2 \cdot Na_2O_{(Ti)} + H_3O^-_{(SBF)} \xrightarrow{36^0 C} (Ti - OH)^-_{(Ti)} + Na^+ \quad (2)$$

Assimilation of Ca ions from SBF and formation of $TiO_2 \cdot CaO_{(Ti)}$ following formula:

$$(Ti - OH)^-_{(Ti)} + Ca^{2+}_{(SBF)} \xrightarrow{36^0 C} TiO_2 \cdot CaO_{(Ti)} \quad (3)$$

Continued assimilation of Ca ions from SBF has as result a positive electrical charge of the surface layer of $TiO_2 \cdot CaO_{(Ti)}$ favoring the deposition of negative phosphates ions and formation of $CaHPO_{4(Ti)}$ on the surface of substrate:

$$(TiO_2 \cdot CaO)_{(Ti)} + Ca^{2+}_{(SBF)} \xrightarrow{36^0 C} CaHPO_{4(Ti)} \quad (4)$$

Transformation of Ca phosphates in apatite in SBF medium as a natural chemical product, more stable at the reaction environment temperature.

$$CaHPO_{4(Ti)} \xrightarrow{at\ 36^0 C,\ in\ SBF} Ca_{10}(PO_4)_6 \cdot (OH)_{2(Ti)} \quad (5)$$

b) Biomimetic treatment in supersaturated calcification solutions (*SCS*) consisted in two steps: treatment in alkaline solutions of NaOH and treatment in acid solutions of SCS.

- metallic samples oxidizing in NaOH diluted solutions at 160 ^{0}C, during 48 hours, in autoclaves with $\mathbf{Na_2Ti_5O_{11}}$ formation following next chemical formula:

$$Ti + 2\,NaOH \xrightarrow{160^0 C} Na_2Ti_5O_{11} \quad (6)$$

- formation and deposition of apatite and calcium phosphate ceramic layer on the surface of metallic samples, in SCS solutions, following next formula:

1) $H_2PO_4^- \rightarrow HPO_4^{2-} + H^+$ (7)

2) $HPO_4^{2-} \rightarrow PO_4^{3-} + H^+$ (8)

3) $H^+ + HCO^{3-} \rightarrow H_2O + CO_2$ (9)

4) $10\,Ca^{2+} + 6\,PO_4^{3-} + 2\,OH^- \xrightarrow{at\ 36^0 C} Ca_{10}(PO_4)_6(OH)_2$ (10)

(hydroxyapatite)

5) $Ca^{2+} + HPO_4^{2-} + 2\,H_2O \xrightarrow{at\ 36^0 C} CaHPO_4 \cdot 2\,H_2O$ (11)

(brushite)

First two reactions amplify the solution acidity by HCl formation and enable Ca^{2+} ions formation and concentration growing.

The third reaction leads to solution pH growing by hydrogen ions consumption and to Ca ions supersaturation. According to fourth reaction, consumption of OH ions leads to lower pH values of solution during hydroxyapatite coating. Following mentioned treatments, it is possible to pass successively from superficial metallic structure to ceramic structure as in optical microscopy images depicted in Fig.1.

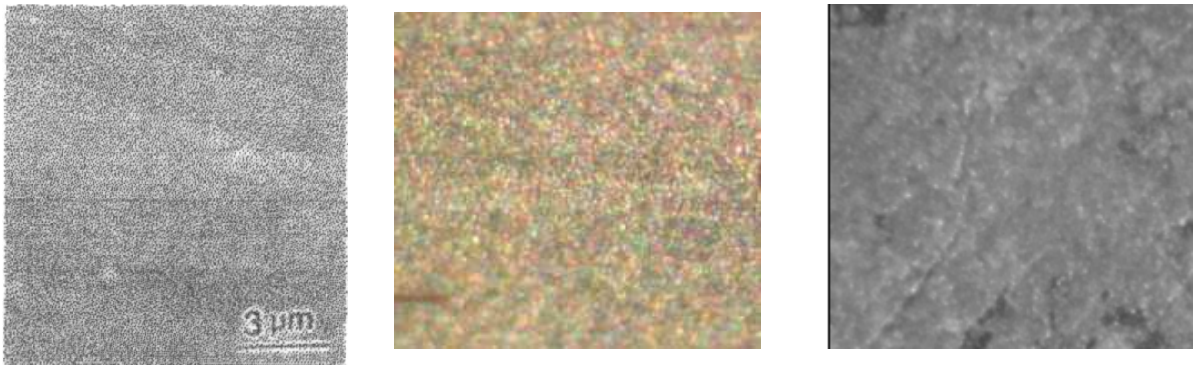

Metallic structure *Oxidized structure* *Ceramic structure*

Fig.1. Optical microstructure of successive transformation of metallic surface to ceramic surface.

3. Results and discussion

3.1. Optical microstructure

Experiments with titanium and titanium alloys samples were developed starting on May 2006 under a Romanian CNCSIS financed grant, processing 4 lots of samples by month. Experiments had as objective the verification of technical parameters of bioactive ceramic formation and deposition on samples according to data offered by published scientific papers and the determination of new series of original parameters of coating in biomimetic conditions. As valid samples were admitted those having a uniform deposition of ceramic layer (minimum about 70 % of the sample surface) as seen in Fig.2, after a micro and a macrostructural examination.

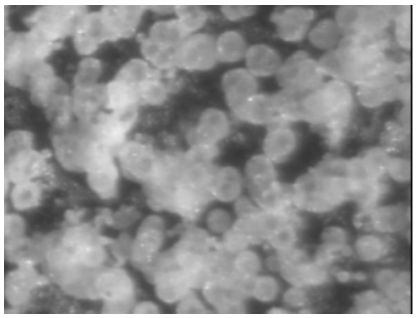

Fig.2. Optical mircostructure of the ceramic layer of samples (x 100).

Lots having a ceramic layer between 40 and 60 % of sample surface were considered having aleatory layers and those with a ceramic layer under 40 % of surface were considered as uncorresponding as in Fig.3.

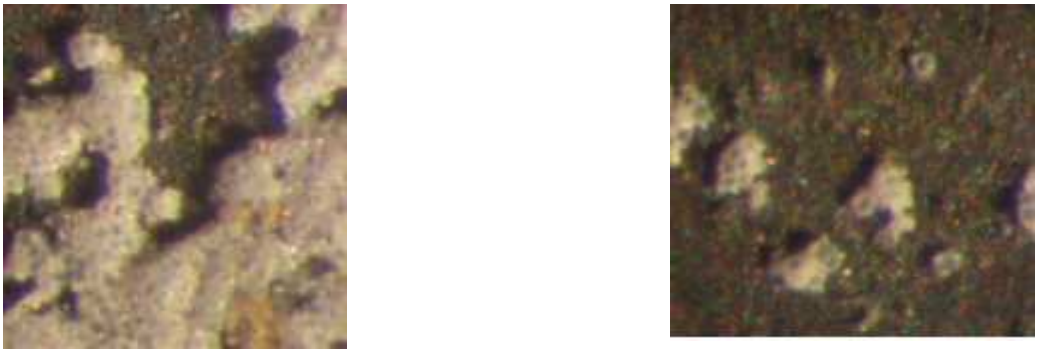

a) *b)*

Fig. 3. Optical microstructure of (a) aleatory ceramic layer and (b) uncorresponding ceramic layers.

3.2. Ceramic layer study by X-ray diffraction (XRD) analysis

X-ray diffraction (XRD) analysis is frequently used in thin layers investigation for identification and highlighting of chemical nature of layers components. In present research, X-ray diffraction analysis was performed with a DRON-2.0 diffractometer with a CuKα radiation in the laboratories of National Institute of Physics from Iasi.

Identification and evidencing of ceramic layer components was accomplished using Bragg law:

$$2\,d\,\sin\Theta = n\,\lambda \qquad (12)$$

were **λ** is the wave length interatomic, **d** is planes distance and **Θ** is diffraction angle.

A lot of 11 samples with biomimetic coating deposition by SBF and SCS methods were analyzed by X-ray diffraction. XRD patterns of the biomimetic apatite layers are presented in the below pictures. XRD patterns show the next chemical components: - Metallic titanium as basic support element;

- $Na_2Ti_5O_{11}$, a complex oxyde as intermediary layer;
- Apatite, as surface ceramic layer;
- Calcium phosphate ceramic layer (in SCS method).

Fig. 4 shows two XRD patterns obtained from samples treated by the biomimetic methods SBF and SCS. Presence of the apatite thin layer and titanium oxyde layer are highlighted by specific peaks from Fig. 4.

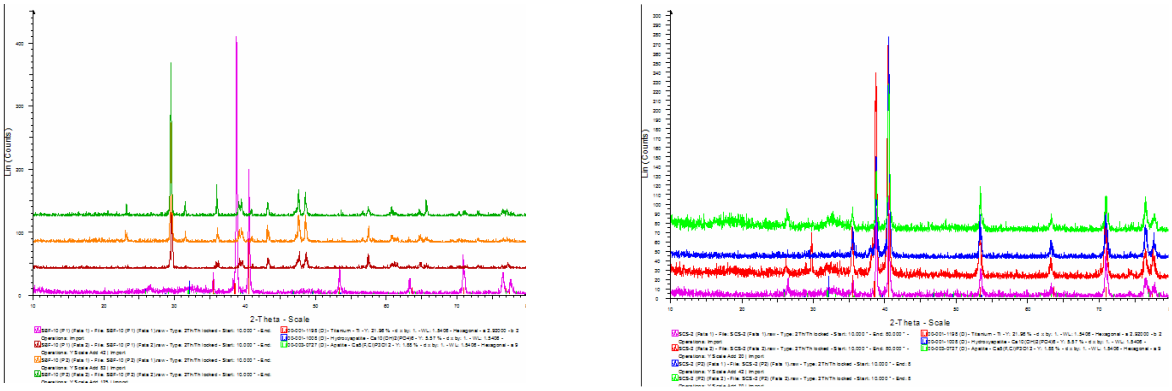

a) XRD pattern of the apatite layer deposition in the biomimetic SBF method

b) XRD pattern of the ceramic layer deposition in the biomimetic SCS method

Fig.4. XRD patterns of apatite coatings of samples treated by biomimetic methods with SBF and SCS

3.3. Electronic microscopy analysis (SEM) of ceramic layer

Scanned electronic microscopy (SEM) of samples was performed at "P. Poni" National Institute of Macromolecular Chemistry from Iasi. Optical microstructures show the presence of ceramic microcrystalline apatite on the surface of titanium samples as in Fig. 5.

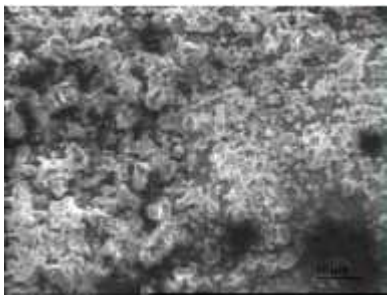

a) The SEM micrograph of biomimetic apatite layer in SBF method.

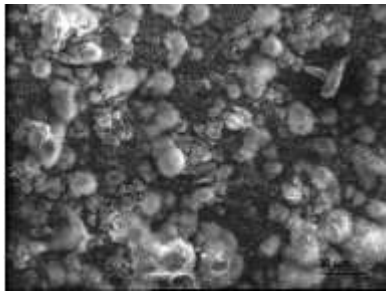

b) The SEM micrograph of biomimetic apatite layer in SBF method.

Fig. 5. The SEM micrographs of biomimetic apatite layer

4. Conclusions

Results of experimental research confirmed the possibility of biomimetic coating of titanium and titanium alloys through two biomimetic methods.

Methods and investigation instruments were tested and verified in two research approaches in order to clarify all parameters of the apatite coating process of titanium samples.

A multidisciplinary cooperation was started in order to study the ceramic layer by optical and electronic microscopy and by X-ray diffraction analysis in officialy attestated laboratories of different organizations.

The biomimetic coating method with supersaturated calcification solutions (SCS) has as main advantage the elimination of a 600 ^{0}C thermal treatment, which can affect the mechanical properties, and the structure of the metallic support, a very important issue in the elaboration of real implants.

Apatite layer properties and structure studies were performed by modern investigation methods of optical and electronic microscopy and by X-ray diffraction analysis according to the international research practice.

Experimental results show that experimental parameters were correctly identified and correlated and it is possible to approach a new research step related to the bioactive apatite coating of dental and orthopedic implants.

Acknowledgements

Authors acknowledge with thanks the financial support of The Education and Research Ministry of Romania under CNCSIS 828/2006 Research Grant.

Received September 20, 2007

a) "Gr.T.Popa" University of Medicine and Pharmacy, Medical Bioengineering Faculty, Iaşi
b) "Gh. Asachi" Technical University of Iaşi, Faculty of Chemical Engineering
c) "Gh. Asachi" Technical University of Iaşi, Faculty of Materials Science and Engineering
d) National Institute of Technical Physics, Iasi
e) INGMET Research and Trading Company, Iasi
f))S.C.MITTAL STEEL Iaşi S.A

REFERENCES

1. Hyun – Min Kim and Kokubo, T. - *Preparation of bioactive Ti and its alloy via simple chemical surface treatment,* **Journal of Biomedical Materials Research**, **32**, 1996, **134 - 142.**
2. Kokubo, T. - *Formation of biologically active bone like apatite on metals and polymers by a biomimeticprocess,* **Thermodynamic Acta, 12**, 1999, **479-490.**
3. Takadama, H., and Kokubo, T. - *An X-ray spectroscopy study of the process of apatite formation on bioactive titanium metal,* John Willey & Sons, 2001
4. Wei, M.,.Kim, H.M and Kokubo, T. - *Optimizing the bioactivity of alkaline-treated titanium alloy.* **Materials Science and Engineering**, **C20**, 2002, **125-134.**
5. Haibo, W., Lee, J.K., MoursI, A. and Lannutti, J. - **J. Biomed. Mater. Res**., **68A**, 2004, **61-68**.

CERCETARI PRIVIND IMPLANTURILE METALO-CERAMICE BIOACTIVE

Rezumat: Titanul şi aliajele acestuia sunt materiale metalice rezistente şi biocompatibile şi sunt larg utilizate ca implanturi ortopedice şi stomatologice. Totuşi aceste materiale nu sunt bioactive şi de aceea se cerceteaza diverse procedee de acoperire cu ceramici bioactive, in special cu hidroxiapatită. Materialele bioactive formează un strat de de apatită similar osului pe suprafeţele implanturilor şi se lipesc de os prin legaturi biologice. În scopul obţinerii unor acoperiri ceramice, pe probe metalice din titan si aliaje de titan, s-au utilizat două metode biomimetice şi s-au preparat corespunzător două solutii: o soluţie de fluid biologic sintetic- (SBF) şi o soluţie calcică suprasaturată-(SCS). Straturile micronice de apatita depuse pe epruvete au fost investigate cu ajutorul microscopiei optice, electronice(SEM) şi prin difracţie cu raze X (XRD), studiile efectuate au confirmat parametri tehnici de acoperire si unele caracteristici ale stratului .

BULETINUL INSTITUTULUI POLITEHNIC DIN IAŞI
Tomul LIII (LVII), Fasc. 1, 2007
Secția
ŞTIINȚA ŞI INGINERIA MATERIALELOR

THE INFLUENCE OF THE PARAMETERS OF THE HEAT TREATMENT UNDERGONE BY CERTAIN ALUMINIUM BRONZES ON STRUCTURE AND MICROHARDNESS

BY

COSTEL ROMAN[(1)], MIRCEA BELOIU[(2)], ROMEO CHELARIU[(1)], IOAN CARCEA[(1)], CORNEL MUNTEANU[(1)]

Abstract. Aluminium bronzes belong to the category of special bronzes that also contain, besides Cu and Al, which are the main components, Fe, Mn, Ni, Co as alloy components. These are specific for cast parts subjected to high mechanical stresses and working in aggressive environments. The choice of technological hardening and tempering parameters depends on the chemical composition of the alloy and of the characteristics variation during secondary phase precipitation. This paper studies, from the structural and microhardness viewpoint, the influence of certain technological parameters, like temperature and hardening and tempering hold time, applied to some aluminium bronzes: CuAl11Fe3, CuAl11Fe3 Ni1.5 and CuAl11Fe3 Ni1.5 Co1.

Keywords: Aluminium bronze, microhardness, heat treatment, microstructure

1. Introduction

Aluminium bronzes belong to the category of special bronzes that also contain, besides Cu and Al, which are the main components, Fe, Mn, Ni, Co as alloy components. These are specific for cast parts subjected to high mechanical stresses and working in aggressive environments.

The heat treatments applied to aluminium bronzes are designed either to improve their operation, mechanical, physical and chemical characteristics, their stability in time and their operation in specific operation circumstances (low or high temperatures, corrosive environments), or to enable less difficult technological processes used to manufacture parts with these alloys.

Martensitic hardening is applied to aluminium bronzes that allow the suppression of $\beta \xrightarrow{565°C} (\alpha + \gamma_2)$ diffusion eutectoid transformation, for high speed cooling and high hardness martensitic phase formation. This martensite decomposes upon the subsequent tempering, thus resulting into high resistances [1,2].

The α phase is a solid aluminium in copper solution, with crystalline structure in cubic system with K_2[A1] centered faces, with maximum solubility for a 9.4% aluminium content at a temperature of 565˚C.

The β phase is a solid intermediate aluminium solution based on the Cu_3Al (Ce=3/2) electronic compound crystallized in cubic system with K_3[B32] centered

volume, of the Cu_3AlMn type with $a=5.84$ Å and 4 molecules in the basic cell. It results directly from the 8.5÷15%Al melt or from the eutectic reaction that occurs at a temperature of 1037°C.

The γ phase is also an intermetallic phase generated by the $Cu_{32}Al_{19}$ electronic compound. This phase includes de phenomenon of polymorphism, and we distinguish the γ_1 phase, corresponding to the Cu_9Al_4 (Ce=21/13) electronic compound crystallized in cubic α-Mn (A12) system and the γ_2 cubic network phase, specific for the $Cu_{32}Al_{19}$ electronic compound.

The hardening and tempering improve the corrosion resistance of the aluminium bronzes, especially the dealuminizing resistance in sea water, due to anode stage scattering, thus preventing corrosion spreading in depth [2].

The choice of technological hardening and tempering parameters depends on the chemical composition of the alloy and of the characteristics variation during secondary phase precipitation.

This paper studies, from the structural and microhardness viewpoint, the influence of certain technological parameters, like temperature and hardening and tempering hold time, applied to some aluminium bronzes: CuAl11Fe3, CuAl11Fe3Ni1.5 and CuAl11Fe3 Ni1.5 Co1. This would also allow to determine the influence of Ni and Ni + Co additions, respectively.

2. Materials and methods

The chemical composition of the alloys under survey is shown in Table 1.

Table 1 Chemical composition of copper alloys

Alloy symbol	Alloy type	Chemical composition, mass %							
		Al	Fe	Ni	Co	Sn	Zn	Mn	Cu,
1	CuAl11Fe3	10.60	4.20	0.00	0.00	0.012	0.053	0.372	rest
2	CuAl11Fe3Ni1,5	10.50	4.20	0.89	0.00	0.018	0.046	0.366	rest
3	CuAl11Fe3Ni1,5Co1	9.96	3.96	1.54	1.00	0.017	0.052	0.365	rest

The alloys we studied were obtained in an induction heated furnace with a 35kg graphite crucible. The load consisted of electrolytically refined metals. During the performance, the metal bath obtained was protected by a flux (Cupral) layer. Before the alloying of the melted copper bath with Al, Fe, Ni and Co, respectively, a phosphorized copper deoxidation was carried out.

The casting was performed in 300°C hot metal moulds with cylindrical cross-section, that were sampled for metallographic analysis and microhardness study.

The alloy samples studied underwent hardening and tempering treatments in a heating furnace with VULCAN A-130 electric resistance and a temperature accuracy of ±5°C.

In order to study the structural changes and the influence on microhardness, the hardening and tempering were performed at different temperatures and durations,

according to Table 2.

Table 2 Technological parameters of heat treatment

Metallurgical processing	**Technological parameters**				**Microhardness [daN/mm^2]**		
					CuAl11Fe3	CuAl11Fe3Ni1.5	CuAl11Fe3Ni1.5Co1
Casting	Solidification using metallic mold pre-heated at 300^{0}C				**196.17**	**238.86**	**277.73**
	Air cooling						
Quenching	Temperature of maintaining	T_{m1} = 700 ^{0}C	Time	t_m = 2 h	**227.61**	**236.86**	**290.35**
		T_{m2} = 900 ^{0}C			**242.05**	**279.78**	**367.14**
Quenching 1+ annealing	Temperature of maintaining	T_{m1} = 300 ^{0}C	Time	t_{m1} = 4 h	244.61	248.79	236.98
				t_{m2} = 6 h	265.43	287.99	242.10
				t_{m3} = 8 h	**282.80**	271.12	211.66
		T_{m2} = 450 ^{0}C	Time	t_{m1} = 4 h	265.41	285.61	235.69
				t_{m2} = 6 h	276.44	287.89	**244.63**
				t_{m3} = 8 h	246.59	**310.84**	236.00
		T_{m3} = 600 ^{0}C	Time	t_{m1} = 4 h	185.39	197.61	198.00
				t_{m2} = 6 h	**179.02**	**174.98**	**181.76**
				t_{m3} = 8 h	197.77	193.45	197.86
Quenching 2+ annealing	Temperature of maintaining	T_{m1} = 300 ^{0}C	Time	t_{m1} = 4 h	**307.83**	**334.10**	**391.95**
				t_{m2} = 6 h	284.93	307.34	325.14
				t_{m3} = 8 h	290.67	301.45	290.07
		T_{m2} = 450 ^{0}C	Time	t_{m1} = 4 h	249.79	299.16	287.39
				t_{m2} = 6 h	263.47	299.94	342.27
				t_{m3} = 8 h	257.36	287.54	277.34
		T_{m3}= 600 ^{0}C	Time	t_{m1} = 4 h	**177.41**	216.12	203.75
				t_{m2} = 6 h	188.31	**186.86**	212.35
				t_{m3} = 8 h	205.46	196.32	**202.50**

Hardened samples cooling down to 700°C and 900°C, respectively, were achieved in water and 20% NaCl solution at environment temperature (about 20°C). The cooling of the tempered samples was performed in the air.

The metallographic analysis was performed by means of an image collection and processing device attached to an MC9 microscope.

Sample microhardness determination was carried out on a PMT3 microhardnessmeter.

3. Experimental data and discussions

3.1 Structural analysis

The figures 1-3 below show the microstructures of the samples in which changes in the morphology of the cast, hardened and tempered states were noticed.

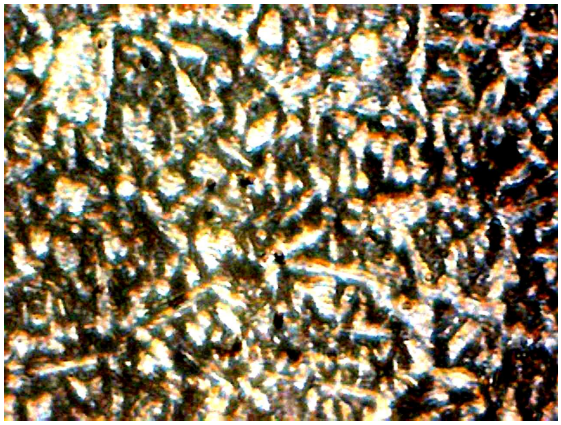

a) CuAl11Fe3 turnat

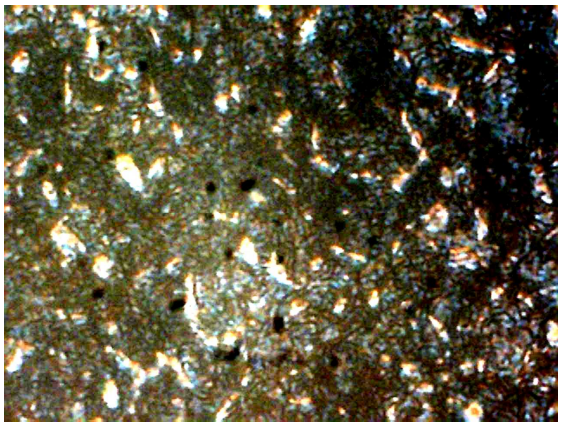

b) CuAl11Fe3 quenching 700°C,2h, salt solution cooling

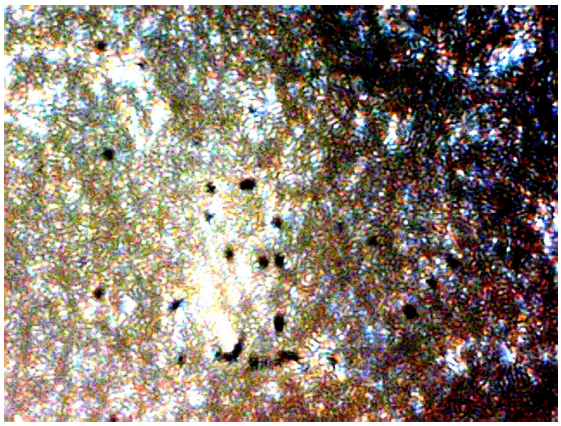

c) CuAl11Fe3 quenching 900°C,2h, salt solution cooling

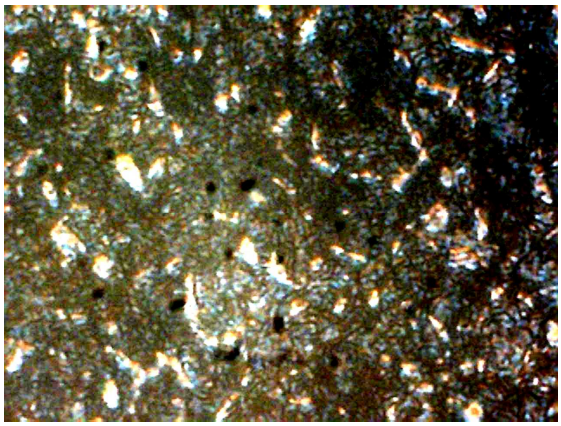

d) CuAl11Fe3 quenching 700°C,2h, salt solution cooling, annealing 450 ^{0}C, 6h, air cooling, cooling

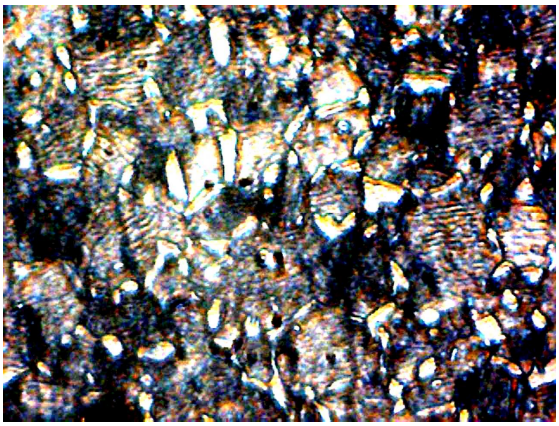

e) CuAl11Fe3 quenching 900°C,2h, salt solution cooling, annealing 300 ^{0}C, 4h, air

Figure 1. Representative microstructures of Cu Al11Fe3, depending on metallurgical processing.

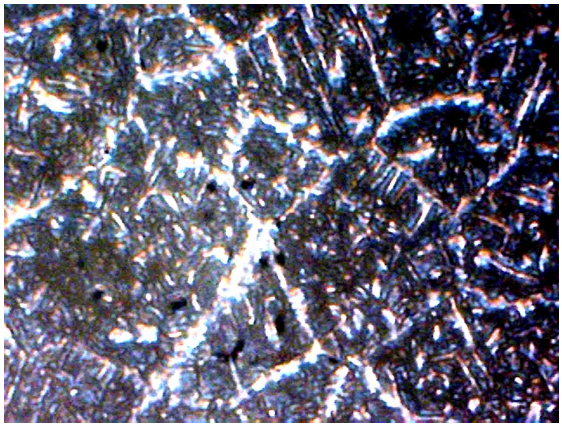

a) as-cast CuAl11Fe3Ni1.5

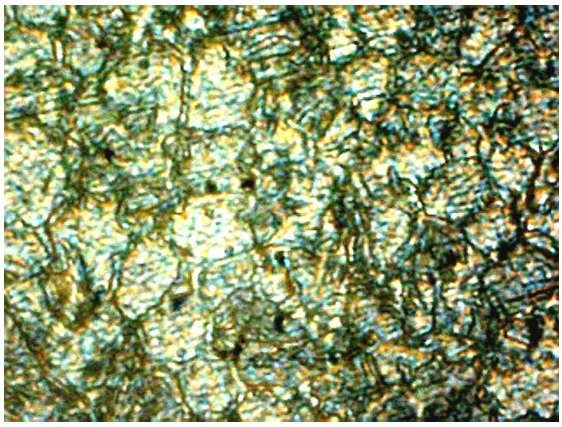

b) CuAl11Fe3Ni1.5 quenching 700°C,2h, salt solution cooling

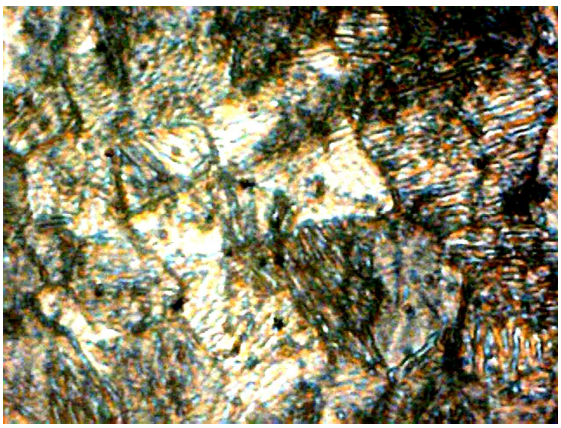

c) CuAl11Fe3Ni1.5 quenching 900°C,2h, salt solution cooling

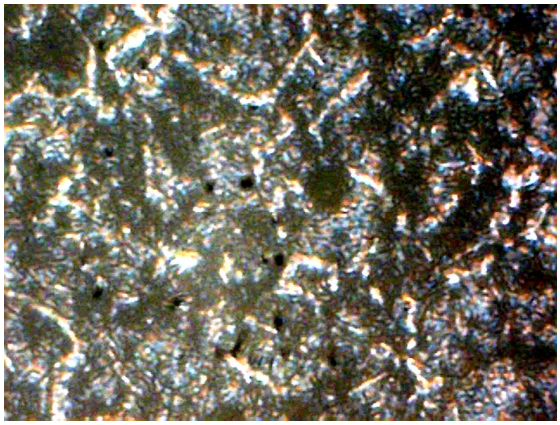

d) CuAl11Fe3Ni1.5 quenching 700°C,2h, salt solution cooling, annealing 450 ^{0}C, 6h, air cooling, cooling

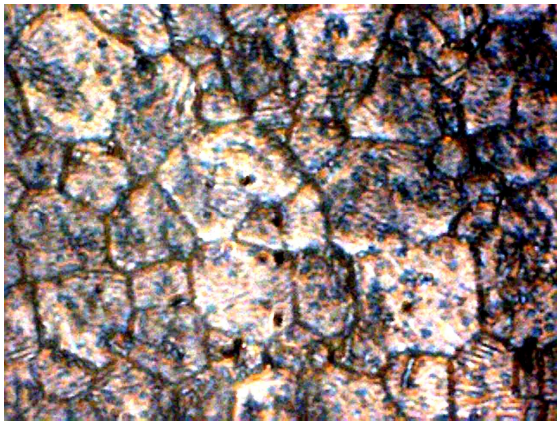

e) CuAl11Fe3Ni1.5 quenching 900°C,2h, salt solution cooling, annealing 300 ^{0}C, 4h, air

Figure 2. Representative microstructures of Cu Al11Fe3Ni1.5, depending on metallurgical processing.

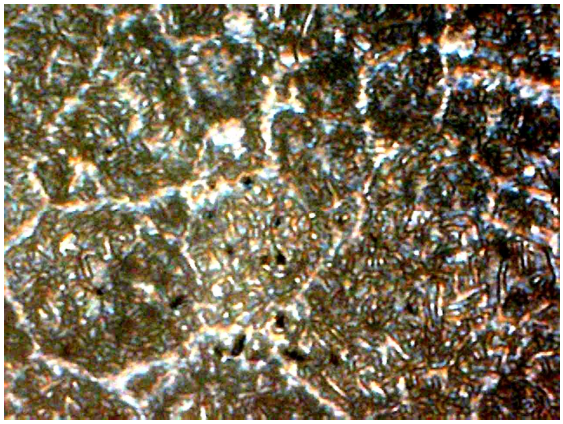

a)as-cast CuAl11Fe3Ni1.5 Co1

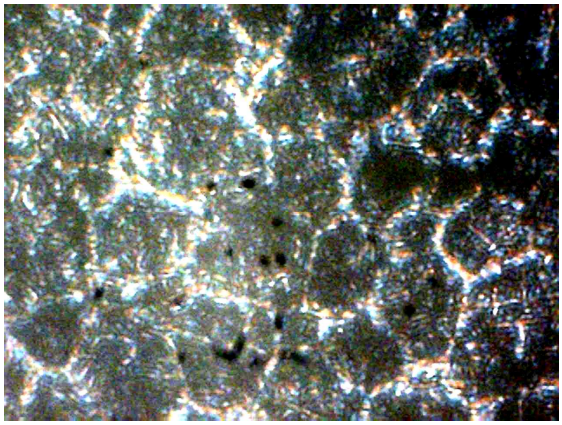

b) CuAl11Fe3Ni1.5 Co1 quenching 700^{o}C,2h, salt solution cooling

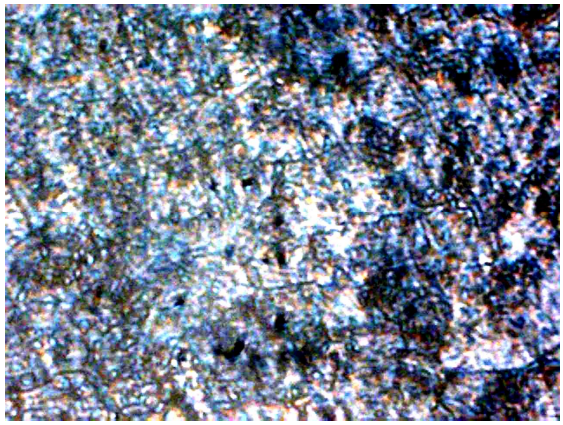

c) CuAl11Fe3Ni1.5 Co1 quenching 900^{o}C,2h, salt solution cooling

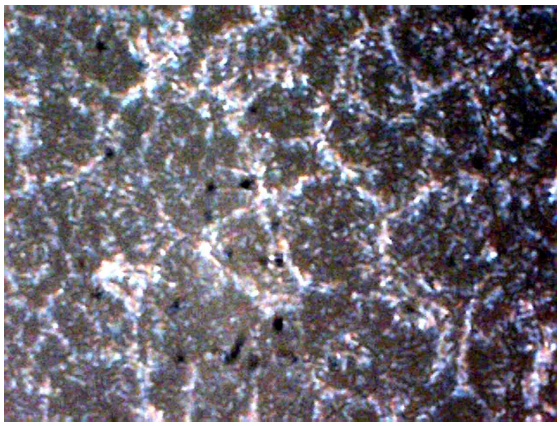

d) CuAl11Fe3Ni1.5 Co1 quenching 700^{o}C,2h, salt solution cooling, annealing 450 ^{0}C, 6h, air cooling,

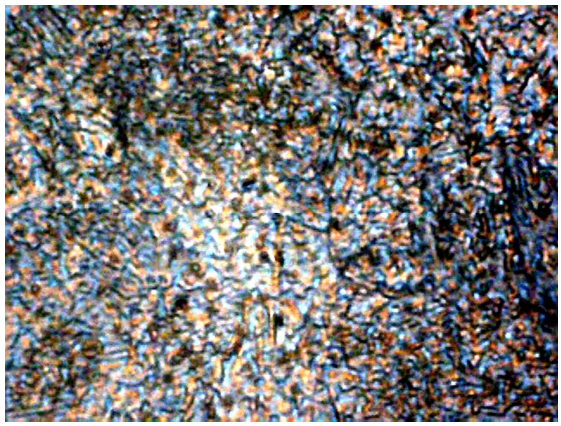

e) CuAl11Fe3Ni1.5Co1 quenching 900^{o}C,2h, salt solution cooling, annealing 300 ^{0}C, 4h, air cooling

Figure 3. Representative microstructures of Cu Al11Fe3Ni1.5Co1, depending on metallurgical processing.

.2 Microhardness measurements

The figures 4-6 below are a graphical representation of microhardness variations of the samples under survey, depending on the type of alloy and heat treatment.

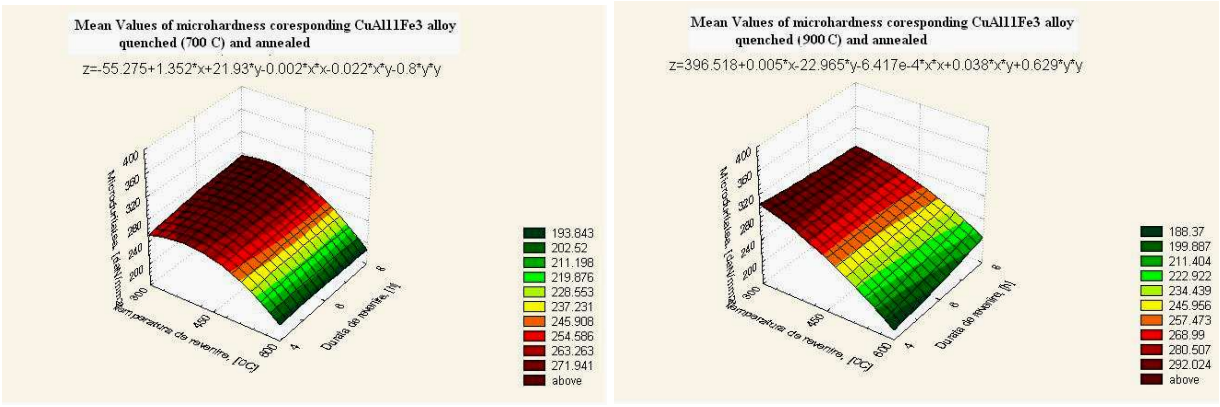

a) b)

Figura 4. Microhardness of CuAl11Fe3 alloy depending on the technological parameters of heat treatment

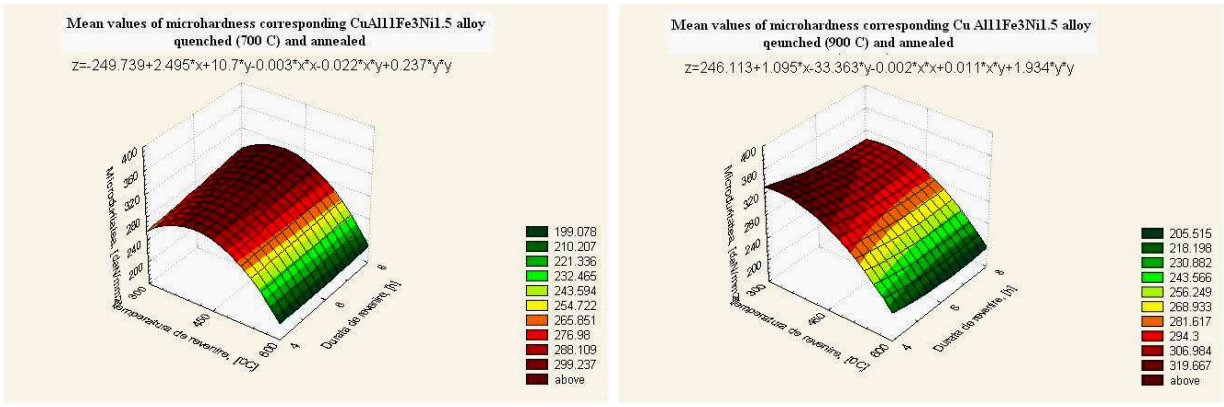

a) b)

Figura 5. Microhardness of CuAl11Fe3Ni1.5 alloy depending on the technological parameters of

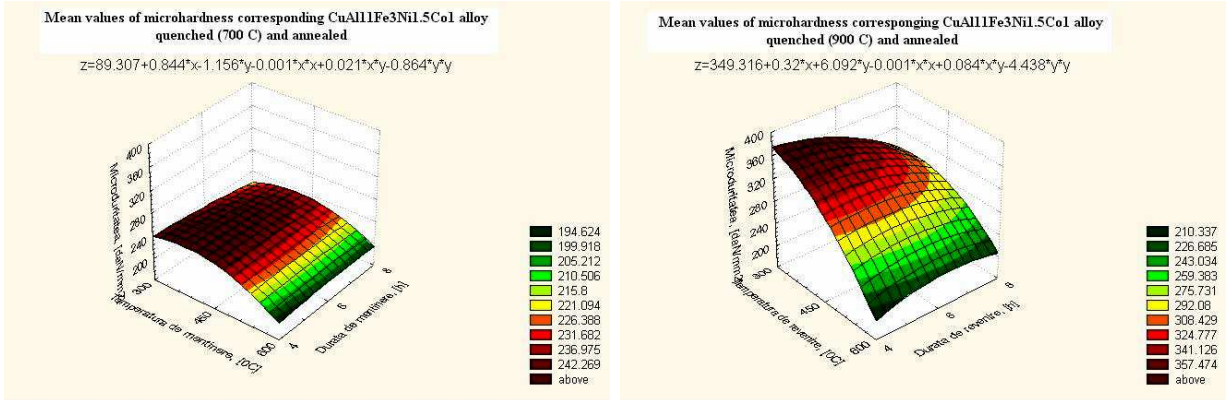

heat treatment

a) b)

Figura 6. Microhardness of CuAl11Fe3Ni1.5Co1 alloy depending on the technological parameters of heat treatment

The differences between the mean values of the microhardness of the three cast alloys are significant from the statistical standpoint.

After the first 700°C hardening, there are significant differences only between the mean values of the CuAl11Fe3Ni1.5Co1–CuAl11Fe3, CuAl11Fe3Ni1.5Co1-CuAl11Fe3Ni1.5 alloys. After the second 700°C hardening, there are significant differences between the mean values of the microhardness of the three alloys. For the

CuAl11Fe3 alloy there are no significant differences between the microhardness after the two hardenings. For the CuAl11Fe3Ni1.5, CuAl11Fe3Ni1.5Co1 the differences are significant. Regardless of the alloy, for the temperings after the first hardening, the hold temperature and its interaction with the hold time have a significant influence. The highest values are at hold temperatures between 300÷450°C and hold times between 6÷8 h. The lowest values are at a hold temperature of 600°C and a hold time of 6 h. For the temperings after the second hardening, the hold temperature and its interaction with the hold time have a significant influence on the CuAl11Fe3 alloy. For the temperings after the second hardening, the hold temperature and the hold time have a significant influence on the CuAl11Fe3Ni1.5 alloy. For the temperings after the second hardening, both the hold temperature and time and their interaction have a significant influence on the CuAl11Fe3Ni1.5Co1 alloy. The highest values, regardless of the alloy, are at a hold temperature of 300°C and a hold time of 4 h. The lowest values, regardless of the alloy, are at a hold temperature of 600°C, but for hold times between 4÷8 h.

4. Conclusions

The analysis of the microstructures and charts shown above enables us to conclude the following:

(1) the nickel and cobalt alloying elements have a significant influence on the microstructure and microhardness of the cast samples. The dendritic structure and microhardness of 196.17 daN/mm^2 of the CuAl11Fe alloy turn into a grain structure and a microhardness of 277.73 daN/mm^2 for the CuAl11FeNi1.5Co1 alloy;

(2) the samples hardened at 700°C and 900°C respectively, we noticed a refinement of the structure and an increase in microhardness with the addition of nickel and cobalt and with the increase of the hardening temperature;

(3) the tempered samples with the highest mean values of microhardness are those hardened at 900°C and tempered at 300°C, with a hold time of 4 hours.

Received April 30, 2007

(1) The "Gh.Asachi" Technical University Iaşi
(2) S.C. Petrotub S.A. Roman

References

1. Ienciu, M., s.a. *Elaborarea şi turnarea aliajelor neferoase speciale,* Ed. Did. şi Ped., Bucureşti, 1985
2. Ienciu, M., s.a. *Elaborarea şi turnarea aliajelor neferoase,* Ed. Did. şi Ped., Bucureşti, 1982
3. Geru, N., s.a. , *Analiza structurii materialelor metalice*, Editura Tehnică, Bucureşti, 1991
4. Popescu,N., s.a, *Tratamente termice şi prelucrări la cald,* Ed. Did. şi Ped., Bucureşti, 1983.

INFLUENȚA PARAMETRILOR TRATAMENTULUI TERMIC APLICAT UNOR BRONZURI CU ALUMINIU ASUPRA STRUCTURII SI MICRODURITĂȚII

Rezumat. Alegerea parametrilor tehnologici ai operațiilor de călire şi revenire depinde de compoziția chimică a aliajului şi de modul de variație a proprietăților in timpul precipitării fazelor secundare. În prezenta lucrare s-a cercetat, din punct de vedere structural şi al microdurității, influența unor parametri tehnologici ca temperatura şi timpul de menținere la călire şi revenire aplicate unor bronzuri cu aluminiu: $CuAl_{11}Fe_3$, $CuAl_{11}Fe_3Ni_{1,5}$ şi $CuAl_{11}Fe_3Ni_{1,5}Co_1$.

BULETINUL INSTITUTULUI POLITEHNIC DIN IAŞI
Tomul LIII (LVII), Fasc. 1, 2007
Secția
ŞTIINȚA ŞI INGINERIA MATERIALELOR

EFFECT OF Al_2O_3 AND GRAPHITE REINFORCEMENT PARTICLES IN THE ALUMINUM ALLOY PARTICULATE COMPOSITE

BY

GABRIELA POPESCU, PETRU MOLDOVAN, IOANA APOSTOLESCU and SIMONA BEJAN

Abstract: Discontinuously reinforced aluminium matrix composite have received much attention for both academics and manufacturing industries in the last years. Taking into consideration this new opportunities, the paper gives an overview of a National Research Project, **MAT – COM**, regarding the motivation, the objectives and the partnership. The research was focused to synthesis and characterization of new composite materials with aluminium alloy matrix reinforced with alumina (Al_2O_3) and graphite (whiskers) particles using liquid state processing. Two processing techniques will be experimented; first, will be the VORTEX technique, and second infiltration of aluminium matrix through alumina free power. Also, an experimental technique will be developed applying both gravity and centrifugal casting to melt composites. The processing techniques parameters will be presented and discussed.

Keywords: aluminium matrix, alumina particle, graphite particles, Vortex, infiltration

1. Introduction

During the past 40 years, materials design has shifted emphasis to pursue light weight, environment friendliness, low cost, quality, and performance. Parallel to this trend, metal-matrix composites (MMCs) have been attracting growing interest [1][2][3][4]. MMCs' attributes include alterations in mechanical behaviour (e.g., tensile and compressive properties, creep, notch resistance, and tribology) and physical properties (e.g., intermediate density, thermal expansion, and thermal diffusivity) by the filler phase; the materials' limitations are thermal fatigue, thermochemical compatibility, and low-transverse creep resistance.

The particulate reinforcements have been classified as the by-products from other technologies (e.g., SiC, SiO_2, Al_2O_3, aluminosilicates, graphite, and fly-ash) and are readily available or are naturally renewable at affordable cost (e.g., coconut shell char, mica, palm-kernel shell char, and zircon). Further, the potential nature of these filler materials is attractive.

The National Research Project, **MAT – COM**, put the basis of a powerful partnership formed by SC INTEC SA as coordinator, UPB-BIOMAT – P1, Technical University Cluj-Napoca – P2, 'Valahia' Univerity Targoviste – P3, 'Lucian Blaga' University Sibiu – P4, SC ICEM SA – P5, SC ICTCM SA – P6, INCD-ISIM – P7, IPMTB – P8 and SC UTTIS SRL – P9 having as motivation and objectives to provide results, information and solutions to MMCs and CMCs processing technologies, new applications worldwide spread of them and their mechanical, tribological, physical and electric properties.

2. Technique for obtaining composite materials

A. Vortex technique

The main techniques to obtain the mixing are:

- ✓ Introducing into the melt the reinforcing material by mechanical stirring;
- ✓ Injecting the particles into the alloy jet at the melt casting into shape with the help of an injection pistol;
- ✓ Adding of reinforcing materials into the liquid matrix by ultrasounds;
- ✓ Introducing the reinforcing materials into a metallic bath stirred electromagnetically;
- ✓ Centrifugal dispersion of the particles into the melt.

The composite mixture, metallic matrix – reinforcing materials, can be cast by conventional casting techniques, such as gravitational casting, casting under pressure and centrifugal casting, or techniques like, casting under pressure, spray deposition, ultra fast cooling or laser injection.

The method based on mechanical mixing of the components imposed by its simplicity and its relative low cost. The easiest way of obtaining consists in adding of reinforcing materials in the cone created into the melt, its mechanical stirring, with the help of a palette stirrer (**VORTEX technique**). The liquid alloy, representing the matrix, it is powerful stirred to create a vortex zone in which it is supplied Al_2O_3 or C (graphite), by specific dosage devices. Introducing progressively the reinforcing materials, the stirring intensity is lowered, a fact that imply an adjustment of the stirring rotation function of reinforcing material proportion introduced into alloy.

For metal matrix composite elaboration from Al alloys by Vortex method it exist the possibility of metallic melt oxidation at the surface. In order to avoid this melt oxidation it is necessary that the stirring, the one that increase the contact surface of melt with the air, to be done into a controlled atmosphere or in inert protection gas injection conditions over the metallic bath. The best results were obtained still for composite materials elaboration in vacuum.

The feeding and dispersion degree of the reinforcing material into the metallic matrix depends on stirring time. In the initial state, the reinforcing material can penetrate the melt as agglomerates, but due to continuous stirring take place its dispersion.

Even if the mechanical stirring methods give satisfactory results, there are some disadvantages that limit the usage of this technique:

- ✓ The possibility of adding a relative small proportion of reinforcing material, because, generally it is not always wetted properly by the liquid matrix; this determines the usage of special treating methods of reinforcing materials, which increase the cost price of composite material;
- ✓ The possibility of reinforcing material agglomerates during feeding and untotal dispersion of them when continuing stirring;
- ✓ Reinforcing materials fragmentation due to mechanical stresses at which they are subjected during stirring;
- ✓ Solid phase floated by binding to gas bubbles stirred into metallic bath.

In the mixing/vortex method, the pretreated and prepared filler phase is introduced in a continuously stirred molten matrix and then cast. The use of an inert

atmosphere or vacuum other than air is essential to avoid the entrapment of gases. Mixing can be affected ultrasonically or by reciprocating rods, centrifuging, or zero-gravity processing that utilizes an ultrahigh vacuum and high temperatures for long periods of time. A method of inertial injection has been developed for this process [5]. Difficulties, such as the segregation/settling of secondary phases in the matrix, agglomeration of ceramic particulate, particulate fracture during agitation, and extensive interfacial reactions, are often encountered. The DURAL process, which incorporates SiC and Al_2O_3 particles into molten aluminum, makes use of this method.

B. Infiltration

The infiltration process states in the existence of a porous preform from reinforcing material in which it is infiltrated the liquid alloy of the aluminium metallic matrix, the melt filling the interstitials and the preform pores (made of reinforcing material), resulting in this way the composite material. In figure 1 are presented two infiltration models.

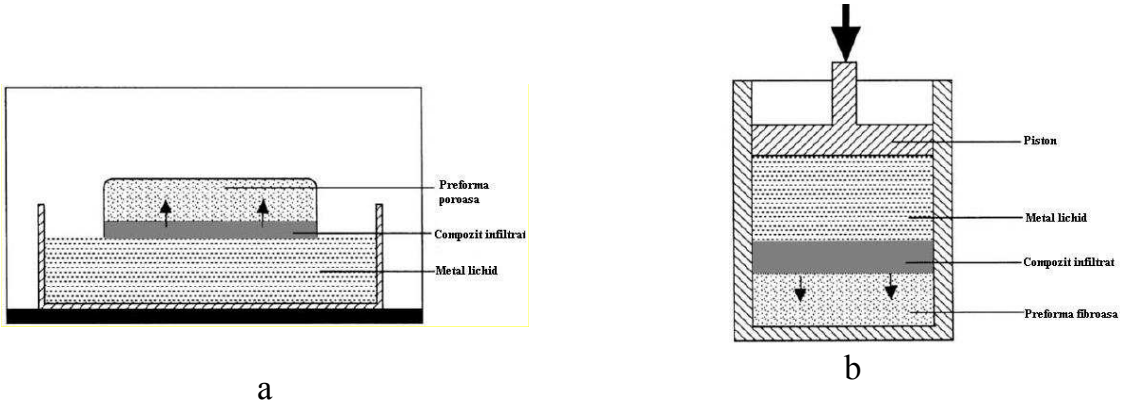

Fig.1. Schematic representation: a. Spontaneous infiltration; b. Infiltration under pressure

The considered parameters for infiltration are: initial composition, morphology, volume fraction, initial composition and the temperature of reinforcing material, the nature and amplitude of applied external force.

Infiltration under pressure is made to replace the insufficient wetting and to accomplish the mechanical load needed to force the liquid metal into the unwett matrix. Pressure can be applied by an inert gas, ex. Ar, or mechanically by a piston or a hydraulically press. Generally the pressure applied mechanically is greater than that applied by gas. The composites obtained by this method have generally a lower porosity. The major disadvantage of this technique would be the possibility of cracking or perform deformation due to the applied pressure.

The Al-Si alloy matrix composites reinforced with alumina were obtained by low pressure infiltration combined with a low vibration motion of 3kHz. The centrifugal casting methods were adapted to produce the tubular reinforcement of the metal. Also were studied the infiltration processes that use electromagnetic fields to infiltrate the material in preform.

A major advantage of infiltration process is that allows the obtaining of some complex shapes for parts totally or partially reinforced in a large frame of materials.

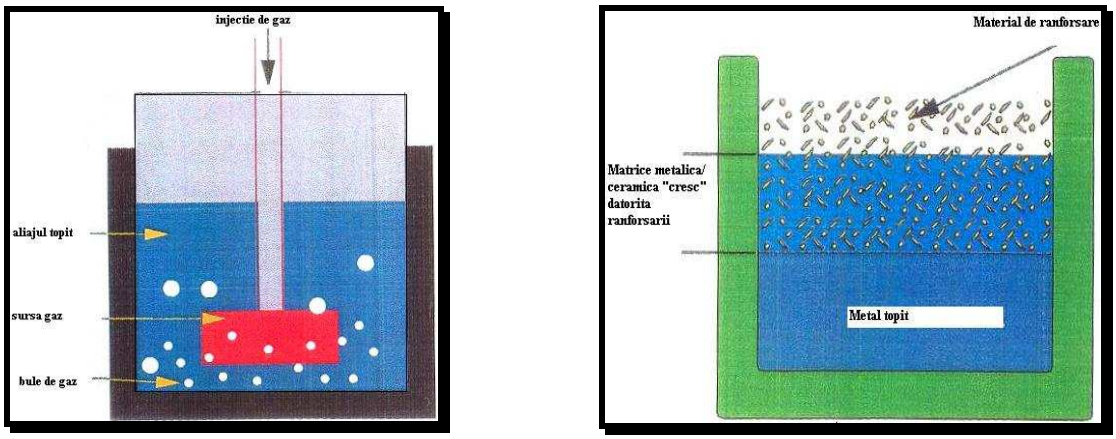

a *b*

Fig.2. Infiltration under pressure: a –in-situ method with gaseous reactants; b – Lanxide in-situ process principle

For parts reinforced in matrix at cold it is used high pressure and in this way can be reduced the reactions between the reinforcing material and matrix and there by can be obtained matrices without defects. A disadvantage of infiltration process is that the reinforcing material has to be a preform. The final product can be homogeneous due to infiltration or due to clusters formation from reinforcing material which can affect the mechanical properties of composite materials. To avoid or correct these defects will be requested a further preparation of the composites obtained and this operation will increase considerably the finite product price.

In infiltration, the molten metal penetrates a pretreated, formed, and prepared particulate bed or preform with pressure or without pressure (pressureless infiltration). In the latter case, however, the molten alloy infiltrates the reinforcement by percolation. This method is normally carried out in air, inert gas, or evacuated atmosphere. Mortensen et al. [6] have associated this technique with such disadvantages as reinforcement-reinforcement contact, structural distortion of the preform, large grain size, and undesirable interfacial reactions that culminate into microstructural inhomogeneity.

The first commercial application was the fabrication of aluminum-alloy diesel pistons containing alumina short fibers by Toyota Motor Corporation [7][8][9]. Squeeze casting was the primary manufacturing mode. Aluminum-alloy melt was poured into a porous alumina short-fiber preform inserted into a preheated die, and a squeeze pressure was applied in a hydraulic press. The composite aluminum pistons possessed better performance attributes than the unreinforced ones.

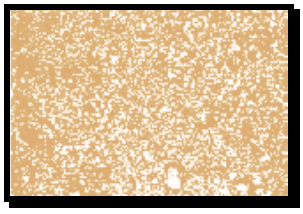

Fig.3. A micrograph of aluminium reinforced with Al_2O_3. Penetration of the molten metal was difficult because of wide particle-size distribution of the reinforcement. [10]

The major difficulty in the preparation of cast graphite/aluminum-alloy composites appears to stem from nonwetting of graphite by aluminum melts. The contact angle of aluminum with graphite is about 155°C and is reported to remain unwettable at temperatures between the melting point of aluminum and 1,080°C [11][12][13]. The major interest by scientists in the molten processing of this class of composites is, therefore, geared toward achieving good matrix-graphite wetting. The incorporation of coated graphite particles in a vortex through gas injection or with the aid of ultrasonic stirring and the addition of interfacial active elements [14][15] has been reported to yield good results, although this is associated with high indirect costs.

A simple and inexpensive vortex method has dispersed uncoated but heat-treated graphite particles into the LM13 melts at a temperature above the liquidus [11]. It was possible to disperse only 3 wt.% graphite, with a percentage recovery in the casting of 98%. No pores or voids are visible at the graphite-alloy interface, indicating good wetting. The tested mechanical properties of the composites containing up to 3 wt.% graphite are found to be adequate for several tribologic applications.

3. Effect of ceramic reinforcements on the behaviour of aluminium matrix in AMCs

Presence of relatively large (more than 10%) volume fraction of ceramic reinforcement (whisker/particle/short fiber/continuous fiber) profoundly effect the behaviour of aluminium matrix in aluminium matrix composites during manufacturing, heat treatment and their subsequent use in service [16][17][18]. These changes include both intrinsic and extrinsic ones.

Intrinsic effects

Intrinsic effects include microstructural changes, heat treatment characteristics and thermal stresses. These changes significantly alter and expand the physical, mechanical and tribologic property limits of aluminium alloys. Salient features of intrinsic effects caused by ceramic reinforcements are summarized below.

a) Solidification structure of AMCs: Presence of ceramic reinforcement can alter the solidification behaviour of aluminium alloys in several alloys. Ceramic reinforcement can serve as a barrier to diffusion of heat and solute, catalyze the heterogeneous nucleation of phases crystallizing from the melt, restrict fluid convection, and induce morphological instabilities in the solid–liquid interface.

b) Effect of ceramic reinforcement on the age-hardening characteristics of aluminium alloys: The age hardening characteristics of aluminium alloys are generally modified by the introduction of ceramic reinforcement. These modifications depend on the matrix composition, the size, the morphology and volume fraction of the reinforcement and the method of composite production.

Much of these changes in the age hardening characteristics of aluminium alloys due to the incorporation of ceramic reinforcement are attributed partly due to enhanced dislocation density. Large mismatch in the expansion coefficient of ceramic reinforcement and aluminium alloy matrix is responsible for increased density of dislocations. The increased density and consequent modifications in the age hardening

response of aluminium alloys is an important intrinsic effect of ceramic reinforcements.

c) Thermal residual stresses: Aluminium matrix composites often experience fabrication temperature in excess of 500^{o}C, and large thermal residual stresses are included on cooling. Magnitude of thermal residual stresses developed is related to many variables including the type of reinforcement, volume fraction, diameter and aspect ratio. Mechanical behaviour of AMCs is profoundly affected by thermal residual stresses. Presence of residual stresses caused by ceramic reinforcement results a symmetrical yielding, and also affects fatigue and creep behaviour of AMCs.

Extrinsic effects of ceramic reinforcement

Incorporation of ceramic reinforcement in Al alloys leads to significant improvement in the sliding wear resistance of Al MMCs as measured by the pin-on-disc set up against a hardened steel disc and this is attributed to the intrinsic effect of SiCp [19][20]. When AMC brake disc slides against brake pad adherent tribolayer are formed on the surface of AMC disc at the contact region. Tribolayers thus formed further enhances the wear resistance of the AMC discs. Tribolayers consisting of mixed oxides are formed due to transfer of material from the brake pad on to the AMC disc during sliding. Material transfer and formation of tribolayers is primarily caused by the SiCp which stands proud of the matrix on the surface of AMC disc. Hence, tribolayer formation is caused by the extrinsic effect of SiC reinforcement in AMCs.

4. Comparison between the wear behaviour of the Al/Al_2O_3 composite and Al/Al_2O_3/C metal matrix hybrid composite at room temperature and at high temperatures

The metallic matrix composite Al/Al2O3 and the hybrid composite Al/Al_2O_3/C were manufactured by infiltration by pressure method. The optimum aging time for Al/Al_2O_3/C composite was of 7 hours and the one for Al/Al_2O_3 composite lowered when the volume fraction grow up. The wear behaviour of these two aluminium matrix composite materials has been characterized by abrasive wear test in different conditions (volume fraction, sliding rate).

The composites wear resistance was improved by the presence of reinforcing elements. In order to analyze the wear mechanism, the surfaces subjected to wear were examined by SEM. The predominant mechanism of MMC's was the wear by adherent abrasion at all the sliding rates intervals at room temperature, and a different mechanism at high temperatures. The mechanism of wear by adherent abrasion was predominant at lower or intermediate sliding rates, and the melt and its wear by sliding were the predominant mechanisms at higher sliding rates.

The hybrid composite Al/Al_2O_3/C wear resistance it is a good one in condition of high sliding rates due to carbon solid lubrication [21][22].

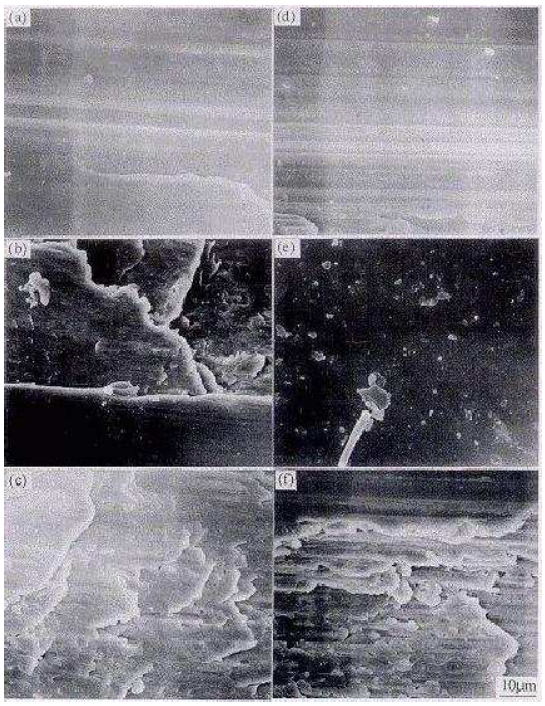

Figure 4. SEM analysis of surfaces subjected to wear mechanism

5. Conclusions

The major advantages of AMCs compared to unreinforced materials are as follows:

- ✓ Greater strength
- ✓ Improved stiffness
- ✓ Reduced density (weight)
- ✓ Improved high temperature properties
- ✓ Controlled thermal expansion coefficient
- ✓ Thermal/heat management
- ✓ Enhanced and tailored electrical performance
- ✓ Improved abrasion and wear resistance
- ✓ Control of mass (especially in reciprocating applications)
- ✓ Improved damping capabilities.

Received May 10, 2007 *The "Politehnica" University Bucharest*

REFERENCES

1. S.V. Nair, J.K. Tien, and R.C. Bates, **Intl. Met. Rev**., 31 (1985), p. 275.
2. P.K. Rohatgi, S. Ray, and Y. Liu, **Intl. Mater. Rev**., 37 (1993), p. 129.
3. K.K. Chawla, **Composite Materials Science and Engineering** (New York: Springer-Verlag, 1992) p. 102.
4. I.A. Ibrahim, F.A. Mohammed, and E.J. Lavernia, **J. Mater. Sci.,** 26 (1991), pp. 1137-1155.
5. B.M. Cox et al., in Ref. 15, pp. 88-99.
6. Mortensen, J.A. Cornie, and M.J.C. Flemings, **Metall. Trans.**, 19A (1988), p. 709.

7. T. Donomoto et al., SAE technical paper no. 83052 (Detroit, MI: SAE, 1983).
8. R. Kreibar, T. Morel, and M. Toaz, SAE paper 910632 (Detroit, MI: SAE, 1991).
9. D.J. Lloyd, **Intl. Mater. Rev**., 39 (1) (1994), pp. 1-23.
10. J. Yang and D.D.L. Chung, **J. Mater. Sci.**, 24 (1989), pp. 3605-3612.
11. B.P. Krishnan, M.K. Surappa, and P.K. Rohatgi, **J. Mater. Sci**., 16 (1981), pp. 1209-1216.
12. A.A. Baker***, Mater. Sci. Eng****.,* 17 (1975), p. 177
13. S. Das et al., **Mater. Trans***., JIM*, 32 (2) (1991), pp. 189-194.
14. F.A. Badia et al., **AFS Trans**., 79 (1971), p. 265.
15. V.G. Gorbunov et. al., **Russ. Cast Prod**., 8 (1974), p. 348.
16. Asthana R 1998 **Solidification processing of reinforced metals** (Trans. Tech. Publ.)
17. Clyne TW (ed.) 2000 *Comprehensive composite materials,* **Vol. 3. Metal matrix composites** (ser. eds) A Kelly, C Zweben (Oxford: Pergamon)
18. Clyne T W **2001 Metal matrix composites**: Matrices and processing. In *Encyclopedia of materials science and technology* (ed.) A Mortensen (Elsevier)
19. Clyne T W, Withers P J 1993 *An introduction to metal matrix composites* (Cambridge: University Press)
20. Lloyd D J 1999 *Particle reinforced aluminium and magnesium matrix composites*. **Int. Mater. Rev**. 39: 1–23
21. Maruyama B 1998 *Progress and promise in aluminium metal matrix composites*. **The AMPTIAC NewsLett.** 2(3):
22. Surappa M K, Rohatgi P K 1981 *Preparation and properties of aluminium alloy ceramic particle composites*. **J. Mater. Sci.** 16: **983–993**

EFECTELE PARTICULELOR DE ARMARE AL_2O_3 ŞI GRAFIT ASUPRA COMPOZITELOR CU MATRICE DIN ALIAJ DE ALUMINIU

Rezumat: "Compozitele cu matrice de aluminiu armate cu particule discontinue au primit o deosebită atenție în ultimii ani atât în mediul universitar cât şi în cel industrial. Luând în calcul noile posibilități, această lucrare prezintă Proiectul Național de Cercetare **MAT – COM**, privind motivația, obiectivele şi parteneriatul. Cercetarea s-a bazat pe sinteza şi caracterizarea noilor materiale compozite cu matrice de aluminiu armate cu particule de alumină (Al_2O_3) şi grafit (whiskers) folosind procesarea în stare lichidă. Două tehnici de procesare vor fi experimentate; prima va fi cea a procedeului VORTEX, iar a doua va fi infiltrarea matricei de aluminiu în pulberea liberă de alumină. De asemenea, o tehnică experimentală va fi efectuată aplicând atât turnarea gravitațională cât şi cea centrifugală a compozitelor topite. Vor fi discutați şi prezentați parametrii de procesare tehnologică.